Institut für Strömungsmechanik
und Elektronisches Rechnen im Bauwesen
der Leibniz Universität Hannover

Bericht Nr. 75/2008

Stefan Schimmels

Numerical Simulation of the Influence of Circular Cylinders on Mixing and Entrainment in Natural Density Currents

ISSN 0177 − 9028

Institut für Strömungsmechanik
und Elektronisches Rechnen im Bauswesen
Leibniz Universität Hannover
Appelstraße 9a, D-30167 Hannover

Tel.: +49 − 511 − 762 − 3568
Fax.: +49 − 511 − 762 − 3777
URL: http://www.hydromech.uni-hannover.de

Von der Fakultät für Bauingenieurwesen und Geodäsie der Leibniz Universität Hannover zur Erlangung des Grades Doktor-Ingenieur genehmigte Dissertation.

Referent: apl. Prof. Ph.D., habil. Mark Markofsky
Koreferent: Prof. Dr. Hans Burchard

Tag der Promotion: 21. Dezember 2007

Abstract

The present work is concerned with the determination of the impact of circular cylinders on the dilution of density currents, motivated by the planned errection of offshore wind farms in the Baltic Sea. The analysis is mainly based on fully three-dimensional numerical simulations and the physical background of the model with special emphasis on the nature and modeling of turbulence is explained in detail first. Additionally the numerical methods used to solve the governing equations are shortly described.

The core of the work begins with a discussion of the basic principles of the cylinder flow and a first validation of the numerical model with laboratory measurements from the literature for the neutral density shear-free flow around a circular cylinder. Afterwards the general effects of stratification on the flow will be introduced and essential parameters to describe these effects are worked out. By the example of wind-induced mixing of a stably stratified fluid essential parameters for the numerical simulation of density currents are determined. A thoroughly derived depth-integrated theory provides the basis for an analysis of undisturbed density currents and for the validation of the numerical model to simulate these currents. Additional simulations of fundamental flow configurations and the comparison with field measurements in the Arkona Basin in the Baltic Sea provide the necessary credibility for the present numerical model to simulate the additional cylinder induced entrainment rates.

The impact of a circular cylinder on the dilution of a density current is finally investigated by numerical simulations on a natural scale. The resulting flow field, entrainment rates and mixing efficiencies are analyzed and the influence of the governing parameters for the flow are investigated. The cylinder Reynolds number in the present order of magnitude shows up to be an unimportant parameter but entrainment clearly depends on the densimetric Froude number and the current depth to cylinder diameter ratio. If earth rotation and Coriolis forces are considered the Ekman number is a further governing parameter. By a principal analysis it is shown that the local impact of the cylinder is quite significant but the global effect of offshore wind farms on density currents in the Baltic Sea turns out to be rather small.

Zusammenfassung

Die vorliegende Arbeit befasst sich mit der Bestimmung des Einflusses von Kreiszylindern auf die Durchmischung von Dichteströmungen, motiviert durch die geplante Errichtung von Offshore Windparks in der Ostsee. Der Schwerpunkt liegt auf voll dreidimensionalen numerischen Simulationen, so dass zunächst die physikalischen Grundlagen des Modells und insbesondere das Phänomen von Turbulenz und deren Modellierung ausführlich erläutert werden. Zusätzlich werden die numerischen Methoden zur Lösung der Grundgleichungen kurz beschrieben.

Der eigentliche Kern der Arbeit beginnt mit einer Betrachtung der grundlegenden Prinzipien der Zylinderumströmung und einer ersten Validierung des numerischen Modells anhand von Labormessungen aus der Literatur für eine dichteneutrale, ungescherte Strömung um einen Kreiszylinder. Anschließend wird der generelle Einfluss einer Dichteschichtung auf die Strömung vorgestellt und die wesentlichen Parameter zu deren Beschreibung herausgearbeitet. Anhand der windinduzierten Durchmischung einer stabilen Dichteschichtung werden entscheidende Größen für die numerische Simulation von Dichteströmungen bestimmt. Die Herleitung einer tiefenintegrierten Theorie bildet schließlich die Grundlage für eine prinzipielle Analyse unbeeinflusster Dichteströmungen und für die Validierung des numerischen Modells. Zusätzliche Prinzipstudien und der Vergleich mit Naturmessungen im Arkona Becken in der Ostsee geben dem verwendeten numerischen Modell die nötige Glaubwürdigkeit für die Simulationen der zylinderinduzierten Einmischung.

Der Einfluss eines Kreiszylinders auf die Durchmischung einer Dichteströmung wird schließlich anhand numerischer Simulationen im Naturmaßstab untersucht. Das Strömungsfeld, Einmischungsraten und Mischungseffizienz werden analysiert und der Einfluss der bestimmenden Parameter wird untersucht. Dabei stellt sich heraus, dass die Reynoldszahl in der vorliegenden Größenordnung einen unbedeutenden Parameter darstellt, aber die Einmischung eindeutig von der densimetrischen Froudezahl und dem Verhältnis zwischen der Dicke der Strömung und dem Zylinderdurchmesser abhängt. Die Untersuchung zeigt, dass die lokale Einwirkung des Zylinders zwar signifikant ist, der globale Einfluss von Offshore Windparks auf Dichteströmungen in der Ostsee aber eher gering ausfällt.

Content

1 Introduction

1.1 General

Density currents also referred to as gravity currents or buoyancy currents are a common phenomenon in nature and man-made situations. These currents are driven by buoyancy when an external force field like gravity acts on small differences in density in liquids or gases. From this definition it is apparent that all three terminologies above are comparably meaningful. Although there is some tendency in the literature to use the synonym 'gravity current', for the present thesis 'density current' has been preferred. Not only because a quick search on www.google.com supports this choice[1] but much more because it is felt that gravity is only one possible (even though the most common) source for an external force field while the difference in density is a unique property of these currents.

A density difference can either exist between two fluids or between different parts of the same fluid caused by a difference in temperature, salinity, or concentration of suspended sediment. A nice example from everyday life can be observed when a window or door is opened on a cold day and the warm lighter air from inside flows out through the upper part of the opening while below the cold heavier air from outside flows into the room. It can be recommended to try out this interesting experiment at home by detecting the current with a candle or puffs of smoke.

Anyway, from a scientific point of view this example might be of rather limited interest but there are many density currents in natural situations and industrial applications which have received much attention in the past and might gain even more in the future. The pioneering experimental work of Ellison & Turner (1959), for instance, was inspired by the desire for a theoretical description of methane gas

[1] about 160000 results for "density current",
about 54900 results for "gravity current".

climbing up the roof of coal mines. Many other examples of density current phenomena are discussed in the review work of Simpson (1987). Atmospheric currents like thunderstorm outflows which result from the cold air in the core of the thunderstorm propagating into the warmer surroundings or sea breeze fronts occurring when the air above the land is heated by the sun and cooler air from the sea flows inland. Oceanic currents like the well known Gulf Stream or turbidity currents caused by the slumping of sediments that have accumulated at the head of a submarine canyon. Comparable to the latter are volcanic lava flows or avalanches which can also be considered as density currents, although here the terminology gravity current might be better suited.

1.2 Motivation

The major emphasis of the present thesis lies on density currents in the Baltic Sea which occur a few times per year. A map of the Baltic Sea is shown in Figure 1.1 where also the presumable pathways of the density currents are sketched by the full and dashed lines. Before the nature of these currents and the motivation for this thesis is briefly discussed, however, it might be useful first to make some general comments on the characteristics of the Baltic Sea.

The Baltic Sea can be regarded as the largest Fjord in the world and as such it is an enclosed brackish inland sea connected to the North Sea by the Danish straits made up of Kattegat and Skagerrag. Brackish waters are saltier than fresh water but less salty than sea water. An enclosed Fjord is constantly filled by fresh water through river runoff from the surrounding continent and at the same time it is connected to the salty waters of the open ocean. The average salinity in the upper layers of the Baltic Sea is about 8 PSU[1] and is a result of the mixing process between the fresh river water (and rainfall) with the saline water from the open ocean with an average salinity of about 35 PSU.

[1] PSU: Practical Salinity Unit. 1 PSU corresponds to about 1 ‰ salt which is the former definition for salinity, see chapter 2.5 for details.

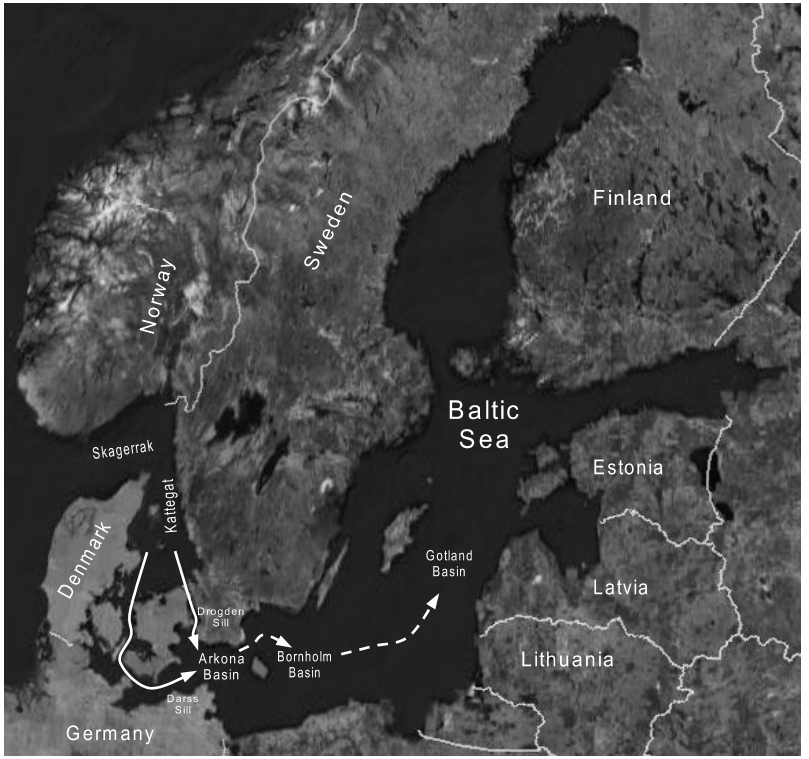

Figure 1.1: Map of the Baltic Sea (©2007 Google™) with sketched pathways of dense bottom currents.

In a usual situation the lighter brackish waters of the Baltic Sea flow out to the North Sea in a surface layer while the heavier ocean waters enter the Baltic Sea as a dense bottom current. These currents however, are most intense in the Danish straits where they are subject to intense mixing and are constantly diluted by the lighter brackish waters above. Due to the resulting small density difference in height of Darss and Drogden Sill and the Arkona Basin, respectively these currents will not penetrate far into the bottom layers of the central Baltic Sea but are very soon completely mixed with the almost stagnant lighter upper layer. The dashed lines in Figure 1.1 are therefore not representative for the usual situation where all dynamics are more or less restricted to the surface layer. Much more they correspond to special situations

which are very intensive inflow events occurring on an inter-annual time scale (major inflows) or slightly less intense inflow events occurring a few times per year (medium inflows). Both are important for the natural chemical and biological balance of the central Baltic Sea, as to be discussed next.

Typical for the Baltic Sea is the topographical subdivision into basins that have formed during the last ice age. From the topographical map of the southern part of the Baltic Sea in Figure 1.2 the Arkona Basin, Bornholm Basin and Gotland Basin denoted in Figure 1.1 can be clearly identified by the contour lines. It is further seen that the average depth in the Arkona Basin is about 50 m, in the Bornholm Basin about 100 m and in the Gotland Basin, representative for the central Baltic Sea, it is around 200 m.

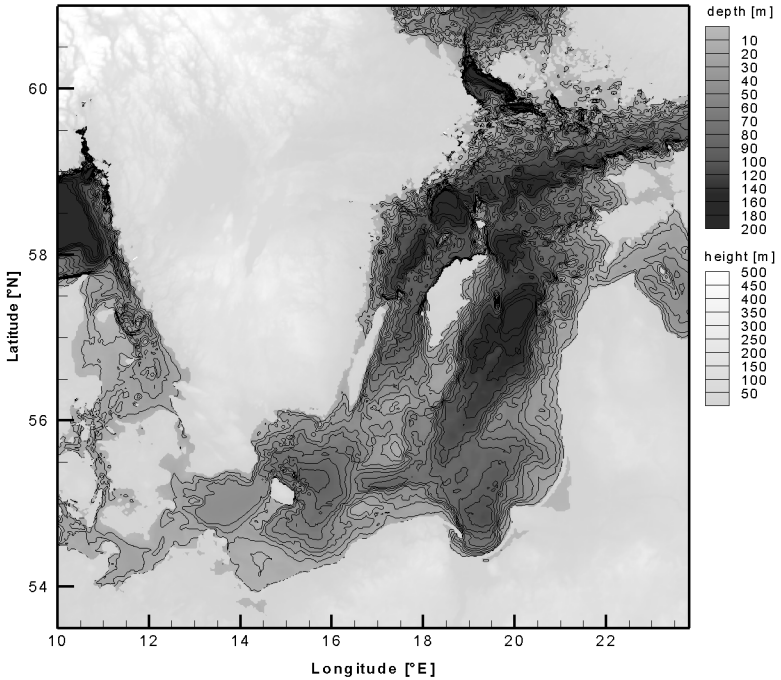

Figure 1.2: Topography contours for the southern Baltic Sea.

As mentioned above in a normal situation all dynamics are restricted to the surface layer and the bottom waters below remain more or less untouched. This leads to the formation of a halocline (large salinity (density) change over small vertical distance) which further prevents mixing of the bottom layers. The stagnant waters below the halocline suffer from an oxygen deficit caused by mineralization of organic matter as recently discussed for the eastern Gotland basin by Nausch et al. (2003). The only mechanism to ventilate the halocline and replace the deep waters in the central basins of the Baltic Sea with oxygen rich waters from the North Sea are major and medium inflow events which have been intensively investigated in the past years (e.g. Matthäus & Franck (1992), Feistel et al. (2003), Burchard et al. (2005)).

Unlike in the normal situation the more intense events are driven by a sea level difference between the Kattegat and the Baltic Sea such that the saline North Sea water is advected towards and over Darss and Drogden Sill and continues to flow into the Arkona basin. Following the definitions of Matthäus & Franck (1992) the density difference between these current and the ambient Baltic Sea at the sills must be at least about 7 kg/m³ and is usually 30 – 70 % higher. As the current travels down the depth contours into the Arkona Basin and further on, it is constantly diluted by the surrounding lighter waters such that the density difference and hence the driving force for the current is steadily decreasing.

The density anomaly of medium inflow events often ranges between 7 and 8 kg/m³ in the Bornholmgatt, the connection between the Arkona Basin and Bornholm Basin (see Figure 1.1). This is regarded to be sufficient for the current to further penetrate into the intermediate layers of the Bornholm Basin and probably even reach the eastern Gotland Basin (Burchard et al. (2005)). Although the occurrence of major inflow events slightly decreased over the last decades (Matthäus & Franck (1992), Feistel et al. (2003)) it can be assumed that the unaffected ecosystem of the Baltic Sea still benefits from a frequent refreshment of the deep waters of the Baltic proper by oxygen rich bottom currents from the North Sea.

However, in line with the European wide pushing of renewable energies several offshore wind energy farms are planned to be installed in the Baltic Sea especially within the Arkona Basin. Thus, the question arises how these man made structures

will enhance the mixing of dense bottom currents passing the wind farms and consequently influence the ecological balance of the central Baltic Sea. This question is the keynote for the present thesis and even if in principle several constructions are thinkable for the foundation of an offshore wind energy device (see e.g. GIGAWIND (2004)) the major emphasis here is on monopiles which are further idealized as a circular cylinder. This alleged simplification is not only made as monopiles are the most common foundation but much more because it provides the best way to generally analyze the basic processes involved and further allows for a transformation of the results to other situations.

1.3 Structure of the thesis

In order to investigate the influence of circular cylinders on the mixing of density currents in this thesis only numerical methods are used. The general physical background and the governing differential equations for these models are presented in chapter 2. Turbulence is the major cause for mixing and as such it plays a major role in the present work. Due to its randomness and the small scales involved it is impossible to directly account for turbulence in a numerical model. Thus, chapter 3 starts with an introduction of the nature of turbulence which is followed by a thorough discussion of the state of the art in turbulence modeling with emphasis on the Reynolds averaged Navier-Stokes equations which are the base for this thesis. The numerical methods to solve the governing equations are subsequently illustrated in chapter 4.

The next chapters are dedicated to the validation of the numerical model and the introduction to the relevant physical processes of the present problem. Chapter 5 deals with the unstratified flow around a circular cylinder. After a summary of the characteristics of this special kind of flow numerical simulations with the present model are compared to data from the literature and the advantages and drawbacks of different turbulence models will be worked out. In chapter 6 the influence of stratification is discussed and relevant parameters for stratified flows are introduced. The concept of entrainment to describe the effect of mixing is explained and finally the numerical model is validated against a simple wind entrainment experiment in

order to show its general capability for the simulation of stratified flows. This validation will also be used to show the strengths and weaknesses of the individual turbulence models for stratified flows and to get a first hint for the appropriate model in order to simulate the flow of density currents around a circular cylinder.

However, before the effects of cylindrical structures on density currents are analyzed in detail it is useful first to understand the physics of unaffected natural density currents and approve the ability of the numerical model to simulate them. This is done in chapter 7 where a depth integrated theory for undisturbed density currents under the influence of Coriolis forces is derived and the numerical model is successfully validated against this theory. A comparison of the numerical results with measurements of a density current in the Arkona Basin north of Kriegers Flak will provide further credibility into the numerical model, but it will also turn out that the two-equation turbulence models used here provide unphysical results if Coriolis forces are not present. However, in view of a general analysis of the influence of a circular cylinder on density currents it is desirable to neglect Coriolis forces at first and it will finally be shown that the discrepancies of the two-equation models can be tolerated if only a part of the current is regarded in a finite three-dimensional channel.

After the physical background has been thoroughly discussed and the numerical model has been extensively validated against theory and measurements chapter 8 at last deals with additional entrainment induced by circular cylinders. First Coriolis forces are neglected to analyze the basic flow features and the principal mechanisms of entrainment behind the cylinder without the effect of secondary currents in the undisturbed flow field. The results are influenced by many parameters the most important being the Froude number and the ratio of current depth to cylinder diameter. As the numerical simulations are computationally very expensive it is not possible to investigate all aspects in detail but it was tried to work out the basic principles by representative examples. Finally some additional simulations in a rotating frame of reference with the effect of Coriolis forces will show that the flow topology behind the cylinder is indeed much more complex but the entrainment rates are comparable to those presented before in a fixed frame without Coriolis forces.

1.4 Notation

The mathematical expressions to explain the physics in this thesis are all derived in a Eulerian frame of reference, i.e. all variables like velocity, pressure or salinity depend on time and space and spatial coordinates are fixed. Assuming a Cartesian coordinate system with coordinates x, y, and z the velocity in x-direction for instance is actually $u(t, x, y, z)$. However, to make the equations better readable the dependency on time and space is taken to be self evident and the expression in brackets is omitted. In this case the velocities in x-, y-, and z-direction are usually denoted by u, v, and w, but the resulting equations can still be quite long and hard to interpret. Therefore unless not otherwise mentioned index notation is exclusively used to further condense the writing. By that the spatial coordinates x, y, z are replaced by indices 1, 2, 3 and a vector (e.g. the velocity vector) can be written as

$$u_i = \left[u_1, u_2, u_3,\right]^T = \left[u_x, u_y, u_z\right]^T = \left[u, v, w\right]^T ,$$

while a matrix (e.g. the stress tensor in the momentum balance (2.2)) simplifies to

$$\tau_{ij} = \begin{bmatrix} \tau_{11} & \tau_{12} & \tau_{13} \\ \tau_{21} & \tau_{22} & \tau_{23} \\ \tau_{31} & \tau_{32} & \tau_{33} \end{bmatrix} = \begin{bmatrix} \tau_{xx} & \tau_{xy} & \tau_{xz} \\ \tau_{yx} & \tau_{yy} & \tau_{yz} \\ \tau_{zx} & \tau_{yz} & \tau_{zz} \end{bmatrix} .$$

Index notation allows for further simplifications if Einstein summation convention is used which means that if an index variable appears twice it implies summing up over all possible index values. Taking the incompressible mass balance (2.6) as an example it appears that

$$\frac{\partial u_j}{\partial x_j} = \frac{\partial u_1}{\partial x_1} + \frac{\partial u_2}{\partial x_2} + \frac{\partial u_3}{\partial x_3} = \frac{\partial u}{\partial x} + \frac{\partial v}{\partial y} + \frac{\partial w}{\partial z} ,$$

which is a significant reduction of the complete expression.

2 Theory

2.1 Governing equations

Any flow is governed by the principle of mass balance and momentum balance. In the most general form these are expressed as:

$$\frac{\partial \rho}{\partial t} + \frac{\partial \rho u_j}{\partial x_j} = 0 \,, \tag{2.1}$$

$$\frac{\partial \rho u_i}{\partial t} + \frac{\partial \rho u_i u_j}{\partial x_j} = \frac{\partial \tau_{ij}}{\partial x_j} - \frac{\partial p}{\partial x_i} + \rho g_i + F_i \,, \tag{2.2}$$

where

ρ	: fluid density [kg/m³]
u	: velocity [m/s]
τ_{ij}	: stress tensor [N/m²]
p	: pressure [N/m²]
g	: external force per unit mass (e.g. gravity) [m/s²]
S_m	: mass source [kg/m³s]
F	: external body force [N/m³].

If the fluid is assumed to be Newtonian, such as air and water, the stress tensor τ_{ij} linearly depends on the rate of strain in the fluid with the constant of proportionality being the molecular viscosity μ of the fluid. Hence, the stress tensor can be expressed as

$$\tau_{ij} = \mu \left(\frac{\partial u_i}{\partial x_j} + \frac{\partial u_j}{\partial x_i} \right) - \frac{2}{3} \mu \frac{\partial u_k}{\partial x_k} \delta_{ij} \,. \tag{2.3}$$

where the first term on the right hand side is given through twice the rate of strain tensor and the second term is governed by the volumetric strain rate that will vanish under the incompressibility assumption as shown in the next section. The rate of strain is a symmetric tensor given by

$$S_{ij} = \frac{1}{2}\left(\frac{\partial u_i}{\partial x_j} + \frac{\partial u_j}{\partial x_i} \right). \tag{2.4}$$

The molecular viscosity μ as well as the density ρ are actually functions of the local thermodynamic state, i.e. pressure and temperature. Any other dissolved or undissolved quantity like salt or sediments, respectively, will also influence the fluid properties.

Viscosity varies the strongest with temperature for most fluids. For example the viscosity of water decreases at a rate of about 3 % per degree temperature rise and for air it increases by about 0.3 % per degree rise. However, if temperature differences are small within the fluid, then μ can assumed to be constant and taken outside the derivative in (2.2). It should be noted that the influence of the molecular viscosity on the flow decreases with increasing turbulence intensity and hence can be even completely neglected in medium to strong turbulent flows (cf. chapter 3).

Equations (2.1) and (2.2) are the most general form of the Navier-Stokes equations as derived independently by Claude Louis Navier in 1822 and George Gabriel Stokes in 1845. In the following some simplifications to these equations will be introduced and some extensions regarding gravity currents are presented to finally arrive at the set of governing equations relevant in this thesis.

2.2 Incompressibility

To investigate the effect of incompressibility on the governing equations it is useful to start with rewriting the conservation of mass equation (2.1) in terms of a moving (Lagrangian) frame of reference as:

$$\frac{1}{\rho}\frac{D\rho}{Dt}+\frac{\partial u_j}{\partial x_j}=0\,. \tag{2.5}$$

It becomes clear that density is only important for mass conservation if its material derivative, i.e. the rate of change following a fluid particle, per unit mass has the same order of magnitude as the divergence of velocity. Except for pressure all other density influencing quantities are transported by the flow and will never yield large enough density gradients. However, pressure variations can be quite significant locally, provided the Mach number, which expresses the relation between the fluid velocity and the speed of sound, is high enough. High enough in this context means that the fluid velocity is at most 30 % of the speed of sound. For example, in air maximum velocities of 100 m/s still allow for the incompressibility assumption and water remains incompressible even up to 300 m/s. Since all considered velocities here are much smaller the fluids can be regarded as incompressible without objection.

If the left hand side of equation (2.2) is further simplified by use of (2.1) the mass and momentum balance for an incompressible fluid can be written as:

$$\frac{\partial u_j}{\partial x_j}=0\,, \tag{2.6}$$

$$\rho\left(\frac{\partial u_i}{\partial t}+u_j\frac{\partial u_i}{\partial x_j}\right)=\frac{\partial}{\partial x_j}\mu\left(\frac{\partial u_i}{\partial x_j}+\frac{\partial u_j}{\partial x_i}\right)-\frac{\partial p}{\partial x_i}+\rho g_i+F_i\,, \tag{2.7}$$

Due to the incompressibility assumption density completely disappears from the mass balance (2.6). The major impact on the momentum equation (2.7) comes from the stress tensor (2.3) where the second term on the right hand side vanished because of the incompressible mass balance. All other terms remain unaffected by the incompressibility assumption and density is still present as a flow variable. However, also the momentum balance can be further simplified under the assumption that density changes are small as will now be explained in the next section.

2.3 Boussinesq approximation

By the incompressibility assumption density disappeared in the mass balance equation whereas it is still kept in the momentum balance. Boussinesq (1903) suggested that if density changes are small they can be neglected except in the gravity term.

If a state of reference is assumed with constant density ρ_0 everywhere and a reference pressure p_0 given by $\partial p_0 / \partial x_j = \rho_0 g$, density and pressure can be written as $\rho = \rho_0 + \Delta\rho$ and $p = p_0 + \Delta p$, where $\Delta\rho$ and Δp are small perturbations from the state of reference. Subtracting this state from (2.7) and assuming μ to be constant one obtains

$$\left(1+\frac{\Delta\rho}{\rho_0}\right)\left(\frac{\partial u_i}{\partial t}+u_j\frac{\partial u_i}{\partial x_j}\right)=\nu\frac{\partial}{\partial x_j}\left(\frac{\partial u_i}{\partial x_j}+\frac{\partial u_j}{\partial x_i}\right)-\frac{1}{\rho_0}\frac{\partial \Delta p}{\partial x_i}+\frac{\Delta\rho}{\rho_0}g_i+\frac{1}{\rho_0}F_i, \qquad (2.8)$$

where $\nu = \mu/\rho_0$ is the kinematic viscosity.

From (2.8) it becomes clear that small changes in density only slightly alter the inertia terms on the left hand side and can be neglected there. However, together with gravity density differences are very important and cannot be neglected. They define the buoyancy force $\left(\Delta\rho/\rho_0\right)g_i$ which e.g. drives the convective motion if a layer of fluid is heated. For a density current it can be seen that it obeys exactly the same principles like open channel flow except for the fact that everything does not happen under full gravity but in a reduced gravity field as expressed by the buoyancy force term. Provided mixing with the ambient fluid is small (for open channel flow it is actually zero) all well known phenomena like hydraulic jumps or backwater curves can be transferred to density currents with the only difference of enlarged length and time scales.

Reintroducing the state of reference in (2.8), the Navier-Stokes equations under the Boussinesq assumption can be written as:

$$\frac{\partial u_j}{\partial x_j} = 0\,, \tag{2.9}$$

$$\frac{\partial u_i}{\partial t} + u_j \frac{\partial u_i}{\partial x_j} - \nu \frac{\partial^2 u_i}{\partial x_j \partial x_j} = -\frac{1}{\rho_0}\frac{\partial p}{\partial x_i} + \frac{\rho}{\rho_0} g_i + \frac{1}{\rho_0} F_i\,, \tag{2.10}$$

The viscous stress term has been simplified making use of the incompressible mass balance (2.9). Then it has been brought to the left hand side of (2.10) in order to show that the momentum balance can be interpreted as a transport equation in which momentum is transported by advection and diffusion and altered by source and sink terms on the right hand side. The kinematic viscosity $\nu = \mu/\rho_0$ thus plays the role of a diffusivity for momentum.

2.4 Rotating frame of reference

The equations of motion as derived so far are valid in a fixed or inertial frame of reference. However, one often is confronted with a rotating reference frame like in engineering applications with impellers in mixing tanks or rotating turbo machinery blades or, as in the present case, in geophysics with large scale flows on the rotating earth. The coordinate system which is assumed here is fixed on the earth surface with the *x*-axis pointing eastwards, the *y*-axis pointing northwards and the *z*-axis pointing vertically upwards. The speed of rotation is defined by the angular velocity of the earth which is approximately

$$\omega = \frac{2\pi}{86164\ \mathrm{s}} = 7.2921 \cdot 10^{-5}\ \frac{1}{\mathrm{s}}\,. \tag{2.11}$$

As sketched in Figure 2.1 the origin of the inertial coordinate system (index *i*) is assumed to be located in the geocenter and the position vector $\vec{r}$ is pointing to the rotating coordinate system (index *r*). Any vector $\vec{\phi}^{(i)}$ in the inertial coordinate system is related to the vector $\vec{\phi}^{(r)}$ in the rotating coordinate system by

$$\vec{\phi}^{(i)} = \vec{\phi}^{(r)} + \vec{\omega} \times \vec{r}\ . \tag{2.12}$$

Furthermore, the rate of change of any vector in the systems obeys

$$\left(\frac{d\vec{\phi}^{(i)}}{dt}\right)^{(i)} = \left(\frac{d\vec{\phi}^{(i)}}{dt}\right)^{(r)} + \vec{\omega}\times\vec{\phi}^{(i)}. \tag{2.13}$$

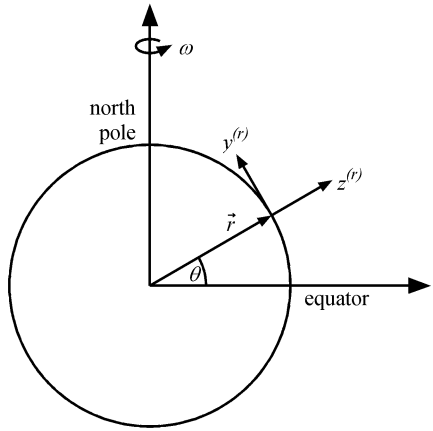

Figure 2.1: Definition sketch of the rotating coordinate system on the earth.

Applying (2.13) on the velocity vector and using relation (2.12) one obtains

$$\begin{aligned}\left(\frac{d\vec{u}^{(i)}}{dt}\right)^{(i)} &= \left(\frac{d\left(\vec{u}^{(r)}+\vec{\omega}\times\vec{r}\right)}{dt}\right)^{(r)} + \vec{\omega}\times\left(\vec{u}^{(r)}+\vec{\omega}\times\vec{r}\right)\\ &= \left(\frac{d\vec{u}^{(r)}}{dt}\right)^{(r)} + \left(\frac{d\vec{\omega}}{dt}\right)^{(r)}\times\vec{r} + \vec{\omega}\times\left(\frac{d\vec{\omega}}{dt}\right)^{(r)} + \vec{\omega}\times\vec{u}^{(r)} + \vec{\omega}\times\left(\vec{\omega}\times\vec{r}\right)\end{aligned} \tag{2.14}$$

Assuming that the angular velocity ω to be constant in time (which is true for the rotating earth) and noting that the rate of change of position vector $\vec{r}$ is given by the velocity vector $\vec{u}^{(r)}$ in the rotating frame of reference, then (2.14) becomes

$$\left(\frac{d\vec{u}^{(r)}}{dt}\right)^{(r)} = \left(\frac{d\vec{u}^{(i)}}{dt}\right)^{(i)} - 2\vec{\omega}\times\vec{u}^{(r)} - \vec{\omega}\times\left(\vec{\omega}\times\vec{r}\right). \tag{2.15}$$

In a rotating frame of reference a fluid particle experiences two fictitious forces, the Coriolis force acting perpendicular to the path of motion and the centrifugal force acting perpendicular to the axis of rotation. The latter is zero at the poles, has its maximum at the equator and generally reduces gravity. However, the maximum centrifugal force (per unit mass) is $\omega^2 r = 7.2921 \cdot 10^{-10} \cdot 6378 \cdot 10^3 = 0.0339$ m/s² at the equator. Hence, compared to the standard acceleration of gravity which is much more than two orders of magnitude larger (g = 9.80655 m/s²) it can be neglected without objection.

The same argumentation applies to the vertical component of the Coriolis force. Neglecting vertical velocities and expressing the angular velocity vector in terms of latitude the Coriolis force (per unit volume) is written as

$$F_{cor} = -2\rho\vec{\omega} \times \vec{u} = \rho \begin{bmatrix} (2\omega \sin\theta) v \\ -(2\omega \sin\theta) u \\ 0 \end{bmatrix}. \tag{2.16}$$

As sketched in Figure 2.1 the angular velocity vector points out of the ground at the North Pole. Thus, the angular velocity is positive in northern and negative in the southern hemisphere and (2.16) shows that a current north of the equator is deflected to the right and south of the equator to the left.

Introducing the Coriolis parameter (also known as Coriolis frequency)

$$f = 2\omega \sin\theta \tag{2.17}$$

and the Coriolis tensor

$$F_{ij} = \begin{bmatrix} 0 & f & 0 \\ -f & 0 & 0 \\ 0 & 0 & 0 \end{bmatrix}, \tag{2.18}$$

the Navier-Stokes equations under the Boussinesq assumption on the rotating earth finally become:

$$\frac{\partial u_j}{\partial x_j} = 0\,, \tag{2.19}$$

$$\frac{\partial u_i}{\partial t} + u_j \frac{\partial u_i}{\partial x_j} - \nu \frac{\partial^2 u_i}{\partial x_j \partial x_j} = -\frac{1}{\rho_0}\frac{\partial p}{\partial x_i} + \frac{\rho}{\rho_0} g_i + F_{ij} u_j\,, \tag{2.20}$$

where density differences in the Coriolis term have been neglected for the same reason that applied to the inertia terms in section 2.3.

2.5 Equation of state

As mentioned above, the density of a fluid or gas is determined by pressure and temperature as well as dissolved substances like salt or undissolved materials like suspended sediments. What is still missing, however, is a functional relationship between the governing quantities and density.

First of all, it should be ascertained which quantities are relevant for density changes in the present case. Starting with pressure it was already assumed in section 2.2 that a fluid is incompressible unless the Mach number does not exceed the threshold value of 0.3. Strictly speaking, however, this is not the only criterion as actually every medium is compressible if pressure is large enough. The static pressure increases with depth according to

$$\frac{dp}{dz} = -\rho g\,. \tag{2.21}$$

With the speed of sound given by

$$c^2 = \frac{dp}{d\rho}\,, \tag{2.22}$$

the increase of density per unit mass with depth can be expressed as

$$\frac{1}{\rho}\frac{d\rho}{dz} = \frac{1}{\rho c^2}\frac{dp}{dz} = -\frac{g}{c^2}\,. \tag{2.23}$$

A 10 % density change for air (c ≈ 333 m/s) requires a depth of about 1 km. For sea water (c ≈ 1500 m/s) the according depth would even be more than 20 km which shows that in the present case the incompressibility assumption indeed holds and density variations are pressure independent.

Suspended sediments may severely increase the density of a fluid which can be determined by a mixing calculation as

$$\rho = \rho_0 + \frac{\rho_S - \rho_0}{\rho_S} C_S \tag{2.24}$$

where ρ_S is the dry density of the suspended material and C_S the concentration in mass per volume. A concentration of 1 kg/m³ sediment with a dry density of, say, $\rho_S = 2000$ kg/m³ thus would increase water density by about 0.5 ‰. However, as sediment transport is not regarded in this thesis its influence on density can be neglected, too.

The relation between density and temperature is given through a thermal expansion coefficient given by

$$\beta = -\frac{1}{\rho}\left(\frac{\partial \rho}{\partial T}\right)_p , \tag{2.25}$$

where index p denotes that the partial derivative is taken at constant pressure. For an ideal gas β is simply $1/T$. For fluids like water, however, gas dynamics do not apply and the relationship must be determined empirically as is done in the Joint Panel on Oceanographic Tables and Standards of the UNESCO (1987) where density is defined as a fifth order polynomial of temperature:

$$\rho(S,T) = a_0 + a_1 T + a_2 T^2 + a_3 T^3 + a_4 T^4 + a_5 T^5 , \tag{2.26}$$

with

$a_0 = 999.842594$, $a_1 = 6.793952 \cdot 10^{-2}$, $a_2 = -9.095290 \cdot 10^{-3}$,

$a_3 = 1.001685 \cdot 10^{-4}$, $a_4 = -1.120083 \cdot 10^{-6}$, $a_5 = 6.536332 \cdot 10^{-9}$.

For salt, which can only be dissolved in fluids, the same difficulty arises and a relationship between density and salinity can only be given empirically. The functional form for density depending on temperature and salinity proposed by UNESCO (1980a) is

$$\rho(S,T) = \rho(T) + \left(b_0 + b_1 T + b_2 T^2 + b_3 T^3 + b_4 T^4\right) S + \left(c_0 + c_1 T + c_2 T^2\right) S^{3/2} + d_0 S^2 \quad (2.27)$$

with

$$b_0 = 8.24493 \cdot 10^{-4}, \quad b_1 = -4.0899 \cdot 10^{-3}, \quad b_2 = 7.6438 \cdot 10^{-5},$$
$$b_3 = -8.24670 \cdot 10^{-7}, \quad b_4 = 5.3875 \cdot 10^{-9}, \quad c_0 = -5.7247 \cdot 10^{-3},$$
$$c_1 = 1.02270 \cdot 10^{-4}, \quad c_2 = -1.6546 \cdot 10^{-6}, \quad c_3 = 4.8314 \cdot 10^{-4}.$$

The unit for temperature is centigrade and salinity is given in PSU which is the Practical Salinity Unit also defined by UNESCO (1980a,b) as the electrical conductivity ratio of a sea water sample to a standard potassium chloride (KCl) solution. As a rule of thumb it can be kept in mind that 1 PSU approximately corresponds to 1 g of salt per liter solution.

The functional relationship (2.27) is displayed in Figure 2.2 on the next page. Three distinct features can be deduced from the graphical representation of the dependency of density from temperature and salinity:

- Density decreases with increasing temperature and increases with increasing salinity. The influence of temperature is much less than that of salinity.
- For low salinity and low temperatures the decrease of density with increasing temperature is rather small. In fact, for very low salinity density even increases below 4 °C.
- While the relationship between density and temperature is quite nonlinear the increase with salinity is almost linear as can be estimated by the almost constant distance between the contour lines.

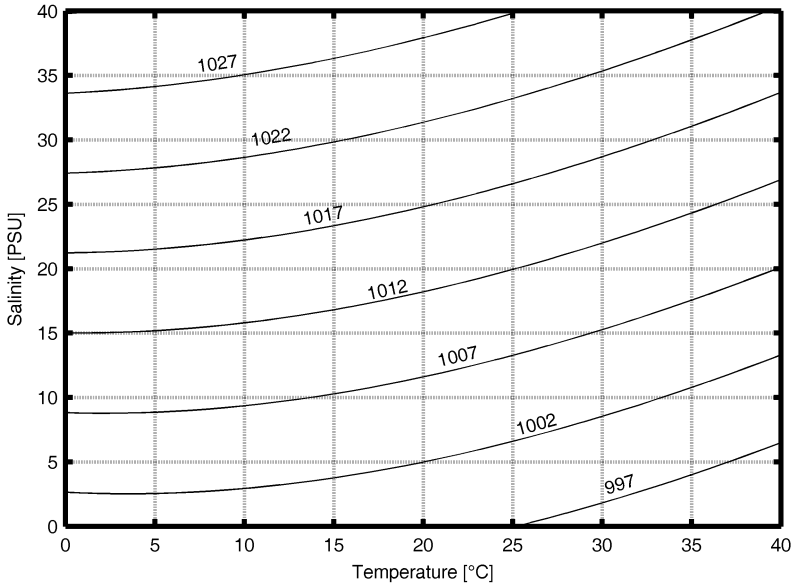

Figure 2.2: Density of water in kg/m³ as function of temperature and salinity.

2.6 Transport equations

Up to this point the governing equations are almost complete. Mass and momentum are conserved under the assumption of incompressibility and moderate density changes which can be determined by temperature and salinity. However, temperature and salinity are not constant but are transported with the flow. Hence, in addition to the Navier-Stokes equations further transport equations for temperature and salinity must be defined in order to close the problem.

A transport equation for temperature can be formally derived from the first law of thermodynamics, stating that the rate of change of stored energy equals the sum of heat addition and rate of rate of work done to a material volume. Writing this balance in differential form and subtracting the kinetic energy equation (3.4) which

will be derived in the next chapter, one obtains the balance equation for internal energy (for incompressible flows):

$$\rho\left(\frac{\partial}{\partial t}e + u_j\frac{\partial}{\partial x_j}e\right) = -\frac{\partial q_j}{\partial x_j} + \varepsilon\,, \tag{2.28}$$

where e is the internal energy and q_j is the heat flux. Following the Fourier law the heat flux is proportional to the temperature gradient

$$q_i = -\lambda\frac{\partial T}{\partial x_i}\,, \tag{2.29}$$

where the constant of proportionality λ is the thermal conductivity, which generally varies with temperature. However, as these variations are usually small over a significant range of temperatures it can be assumed to be constant for the present purposes. Air for example has a thermal conductivity of $\lambda \approx 0.025$ W/(m K) and for water $\lambda \approx 0.6$ W/(m K), showing that air is a much better insulator than water.

A relationship between internal energy and temperature is given through the specific heat capacity (or simply specific heat) C, which is the measure of heat energy required to raise the temperature of a given amount of a substance by one degree Kelvin (or Celsius). One generally has to distinguish whether the temperature rise takes place at constant pressure (suffix p) or constant volume (suffix v). For liquids like water the difference for the specific heats is only small, but for gases like air it can be up to 60 %. For air the difference is about 40 % giving specific heats of $C_p \approx 1005$ J/(kg K) and $C_v \approx 718$ J/(kg K) at 0 °C and sea level. For water at 20 °C the specific heat is $C = C_p \approx C_v \approx 4181$ J/(kg K). Hence, the balance equation for internal energy can be transformed into a heat equation like

$$\rho C_p\left(\frac{\partial T}{\partial t} + u_j\frac{\partial T}{\partial x_j}\right) = \lambda\frac{\partial^2 T}{\partial x_j \partial x_j} + \varepsilon\,, \tag{2.30}$$

where the internal energy has been substituted by $e = C_v T$.

The dissipation of kinetic energy ε appears in the internal energy and in the heat equation as a source term while it is a sink term in the kinetic energy equation (3.4). This shows that the energy that is lost in the flow field is used to heat the fluid. However, in usual this term is rather small and can be neglected. Introducing the thermal diffusivity $\kappa_T = \lambda / \rho C_p$, the heat equation finally reduces to

$$\frac{\partial T}{\partial t} + u_j \frac{\partial T}{\partial x_j} - \kappa_T \frac{\partial^2 T}{\partial x_j \partial x_j} = 0 \,, \tag{2.31}$$

which is a general transport equation for temperature without external sources like, e.g. sun radiation, which would enter the right hand side of (2.31).

Following the concept of a general transport equation the according equation for salt is

$$\frac{\partial S}{\partial t} + u_j \frac{\partial S}{\partial x_j} - \kappa_S \frac{\partial^2 S}{\partial x_j \partial x_j} = 0 \,, \tag{2.32}$$

where κ_S is the haline diffusivity.

The relation between momentum diffusivity (kinematic viscosity) and thermal diffusivity is called Prandtl number *Pr* while that between momentum diffusivity and haline diffusivity (like any other mass diffusivity) is called Schmidt number *Sc*. For water ($\nu \approx$ 1e-6 m/s²) the Prandtl and Schmidt numbers are $Pr \approx 7$ and $Sc \approx 700$, giving $\kappa_T \approx 1.4 \cdot 10^{-7}$ m²/s and $\kappa_S \approx 1.4 \cdot 10^{-9}$ m²/s, respectively. The idea of a relation between the diffusive transport of momentum and temperature or salt will be picked up in the next chapter about turbulence modeling.

2.7 Summary

In this chapter the governing equations have been introduced and the relevant assumptions to simplify and extent these equations have been illustrated. To sum up, the whole problem can be described by the incompressible Navier-Stokes equations under the Boussinesq assumption in a rotating frame of reference together with

transport equations for temperature and salinity as well as an equation of state for density depending on temperature and salinity. They form a closed set of equations for the unknown variables which is written as

a) $$\frac{\partial u_j}{\partial x_j} = 0 ,$$

b) $$\frac{\partial u_i}{\partial t} + u_j \frac{\partial u_i}{\partial x_j} - \nu \frac{\partial^2 u_i}{\partial x_j \partial x_j} = -\frac{1}{\rho_0} \frac{\partial p}{\partial x_i} + \frac{\rho}{\rho_0} g_i + F_{ij} u_j ,$$

c) $$\frac{\partial T}{\partial t} + u_j \frac{\partial T}{\partial x_j} - \kappa_T \frac{\partial^2 T}{\partial x_j \partial x_j} = 0 , \qquad (2.33)$$

d) $$\frac{\partial S}{\partial t} + u_j \frac{\partial S}{\partial x_j} - \kappa_S \frac{\partial^2 S}{\partial x_j \partial x_j} = 0 ,$$

e) $$\rho = \rho(T, S) .$$

In principle (2.33) is valid for laminar as well as turbulent flows. However, the validity for turbulent flows is limited due to the randomness and range of scales of turbulent fluctuations on the one hand and the limited computational power on the other hand. It will be shown in the next chapter which further assumptions have to be made if the flow is turbulent.

3 Turbulence modeling

3.1 General

In contrast to laminar flows which are well ordered with fluid particles following the pathlines, turbulent flows are characterized by chaotic fluctuating motions, i.e. random deviations from the mean flow paths. The goal of this chapter is to give a short introduction to the general nature of turbulence and point out the consequences on the numerical modeling of turbulent flows. Turbulence is maybe the most challenging task in fluid mechanics and there is a huge amount of literature on this complicated topic. A very good overview is provided by the book of Pope (2000) which also served as the major reference for this chapter and can be recommended for further, more detailed information.

The random turbulent fluctuations lead to enhanced mixing of transported quantities like momentum, temperature or salinity and will increase the energy loss of the mean flow. The latter becomes clear if the incompressible momentum balance is transformed into a kinetic energy equation by multiplying it with the velocity vector:

$$\rho\left(\frac{\partial}{\partial t}\frac{u_i^2}{2}+u_j\frac{\partial}{\partial x_j}\frac{u_i^2}{2}\right)=u_i\frac{\partial\tau_{ij}}{\partial x_j}-u_i\frac{\partial p}{\partial x_i}+\rho u_i g_i\,, \tag{3.1}$$

where Coriolis terms have canceled out. The viscous stress tensor is given by

$$\tau_{ij}=\mu\left(\frac{\partial u_i}{\partial x_j}+\frac{\partial u_j}{\partial x_i}\right), \tag{3.2}$$

and will alter kinetic energy by viscous stress gradients. However, the total rate of work done by viscous surface forces on a fluid element is actually given by $\partial\left(\tau_{ij}u_i\right)\big/\partial x_j$ which can be decomposed into

$$\frac{\partial u_i\tau_{ij}}{\partial x_j}=u_i\frac{\partial\tau_{ij}}{\partial x_j}+\tau_{ij}\frac{\partial u_i}{\partial x_j}\,. \tag{3.3}$$

The first term on the right hand side is the rate of increase of kinetic energy by local acceleration of the fluid and the second term is the deformation work rate which increases internal energy of a fluid element by deforming it. The same argumentation applies to the pressure term as it is also a surface force on a fluid element. Defining the kinetic energy per unit mass $E = u_i^2/2$, inserting (3.3) into (3.1) and dropping $p\,\partial u_i/\partial x_i$ − which is zero due to the incompressible mass balance − one obtains

$$\frac{\partial}{\partial t}E + \frac{\partial}{\partial x_i}u_i E = \frac{1}{\rho}\frac{\partial u_i \tau_{ij}}{\partial x_j} - \frac{1}{\rho}\frac{\partial u_i p}{\partial x_i} + u_i g_i - \varepsilon \,. \tag{3.4}$$

The second term on the left hand side and the first two terms on the right hand side are in divergence form and hence they represent fluxes which do not alter the kinetic energy balance. The third term on the right hand represents an increase of kinetic energy if the fluid velocity is in direction of external forces and a decrase in the opposite case. The last term is defined as

$$\varepsilon = \frac{\tau_{ij}}{\rho}\frac{\partial u_i}{\partial x_j} = \nu\left(\frac{\partial u_i}{\partial x_j} + \frac{\partial u_j}{\partial x_i}\right)\frac{\partial u_i}{\partial x_j}\,, \tag{3.5}$$

and represents the dissipation of kinetic energy. It always appears as a sink in the balance equation as viscosity is a positive quantity and the other terms on the right hand side correspond to the scalar strain rate, which is also always positive by definition (cf. eq. (3.61) and comments). This shows that energy is dissipated through the viscosity of the fluid and the velocity gradients in the flow field. Hence, if these gradients are large as is the case for random turbulent motion the dissipation of kinetic energy will also increase.

In a turbulent flow energy is dissipated at very small scales where the gradients are largest. However the question arises how small these scales really are. This can be best explained by assuming that the chaotic turbulent motions are due to eddies of various sizes. The largest of which fill out the whole turbulent flow region and the smallest will be dissipated by viscous diffusion. Energy is transported in a cascading manner from the large scale to the small scale structures.

Kolmogorov (1941a,b) suggested that the size of the dissipating eddies depends on the relevant parameters for the smallest eddies which are the energy dissipation ε and the kinematic viscosity ν. If the typical velocity for the smallest vortices is denoted by u' and the typical length scale is λ then for dimensional reasons the energy dissipation - which has the unit m²/s³ - of the smallest eddies is given by

$$\varepsilon \sim \frac{u'^3}{\lambda} \tag{3.6}$$

and the kinematic viscosity must be of order

$$\nu \sim u'\lambda \tag{3.7}$$

From (3.6) and (3.7) an estimate of the smallest length scale in a flow − also termed as Kolmogorov micro scale − can be deduced:

$$\lambda = \left(\frac{\nu^3}{\varepsilon}\right)^{1/4} \tag{3.8}$$

In analogy to the dissipation on the micro scale (3.6) the dissipation for the largest eddies can be assumed to be

$$\varepsilon \sim \frac{U^3}{L}, \tag{3.9}$$

where U and L are typical velocity and length scales of the turbulent flow region, e.g. mean velocity and diameter for pipe flow. Equality of dissipation on the macro and micro scale gives

$$\lambda = \left(\frac{\nu^3}{U^3}L\right)^{1/4} \tag{3.10}$$

or introducing the Reynolds number $\mathrm{Re} = UL/\nu$

$$\lambda = \frac{L}{\mathrm{Re}^{3/4}}, \tag{3.11}$$

which shows that the smallest length scales (and time scales accordingly) in a flow decrease with increasing Reynolds number.

Another view on the energy cascade is given by the energy spectrum. Most often these spectra express energy as a function of wave number k which is the reciprocal of wave length and hence a measure for eddy sizes. Please note that the wave number is not mixed up with turbulent kinetic energy which is also expressed by a lower case k and will be introduced later. Typical energy spectra for various experiments compiled by Saddoughi & Veeravalli (1994) are shown in Figure 3.1.

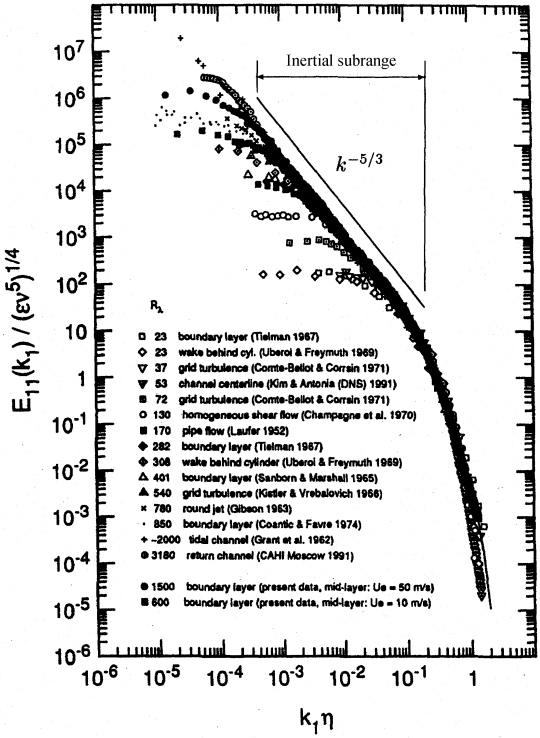

Figure 3.1: One dimensional normalized energy spectra for various experiments compiled by Saddoughi & Veeravalli (1994).

Several features of turbulence can be deduced from Figure 3.1.

- For small wave numbers (large wave length) the energy content in the flow is high and decreases with increasing wave number.
- The energy cascade is found in the inertial subrange where the spectrum has a universal slope proportional to $k^{-5/3}$.
- The inertial subrange becomes larger with increasing Reynolds number showing that the range of eddy sizes also increases with Reynolds number.
- For lower wave numbers the spectrum depends on the specific flow field and on the Reynolds number while at larger wave numbers (smaller length scales) all spectra come together. This indicates the universal character of turbulence at small scales and its independence of the large scale flow field and Reynolds number.
- The severe decrease of energy after the inertial subrange represents the dissipation of the smallest eddies by viscosity.

All these issues are typical for any turbulent flow field and should be regarded in a numerical simulation.

3.2 Direct Numerical Simulation (DNS)

In principle the governing equations (2.33) are valid for any kind of flow no matter if it is laminar or turbulent. A Direct Numerical Simulation (DNS) makes use of this fact and uses no assumptions to model the effects of turbulence but directly solves the governing equations. To accurately reproduce the turbulence cascade, the dissipation of energy and turbulent mixing, this requires that the numerical grid is fine enough to resolve the smallest scales.

For a typical gravity current in the Arkona basin in the Baltic Sea which is of major interest in this thesis the velocity is in the order of $U \approx 0.5$ m/s and the thickness is in the order of $D \approx 10$ m (see e.g. Arneborg et al. (2007)). Thus, the Reynolds

number is $Re \approx 5 \cdot 10^6$ and according to (3.11) the smallest scales are in the order of $\lambda \approx 0.1$ mm. The numerical simulation of only 1 m³ of such a current would require about $1 \cdot 10^{12}$ grid cells which is by far more than can be handled by the most powerful modern super computers. Although the size of the required time step (which is in the order of milliseconds) has not been regarded yet, it is already clear that a DNS for simulations on the natural scale is definitely unthinkable.

In a laboratory experiment the Reynolds number will be naturally much smaller if the same fluid (same viscosity) is used. If the Froude number (to be introduced later) is kept constant in an experiment on a 1/100 scale, for instance, the Reynolds number will decrease by a factor of 1000. Taking the example above, the velocity in the experiment would be in the order of $U \approx 0.05$ m/s, the thickness of the current in the order of $D \approx 0.1$ m and the Reynolds number would be $Re \approx 5 \cdot 10^3$. The minimum scales are still very small in the order of $\lambda \approx 0.2$ mm and preclude the simulation of a large domain. However, to resolve the whole current depth in a cube of 0.1^3 m^3 requires about $125 \cdot 10^6$ grid cells which is still quite a lot but a realistic number to be handled by high performance computers.

These examples clearly show that a DNS is restricted to relatively small Reynolds numbers of $Re = O(10^3)$ and accordingly small outer scales. Therefore it will be not regarded further in this thesis. However, it has been used as a very powerful tool for fundamental research which gave some completely new insights into the issues of turbulence. Some of them will partly be revisited in the next chapters.

3.3 Large Eddy Simulation (LES)

If the size of the computational domain and the Reynolds number increase it becomes impossible to resolve the smallest turbulent scales and model assumptions have to be made in order to close the problem. The Large Eddy Simulation (LES) is a first step in this direction as most scales of the turbulent flow field (the large eddies) are still resolved by the numerical grid while the isotropic smaller scales are accounted for by a model. This concept makes LES to be a compromise between

the DNS and the RANS (Reynolds Averaged Navier-Stokes) approach where the whole turbulent flow field is modeled as to be explained in the next chapter.

The governing equations for LES can be formally obtained by filtering the original Navier Stokes equations such that eddies with scales smaller than the filter width are filtered out and the resulting equations govern the dynamics of the large eddies. In principle any flow quantity ϕ can be split up into a 'grid scale' $\overline{\phi}$ and a 'subgrid scale' ϕ' :

$$\phi = \overline{\phi} + \phi' \,, \tag{3.12}$$

where the terminology 'grid' stems from the interpretation of the filter to sift out the small eddies like they were falling through a grid. The 'grid scale' denotes the filtered variable which is given by

$$\overline{\phi}(x_i) = \int_{\Omega} \phi(x_i') G(x_i, x_i'; \Delta_i) \mathrm{d}x_i' \,, \tag{3.13}$$

where Ω is the fluid domain and G is the filter function with the characteristic filter width Δ_i. Several filter functions can be used the most common being the top-hat or box filter, the cut-off filter and the Gauss filter each of which having its individual advantages and disadvantages. This explicit filtering approach is generally independent of the numerical scheme but in case a Finite Difference or Finite Volume scheme is applied to discretize the differential equations it is convenient to use a box filter with the filter width given by the extent of the grid cells. A general formulation independent of the cell shape is obtained if the cell volume V is used as the box filter width such that

$$\overline{\phi} = \frac{1}{V} \int_{V} \phi(x_i') \mathrm{d}x_i' \,, \quad x_i' \in V \,. \tag{3.14}$$

Applying the filter to the Navier Stokes equations and obeying the mathematical rules for filtering, the balance equations for mass, momentum and temperature can be written in terms of the filtered quantities:

$$\frac{\partial \overline{u}_j}{\partial x_j} = 0\,, \tag{3.15}$$

$$\frac{\partial \overline{u}_i}{\partial t} + \overline{u}_j \frac{\partial \overline{u}_i}{\partial x_j} - \nu \frac{\partial^2 \overline{u}_i}{\partial x_j \partial x_j} = -\frac{1}{\rho_0}\frac{\partial \overline{p}}{\partial x_i} + \frac{\overline{\rho}}{\rho_0} g_i + F_{ij}\overline{u}_j - \frac{\partial \tau_{ij,SGS}}{\partial x_j}\,, \tag{3.16}$$

$$\frac{\partial \overline{T}}{\partial t} + \overline{u}_j \frac{\partial \overline{T}}{\partial x_j} - \kappa_T \frac{\partial^2 \overline{T}}{\partial x_j \partial x_j} = -\frac{\partial q_{j,SGS}}{\partial x_j}\,. \tag{3.17}$$

where the temperature equation has been chosen as a proxy for any transported quantity. It turns out that the filtered balance equations resemble the original Navier Stokes equations except for the additional terms on the right hand side which represent the subgrid scale momentum and temperature fluxes given by

$$\tau_{ij,SGS} = \overline{u_i u_j} - \overline{u}_i \overline{u}_j\,, \tag{3.18}$$

$$q_{j,SGS} = \overline{T u_j} - \overline{T}\overline{u}_j\,. \tag{3.19}$$

These terms are unknown and require model assumptions. The first model was proposed by Smagorinsky (1963) and established over the years as the standard model for LES which is still successfully used today. It is based on the turbulent viscosity/diffusivity assumption (to be described in the next chapter) which relates the subgrid scale fluxes to the gradients of the filtered grid scale quantities:

$$\tau_{ij,SGS} = -\nu_t \left(\frac{\partial \overline{u}_i}{\partial x_j} + \frac{\partial \overline{u}_j}{\partial x_i} \right) = -2\nu_t \overline{S}_{ij}\,, \tag{3.20}$$

$$q_{j,SGS} = \frac{\nu_t}{\sigma_t}\frac{\partial \overline{T}}{\partial x_j}\,, \tag{3.21}$$

where $\overline{S}_{ij}$ is the strain rate of the resolved scale, ν_t is the turbulent viscosity and the turbulent diffusivity is defined by the turbulent Prandtl number σ_t (also to be explained in the next chapter) which is usually in the order of $\sigma_t = 1$. The turbulent viscosity is assumed to be proportional to a turbulent length scale and a turbulent velocity scale (cf. next chapter) and is modeled by

$$\nu_t = L_{SGS}^2 \left| \bar{S}_{ij} \right|, \tag{3.22}$$

where L_{SGS} is the subgrid scale mixing length and $\left| \bar{S}_{ij} \right| = \sqrt{2 \bar{S}_{ij} \bar{S}_{ij}}$ is the scalar shear rate of the resolved scale. The mixing length is usually related to the filter width by

$$L_{SGS} = C_S \Delta = C_S \left(\Delta_1 \Delta_2 \Delta_3 \right)^{1/3} = C_S V^{1/3}, \tag{3.23}$$

where C_S is a constant named after Smagorinsky. For homogenous isotropic turbulence in the inertial subrange Lilly (1967) derived a theoretical value for the Smagorinsky constant of $C_S = 0.165$. However, it turned out that this value is too high and causes excessive damping of large-scale fluctuations in anisotropic mean shear and transitional flows as e.g. in the presence of solid boundaries. In these cases the Smagorinsky constant has to be reduced and many practical applications suggest a typical range of $0.065 < C_S < 0.1$.

It is obvious that the Smagorinsky constant is unlikely to be a constant and Germano (1991, 1992) and subsequently Lilly (1992) conceived a theory by which C_S is dynamically computed based on the information provided by the resolved scales of motion. It is beyond the scope of the present work to go through the details of this approach as it is only one of many others that have been suggested over the last years. More details about the theory and applications of DNS and LES can be found in Breuer (2002) who also gives a nice review of the history of these methods and refers to a huge amount of further literature about this topic.

Even with the simplest subgrid scale model of Smagorinsky (1963) LES provides a reliable and robust approach for the simulation of turbulent flows since a large part of the fluctuating flow field is not modeled but directly resolved by the numerical grid. However, this superiority compared to the RANS models, to be followed next, is also the major drawback of the method as the required fine resolution of the computational grid is associated with a high numerical effort and still precludes the application on natural scales with high Reynolds numbers. Therefore the working horse for the present thesis will be the RANS equations but LES results from the literature will serve as a reference for the flow around a circular cylinder in chapter 5.

3.4 Reynolds Averaged Navier-Stokes Equations (RANS)

The Reynolds Averaged Navier-Stokes equations are founded on the idea that the variables in a randomly fluctuating turbulent flow field can be split up into a mean and a fluctuating part according to

$$\phi = \overline{\phi} + \phi' \,, \tag{3.24}$$

where ϕ symbolizes any flow variable and the overbar and prime denote the mean and fluctuating part, respectively. In general the mean value can be interpreted as an ensemble average which represents the mean value of an infinite number of identical experiments

$$\overline{\phi} = \lim_{N\to\infty} \frac{1}{N} \sum_{i=1}^{N} \phi_i \,. \tag{3.25}$$

For stationary flows this is identical to the temporal mean.

The mean and the fluctuating parts have to obey among others the following rules:

$$\overline{\phi'} = 0; \qquad \overline{\overline{\phi}} = \overline{\phi}; \qquad \overline{\overline{\phi}\phi'} = 0; \quad \overline{\overline{\phi}\overline{\phi}} = \overline{\phi}\overline{\phi} \,. \tag{3.26}$$

Applying (3.24) to the unknown variables and inserting these into the governing equations (2.33), averaging like in (3.25) and obeying the rules in (3.26) will result in a set of Reynolds averaged equations. The procedure is demonstrated for the continuity equation (2.33)(a). Inserting the composed velocities and averaging gives

$$\overline{\frac{\partial \overline{u}_j}{\partial x_j} + \frac{\partial u_j'}{\partial x_j}} = 0 \,. \tag{3.27}$$

As the mean of the fluctuations is zero it immediately follows that continuity of the mean flow field obeys the same rules like its instantaneous counterpart

$$\frac{\partial \overline{u}_j}{\partial x_j} = 0 \,. \tag{3.28}$$

Combining (3.27) and (3.28) gives an additional continuity equation for the fluctuations

$$\frac{\partial u_j'}{\partial x_j} = 0 \,. \tag{3.29}$$

which can be used in the derivation of the momentum balance to give

$$\frac{\partial \overline{u}_i}{\partial t} + \overline{u}_j \frac{\partial \overline{u}_i}{\partial x_j} - \nu \frac{\partial^2 \overline{u}_i}{\partial x_j \partial x_j} = -\frac{1}{\rho_0}\frac{\partial \overline{p}}{\partial x_i} + \frac{\overline{\rho}}{\rho_0} g_i + F_{ij}\overline{u}_j - \frac{\partial \overline{u_i' u_j'}}{\partial x_j} \,. \tag{3.30}$$

The Reynolds averaged momentum balance looks also exactly like the instantaneous one (2.33)(b) except for the last term on the right hand side which appears due to the nonlinearity of the advective terms. As this term is of a similar form like the molecular stress term in (2.2) the correlations $\overline{u_i' u_j'}$ are called Reynolds stresses and form the Reynolds stress tensor. The terminology stress in this context might be a bit misleading as the correlations of the fluctuations do not really exert stresses on the fluid but much more enhance the momentum flux in the flow. Thus, turbulent momentum flux might be a better expression.

Applying the same procedure to the temperature and salt balance (2.33)(c)(d) yields

$$\frac{\partial \overline{T}}{\partial t} + \overline{u}_j \frac{\partial \overline{T}}{\partial x_j} - \kappa_T \frac{\partial^2 \overline{T}}{\partial x_j \partial x_j} = -\frac{\partial \overline{T' u_j'}}{\partial x_j} \,, \tag{3.31}$$

$$\frac{\partial \overline{S}}{\partial t} + \overline{u}_j \frac{\partial \overline{S}}{\partial x_j} - \kappa_S \frac{\partial^2 \overline{S}}{\partial x_j \partial x_j} = -\frac{\partial \overline{S' u_j'}}{\partial x_j} \,, \tag{3.32}$$

where the additional terms are the turbulent temperature and salinity fluxes. Finally, for the equation of state the turbulent fluctuations might be neglected to give

$$\overline{\rho} = \rho(\overline{T}, \overline{S}) \,. \tag{3.33}$$

Due to the additional unknowns given by the turbulent fluxes the equation system is no longer closed and further transport equations are needed for these variables. In

principle it is possible to derive such equations as will be shown in chapter 3.6. However, again due to the nonlinearity in the advective terms there appear new unknown correlations of higher order like $\overline{u_i' u_j' u_k'}$ and it is impossible to close the problem in this way. Hence, further assumptions are necessary for closure and the level at which they are applied will determine the order of a model. If, for example, only correlations of second order are regarded and all others are modeled one has a second order model or a second moment closure.

3.4.1 Turbulent viscosity/diffusivity assumption

Now, even if the second moment closure is the simplest one the correlations that appear in (3.30), (3.31) and (3.32) require 12 (the turbulent momentum flux tensor is symmetric) additional transport equations and the solution of the problem becomes quite expensive. Turbulence models that directly rely on the transport equations for the turbulent fluxes will be discussed later in chapters 3.6 and 3.7, but first it is useful to start with simpler models that are numerically much cheaper.

One way to reduce the numerical effort is the turbulent viscosity (diffusivity) assumption also defined as eddy viscosity assumption. It is also attributed to Boussinesq (1877) and sometimes referred in the literature simply as Boussinesq assumption or Boussinesq approximation which should not be confused with the assumptions introduced in chapter 2.3. The basic idea lies in the fact that the turbulent momentum fluxes can be interpreted as stresses and thus can be related to the mean rate of strain by a viscosity, like the molecular stresses in (2.3):

$$\overline{u_i' u_j'} = -\nu_t \left(\frac{\partial \overline{u}_i}{\partial x_j} + \frac{\partial \overline{u}_j}{\partial x_i} \right) + \frac{2}{3} k \delta_{ij} \,. \tag{3.34}$$

The second term on the right hand sight is necessary in order for the trace of the turbulent momentum flux tensor to give the right turbulent kinetic energy which is defined by (remind: Einstein summation convention):

$$k = \frac{1}{2} \overline{u_i' u_i'} \,. \tag{3.35}$$

In chapter 2.6 the Prandtl and Schmidt numbers had been introduced. If this concept is adopted to the turbulent fluxes these can be expressed accordingly as

$$\overline{T'u_j'} = -\frac{\nu_t}{\sigma_T}\frac{\partial \overline{T}}{\partial x_j}, \tag{3.36}$$

$$\overline{S'u_j'} = -\frac{\nu_t}{\sigma_S}\frac{\partial \overline{S}}{\partial x_j}, \tag{3.37}$$

where σ_T, σ_S define the turbulent Prandtl numbers for temperature and salinity and have values in the order of 1.

Inserting (3.34), (3.36), (3.37) into the averaged balance equations (3.30), (3.31), (3.32) and recalling the continuity equation (3.28) and the equation of state (3.32) one arrives at the RANS and transport equations which are the basis for this thesis:

a) $$\frac{\partial \overline{u}_j}{\partial x_j} = 0,$$

b) $$\frac{\partial \overline{u}_i}{\partial t} + u_j\frac{\partial \overline{u}_i}{\partial x_j} - \frac{\partial}{\partial x_j}\left((\nu + \nu_t)\frac{\partial \overline{u}_i}{\partial x_j}\right) = -\frac{1}{\rho_0}\frac{\partial \overline{p}}{\partial x_i} + \frac{\rho}{\rho_0}g_i + F_{ij}\overline{u}_j,$$

c) $$\frac{\partial \overline{T}}{\partial t} + \overline{u}_j\frac{\partial \overline{T}}{\partial x_j} - \frac{\partial}{\partial x_j}\left(\left(\kappa_T + \frac{\nu_t}{\sigma_T}\right)\frac{\partial \overline{T}}{\partial x_j}\right) = 0, \tag{3.38}$$

d) $$\frac{\partial \overline{S}}{\partial t} + \overline{u}_j\frac{\partial \overline{S}}{\partial x_j} - \frac{\partial \overline{S}}{\partial x_j}\left(\left(\kappa_S + \frac{\nu_t}{\sigma_S}\right)\frac{\partial \overline{S}}{\partial x_j}\right) = 0,$$

e) $$\rho = \rho(\overline{T}, \overline{S}).$$

It should be noted that the turbulent viscosity and the corresponding diffusivities are usually some orders of magnitude larger than their molecular counterparts which are therefore sometimes omitted. Moreover, in contrast to the molecular quantities the turbulent viscosity is not a constant but depends on the flow and turbulence field. Hence, it must be kept inside the derivative in the diffusion term.

The turbulent viscosity assumption reduces the number of unknowns from 12 to 3 or if the turbulent Prandtl numbers are assumed to be constant, which will be done here for the time being, only to 1 unknown, the turbulent viscosity.

3.4.2 Mixing length model

The turbulent viscosity can be determined in several ways the easiest of which is based on the mixing length hypothesis by Prandtl (1925), which assumes that the turbulent viscosity is proportional to the rate of strain of the mean velocity field

$$\nu_t = l_m^2 \frac{\partial u_i}{\partial x_j}, \tag{3.39}$$

where the constant of proportionality is defined by the mixing length l_m. This does not solve the problem yet as the mixing length is still unknown. For a turbulent boundary layer it can be shown to be $l_m = \kappa y$, where y is the distance from the wall and $\kappa \approx 0.41$ is the von Kármán constant (cf. eq. (3.145) in chapter 3.8). In open channel flow the shear stress decreases linearly from the bottom to the free surface implying a mixing length of the form $l_m = \kappa y(1-y/H)^{1/2}$, where H is the water depth. For a turbulent mixing layer the relation is $l_m \approx 0.07\delta(x)$, where $\delta(x)$ is the mixing layer width.

From all these definitions it can be seen that the mixing length is a function of position and must be specified explicitly. For more complex flows this requires a lot of guesswork and one should have little confidence in the resulting mean velocity field. Another drawback of the mixing length model lies in the fact that the influence of stratification on the turbulence field is not regarded in the model and must be implemented a posteriori through empirical relations. Even if the mixing length model seems to be quite crude it is still used today (e.g. Wurpts (2006)) as in very simple circumstances, like the open channel flow example above, the assumptions of the mixing length model are justified. However, the flow of a density current around a cylindrical structure is by far anything else than a simple configuration and the mixing length model will not be regarded further in the present work.

3.5 Two equation models

A more sophisticated way was proposed independently by Kolmogorov (1942) and Prandtl (1945). In analogy to the molecular viscosity they suggested that the turbulent viscosity is proportional to the product of a turbulent length scale (like the mixing length) and a turbulent velocity scale

$$\nu_t \sim VL \,. \tag{3.40}$$

For dimensional reasons the velocity and length scale could be given by

$$V \sim k^{1/2} \,, \tag{3.41}$$

$$L \sim \frac{k^{3/2}}{\varepsilon} \,. \tag{3.42}$$

With k being the turbulent kinetic energy and ε its dissipation rate the turbulent viscosity becomes

$$\nu_t = c_\mu \frac{k^2}{\varepsilon} \,, \tag{3.43}$$

where c_μ is the constant of proportionality. The remaining task is to find appropriate transport equations for the turbulent quantities. As there will be two additional equations for the turbulence closure to be solved these models are referred to as two-equation models.

A transport equation for turbulent kinetic energy k can be derived in different ways. One way leads over the momentum balance for the turbulent fluctuations which is obtained by subtracting the Reynolds averaged momentum balance (3.30) from the instantaneous momentum balance (2.33) giving

$$\frac{\partial u_i'}{\partial t} + \left(\overline{u}_j + u_j'\right)\frac{\partial u_i'}{\partial x_j} + u_j'\frac{\partial \overline{u}_i}{\partial x_j} - \nu\frac{\partial^2 u_i'}{\partial x_j \partial x_j} = -\frac{1}{\rho_0}\frac{\partial p'}{\partial x_i} + \frac{\rho'}{\rho_0}g_i + F_{ij}u_j' + \frac{\partial \overline{u_i' u_j'}}{\partial x_j} \,. \tag{3.44}$$

Taking the definition of turbulent kinetic energy k in (3.35), multiplying (3.44) with u_i' and averaging yields an expression for the transport of k:

$$\frac{\partial k}{\partial t}+\overline{u}_j\frac{\partial k}{\partial x_j}+\frac{1}{2}\frac{\partial \overline{u_j'u_i'u_i'}}{\partial x_j}-\nu\frac{\partial^2 k}{\partial x_j\partial x_j}=-\frac{1}{\rho_0}\frac{\partial \overline{u_j'p'}}{\partial x_j}-\overline{u_i'u_j'}\frac{\partial \overline{u}_i}{\partial x_j}+\frac{g_j}{\rho_0}\overline{\rho'u_j'}-\varepsilon\,, \tag{3.45}$$

where the Coriolis term and the turbulent momentum flux term have vanished. The last term on the right hand side denotes the dissipation of turbulent kinetic energy and is given by

$$\varepsilon=\nu\overline{\frac{\partial u_i'}{\partial x_j}\frac{\partial u_i'}{\partial x_j}}\,. \tag{3.46}$$

Hence, it represents an unknown and must be determined somehow, which will be discussed later. The third order correlations on the left hand side of (3.45) and the pressure correlation on the right hand side are also unknown and need model assumptions. As both are in divergence form they represent fluxes of turbulent kinetic energy which can be modeled both together using the turbulent viscosity assumption. Introducing a turbulent Prandtl number for turbulent kinetic energy, σ_k, equation (3.45) becomes

$$\frac{\partial k}{\partial t}+\overline{u}_j\frac{\partial k}{\partial x_j}-\frac{\partial}{\partial x_j}\left(\left(\nu+\frac{\nu_t}{\sigma_k}\right)\frac{\partial k}{\partial x_j}\right)=-\overline{u_i'u_j'}\frac{\partial \overline{u}_i}{\partial x_j}+\frac{g_j}{\rho_0}\overline{\rho'u_j'}-\varepsilon\,. \tag{3.47}$$

Equation (3.47) shows that turbulent kinetic energy is transported by advection in the mean flow field and (turbulent) diffusion. It is produced and dissipated by the terms on the right hand side. The last term denotes the dissipation rate as discussed above. The first and second term represent production by shear in the mean flow and production by buoyancy. The shear production term also appears with its sign reversed in the kinetic energy equation for the mean flow field which can be derived by multiplying the mean momentum equations by $\overline{u}_i$ and averaging. This shows the principle of energy transfer between the mean and the turbulent flow fields. Shear in the mean flow field will usually decrease mean kinetic energy and increase turbulent kinetic energy.

The buoyancy term can have either sign depending on stratification. In a stable situation with density increasing in the direction of the external force g_j, the buoyancy flux will be in the opposite direction contributing to a decrease of turbulent kinetic energy and eventually an increase of mean potential energy. In an unstable situation, like convective heat transfer the process is vice versa and turbulent kinetic energy is increased while potential energy decreases.

Symbolizing the production terms by P and G, respectively results in the final form for the transport equation for turbulent kinetic energy:

$$\frac{\partial k}{\partial t} + \overline{u}_j \frac{\partial k}{\partial x_j} - \frac{\partial k}{\partial x_j}\left(\left(\nu + \frac{\nu_t}{\sigma_k}\right)\frac{\partial k}{\partial x_j}\right) = P + G - \varepsilon \,. \tag{3.48}$$

However, P and G still contain the unknown momentum and buoyancy fluxes and need further model assumptions. In accordance with the turbulent viscosity assumption in (3.34) the shear production term can be written as

$$P = \nu_t \left(\frac{\partial \overline{u}_i}{\partial x_j} + \frac{\partial \overline{u}_j}{\partial x_i}\right)\frac{\partial \overline{u}_i}{\partial x_j}, \tag{3.49}$$

where the second term on the right hand side of (3.34) cancelled out because of incompressibility. To model the buoyant production in a similar manner the turbulent buoyancy flux must be modeled first. This can be done if the turbulent buoyancy flux is first expressed in terms of turbulent temperature and salinity fluxes:

$$\overline{\rho' u_i'} = \overline{T' u_i'}\frac{\partial \rho}{\partial T} + \overline{S' u_i'}\frac{\partial \rho}{\partial S}, \tag{3.50}$$

where ρ is given by (3.38)(e). Recalling the turbulent diffusivity assumption in (3.36) and (3.37) and assuming equal turbulent Prandtl numbers for temperature and salinity ($\sigma_t = \sigma_T = \sigma_S$) the turbulent buoyancy flux then simplifies to

$$\overline{\rho' u_i'} = -\frac{\nu_t}{\sigma_t}\frac{\partial \rho}{\partial x_i}. \tag{3.51}$$

and the buoyancy production term under the turbulent viscosity assumption can be defined as

$$G = -\frac{g_j}{\rho_0}\frac{\nu_t}{\sigma_t}\frac{\partial \rho}{\partial x_j}. \tag{3.52}$$

As the turbulent viscosity is positive by definition this formulation is consistent with the above findings that turbulent kinetic energy decreases in a stable stratification when density increases in the direction of the external force field.

With the transport equation for turbulent kinetic energy (3.48) it is possible to determine the turbulent velocity scale (3.41) which is needed for the calculation of turbulent viscosity from (3.40). However, the turbulent length scale is still unknown and must be established by a second transport equation. Furthermore (3.48) is not yet fully closed as the dissipation rate is still unknown. For this reason and from the definition of the turbulence length scale in (3.42) it seems straightforward to define a transport equation for ε which leads to the very popular class of *k*-ε models.

3.5.1 *k*-ε models

For the determination of the turbulent viscosity in the *k*-ε models two additional transport equations one for turbulent kinetic energy k and one turbulent dissipation rate ε are solved. The transport equation for k has been derived above and the formulation given by (3.48) is generally adopted in almost all two equation models. A transport equation for ε can also be derived formally by multiplying (3.44) with the operator $2\nu\,\partial u_i/\partial x_k\,\partial/\partial x_k$ and averaging. However, almost all terms in the resulting equation contain unknowns and must be modeled. Hence, although all *k*-ε models rely on the same transported quantities, especially the transport equations for the turbulent dissipation rate eventually differ significantly from model to model.

Before continuing with the specific models it is useful to recall some definitions and determine new ones that will appear in the specific models. The major task of the turbulence models described here is the determination of the turbulent viscosity ν_t which is defined through (3.40) as the product of a turbulent velocity scale and a

turbulent length scale. However, for dimensional reasons it could as well be defined by a turbulent velocity scale squared multiplied by a turbulent time scale:

$$\nu_t \sim V^2 \cdot T \,. \tag{3.53}$$

With the definitions given by equation (3.41) and (3.43) the turbulent time scale is

$$T = k/\varepsilon \,. \tag{3.54}$$

This definition will be especially important in conjunction with the *k-ω* models treated in the next section (cf. equation (3.79)). Here it will be used to define the dimensionless turbulent shear number which requires a further time scale determined by the shear in the mean flow field.

Another important definition results from the rate of strain tensor of the mean flow field, which is − according to equation (2.4) − given by

$$S_{ij} = \frac{1}{2}\left(\frac{\partial \overline{u}_i}{\partial x_j} + \frac{\partial \overline{u}_j}{\partial x_i} \right), \tag{3.55}$$

and appears e.g. in the shear production term (3.49) which can be rewritten as

$$P = \nu_t 2 S_{ij} \frac{\partial \overline{u}_i}{\partial x_j} \,. \tag{3.56}$$

Any tensor can be split up in a symmetric and an asymmetric tensor like

$$\frac{\partial \overline{u}_i}{\partial x_j} = \frac{1}{2}\left(\frac{\partial \overline{u}_i}{\partial x_j} + \frac{\partial \overline{u}_j}{\partial x_i} \right) + \frac{1}{2}\left(\frac{\partial \overline{u}_i}{\partial x_j} - \frac{\partial \overline{u}_j}{\partial x_i} \right), \tag{3.57}$$

where the first term on the right hand side is the rate of strain tensor (3.55) and the second term represents the rate of rotation tensor given by

$$\Omega_{ij} = \frac{1}{2}\left(\frac{\partial \overline{u}_i}{\partial x_j} - \frac{\partial \overline{u}_j}{\partial x_i} \right). \tag{3.58}$$

Noting further that the product of a symmetric tensor with any other tensor equals the product of the symmetric tensor with the symmetric part of the other tensor, (3.56) becomes

$$P = \nu_t 2 S_{ij} S_{ij} \,, \tag{3.59}$$

which can finally be simplified to

$$P = \nu_t S^2 \,, \tag{3.60}$$

where the scalar strain rate is given by

$$S = \sqrt{2 S_{ij} S_{ij}} \,. \tag{3.61}$$

As the unit of the strain rate is 1/s the product with the turbulent time scale T defined in (3.54) further yields the dimensionless turbulent shear number

$$\eta = \frac{k}{\varepsilon} S \,, \tag{3.62}$$

which is frequently used as a scaling parameter in turbulence modeling.

Standard *k*-ε model

The standard k-ε model was the first two-equation model and originally presented by Launder & Spalding (1972). The basic assumption in the modeling of the dissipation rate equation is that the production and dissipation of ε is proportional to that of k. The transport equations for the standard k-ε model are

$$\frac{\partial k}{\partial t} + \overline{u}_j \frac{\partial k}{\partial x_j} - \frac{\partial}{\partial x_j}\left(\left(\nu + \frac{\nu_t}{\sigma_k}\right)\frac{\partial k}{\partial x_j}\right) = P + G - \varepsilon \,, \tag{3.63}$$

$$\frac{\partial \varepsilon}{\partial t} + \overline{u}_j \frac{\partial \varepsilon}{\partial x_j} - \frac{\partial}{\partial x_j}\left(\left(\nu + \frac{\nu_t}{\sigma_\varepsilon}\right)\frac{\partial \varepsilon}{\partial x_j}\right) = \frac{\varepsilon}{k}\left(c_{\varepsilon 1} P + c_{\varepsilon 3} G - c_{\varepsilon 2} \varepsilon\right) \,, \tag{3.64}$$

where the production and dissipation terms on the right hand side of (3.64) are scaled by the inverse turbulent time scale and adjusted by constant empirical parameters $c_{\varepsilon 1}$, $c_{\varepsilon 2}$ and $c_{\varepsilon 3}$. The model constants (including c_μ) have been determined by experimental evidence of very simplified situations like decay of shear free turbulence ($c_{\varepsilon 2}$) and homogeneous turbulent shear flow (c_μ, $c_{\varepsilon 1}$).

While the contribution of buoyancy to the budget of kinetic energy can be precisely derived, as shown above, its role in the transport equation for the turbulent dissipation rate is controversially discussed. The general model assumption to treat buoyancy in the same manner like the shear production and the dissipation terms in the ε equation is well agreed, however, the constant $c_{\varepsilon 3}$ is not uniquely defined. It appears to be the case for all other models that will follow and a proper definition of $c_{\varepsilon 3}$ will be discussed in chapter 6.1.5. All other model constants including the turbulent Prandtl numbers for k and ε are given in Table 3.1:

c_μ	$c_{\varepsilon 1}$	$c_{\varepsilon 2}$	σ_k	σ_ε
0.09	1.44	1.92	1.0	1.3

Table 3.1: Model constants for the standard k-ε model

The standard k-ε model being the first of its kind has a broad range of applicability and is incorporated in most numerical models today. It has been applied to a diverse range of problems and the experience with this model is huge. It is well known, that the model predicts the spreading rate of a planar jet fairly well while it significantly overestimates it for a round jet. This is attributed to the model constants and can be remedied by adjusting the values $c_{\varepsilon 1}$ and $c_{\varepsilon 2}$ to the problem. However, such a flow dependent adjustment is of limited value and the round jet anomaly was one reason for the development of more comprehensive k-ε models two of which will follow.

RNG k-ε model

The transport equation for ε in the standard k-ε model was presented to be entirely empirical as a formal derivation from (3.44) yields so many unknowns that need model assumptions. The renormalization group method (RNG) allows for a

derivation of the k-ε equations from the instantaneous Navier-Stokes equations (Yakhot & Orszag (1986)). The transport equations for the RNG k-ε model are given by

$$\frac{\partial k}{\partial t}+\overline{u}_j\frac{\partial k}{\partial x_j}-\frac{\partial}{\partial x_j}\left(\alpha_k\nu_{eff}\frac{\partial k}{\partial x_j}\right)=P+G-\varepsilon\,, \tag{3.65}$$

$$\frac{\partial \varepsilon}{\partial t}+\overline{u}_j\frac{\partial \varepsilon}{\partial x_j}-\frac{\partial}{\partial x_j}\left(\left(\alpha_\varepsilon\nu_{eff}\right)\frac{\partial \varepsilon}{\partial x_j}\right)=\frac{\varepsilon}{k}\left(c_{\varepsilon 1}P+c_{\varepsilon 3}G-c_{\varepsilon 2}\varepsilon-R_\varepsilon\right), \tag{3.66}$$

and, hence, are very similar to those of the standard model. One of the differences is the formulation of the diffusion term where $\nu_{eff}=\nu+\nu_t$ is the sum of the molecular and turbulent viscosities and the inverse effective Prandtl numbers α_k and α_ε are both defined by

$$\left|\frac{\alpha-1.3929}{\alpha_0-1.3929}\right|^{0.6321}\left|\frac{\alpha-2.3929}{\alpha_0-2.3929}\right|^{0.3679}=\frac{\nu}{\nu_{eff}}\,, \tag{3.67}$$

where α_0 = 1.0 and α stands either for α_k or α_ε. For high Reynolds numbers when $\nu \ll \nu_{eff}$ the effective Prandtl numbers converge to $\alpha_k = \alpha_\varepsilon \approx 1.393$.

The RNG theory also yields a different formulation for the turbulent viscosity which is defined by a differential equation. In the high Reynolds number limit, however, this formulation results in the same formulation as equation (3.43) with a slightly lower constant c_μ = 0.0845 as in the standard model. The other constants $c_{\varepsilon 1}$ and $c_{\varepsilon 2}$ are also a direct result of the RNG analysis (Orszag (1996)) and appear to be comparable to those of the standard model. All model constants for the RNG k-ε model are compiled in Table 3.2.

c_μ	$c_{\varepsilon 1}$	$c_{\varepsilon 2}$	α_k	α_ε
0.0845	1.42	1.68	1.393	1.393

Table 3.2: Model constants for the RNG k-ε model

The main difference to the standard k-ε model lies in the additional term R_ε on the right hand side of the transport equation for ε (3.66) which is actually not an outcome of the derivation with RNG theory. It is defined by

$$R_\varepsilon = \frac{c_\mu \eta^3 \left(1 - \eta/\eta_0\right)}{1 + \beta \eta^3} \varepsilon \,, \tag{3.68}$$

where the constants are given by $\eta_0 = 4.38$ and $\beta = 0.012$ and η is the turbulent shear number as defined in (3.62). This term modifies the destruction of turbulent dissipation rate and as such the leading fraction in (3.68) can be understood as a modification of the model constant $c_{\varepsilon 2}$ giving

$$c_{\varepsilon 2}^* = c_{\varepsilon 2} + \frac{c_\mu \eta^3 \left(1 - \eta/\eta_0\right)}{1 + \beta \eta^3} \,. \tag{3.69}$$

In the logarithmic boundary layer the turbulent shear number can be shown to be $\eta \approx 3.0$, giving $c_{\varepsilon 2}^* \approx 2.0$ which is comparable to the value of 1.92 in the standard model. In regions of large strain, where $\eta > \eta_0$, the dissipation of ε will be reduced and therefore ε itself is augmented. This leads to a reduction of k and eventually to a lower turbulent viscosity, which makes the RNG k-ε model more sensitive to the effects of rapid strain and streamline curvature in comparison to the standard model.

Realizable k-ε model

The major discrepancies of the standard k-ε model were mainly attributed to the empirically modeled transport equation for turbulent dissipation. Besides the round jet anomaly it can be shown that the model also does not satisfy some mathematical constraints and, hence, is non-realizable. The normal momentum flux in x-direction, for instance, is a positive quantity by definition and is given in the framework of turbulent viscosity by

$$\overline{u'u'} = -\nu_t 2 \frac{\partial \overline{u}}{\partial x} + \frac{2}{3} k \,. \tag{3.70}$$

However, inserting (3.43) into (3.70) shows that the right hand side will become negative when the strain is large enough, according to

$$\frac{k}{\varepsilon}\frac{\partial \overline{u}}{\partial x} > \frac{1}{3c_\mu} \approx 3.7 \ . \tag{3.71}$$

To make the model realizable the most straightforward way seems to be the reduction of c_μ in regions of large strain. This is supported by experimental evidence as in strong homogeneous shear flow c_μ has been found to be in the order of 0.05 which is significantly less than the standard value of 0.09.

The realizable *k*-ε model proposed by Shih et al. (1995) tries to solve the drawbacks of the standard model by the definition of a new transport equation for ε and by making c_μ variable as originally proposed by Reynolds (1987). The transport equations for the realizable model are

$$\frac{\partial k}{\partial t} + \overline{u}_j \frac{\partial k}{\partial x_j} - \frac{\partial}{\partial x_j}\left(\left(\nu + \frac{\nu_t}{\sigma_k}\right)\frac{\partial k}{\partial x_j}\right) = P + G - \varepsilon \ , \tag{3.72}$$

$$\frac{\partial \varepsilon}{\partial t} + \overline{u}_j \frac{\partial \varepsilon}{\partial x_j} - \frac{\partial}{\partial x_j}\left(\left(\nu + \frac{\nu_t}{\sigma_\varepsilon}\right)\frac{\partial \varepsilon}{\partial x_j}\right) = \frac{\varepsilon}{k}\left(c_{\varepsilon 1} Sk + c_{\varepsilon 3} G - c_{\varepsilon 2}\frac{\varepsilon}{1+\sqrt{\nu\varepsilon}/k}\right). \tag{3.73}$$

The transport equation for *k* is exactly the same as in the standard model (3.64). The equation for ε, however, only adopts the transport terms on the left hand side while the shear production and the dissipation term on the right side are significantly different. The production term no longer involves *P*, the production of *k*, which is believed to better represent the spectral energy transfer. In the new production term *S* is the rate of strain (3.61) and the model parameter $c_{\varepsilon 1}$ is not necessarily constant but might depend on the turbulent shear number (3.62) and is given by

$$c_{\varepsilon 1} = \max\left(0.43, \frac{\eta}{\eta + 5}\right). \tag{3.74}$$

The dissipation term is quite similar to that in the standard model except for the additional term in the denominator which removes the singularity present in the standard model if *k* vanishes.

As stated above c_μ is not a constant but formulated as a function of the mean strain and rotation rates. It is given by

$$c_\mu = \frac{1}{A_0 + A_S u^* k/\varepsilon}, \tag{3.75}$$

where

$$U^* = \sqrt{S_{ij}S_{ij} + \Omega_{ij}\Omega_{ij}} \tag{3.76}$$

and S_{ij} and Ω_{ij} are the mean rate of strain and rate of rotation tensors given by (3.55) and (3.58), respectively. A_0 is constant and given by $A_0 = 4.04$ and A_S is a function of strain rate defined by

$$A_S = \sqrt{6}\cos\phi \tag{3.77}$$

with

$$\phi = \frac{1}{3}\cos\left(\sqrt{6}W\right), \qquad W = \frac{S_{ij}S_{jk}S_{ki}}{\tilde{S}^3}, \qquad \tilde{S} = \sqrt{S_{ij}S_{ij}}\ . \tag{3.78}$$

The realizable k-ε model has been validated for a number of different flows, like jets, shear layers or separated flows and showed a better performance than the standard model throughout. For a turbulent boundary layer, however, c_μ, as defined by (3.75), will recover the standard value of 0.09 and there is almost no difference between both models. Table 3.3 summarizes all model constants for the realizable k-ε model, even c_μ and $c_{\varepsilon 1}$ which are strictly speaking no constants and therefore defined as variable.

c_μ	$c_{\varepsilon 1}$	$c_{\varepsilon 2}$	σ_k	σ_ε
variable	variable	1.90	1.0	1.2

Table 3.3: Model constants for the realizable k-ε model

3.5.2 *k-ω* models

In the preceding section it was shown, that the turbulent viscosity can also be described by a turbulent velocity scale and a turbulent time scale. This is the basis for the *k-ω* models that solve an additional transport equation for ω instead of ε, where ω can be thought of as a specific dissipation rate. It is defined as the inverse turbulent time scale (3.54)

$$\omega = \frac{\varepsilon}{k}\,, \tag{3.79}$$

and therefore sometimes referred to as turbulent frequency.

The original *k-ω* models did not account for buoyancy in the transport equations, however, Umlauf et al. (2003) showed that the inclusion of the buoyancy production term as given by (3.52) is straightforward and extents the applicability of these models to stratified flows and density currents.

Standard *k-ω* model

The standard *k-ω* model was first proposed by Wilcox (1988) and later revised by Wilcox (1998). The original model equations were given in a different form than those for the *k-ε* models presented above. Here the notation of Umlauf et al. (2003) is adopted in which the transport equations for turbulent kinetic energy and specific dissipation rate are given as

$$\frac{\partial k}{\partial t} + \overline{u}_j \frac{\partial k}{\partial x_j} - \frac{\partial}{\partial x_j}\left(\left(\nu + \frac{\nu_t}{\sigma_k}\right)\frac{\partial k}{\partial x_j}\right) = P + G - \varepsilon\,, \tag{3.80}$$

$$\frac{\partial \omega}{\partial t} + \overline{u}_j \frac{\partial \omega}{\partial x_j} - \frac{\partial}{\partial x_j}\left(\left(\nu + \frac{\nu_t}{\sigma_\omega}\right)\frac{\partial \omega}{\partial x_j}\right) = \frac{\omega}{k}\left(c_{\omega 1}P + c_{\omega 3}G - c_{\omega 2}\frac{f_{c_\omega}}{f_{c_\mu}}\varepsilon\right). \tag{3.81}$$

The *k* equation is exactly the same as for the *k-ε* models except for the turbulent Prandtl number and the formulation of the dissipation rate which is given as proportional to the product of *k* and ω:

$$\varepsilon = c_\mu f_{c_\mu} k\omega \,. \tag{3.82}$$

The equation for ω has a similar form like the transport equations for ε above. The production and dissipation terms are scaled by the ratio ω/k and adjusted by the parameters $c_{\omega 1}$, $c_{\omega 2}$ and $c_{\omega 3}$, where the latter is due to the inclusion of the buoyant production term and will be discussed in chapter 6.1.5, according to $c_{\varepsilon 3}$ above. The other two emerging from the original model are not necessarily constants but functions of turbulence intensity, giving a low Reynolds number correction. However, here only the high Reynolds number version is considered where both are constant.

The two additional parameter functions $f_{c\mu}$ and $f_{c\omega}$ were not present in the original model and have been introduced by Wilcox (1998) to enhance the model performance in free shear layer flows. They are given by

$$\begin{aligned} f_{c_\mu} &= \begin{cases} 1 & \chi_k \le 0 \\ \dfrac{1+680\chi_k^2}{1+680\chi_k^2} & \chi_k \le 0 \end{cases}, \\ f_{c_\omega} &= \frac{1+70\chi_\omega}{1+80\chi_\omega}, \end{aligned} \tag{3.83}$$

with

$$\begin{aligned} \chi_k &= \frac{1}{\omega^3}\frac{\partial k}{\partial x_j}\frac{\partial \omega}{\partial x_j}, \\ \chi_\omega &= \frac{\Omega_{ij}\Omega_{jk}S_{ki}}{(c_\mu \omega)^3}, \end{aligned} \tag{3.84}$$

where Ω_{ij} and S_{ij} are the rate of rotation and rate of strain tensors given by (3.55) and (3.58), respectively. All model constants for the standard k-ω model are given in Table 3.4.

c_μ	$c_{\omega 1}$	$c_{\omega 2}$	σ_k	σ_ω
0.09	0.52	0.8	2.0	2.0

Table 3.4: Model constants for the standard *k-ω* model (Wilcox (1998)).

The original model is recovered by setting the parameter functions $f_{c\mu} = f_{c\omega} = 1$ and slightly changing the constants $c_{\omega 1}$ and $c_{\omega 2}$ to 0.55 and 0.83, respectively.

SST k-ω model

The standard *k-ω* model is superior to the *k-ε* models in terms of near wall treatment. As will be shown in the next chapter, the transport equation for ε cannot be integrated down to a wall while this is possible for the ω equation. On the other hand the *k-ε* models are less sensitive in the free stream away from walls which inspired Menter (1994) to derive a model that uses both the accurate and robust formulation of the *k-ω* model in the near wall region and the free-stream independence of the *k-ε* model in the far field.

The shear-stress transport (SST) *k-ω* model blends between the standard *k-ω* model of Wilcox (1988) and the standard *k-ε* model with the equation for ε transformed to an equation for ω. The terminology SST stems from a modification of the turbulent viscosity to account for the transport of principal turbulent shear stress, which is attributed to give the SST *k-ω* model a better performance compared to the both standard models it is based on. The transport equations for k and ω are given by

$$\frac{\partial k}{\partial t} + \overline{u}_j \frac{\partial k}{\partial x_j} - \frac{\partial}{\partial x_j}\left(\left(\nu + \frac{\nu_t}{\sigma_k}\right)\frac{\partial k}{\partial x_j}\right) = P + G - \varepsilon \,, \tag{3.85}$$

$$\frac{\partial \omega}{\partial t} + \overline{u}_j \frac{\partial \omega}{\partial x_j} - \frac{\partial}{\partial x_j}\left(\left(\nu + \frac{\nu_t}{\sigma_\omega}\right)\frac{\partial \omega}{\partial x_j}\right) = \frac{\omega}{k}\left(c_{\omega 1} P + c_{\omega 3} G - c_{\omega 2}\varepsilon\right) + c_{\omega 4} D_\omega \,. \tag{3.86}$$

which resemble the equations for the standard model except for the model constants and the last term on the right hand side of the ω equation. It represents a cross

diffusion term which is a result of the transformation of the *k*-ε equations to the *k*-ω equations. It is given by

$$D_\omega = 2\frac{1}{\sigma_{\omega,2}\omega}\frac{\partial k}{\partial x_j}\frac{\partial \omega}{\partial x_j}\,. \tag{3.87}$$

The blending between the *k*-ω and the *k*-ε formulation can be solely achieved by a blending of the different model constants. These are compiled in Table 3.5 and Table 3.6 where the constants for the standard *k*-ω model in the near wall region are denoted by index 1 and those for the *k*-ε model in the far field by index 2. Note that the constant $c_{\omega 4}$ is 0 for the *k*-ω model and 1 for the *k*-ω version of the *k*-ε model. Hence, it is not a real model constant but has been introduced here to fit the cross diffusion term into the concept of blending the model constants. Also note that the model constants $c_{\varepsilon 1}$ and $c_{\varepsilon 2}$ of the standard *k*-ε model are related to those of the *k*-ω version of the model by $c_{\omega 1,2} = c_{\varepsilon 1} - 1$ and $c_{\omega 2,2} = c_{\varepsilon 2} - 1$. This will be an interesting fact for the derivation of the model constant c_3 in chapter 6.1.5.

c_μ	$c_{\omega 1,1}$	$c_{\omega 2,1}$	$c_{\omega 4,1}$	$\sigma_{k,1}$	$\sigma_{\omega,1}$
0.09	0.55	0.83	0.00	2.0	2.0

Table 3.5: Model constants for the SST *k*-ω model in the near wall region.

c_μ	$c_{\omega 1,2}$	$c_{\omega 2,2}$	$c_{\omega 4,1}$	$\sigma_{k,2}$	$\sigma_{\omega,2}$
0.09	0.44	0.92	1.00	1.0	1.17

Table 3.6: Model constants for the SST *k*-ω model in the far field.

Taking the placeholder ϕ for any of the model constants and marking the near wall constants by superscript (1) and the far field constants by superscript (2), the blending between the models is defined by

$$F_1\phi^{(1)} + (1 - F_1)\phi^{(2)}\,, \tag{3.88}$$

where F_1 is the blending function depending on the wall distance *y* it is given by

$$F_1 = \tanh\left(\Phi_1^4\right), \tag{3.89}$$

with

$$\Phi_1 = \min\left(\max\left(\frac{\sqrt{k}}{c_\mu \omega y}, \frac{500\nu}{\omega y^2}\right), \frac{4\rho k}{\sigma_{\omega,2} D_\omega^+ y^2}\right),$$
$$D_\omega^+ = \max\left(D_\omega, 10^{-10}\right). \tag{3.90}$$

The major advantage of the SST *k*-*ω* model compared to the standard model is the modification of the turbulent viscosity which can be expressed as

$$\nu_t = c_\mu^* \frac{k}{\omega} = c_\mu^* c_\mu \frac{k^2}{\varepsilon}, \tag{3.91}$$

with ε given by (3.82) and the damping function c_μ^* defined as

$$c_\mu^* = \frac{1}{\max\left(1.0, F_2 \frac{S}{0.31\omega}\right)}, \tag{3.92}$$

where S is the strain rate and F_2 is a blending function defined (very similar to F_1) by

$$F_2 = \tanh\left(\Phi_1^2\right),$$
$$\Phi_1 = \max\left(\frac{\sqrt{k}}{c_\mu \omega y}, \frac{500\nu}{\omega y^2}\right). \tag{3.93}$$

The damping function c_μ^* retains the definition of μ_t for the standard *k*-*ω* model in the near wall region and limits the turbulent momentum fluxes only in the far field, where they tend to be overestimated by the standard model.

3.6 Reynolds Stress Models

All turbulence models discussed so far rely on the assumption that the anisotropy of the turbulent fluxes is directly related to the mean velocity gradients with the turbulent viscosity being the function of proportionality. Taking the turbulent momentum fluxes for instance, the anisotropy tensor is given by

$$a_{ij} = \overline{u_i' u_j'} - \frac{2}{3} k \delta_{ij} = -\nu_t \left(\frac{\partial \overline{u}_i}{\partial x_j} + \frac{\partial \overline{u}_j}{\partial x_i} \right) = -2\nu_t S_{ij} \,, \tag{3.94}$$

confer (3.34) and (3.55). This assumption is reasonable for a wide class of shear flows including boundary layers, mixing layers and jets. However, in some particular situations (e.g. an axisymmetric contraction) when the turbulence field is rapidly distorted it can be shown (e.g. Pope (2000)) that the turbulent momentum fluxes are not determined by the mean rate of strain but rather by the total amount of mean strain experienced by the turbulence.

In Reynolds stress models (RSM) the turbulent fluxes are determined by solving the transport equations for each individual correlation and the turbulent viscosity hypothesis is not necessary. However, to close the problem other model assumptions have to be made which will be described in the next sections.

It should be noted that the terminology ‘Reynolds stress model’ actually refers to models in which density is constant and only the transport equations for the turbulent momentum fluxes are solved. If also the turbulent buoyancy fluxes are regarded − as done here − a better term for these models might be ‘second moment closure’ which is often used in the literature. However, the same inconsistency applies to the ‘algebraic stress models’ described in the next chapter for which no other name has been used. Therefore to be consistent in the inconsistency the term Reynolds stress model will be used here, keeping in mind that the density field is variable and also transport equations for the density determining quantities are solved.

3.6.1 Transport equations for turbulent momentum fluxes

The derivation of the transport equations for the turbulent momentum fluxes is quite tedious and will not be given here in detail. It can formally be obtained by multiplying the transport equation for u_i' (3.44) with u_i', exchanging indices to obtain another equation, adding these equations together and averaging, which finally results in

$$\begin{aligned}
&\frac{\partial \overline{u_i'u_j'}}{\partial t} + \overline{u}_k \frac{\partial \overline{u_i'u_j'}}{\partial x_k} - \left\{ \nu \frac{\partial^2 \overline{u_i'u_j'}}{\partial x_k \partial x_k} - \frac{\partial \overline{u_i'u_j'u_k'}}{\partial x_k} - \frac{1}{\rho_0} \left(\frac{\partial \overline{u_i'p'}}{\partial x_j} + \frac{\partial \overline{u_j'p'}}{\partial x_i} \right) \right\} = \\
&- \left\{ \overline{u_i'u_k'} \frac{\partial \overline{u}_i}{\partial x_k} + \overline{u_j'u_k'} \frac{\partial \overline{u}_j}{\partial x_k} \right\} - \left\{ \overline{u_i'u_k'} F_{ik} + \overline{u_j'u_k'} F_{jk} \right\} \\
&- \frac{1}{\rho_0} \left\{ g_i \overline{u_j'\rho'} + g_j \overline{u_i'\rho'} \right\} \\
&+ \frac{1}{\rho_0} \left\{ \overline{p' \left(\frac{\partial u_i'}{\partial x_j} + \frac{\partial u_j'}{\partial x_i} \right)} \right\} \\
&- 2\nu \overline{\frac{\partial u_i'}{\partial x_k} \frac{\partial u_j'}{\partial x_k}} \, .
\end{aligned} \tag{3.95}$$

This rather complicated expression has already been grouped to further simplify the notation by introducing tensors for the various groups. In (3.95) the first line represents advective (A_{ij}) and diffusive (D_{ij}) transport, the second line production by shear (P_{ij}) in the mean flow field and by Coriolis forces (C_{ij}), the third line production by buoyancy (G_{ij}), the fourth line redistribution due to pressure-strain correlations (Π_{ij}) and the last line the dissipation rate (ε_{ij}).

The effect of the Coriolis force due to the rotation of the earth is rather small and C_{ij} can usually be neglected. Taking the remaining tensors and noting that A_{ij} is given by a total derivative the transport equations for the turbulent momentum fluxes can be compactly written as

$$\frac{d\overline{u_i'u_j'}}{dt} - D_{ij} = P_{ij} + G_{ij} + \Pi_{ij} - \varepsilon_{ij} \, . \tag{3.96}$$

Of the various terms in (3.95) and (3.96), respectively, only P_{ij} is known as it solely contains $\overline{u}_i$ and $\overline{u_i'u_j'}$ for which transport equations are solved. All other terms need some model assumptions that will be discussed next.

Dissipation

Starting with the last term on the right hand side, it can be shown (e.g. Pope (2000)) that in high Reynolds number flows the dissipation rate is locally isotropic such that ε_{ij} can be modeled by

$$\varepsilon_{ij} = \frac{2}{3}\varepsilon\delta_{ij} \,. \tag{3.97}$$

However, this does not solve the problem yet as ε is still an unknown quantity. Hence, all Reynolds stress models require an additional transport equation for ε in order to close the equations.

Diffusion

The diffusion term on the left hand side contains fluxes due to molecular diffusion as well as fluctuating velocities and pressure. The molecular term is in closed form and needs no models assumptions. Furthermore, it is only important in the near wall region and can be neglected in the free stream. The velocity and pressure fluctuation terms on the other hand have to be modeled which is commonly done for both terms together using the concept of turbulent diffusion.

The definition of the turbulent kinetic energy (3.35) suggests the unknown fluxes of D_{ij} to be modeled according to the assumptions made in (3.47). Neglecting the molecular diffusion and using the idea of turbulent diffusion D_{ij} can be written as

$$D_{ij} = \frac{\partial}{\partial x_k}\left(\frac{\nu_t}{\sigma_k}\frac{\partial\overline{u_i'u_j'}}{\partial x_k}\right), \tag{3.98}$$

where the turbulent Prandtl number σ_k is assumed to be the same like that in the transport equation for k. This is self-evident as another way to derive a transport equation for k (cf. chapter 3.5) is taking the trace (setting $i = j$) of (3.95).

However, in Reynolds stress models the turbulent viscosity hypothesis is not needed to close the mean flow equations and hence, ν_t is basically an unknown quantity. Daly & Harlow (1970) proposed a generalized gradient-diffusion model given by

$$D_{ij} = \frac{\partial}{\partial x_k}\left(\left\{ -c_s \frac{k}{\varepsilon} \overline{u_k' u_l'} \right\} \frac{\partial \overline{u_i' u_j'}}{\partial x_l} \right), \tag{3.99}$$

where the diffusion coefficient is given in curly braces and c_s is a model constant for which Launder (1990) suggests a value of $c_s = 0.22$. However, it turns out that the anisotropic nature of the diffusion coefficient given by the model of Daly & Harlow in (3.99) might result in numerical instabilities. Hence, Lien & Leschziner (1994) suggest that it is more convenient to recover the definition of the isotropic turbulent viscosity coefficient given by (3.43) and use (3.98) as the general model for any diffusion term appearing in a Reynolds stress model. Using the generalized model (3.99), Lien & Leschziner (1994) derived a value of $\sigma_k = 0.82$ for the turbulent Prandtl number.

Pressure-strain

The most crucial part of the Reynolds stress models is the pressure-strain term Π_{ij} which disappears in the turbulent kinetic energy equation ($\Pi_{ii} = 0$) and is attributed to redistribute energy among the Reynolds stresses. The basic idea stems from a Poisson equation for the turbulent pressure fluctuations which is obtained by taking the divergence of (3.44) and shows that the fluctuating pressure field can be decomposed into a ‘rapid’ and a ‘slow’ pressure. The first of which will react immediately to a change in the mean velocity gradients and cause anisotropy among the Reynolds stresses while the second will redistribute energy much more slowly and leads to a return to isotropy. Following this idea Π_{ij} can be modeled by

$$\Pi_{ij} = \Pi_{ij}^{(s)} + \Pi_{ij}^{(r)}, \tag{3.100}$$

where the slow and rapid parts are defined as

$$\Pi_{ij}^{(s)} = -C_s \frac{\varepsilon}{k}\left(\overline{u_i' u_j'} - \frac{2}{3}k\delta_{ij}\right), \tag{3.101}$$

$$\Pi_{ij}^{(r,P)} = -C_{r,P}\left(P_{ij} - \frac{2}{3}P\delta_{ij}\right), \tag{3.102}$$

$$\Pi_{ij}^{(r,G)} = -C_{r,G}\left(G_{ij} - \frac{2}{3}G\delta_{ij}\right). \tag{3.103}$$

The model constants are given by $C_s = 1.8$, $C_{r,P} = 0.6$ and $C_{r,G} = 0.5$ and P and G are defined as the traces of the according tensors P_{ij} and G_{ij}, respectively. Hence,

$$P = \frac{1}{2}P_{ii} \;,\; G = \frac{1}{2}G_{ii} \,. \tag{3.104}$$

This is the basic model for the pressure strain term and goes back to the suggestions of Launder et al. (1975) who combined the proposals of Rotta (1951) for the slow term and Naot et al. (1970) for the rapid shear production term. Later the model was extended by Gibson & Launder (1976) to account for the effects of buoyancy with the rapid buoyancy production term.

While the form of the slow pressure-strain term is generally agreed the rapid shear production term has been intensively discussed. This can be best explained if Π_{ij} is written in a more general form (see e.g. Speziale (1991), Pope (2000)) as

$$\Pi_{ij} = -c_1\varepsilon b_{ij} + c_2 k S_{ij} + c_3 k \Sigma_{ij} + c_4 k Z_{ij} + c_5 \Gamma_{ij} \,, \tag{3.105}$$

where b_{ij} is the normalized anisotropy tensor defined as

$$b_{ij} = \frac{a_{ij}}{2k} = \frac{\overline{u_i' u_j'} - 2/3\, k\delta_{ij}}{2k} \,. \tag{3.106}$$

and the other tensors are given by

$$\Sigma_{ij} = S_{ik}b_{kj} + S_{jk}b_{ki} - \frac{2}{3}S_{kl}b_{lk}\delta_{ij} \,. \tag{3.107}$$

$$Z_{ij} = \Omega_{ik} b_{kj} + \Omega_{jk} b_{ki} \,. \tag{3.108}$$

$$\Gamma_{ij} = -\left(G_{ij} - \frac{2}{3} G_{ij} \delta_{ij} \right). \tag{3.109}$$

with the tensors of mean strain and rotation rate S_{ij} and Ω_{ij} given by (3.55) and (3.58), respectively. The first and last term on the right hand side of (3.105) recover the slow pressure-strain and the buoyancy production term of the basic model given by (3.101) and (3.103), respectively. The other three terms refer to the rapid pressure-strain relation and account for an increase of anisotropy due to shear and vorticity in the mean flow field.

There are many models that have been proposed to model the pressure-strain term. All of them can be written in the general form given by (3.105) and only differ in the model constants c_1 – c_5. Some of the models that have been developed for oceanographic applications are given in Table 3.7 at the end of this section.

Buoyancy production

The remaining term to be modeled is the buoyancy production G_{ij}, which contains the still unknown buoyancy fluxes $\overline{\rho' u_i'}$. A very simple model assumption (Fluent (2005)) would be to apply the turbulent diffusion assumption (3.52) such that

$$G_{ij} = -\frac{\nu_t}{\sigma_t} \left(g_i \frac{\partial \rho}{\partial x_j} + g_j \frac{\partial \rho}{\partial x_i} \right). \tag{3.110}$$

However, this approach is rather unfavorable as it implies modeling the turbulent temperature and salinity fluxes in the mean transport equations (3.31) and (3.32) with the turbulent viscosity assumption using (3.36) and (3.37). Hence, the advantages that are gained for the mean momentum equations by solving the transport equations for the individual momentum fluxes might get lost if the transport equations for the density determining quantities are modeled on a lower level.

Therefore a more consistent approach is to solve additional transport equations for the turbulent temperature and salinity fluxes and to evaluate the total turbulent buoyancy flux from (3.50). As shown before the transport equations for temperature and salinity are very similar with the only difference being the diffusion coefficients. The same appears to be true for the turbulent fluxes and it is therefore sufficient to derive only one transport equation which will be done next for the turbulent temperature fluxes.

3.6.2 Transport equations for turbulent temperature fluxes

The transport equations for the turbulent temperature fluxes are derived in a similar way like the turbulent momentum flux equations above. First a transport equation for the temperature fluctuations T' is needed which is achieved in a similar manner like the transport equation for u' (3.44) and results in

$$\frac{\partial T'}{\partial t}+\left(\overline{u}_j+u_j'\right)\frac{\partial T'}{\partial x_j}-\kappa_T\frac{\partial^2 T'}{\partial x_j\partial x_j}=u_j'\frac{\partial \overline{T}}{\partial x_j}+\frac{\partial \overline{T'u_i'}}{\partial x_j}, \tag{3.111}$$

where the Coriolis terms have been neglected. Multiplying (3.111) by u_i' and (3.44) by T', adding both together and averaging gives the transport equations for the turbulent temperature fluxes written as

$$\begin{aligned}
&\frac{\partial \overline{T'u_i'}}{\partial t}+\overline{u}_j\frac{\partial \overline{T'u_i'}}{\partial x_j}-\left\{\kappa_T\overline{u_i'\frac{\partial T'}{\partial x_j\partial x_j}}+\nu\overline{T'\frac{\partial u_i'}{\partial x_j\partial x_j}}-\frac{\partial \overline{T'u_i'u_j'}}{\partial x_j}-\frac{1}{\rho_0}\frac{\partial \overline{T'p'}}{\partial x_i}\right\}=\\
&-\left\{\overline{u_i'u_j'}\frac{\partial \overline{T}}{\partial x_j}+\overline{T'u_i'}\frac{\partial \overline{u}_j}{\partial x_i}\right\}-\left\{\overline{T'u_j'}F_{ij}\right\}\\
&-\frac{g_i}{\rho_0}\overline{T'\rho'}\\
&+\frac{1}{\rho_0}\overline{p'\frac{\partial T'}{\partial x_j}}\\
&-2\left(\kappa_T+\nu\right)\overline{\frac{\partial T'}{\partial x_j}\frac{\partial u_i'}{\partial x_j}}\,.
\end{aligned} \tag{3.112}$$

Neglecting the Coriolis term (last term in line two) and the dissipation term (last line) − which is justified assuming high Reynolds numbers − (3.112) can be written in compact form as

$$\frac{d\overline{T'u_i'}}{dt} - D_i^T = P_i^T + G_i^T + \Pi_i^T \,, \tag{3.113}$$

Also here the only term that needs no model assumptions is the production term P_i^T all other terms will be modeled as described next.

Diffusion

The diffusion term D_i^T is modeled in a similar manner like D_{ij} above using the turbulent diffusion assumption. Assuming high Reynolds numbers and neglecting the molecular contributions the diffusion term is modeled by

$$D_i^T = \frac{\partial}{\partial x_k}\left(\frac{\nu_t}{\sigma_T}\frac{\partial\overline{T'u_i'}}{\partial x_k}\right), \tag{3.114}$$

where the turbulent Prandtl number can be adopted from the generalized gradient diffusion model (3.99) to be $\sigma_T = 2.0$ (cf. Rodi 1980).

Buoyancy production

The diffusion term G_i^T contains the unknown correlation $\overline{T'\rho'}$ which must be determined before this term can be evaluated. Recalling the definition of the turbulent buoyancy flux given by (3.50), the turbulent buoyancy fluctuations are accordingly given by

$$\rho' \approx T'\frac{\partial\rho}{\partial T} + S'\frac{\partial\rho}{\partial S} \,. \tag{3.115}$$

As salinity has been neglected the buoyancy production term becomes

$$G_i^T = -\frac{g_i}{\rho_0}\frac{\partial\rho}{\partial T}\overline{T'^2} \,. \tag{3.116}$$

However, this does not solve the problem yet as the temperature variance $\overline{T'^2}$ is still unknown. It can be determined from an additional transport equation which is derived in a similar way like the transport equation for turbulent kinetic energy (3.45) by multiplying (3.111) with T' and averaging. Thus

$$\frac{\partial \overline{T'^2}}{\partial t} + \overline{u}_j \frac{\partial \overline{T'^2}}{\partial x_j} - \left\{ -\frac{\partial \overline{u'_j T'^2}}{\partial x_j} + \kappa_T \frac{\partial^2 \overline{T'^2}}{\partial x_j \partial x_j} \right\} = -2\overline{u'_j T'} \frac{\partial \overline{T}}{\partial x_j} - 2\kappa_T \overline{\frac{\partial T'}{\partial x_j} \frac{\partial T'}{\partial x_j}}, \qquad (3.117)$$

where the term in brackets on the left hand side covers turbulent and molecular diffusion. The first term on the right hand side represents production P^T and the last term dissipation ε^T of $\overline{T'^2}$. While the production term is known, the turbulent diffusion and the dissipation term require model assumptions.

However, instead of solving yet another equation it can be assumed that the transport terms on the left hand side can be neglected and production and dissipation are in balance. The dissipation term is modeled as

$$\varepsilon^T = \frac{1}{c_T} \frac{\varepsilon}{k} \overline{T'^2}, \qquad (3.118)$$

where c^T is a model constant. With the equilibrium assumption $P^T = \varepsilon^T$, the temperature variance can be expressed as

$$\overline{T'^2} = -c_T \frac{k}{\varepsilon} \overline{T' u'_i} \frac{\partial \overline{T}}{\partial x_j}. \qquad (3.119)$$

It should be noted that c^T is not necessarily constant as pointed out by Schumann & Gerz (1995). However, as no proper definition for this quantity has been found yet it is assumed to be a constant in all models that have been derived so far.

Pressure-buoyancy

Although temperature or buoyancy and the rate of strain are somewhat different in nature the pressure-buoyancy term Π_i^T is also modeled in a similar manner like Π_{ij} above. In the general form this is

$$\Pi_i^T = -c_1^T \frac{\varepsilon}{k} \overline{T'u_i'} + c_2^T S_{ij} \overline{T'u_i'} + c_3^T \Omega_{ij} \overline{T'u_i'} - c_4^T G_i^T \,, \tag{3.120}$$

where the first term accounts for the return to isotropy and the last term for the buoyancy production according to the first and last term in (3.105). The other two terms account for the increase of anisotropy due to shear and vorticity in the mean flow field. The model constants for different second moment closures are presented in the next section.

3.6.3 Compilation of model constants

As shown above the major assumptions made in Reynolds stress models are in the modeling of the pressure-strain and pressure-buoyancy terms. Several models have been proposed in the past and all of them only differ in the specific assumptions made on these terms. Hence, the only difference between the models is expressed through the model constants introduced above. Umlauf & Burchard (2005) reviewed the state of the art in second moment closures for geophysical applications recently, comparing many different models for which the constants of the pressure-strain and of the pressure-buoyancy term are compiled in Table 3.7 and Table 3.8, respectively. Note that the notation used here is slightly different from that in Umlauf & Burchard (2005).

	c_1	c_2	c_3	c_4	c_5
Gibson & Launder (1978)	3.600	0.800	1.200	1.200	0.500
Mellor & Yamada (1982)	6.000	0.320	0.000	0.000	0.000
Kanta & Clayson (1994)	6.000	0.320	0.000	0.000	0.000
Luyten et al. (1996)	3.000	0.800	2.000	1.118	0.500
Canuto et al. (2001) A	5.000	0.800	1.968	1.136	0.400
Canuto et al. (2001) B	5.000	0.698	1.966	1.094	0.495
Cheng et al. (2002)	5.000	0.798	1.968	1.136	0.500

Table 3.7: Model constants in the pressure-strain term for different Reynolds stress models.

	c_1^T	c_2^T	c_3^T	c_4^T	c_T
Gibson & Launder (1978)	3.000	0.333	0.333	0.333	1.600
Mellor & Yamada (1982)	3.728	0.000	0.000	0.000	1.220
Kanta & Clayson (1994)	3.728	0.700	0.700	0.200	1.220
Luyten et al. (1996)	3.000	0.333	0.333	0.333	1.600
Canuto et al. (2001) A	5.950	0.600	1.000	0.333	1.440
Canuto et al. (2001) B	5.600	0.600	1.000	0.333	0.954
Cheng et al. (2002)	5.520	0.213	0.357	0.333	1.640

Table 3.8: Model constants in the pressure-buoyancy term for different Reynolds stress models.

Like the LES above the Reynolds stress models are not of major concern for this thesis and will only serve for a comparison in the simulation of the unstratified flow around a cylinder in chapter 5. Therefore the details of the individual models given in Table 3.7 and Table 3.8 will not be discussed any further and can be taken from the specific papers or from Umlauf & Burchard (2005).

However, the quite thorough derivation of the equations and model assumptions made in a Reynolds stress model was necessary in order to introduce the algebraic stress models in the next chapter which will be used as a reference in the discussion about stratified flows in chapters 6 and 7.

3.7 Algebraic Stress Models

The application of Reynolds stress models is computationally extremely expensive as in the general three dimensional case even for a constant density at least 7 differential equations (6 for turbulent momentum fluxes + 1 for the dissipation rate) have to be solved. Therefore it would be desirable if the turbulent fluxes could be determined by algebraic expressions which can be computationally much cheaper evaluated and yet keep the level of modeling.

The transport equations for the turbulent fluxes (3.121) and (3.113) contain derivatives of the transported quantities only on the left hand side while the right hand side is exclusively given by algebraic terms like $\partial\overline{T}/\partial x_j$ or $\overline{u_i'u_j'}$. Hence, if the left hand side can be approximated by an algebraic expression the entire equation becomes algebraic. Thus the fundamental idea of the algebraic stress models (ASM) is to find an appropriate algebraic model for the advective and diffusive transport terms on the left hand side.

This basic idea was first introduced by Rodi (1976) and assumes that the ratio of transport in the Reynolds stress equations (3.121) and transport in the turbulent kinetic energy equation (3.48) is equal to the ratio of Reynolds stresses to turbulent kinetic energy. This provides an algebraic expression for the left hand side of the turbulent momentum flux equations (3.121) defined by

$$\frac{d\overline{u_i'u_j'}}{dt} - D_{ij} = \frac{\overline{u_i'u_j'}}{k}\left(P + G - \varepsilon\right). \tag{3.121}$$

An according approach applied to the turbulent temperature flux equations (3.113) yields

$$\frac{d\overline{T'u_i'}}{dt} - D_i^T = \frac{1}{2}\overline{T'u_i'}\left(\frac{1}{k}\left(P + G - \varepsilon\right) + \frac{1}{T^2}\left(P^T - \varepsilon^T\right)\right), \tag{3.122}$$

where the second term on the left hand side vanishes due to the assumption $P^T = \varepsilon^T$ made in the derivation of (3.119).

Inserting the approximations (3.121) and (3.122) into the transport equations (3.96) and (3.113) results in a nonlinear algebraic equation system which implicitly determines the turbulent fluxes. However, if the model assumptions introduced in the preceding chapter are inserted the equations become rather complicated and tedious to solve (see e.g. Burchard & Baumert (1995)). Hence, it is useful to make some simplifications for a practical applicability of the ASM.

All models given in Table 3.7 and Table 3.8 have been transformed to algebraic stress models by the individuall authors, assuming that turbulence is in equilibrium. This implies that production and dissipation are in balance ($P + G = \varepsilon$) and hence, the left hand side of the transport equations completely vanishes. Therefore the resulting equation system is linearized and things become much easier. Making further use of the boundary layer approximation by assuming that horizontal scales are much larger than vertical scales which is at least justified in shallow coastal waters, it turns out that the remaining turbulent fluxes can be simply expressed as

$$\overline{u'w'} = c_\mu \frac{k^2}{\varepsilon} \frac{\partial \overline{u}}{\partial z}, \tag{3.123}$$

$$\overline{v'w'} = c_\mu \frac{k^2}{\varepsilon} \frac{\partial \overline{v}}{\partial z}, \tag{3.124}$$

$$\overline{u'T'} = c'_\mu \frac{k^2}{\varepsilon} \frac{\partial \overline{T}}{\partial z}, \tag{3.125}$$

where it has been assumed that the vertical coordinate is defined by the z-axis (cf. chapter 2.4). Compared to the definition of the turbulent fluxes using the turbulent viscosity assumption (3.34) and (3.36) it can be seen that (3.123) − (3.125) imply the definition of turbulent viscosity and turbulent diffusivity which are given by

$$\nu_t = c_\mu \frac{k^2}{\varepsilon}, \tag{3.126}$$

$$\nu'_t = c'_\mu \frac{k^2}{\varepsilon}. \tag{3.127}$$

However, in contrast to the similar definition (3.43), c_μ is not a constant like in most two equation models but a function of the squares of the turbulent shear number η, given by (3.62), and a turbulent buoyancy number:

$$\alpha_s = \frac{k^2}{\varepsilon^2} S^2 , \tag{3.128}$$

$$\alpha_N = \frac{k^2}{\varepsilon^2} N^2 . \tag{3.129}$$

The square of the shear frequency S as defined by (3.61) simplifies under the boundary layer approximation to

$$S^2 = \left(\frac{\partial u}{\partial z}\right)^2 + \left(\frac{\partial v}{\partial z}\right)^2 . \tag{3.130}$$

Accordingly N is defined as a buoyancy frequency (also referred to as Brunt Väisälä frequency) and given by

$$N^2 = -\frac{g}{\rho_0}\frac{\partial \rho}{\partial z} . \tag{3.131}$$

The equilibrium assumption and the boundary layer approximation indeed simplify the problem, however, the derivation of the stability functions c_μ and c'_μ remains quite complex, although it is straightforward. Hence, here only the final outcome is presented and the details can be found e.g. in Umlauf & Burchard (2005) or the original papers.

The stability functions for all models given in Table 3.7 and Table 3.8 can be expressed as

$$c_\mu = \frac{n_0 + n_1\alpha_N + n_2\alpha_S}{d_0 + d_1\alpha_N + d_2\alpha_S + d_3\alpha_N\alpha_S + d_4\alpha_N^2 + d_5\alpha_S^2} , \tag{3.132}$$

$$c'_\mu = \frac{n_0^T + n_1^T\alpha_N + n_2^T\alpha_S}{d_0 + d_1\alpha_N + d_2\alpha_S + d_3\alpha_N\alpha_S + d_4\alpha_N^2 + d_5\alpha_S^2} , \tag{3.133}$$

where the constants $n_0 - n_2$, $n_0^T - n_2^T$ and $d_0 - d_5$ are exclusively determined by the constants $c_1 - c_5$, $c_1^T - c_4^T$ and c_T which were introduced for the modeling of the pressure-strain and pressure-buoyancy terms in the preceding chapter. Hence, all the information that can be gained from a complete Reynolds stress model is now comprised in compact form in the stability functions.

However, the Reynolds stresses can not be determined by (3.123) − (3.125) unless the turbulent kinetic energy and the dissipation rate are not known. Therefore an ASM requires the solution of two additional transport equations to determine k and ε and can therefore basically regarded as a two equation model with a (mean and turbulent) flow field dependent definition for the turbulent viscosity and diffusivities. Like in the two equation models usually the first equation is reserved for the transport of k while the remaining second equation can be solved for either quantity that determines a turbulent length scale.

As shown by Umlauf & Burchard (2003) all standard turbulence models given in chapter 3.5 can be expressed in a generic form (this fact was already used in the derivation of the SST k-ω model), which enables a unique comparison of the different approaches. They illustrated that in the equilibrium situation when production equals dissipation there is no big difference which quantity is used for the second equation. However, as also demonstrated by Umlauf et al. (2003) there are situations in which the k-ω model seems to be superior to the k-ε model.

In this thesis the main emphasis is on the classical two equation models given in chapter 3.5 and the ASM are only of minor concern. However, as they can be thought of to be somehow more elaborate they provide a good reference which will be used in chapters 6 and 7.

3.8 Near wall treatment

All equations presented so far are generally valid in the free stream. When a rigid wall is present, however, some modifications have to be made to account for the presence of the wall. Here, it will be assumed that walls are stationary, i.e. they do not move like e.g. impellers, and that they are impermeable, meaning that nothing will leave or enter a domain through a wall. In other words there will be no fluxes through a solid wall (including temperature fluxes, i.e. the wall will have the same temperature as the surrounding fluid). This is the case if the velocity normal to the boundary is zero and if the normal wall gradients of all other variables are zero, too. Mathematically this can be expressed in form of a Dirichlet boundary condition for the velocity and a Neumann boundary condition for other variables in the form

$$u_i n_i = 0\,, \tag{3.134}$$

$$\frac{\partial \phi n_i}{\partial n_i} = 0\,, \tag{3.135}$$

where n_i denotes the unit normal vector to the boundary and ϕ stands for any variable, like pressure, temperature, etc.. Equation (3.134) is sometimes referred to as 'slip' boundary condition as the fluid is still allowed to move tangentially to a wall. However, physical evidence suggests that a fluid particle which is in contact with a wall must have the same velocity like the wall (which is assumed to be zero, here). This requirement immediately leads to the 'no slip' boundary condition where in addition to (3.134) it is required that all velocities at the wall are zero:

$$u_i = 0\,. \tag{3.136}$$

In case of a DNS, (3.135) and (3.136) are the only wall boundary conditions required as all turbulence scales are resolved. However, if a turbulence model is used additional boundary conditions for the turbulent quantities must be defined.

Before continuing with the boundary conditions for the specific turbulence models it is useful to recall the structure of the mean velocity profile in a turbulent boundary

layer as first postulated by Prandtl (1925). The flow is assumed to be parallel to the wall which is along the *x*-axis and the distance to the wall increases in *y*-direction. The velocity profile is a function of wall distance and solely specified by density ρ, viscosity μ and wall shear stress τ_w given by the stress strain relationship (2.3):

$$\tau_w = \mu \left(\frac{d\overline{u}}{dy} \right)_{y=0} . \tag{3.137}$$

Near the wall the viscous stresses will dominate and Reynolds stresses (turbulence) will be of minor importance. Therefore it is useful to define viscous scales, i.e. appropriate velocity and length scales in the near-wall region. These are the friction velocity

$$u_\tau = \sqrt{\frac{\tau_w}{\rho}} , \tag{3.138}$$

and the viscous length scale

$$\delta_v = \nu \sqrt{\frac{\rho}{\tau_w}} = \frac{\nu}{u_\tau} . \tag{3.139}$$

With these scales the actual velocity and wall distance can be given in non-dimensional form as

$$u^+ = \frac{\overline{u}}{u_\tau} , \tag{3.140}$$

and

$$y^+ = \frac{y u_\tau}{\nu} . \tag{3.141}$$

The ‘law of the wall’ suggests that the non-dimensional velocity u^+ is a function of the non-dimensional wall distance y^+

$$u^+ = f(y^+) \tag{3.142}$$

and is valid in the 'inner layer' of the wall. In the 'outer layer' viscosity plays a minor role and turbulence will dominate the mean velocity profile shape. However, as the emphasis here lies on the boundary conditions, the outer layer is not regarded further.

The inner layer can be subdivided in three distinct regions. The first is the 'viscous sublayer' which is the region right next to the wall where molecular viscosity dominates. It extends over $0 < y^+ < 5$ where the no slip condition (3.136) and the definition of the wall shear stress (3.137) suggest that

$$u^+ = y^+ \quad \text{for} \quad 0 < y^+ < 5 \,. \tag{3.143}$$

The third region is the 'logarithmic layer' a few distances further away from the wall at $y^+ > 30$ where the direct effects of the molecular viscosity become negligible. Simple dimensional analysis shows that the velocity gradient in this region is

$$\frac{d\overline{u}}{dy} = \frac{1}{\kappa} \frac{\mathrm{u}_\tau}{\mathrm{y}} \,. \tag{3.144}$$

which after integration and inserting the non-dimensional variables becomes

$$u^+ = \frac{1}{\kappa} \ln y^+ + B \quad \text{for} \quad y^+ > 30 \,, \tag{3.145}$$

where $\kappa \approx 0.41$ is the von Kármán constant named after von Kármán (1930) who introduced this logarithmic law of the wall. The constant of integration is found from experiments (Nikuradse (1932)) to be in the order of $B \approx 5.5$.

In between the 'viscous sublayer' and the 'logarithmic layer' is the 'buffer layer' where viscosity and turbulence are either important. A smooth transition between the two surrounding layers given above implies

$$u^+ = \frac{2}{\kappa} \ln y^+ - 3.05 \quad \text{for} \quad 5 \le y^+ \le 30 \,. \tag{3.146}$$

A mean velocity profile obeying the 'law of the wall' as described above is shown in Figure 3.2.

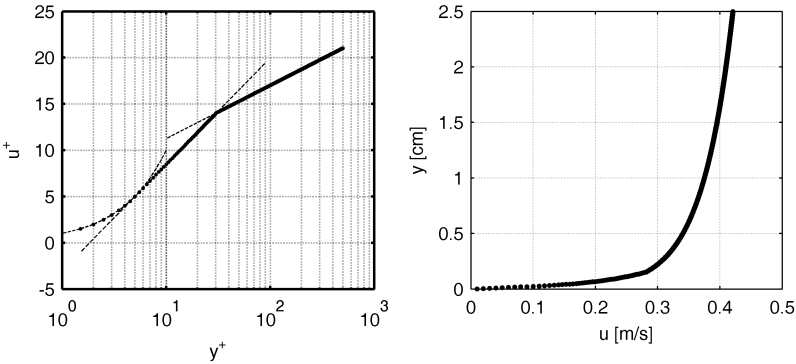

Figure 3.2: Law of the wall. Velocity profiles in the inner region of a turbulent boundary layer. Left: non-dimensional log-plot. Right: dimensional velocity profile.

The 'law of the wall' for the mean velocity profile derived so far is actually only valid for completely smooth walls. However, in reality every wall will have a specific roughness and the question remains how it will influence the velocity profile. Roughness is in general a random variation of the surface structure, but as shown by Nikuradse (1933) in his classical pipe flow experiments, the effect of roughness can be interpreted by equally ordered elements of a specific size giving an equivalent roughness. If the size of the elements is very small such that all elements do not extent the viscous sublayer this is termed the 'hydraulically smooth' case in which roughness will have no effect on the mean velocity profile and the law of the wall above applies. On the other hand, in the 'hydraulically rough' case, roughness elements are large enough to protrude out of the viscous sublayer. This will cause a wake behind each element and the corresponding drag force on the roughness elements will make viscosity negligible for determining the mean velocity profile (and the drag on the surface). In this case the viscous sublayer does not exist and the mean velocity profile is solely given by a logarithmic law, which is defined by

$$u^+ = \frac{1}{\kappa} \ln \frac{y}{k_s} + B_2 \,, \tag{3.147}$$

where the wall distance now is consequently scaled with the equivalent roughness height k_s and the constant $B_2 \approx 8.5$ is obtained from the data of Nikuradse (1933).

A universal law of the wall can be given in terms of a non-dimensional roughness length k_s^+ which is normalized by the friction velocity and the viscous length scale to give

$$k_s^+ = \frac{k_s u_\tau}{\nu} . \tag{3.148}$$

The universal law is defined by

$$u^+ = \frac{1}{\kappa} \ln y^+ + B - \Delta B , \tag{3.149}$$

which is actually the law of the wall for smooth walls (3.145) with the additional constant ΔB which depends on k_s^+ to account for the effects of surface roughness. If the influence of roughness is divided in three categories, 'smooth', 'rough' and 'transitional', the additional constant ΔB can be given by

$$\text{smooth} \quad \left(k_s^+ \le 2.25\right) : \quad \Delta B = 0 , \tag{3.150}$$

$$\text{transitional} \quad \left(2.25 < k_s^+ \le 90\right) : \quad \Delta B = \frac{1}{\kappa} \ln\left(\frac{k_s^+ - 2.25}{87.75} + c_s k_s^+ \right) \sin\left(0.4258\left(\ln k_s^+ - 0.811\right)\right) , \tag{3.151}$$

$$\text{rough} \quad \left(k_s^+ > 90\right) : \quad \Delta B = \frac{1}{\kappa} \ln\left(1 + c_s k_s^+\right) . \tag{3.152}$$

It is readily seen that $\Delta B = 0$ in the 'hydraulically smooth' case immediately recovers (3.145). The constant c_s appearing in (3.151) and (3.152) is intended to adjust the constant B_2 in (3.147) to account for non-uniform roughness elements. Setting $c_s = 1/4$ and inserting (3.152) into (3.149) will recover (3.147) based on Nikuradse's data.

Before determining the wall boundary conditions for each of the turbulence models in detail a general distinction should be discussed first. As seen above the near wall region is subdivided in different regions each of which obeys a specific 'law of the wall' for the mean velocity. From a numerical modeling point of view the question

arises whether it is necessary to completely resolve the boundary layer down to the viscous sublayer or if it might be sufficient to bridge the viscosity affected region and apply boundary conditions that are valid in the logarithmic region. The first approach is computationally much more expensive as the steep gradients below the logarithmic layer have to be resolved. However, if the transported equations for the turbulent quantities can be integrated down to the wall this 'near wall modeling' approach is likely to give better results in any cases in which the bridging of the viscosity affected region is not appropriate.

3.8.1 Near wall treatment for *k*-ε models

Standard wall functions

As pointed out above the idea of the wall function approach is to bridge the viscous sublayer and to provide accurate boundary conditions that are valid in the logarithmic layer. This means that the boundary conditions to be described next are applied at a location $y = y_p$ that is located around $y^+ > 30$, where the subscript p denotes the point at which quantities are evaluated. From a numerical point of view y_p indicates the distance of the grid point closest to a wall.

The boundary conditions for the mean velocities are readily obtained from the generic log-law given by (3.149). Inserting these definitions into the transport equations for k and ε and assuming equilibrium between production and dissipation of turbulent kinetic energy ($P = \varepsilon$) in the logarithmic region k and ε are given by

$$k = \frac{u_\tau^2}{c_\mu^{1/2}}, \tag{3.153}$$

$$\varepsilon = \frac{u_\tau^3}{\kappa y}. \tag{3.154}$$

However, rather than applying these equations directly as Dirichlet boundary conditions it is more convenient to provide boundary conditions that are numerically more robust and revert to the above relations under the ideal conditions. This can be

achieved if the frictional velocity u_τ which is governed by the mean velocity gradient (cf. (3.137) and (3.138)) is replaced by a nominal frictional velocity that is based on turbulent quantities. From (3.153) the nominal frictional velocity can be written as

$$u_\tau^* = c_\mu^{1/4} k_p^{1/2} . \tag{3.155}$$

The corresponding estimates of y^+ and k_s^+ then become

$$y_p^* = \frac{y_p u_\tau^*}{\nu} , \tag{3.156}$$

$$k_s^* = \frac{k_s u_\tau^*}{\nu} , \tag{3.157}$$

and the log-law for the nominal mean velocity can be defined by

$$u_p^* = u_\tau^* \left(\frac{1}{\kappa} \ln\, y_p^* + B - \Delta B \right) . \tag{3.158}$$

The actual velocity is finally obtained from the fact that the ratio of nominal quantities is the same as the ratio of actual quantities, thus

$$u_p^* = \frac{u_p u_\tau^*}{u_\tau} . \tag{3.159}$$

While the transport equation for k is solved for the whole domain with a Neumann boundary condition at the wall

$$\frac{\partial k}{\partial n} = 0 , \tag{3.160}$$

the dissipation rate ε at the wall is explicitly defined by (3.153) and (3.154) and is given by (see e.g. Fluent (2005) or Pope (2000))

$$\varepsilon = \frac{u_\tau^3}{\kappa y_p} = \frac{c_\mu^{3/4} k_p^{3/2}}{\kappa y_p} . \tag{3.161}$$

Two-layer model

As the transport equations for k and ε are derived for high Reynolds number flows they cease to be valid in the viscosity affected near wall region. One possibility to avoid the discrepancies of the wall function approach described above is to employ a low Reynolds number model (e.g. Patel et al. (1985)) where the model constants are modified to account for the viscous effects in the near wall region. Although this approach allows for resolving the complete boundary layer down to wall the computational requirements are very high as the numerical grid at the wall must be fine enough to account for the steep gradients, especially those of the dissipation rate.

An alternative way is to use a one equation model in the near wall region which only solves a transport equation for turbulent kinetic energy and determines a turbulent length scale − which is well known in the near wall region − analytically. The dissipation rate is then found from (3.42). Therefore the idea of the two-layer model is to subdivide the flow domain into an inner − viscosity affected − region and an outer − fully turbulent − region. The demarcation between the two regions is determined by a turbulent Reynolds number based on the wall distance y:

$$\mathrm{Re}_y = \frac{\sqrt{k}\,y}{\nu} . \tag{3.162}$$

In the outer region ($\mathrm{Re}_y > 200$) the common equations can be applied while in the inner region a one equation model is solved.

In the one equation model of Wolfstein (1969) the transport equations for momentum and turbulent kinetic energy are retained. However, the turbulent viscosity in these equations is determined from

$$\nu_t^{(TL)} = f_\mu c_\mu L_t \sqrt{k} , \tag{3.163}$$

where L_t is the turbulent length scale defined as

$$L_t = c_\mu^{-3/4} \kappa y , \tag{3.164}$$

and f_μ is a damping function to account for the retarding effects of the wall on the turbulent momentum fluxes. It is given by

$$f_\mu = 1 - e^{-\mathrm{Re}_y / A_\mu}, \tag{3.165}$$

with $A_\mu = 70$ being a model constant.

The turbulent dissipation rate can be analytically determined from k and L_t as

$$\varepsilon^{(TL)} = f_\varepsilon \frac{k^{3/2}}{L_t}, \tag{3.166}$$

where the damping function f_ε is given by

$$f_\varepsilon = 1 - e^{-\mathrm{Re}_y / A_\varepsilon}, \tag{3.167}$$

with the model constant $A_\varepsilon = c_\mu^{-3/4}\kappa$.

To allow for a smooth transition between the inner and outer region the tow-layer formulations of turbulent viscosity (3.163) and dissipation rate (3.167) are blended with the definitions in the outer region following a suggestion by Jongen (1992):

$$\phi = \lambda \phi^{(FT)} + (1-\lambda)\phi^{(TL)}, \tag{3.168}$$

where ϕ represents either μ_t or ε and the superscripts denote the fully turbulent (FT) or two-layer (TL) formulations. The blending function λ is given by

$$\lambda = \frac{1}{2}\left(1 + \tanh\left(\frac{\mathrm{Re}_y - 200}{40}\right)\right), \tag{3.169}$$

which will tend towards 0 at the wall and approaches 1 in the beginning of the outer region.

In the traditional two-layer model the boundary layer is resolved down to the wall where the closest grid point is located at $y^+ \approx 1$ and the boundary conditions for velocity is given by the viscous law of the wall (3.143). However, a more general

approach where the nearest grid point at the wall can also be located in the logarithmic layer or in the buffer layer can be achieved if the formulations of the laminar (3.143) and the logarithmic (3.149) laws are smoothly blended. Following the suggestions of Kader (1981) the boundary condition for velocity can be defined as

$$u^+ = e^{\Gamma} u^+_{lam} + e^{1/\Gamma} u^+_{log} , \tag{3.170}$$

where the blending function is given by

$$\Gamma = \frac{0.01(y^+)^4}{1+5y^+} . \tag{3.171}$$

3.8.2 Near wall treatment for *k*-ω models

In contrast to the *k*-ε model the *k*-ω model can be integrated down to the wall and the rather inconvenient approach of a low Reynolds number formulation or a two-layer model as described above is dispensable. This simplifies the definition of boundary conditions enormously.

The boundary conditions for the mean velocities are the same as defined in (3.170) for the two layer *k*-ε model. Also the transport equation for k is solved throughout the whole domain with a zero gradient Neumann boundary condition (3.160) at the wall. The boundary condition for ω is given explicitly as a Dirichlet boundary condition in the general form

$$\omega = \frac{\left(u^*_\tau\right)^2}{\nu} \omega^+ . \tag{3.172}$$

In the turbulent logarithmic region ω is given by

$$\omega = \frac{u_\tau}{c_\mu^{1/2} \kappa y_p} . \tag{3.173}$$

For the laminar near wall region ω^+ it is defined as

$$\omega^+ = \min\left(\omega_w^+, \frac{6}{c_{\omega 2}/c_\mu (y_p^*)^2}\right), \tag{3.174}$$

where

$$\omega_w^+ = \begin{cases} \left(\frac{50}{k_s^+}\right)^2 & \text{for} \quad k_s^+ < 25 \\ \frac{100}{k_s^+} & \text{for} \quad k_s^+ \geq 25 \end{cases} \tag{3.175}$$

and the dimensionless roughness length is

$$k_s^+ = \max\left(1.0, k_s^*\right). \tag{3.176}$$

Like for the mean velocity the laminar and turbulent wall laws for the specific dissipation rate are blended according to the definition given by (3.170).

3.8.3 Near wall treatment for RSM and ASM

In Reynolds stress models all boundary conditions are given explicitly as Dirichlet conditions. For the mean velocity and the turbulent dissipation rate either wall functions or the two-layer model as described in chapter 3.8.1 can be applied. The turbulent momentum fluxes are obtained by using the logarithmic law of the wall (3.149), neglecting the transport terms and assuming local equilibrium which is justified in the near wall region. Defining a local coordinate system, where *n* is the normal coordinate, *t* is the tangential coordinate and *b* is the bi-normal coordinate the Reynolds stresses in the wall adjacent cells can be obtained in terms of the frictional velocity from the following universal ratios (cf. Pope (2000)):

$$\frac{\overline{u_t' u_t'}}{u_\tau^2} = 5.1, \quad \frac{\overline{u_n' u_n'}}{u_\tau^2} = 1.0, \quad \frac{\overline{u_b' u_b'}}{u_\tau^2} = 2.3, \quad \frac{\overline{u_t' u_b'}}{u_\tau^2} = -1.0\,. \tag{3.177}$$

Alternatively it can be shown that close to a wall the Reynolds stresses are universally related to turbulent kinetic energy by (cf. Pope (2000)):

$$\frac{\overline{u_t' u_t'}}{k} = 1.098, \quad \frac{\overline{u_n' u_n'}}{k} = 0.247, \quad \frac{\overline{u_b' u_b'}}{k} = 0.655, \quad \frac{\overline{u_t' u_b'}}{k} = -0.255 \,. \tag{3.178}$$

However, this requires the solution of an additional transport equation for k which will be solved throughout the whole domain with a zero gradient Neumann boundary condition at the wall.

In chapter 3.7 it was shown that an algebraic stress model can basically understood as a two equation model with a modification of turbulent viscosity and diffusivity determined algebraically from the underlying RSM. The boundary conditions for an ASM are those that apply to the chosen two equation model and are described above in chapter 3.8.1 and 3.8.2 in case of a k-ε model and a k-ω model, respectively.

4 Numerical methods

The mathematical description of physical processes most often results in a set of (partial) differential equations like those discussed in the preceding two chapters. Numerical methods to solve these equations have been extensively developed over the last decades and today many of them can be assumed to be well established. The major emphasis of the present thesis is therefore on the physical processes and the resulting equations to describe them rather than the numerical methods for their solution. In fact, all simulations presented here were done with the commercial software package FLUENT (Fluent (2005)) which is based on the Finite-Volume-Method. This chapter will therefore only give a short introduction to the basic idea of the Finite-Volume-Method and briefly describe some individual issues. For further details the reader is referred to the literature cited or might get a very nice overview about numerical methods for fluid dynamics in Ferziger & Peric (2002) or the Finite-Volume-Method in particular in Versteek & Malalasekera (1996).

The starting point for the Finite-Volume-Method is the volume integrated form of the differential equations. All balance equations derived in the preceding chapters have a very similar form depicting the transport of the conserved variable by advection, diffusion and due to source terms. The general form of an integrated transport equation can be written as:

$$\int_V \frac{\partial \phi}{\partial t} \mathrm{d}V + \int_V \frac{\partial u_j \phi}{\partial x_j} \mathrm{d}V - \int_V \frac{\partial}{\partial x_j} \left(\Gamma_\phi \frac{\partial \phi}{\partial x_j} \right) \mathrm{d}V = \int_V S_\phi \, \mathrm{d}V \,, \tag{4.1}$$

where ϕ stands for the transported variable and Γ_ϕ and S_ϕ denote the diffusion coefficient and source terms for this variable. To better elucidate the association with the equations given above, Table 4.1 shows the individual settings for the RANS equations, the salinity equation and the equation for turbulent kinetic energy. Please note, that the overbar to denote for the averaging of the variables has been omitted for simplicity.

	ϕ	Γ_ϕ	S_ϕ
continuity	1	0	0
momentum	u_i	$(\nu + \nu_t)$	$-\frac{1}{\rho_0}\frac{\partial p}{\partial x_i} + \frac{\rho}{\rho_0} g_i + F_{ij} u_j$
salinity	S	$\left(\kappa_S + \frac{\nu_t}{\sigma_S}\right)$	0
turbulent kinetic energy	k	$\left(\nu + \frac{\nu_t}{\sigma_k}\right)$	$P + G - \varepsilon$

Table 4.1: Variable settings for the general transport equation (4.1).

Using Gauss' theorem, which shows that the volume integral of the gradient of a variable is equivalent to the surface integral of that variable, allows to eliminate the derivatives in the advective term and diffusive term and (4.1) can be rewritten as

$$\int_V \frac{\partial \phi}{\partial t} \mathrm{d}V + \int_A u_j \phi \, \mathrm{d}A_j - \int_A \Gamma_\phi \frac{\partial \phi}{\partial x_j} \mathrm{d}A_j = \int_V S_\phi \, \mathrm{d}V \,, \tag{4.2}$$

where A_j is the vector normal to a surface element.

The basic idea to arrive at an algebraic equation system which can numerically be solved is to subdivide the computational domain into a finite number of control volumes (grid cells) and to evaluate (4.2) for each individual volume. A sketch of such a grid is shown in Figure 4.1 for a two-dimensional domain to simplify the following comments, but the extension to three dimensions is straightforward. The grid defines the boundaries of the control volume and all flow variables are stored in a computational node located in the center of each cell (collocated grid). Basically the shape of the cells is arbitrary but, as here, in most cases quadrilateral or triangular cells are used in two-dimensional domains and accordingly hexa- or tetrahedral cells in three-dimensional domains.

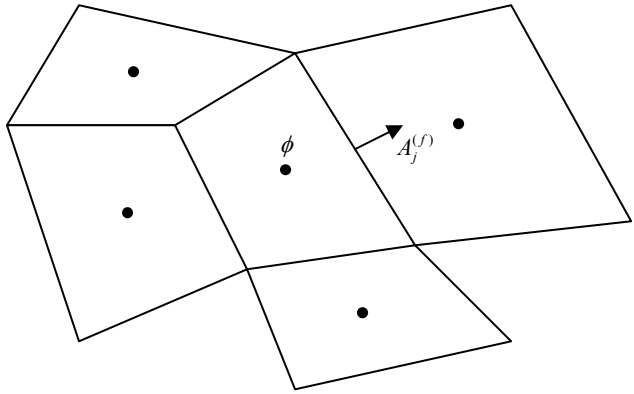

Figure 4.1: Definition sketch for the Finite-Volume Method (two-dimensional).

The discretized form of the general transport equation (4.2) can be written as

$$\frac{\partial \phi}{\partial t} V + \sum_{f=1}^{N_f} u_j^{(f)} \phi^{(f)} A_j^{(f)} - \sum_{f=1}^{N_f} \Gamma_\phi \left(\frac{\partial \phi}{\partial x_j} \right)^{(f)} A_j^{(f)} = S_\phi V \ . \tag{4.3}$$

where

V	: volume of the cell
N_f	: number of faces of the cell
$A_j^{(f)}$	: normal area vector of face (*f*)
$u_j^{(f)}$	: velocity (face flux) vector at face (*f*)
$\phi^{(f)}$	: value of ϕ at face (*f*)
$\left(\partial\phi/\partial x_j\right)^{(f)}$	: gradient at face (*f*)

As each variable is defined at the cell centers it can be interpreted to represent the average value for the corresponding cell and allows the volume integral to be evaluated by simply multiplying the variable with the cell volume. However, the evaluation of the discretized surface integrals requires the knowledge of the fluxes and gradients at the faces of the cell which are unknown a priori. They can be

determined by interpolation between ‘known’ cell-centered values which is most often done slightly different for the advective terms and the diffusion terms.

The most obvious interpolation is linear between the cell-centered values of the neighboring cells yielding a ‘Central-Difference’ scheme for the face value which is second order accurate. This method is frequently used for the diffusion terms but might lead to numerical instabilities if applied to the advective terms. This is due to the dependence of the fluxes on the flow direction and might be avoided if only upstream cells are considered which leads to the wide variety of upwind schemes. The most simple of this group is the ‘First-Order Upwind’ scheme where $\phi^{(f)}$ is not even interpolated but simply set to the cell-center value of ϕ in the neighboring upstream cell. However, this approximation is only of first order accuracy and associated with high numerical diffusion, therefore it should be avoided. A much better accuracy can be obtained by the ‘QUICK’ scheme (Leonard (1979)) where a parabola is fitted through the neighboring downstream cell and the two nearest upstream cells.

At this point the Finite-Volume-Method is actually fully explained as the spatial discretization is complete. Following the above procedure the discretized transport equation (4.3) contains the unknown variable ϕ at the cell center and the unknown values in the surrounding cells. If the temporal derivative is ignored for a while the discretized transport equation in grid cell *P* yields a (linear) expression for variable ϕ_P in terms of neighboring variables ϕ_{nb} which can be written as

$$a_p\phi = \sum_{nb} a_{nb}\phi_{nb} + b\,, \tag{4.4}$$

where a_p and a_{nb} are coefficients resulting from the interpolation schemes and b denotes the contribution of the source term. Similar equations can be written for each cell of the grid resulting in a set of algebraic equations with a sparse coefficient matrix. This linear equation system can then be solved by any suited algorithm and provide a solution for stationary transport of a scalar variable if the velocity field is known. However, the present problem is governed by more than one single equation and the transient term as well as the nonlinearity of the Navier-Stokes equations require some more comments.

The temporal discretization is best explained rewriting (4.3) as

$$\frac{\partial \phi}{\partial t} = F(\phi), \tag{4.5}$$

where $F(\phi)$ corresponds to all other terms in a form equivalent to (4.4). The temporal derivative can be easily discretized using backward differences based on known quantities at previous time levels. A first-order and second-order accurate discretization can be given by

$$\left(\frac{\partial \phi}{\partial t}\right)^{n+1} = \frac{\phi^{n+1} - \phi^{n}}{\Delta t}, \tag{4.6}$$

$$\left(\frac{\partial \phi}{\partial t}\right)^{n+1} = \frac{3\phi^{n+1} - 4\phi^{n} + \phi^{n-1}}{2\Delta t}, \tag{4.7}$$

where Δt is the time step and superscript n denotes the current time level, $n - 1$ the previous time level and $n + 1$ the next (unknown) time level. No matter if (4.6) or (4.7) is used to discretize the temporal derivative the actual time discretization scheme depends on which time level the right hand side of (4.5) is evaluated. If the current (known) time level n is used this results into an explicit scheme which can directly be solved for ϕ^{n+1}, being the only unknown. Even if this might seem computationally quite efficient it possibly requires very small time steps depending on the flow velocity and the grid size according to the Courant-Friedrichs-Lewy (CFL) condition (Courant et al. (1928)). An unconditionally stable scheme with respect to the time step is obtained if $F(\phi)$ is evaluated at the unknown time level $n + 1$. Then, however, also the right hand side contains the unknown variable and ϕ^{n+1} is defined by an implicit scheme, requiring an iterative solution. The equations corresponding to a first-order and second-order scheme are given by

$$\phi^{i} = \phi^{n} + \Delta t F(\phi^{i}), \tag{4.8}$$

$$\phi^{i} = 4/3\phi^{n} - 1/3\phi^{n-1} + 2/3\Delta t F(\phi^{i}), \tag{4.9}$$

where ϕ^{i} is initialized by ϕ^{n} and after the iteration converged ϕ^{n+1} is finally set to ϕ^{i}.

The computational effort for one time step is much higher with the implicit scheme as the equation system has to be solved several times until convergence is achieved. However, first, the time step can be chosen much larger than that for the explicit scheme such that the overall effort might be the same and secondly, the coupling and nonlinearity of the Navier-Stokes equations require iteration anyway.

The above described procedure actually applies to any unsteady transport equation and can also be used to discretize the momentum equations. However, it appears that the fluxes in the advective terms as well as the pressure in the source term are not known a priori and must be obtained as a part of the solution. Furthermore, although pressure is an unknown variable there is no explicit equation for pressure to be determined (due to the incompressibility assumption, cf. chapter 2.2). Apart from the fact that the Navier Stokes equations pose a coupled set of equations this shows that their solution needs special considerations. Many algorithms have been proposed for the solution of the Navier-Stokes equations, the most common being SIMPLE (Patankar & Spalding (1972)), SIMPLEC (van Doormal & Raithby (1984)) and PISO (Issa (1986)). They are all based on the same idea and only slightly differ in some details. However, it is beyond the scope of this chapter to go through all these details and only the basic procedure will be shortly sketched.

The starting point for all algorithms is to use the continuity equation as an equation for pressure, or more precisely for a correction to the pressure field. However, the momentum equations are still nonlinear and require an iterative solution by which the momentum equations and the pressure correction equation are solved sequentially. The basic algorithm can be summarized as follows:

- Update velocity and pressure fields based on pressure correction (if the calculation has just begun an initial solution must be guessed).
- Solve the individual momentum equations using the current values for pressure and face fluxes to update the velocity field.
- Solve the pressure correction equation with the updated velocity field.
- Check for convergence.

The implicit time discretization can be included in this iteration and the sequential solution of the Navier-Stokes equations suggests to incorporate the additional transport equations for turbulent quantities and salinity in the same manner. By that all the equations are solved iteratively for a given time step until the convergence criteria are met and although the equations are solved segregated from one another nonlinearity of the individual equations and inter-equation couplings are fully accounted for. The overall algorithm for the numerical solution of the present problem is sketched in Figure 4.2.

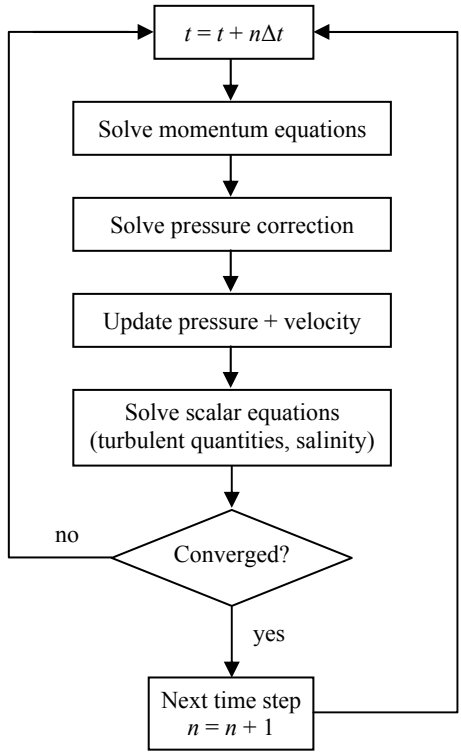

Figure 4.2: Overview of the solution algorithm for the present problem.

All simulations presented in the following chapters were based on the following methods: Second-order time discretization, QUICK scheme for advective terms, PISO scheme for pressure-velocity coupling. For the sake of completeness it should be mentioned that the resulting linear equation systems are solved by a Gauss-Seidel algorithm in conjunction with an algebraic multigrid (AMG) method to accelerate the convergence of the solution. For further details about the solution of linear equation systems the reader is referred to the literature (e.g. Ferziger & Peric (2002), Briggs et al. (2000)).

A final remark should yet be given on the total computational effort for the specific simulations of this thesis. The size of the equation systems and the effort for their solution increases with the number of grid cells needed to discretize the computational domain. While all simulations presented in chapters 5 − 7 could be done on a usual desktop PC with 1 CPU, the total number of grid cells needed to resolve the relevant features for the flow of a density current around a circular cylinder in chapter 8 is between $3\text{-}5 \cdot 10^5$ (cf. chapter 8.2). This problem size can no longer be handled on an ordinary desktop PC and requires the use of high performance computers. By that the whole problem is divided into many smaller ones which are solved parallel on many single CPUs.

As the field of parallel computing is huge[1] the specific issues will not be further discussed here, but the interested reader is again referred to the literature (see footnote). However, it should be mentioned that the present work would not have been possible without the ability to use the Hochleistungsrechner Norddeutschland (HLRN) kindly provided by the Norddeutscher Verbund für Hoch- und Höchstleistungsrechnen (www.hlrn.de). The simulations presented in chapter 8 were parallel computed on 16 CPUs (1.3 GHz Power4) and took about 2 days depending on the individual grid size. The parallel performance was about 90 %, i.e. the same simulations would have taken about 1 month on a usual desktop PC which clearly emphasizes the need for parallel computations.

[1] There is a special journal (Parallel Computing − Systems and Applications, published by Elsevier) and an annular conference (Parallel Computational fluid Mechanics, held since 1992) only on this subject.

5 Flow around a circular cylinder

This chapter is dedicated to an introduction of the characteristics of the flow around a circular cylinder. Furthermore an extensive numerical model test is presented to determine the appropriate turbulence model and grid requirements for the simulations of gravity currents around a circular cylinder in chapter 8.

5.1 Flow characteristics

5.1.1 Governing parameters and different flow states

It is generally agreed that the governing parameter for the flow around a circular cylinder is the Reynolds number based on the undisturbed velocity U_∞ in front of the cylinder and the cylinder diameter d,

$$Re = \frac{U_\infty d}{\nu}. \tag{5.1}$$

However, several circumstances can influence the flow characteristics, in particular:

- Free stream turbulence described by intensity ($I = (2/3k)^{1/2} / U_\infty$) and length scale ($L = c_\mu^{3/4} k^{3/2} / \varepsilon$).
- Roughness of the cylinder surface.
- Vibration of the cylinder in any direction.
- Presence of walls on one or either side of the cylinder d/B, where B is the distance of the cylinder from the wall.
- Aspect ratio between length L and diameter of the cylinder L/d.
- Aspect ratio between height H and diameter of the cylinder H/d when the cylinder has a free end.

For the present work the free stream turbulence and the aspect ratio are of special interest. The prior because of the bottom induced turbulence in the incoming flow and the latter because of the incoming velocity profile which is not shear free and will cause large scale vortical structures which are sensitive to the aspect ratio.

The flow around bluff bodies is characterized by the detachment of the flow from the cylinder surface and the formation of free shear layers that eventually roll up and form vortices behind the structure in the wake. This pattern is also typical for the flow around a circular cylinder but some distinct features vary significantly with the Reynolds number. Zdrakovich (1997) gives an excellent review about experimental evidence for the flow around circular cylinders and suggests to express the Reynolds number dependence by different flow states, each of which can be split up into some subcategories. A summary of the different flow regimes is given in Table 5.1 which has been adopted from Zdrakovich (1997) as well as the following review.

Abbr.	**State**	**Regime**		$\mathbf{Re_{min}}$	$\mathbf{Re_{max}}$
L	Laminar	1	no separation	0	4 - 5
		2	closed wake	4 − 5	30 − 48
		3	periodic wake	30 − 48	180 − 200
TrW	Transition in Wake	1	far wake	180 − 200	220 − 250
		2	near wake	220 − 250	350 − 400
TrSL	Transition in Shear Layers	1	lower	350 − 400	$1.0 \cdot 10^3 - 2.0 \cdot 10^3$
		2	intermediate	$1.0 \cdot 10^3 - 2.0 \cdot 10^3$	$2.0 \cdot 10^4 - 4.0 \cdot 10^4$
		3	upper	$2.0 \cdot 10^4 - 4.0 \cdot 10^4$	$1.0 \cdot 10^5 - 2.0 \cdot 10^5$
TrBL	Transition in Boundary Layers	0	precritical	$1.0 \cdot 10^5 - 2.0 \cdot 10^5$	$3.0 \cdot 10^5 - 3.4 \cdot 10^5$
		1	single bubble	$3.0 \cdot 10^5 - 3.4 \cdot 10^5$	$3.8 \cdot 10^5 - 4.0 \cdot 10^5$
		2	two bubble	$3.8 \cdot 10^5 - 4.0 \cdot 10^5$	$5.0 \cdot 10^5 - 1.0 \cdot 10^6$
		3	supercritical	$5.0 \cdot 10^5 - 1.0 \cdot 10^6$	$3.5 \cdot 10^6 - 6.0 \cdot 10^6$
		4	post-critical	$3.5 \cdot 10^6 - 6.0 \cdot 10^6$	(?)
T	Fully Turbulent	1	invariable	(?)	∞
		2	ultimate		

Table 5.1: Different regimes for the undisturbed flow around an infinitely long cylinder after Zdrakovich (1997).

5.1.2 Laminar state and Transition-in-Wake state

At very low Reynolds numbers the whole flow is initially laminar and will remain so up to $Re \approx 180 - 200$. For creeping flows with Reynolds number below $4 - 5$ there is even no separation. Separation initiates for slightly higher Reynolds numbers and forms a symmetrical closed wake behind the cylinder. With increasing Reynolds number the closed wake will begin to oscillate until the shear layers roll up and form a staggered array of laminar eddies, commonly known as the von Kármán vortex street. However, in the laminar regime the complete eddy street remains laminar and transition to turbulence first sets in in the TrW state for Reynolds numbers greater than about $180 - 200$. Also in this regime the eddy formation is still laminar and turbulence eventually sets in the wake some distance away from the cylinder.

The L and TrW states are restricted to rather very low Reynolds numbers which are only found in highly viscous fluids or for very thin structures in very slow flows. They are not of interest for the present investigation, but they allow for some nice visualization in laboratory experiments which can enhance the understanding of the general flow pattern and the sections that will follow. Figure 5.1 shows some of these visualizations for the two flow states discussed so far. The images are taken from Zdrakovich (1997).

5.1.3 Transition-in-Shear-Layers state

The TrSL state is characterized by the transition to turbulence taking place along the free shear layers while the boundary layers at the cylinder remain completely laminar. Due to the latter this state is often referred to as subcritical and the following state TrBL as supercritical. As in the TrW regime the transition in the shear layers also starts with the development of oscillations which are found at some distance from the cylinder in the TrSL1 regime. With increasing Reynolds number the transition waves will roll up in small eddies along the shear layers and finally roll up in alternating turbulent eddies forming a von Kármán vortex street in TrSL2 regime. In the final TrSL3 a sudden burst to turbulence occurs in the free shear layers and the formation of eddies takes place close to the rear of the cylinder.

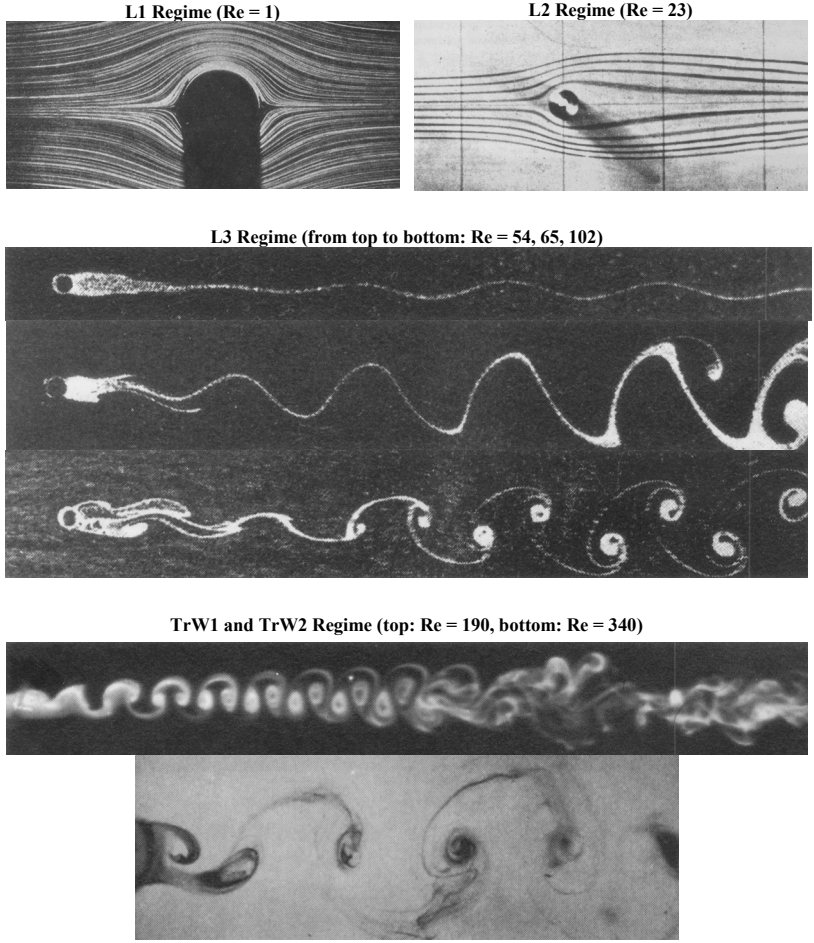

Figure 5.1: Flow visualizations from various experiments for Laminar and Transition-in-Wake regimes. Adopted from Zdrakovich (1997).

As the Reynolds number is increased from the lower ($Re \approx 2 \cdot 10^4$) to the upper ($Re \approx 2 \cdot 10^5$) bound of this regime the burst to turbulence and the eddy formation length move closer and closer to the cylinder until the transition to turbulence takes

place in the boundary layer and the next state begins. A visualization of the different flow patterns in the three TrSL regimes is shown in Figure 5.2, which again is adopted from Zdrakovich (1997).

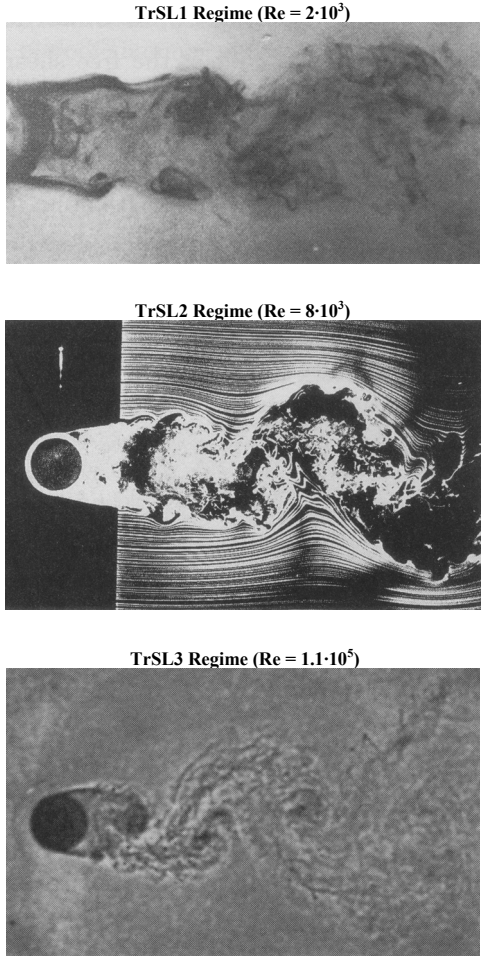

Figure 5.2: Flow visualizations from various experiments for Transition-in-Shear-Layers regime. Adopted from Zdrakovich (1997).

5.1.4 Transition-in-Boundary-Layers state and fully turbulent state

When the transition to turbulence reaches the point of separation this will cause a turbulent boundary layer that is more stable to adverse pressure gradients such that the point of separation will move downstream. The later separation from the cylinder induces higher pressures on the back face which result in an overall reduction of the drag force commonly termed as ‘drag crisis’.

The TrBL0 regime is characterized by the first onset of turbulence in free shear layers along the separation lines which disturbs the near wake and delays the eddy formation. However, the alternating eddy shedding is still prominent and the Strouhal number is constant. As the Reynolds number increases the point of separation will continuously move downstream causing a continuous decrease of the drag force.

The precritical state is abruptly terminated by a sudden increase in the drag force and shedding frequency. This is attributed to the reattachment of the separated shear layers due to the increasing level of turbulence. The thin enclosed laminar region at the cylinder is termed a separation bubble and causes the increase of the pressure force. In the TrBL1 regime only one bubble is formed on any side of the cylinder, however once established it will not change the side anymore. This ultimately leads to asymmetric forces on the cylinder and asymmetric flow patterns in the wake in the one bubble regime.

The asymmetry of the TrBL1 regime ends as abruptly as it started when a second bubble is formed on the opposite side of the cylinder at higher Reynolds numbers. This is the beginning of the TrBL2 regime which is characterized by the separation and reattachment of the shear layers on both sides of the cylinder forming two laminar separation bubbles.

When the Reynolds number is high enough ($Re \approx 5 \cdot 10^5 - 1 \cdot 10^6$) in the TrBL3 regime the separation bubbles will be irregularly disrupted and fragmented along the cylinder span. The irregularity in the separation lines will completely suppress the periodic eddy shedding due to the highly three-dimensional transitional free shear layers.

Visualizations from laboratory experiments in the four flow regimes of the TRBL state mentioned so far are shown in Figure 5.3 which again is adopted from Zdrakovich (1997).

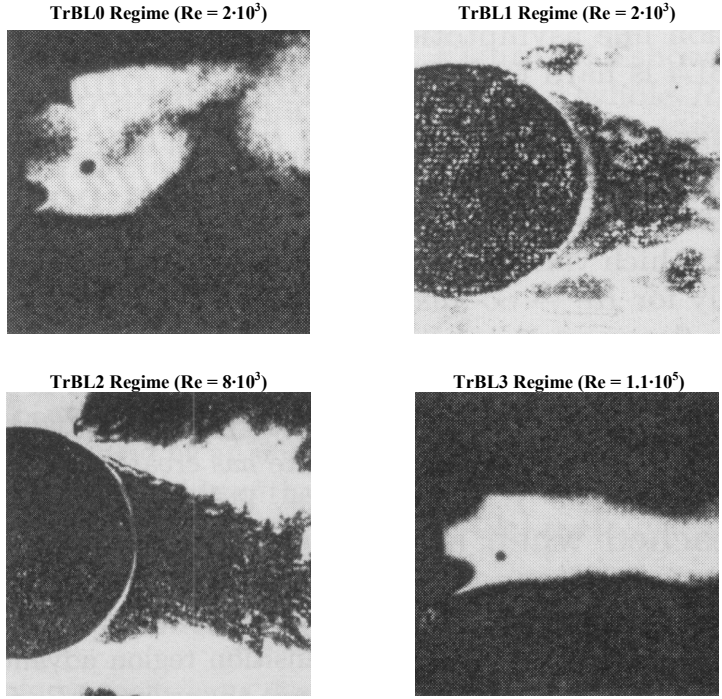

Figure 5.3: Flow visualizations from various experiments for Transition-in-Boundary-Layers regime. Adopted from Zdrakovich (1997).

It was believed for a long time that once the boundary layers became fully turbulent upstream of the separation that further increase in Reynolds number will not effect the flow features and that the TrBL3 state was the ultimate state of the flow. However, Roshko (1961) found by chance that periodic shedding reappears at $Re \approx 3.5 \cdot 10^6$, which is the beginning of the TrBL4 state. Beyond $Re \approx 6.0 \cdot 10^6$ the complete flow field around the cylinder is fully turbulent and further distinctions of subregimes have not been found yet. The upper bound for this regime is therefore $Re \approx \infty$ and the (?) in Table 5.1 marks the uncertainty of the lower bound.

5.2 Definitions

It was found above that the flow around a circular cylinder can be categorized by the dimensionless Reynolds number which generalizes the results of laboratory experiments and allows for an application to other scales. Hence, it is useful to prescribe the characteristics of the flow around a cylinder like the shedding frequency or the drag force in dimensionless numbers to give them a universal matter. Furthermore the periodic eddy shedding suggests that the flow field is decomposed in a mean part, a periodic part and a turbulent part to allow for an analytical description. All these issues will be addressed next.

5.2.1 Strouhal number

The alternating eddy shedding is characterized by a typical frequency which depends on the Reynolds number. The frequency is scaled by the free stream velocity u_∞ and the cylinder diameter d to give the non-dimensional Strouhal number

$$St = \frac{f\,d}{u_\infty}\,. \tag{5.2}$$

It turns out that this number is not only universal but also a constant over a wide range of flow regimes. In the L3 regime the periodic eddy shedding sets in with very low frequencies and the Strouhal number will be in the order of $St \approx 0.1$ in the beginning of the L3 regime. However, with increasing Reynolds number the Strouhal number will gradually increase over the laminar regime to reach a value of about $St \approx 0.2$ when transition to turbulence appears in the wake (TW state). Up to the point when the first separation bubble forms at the cylinder in the TrBL1 regime the Strouhal number will keep this constant value. The laminar bubbles at the cylinder in the TrBL1 and TrBL2 regime cause an increase of the Strouhal number to be around $St \approx 0.4$ although an exact value is hard to determine due to the transient nature of these regimes. As pointed out above eddy shedding ceases when the boundary layer is fully turbulent in front of separation in the TrBL3 regime and the Strouhal number will naturally vanish. As eddy shedding recovers in the TrBL4

regime the Strouhal number will be around 0.19 < St < 0.25, where the range reflects the uncertainties in the few measurements at this high Reynolds numbers.

An extensive compilation of experimental data on the Strouhal number is given by Cantwell & Coles (1983) from which Figure 5.4 has been taken.

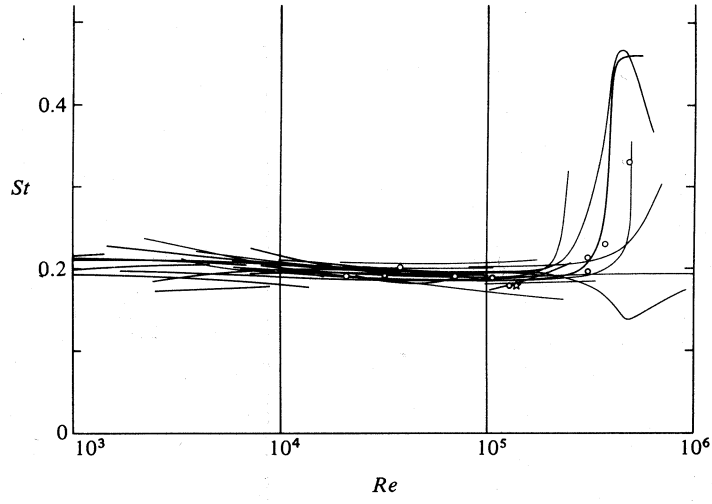

Figure 5.4: Strouhal number dependence on Reynolds number for a circular cylinder (taken from Cantwell & Coles (1983)).

Although the measurements show some scatter it is clearly visible that up to $Re \approx 3 \cdot 10^5$ the onset of TrBL1 the Strouhal number is quite constant around $St \approx 0.2$. Also the rise of the Strouhal number in the bubble regimes can be identified. However, due to the scatter in the very few data points a definition of exact values is precluded.

5.2.2 Drag and lift coefficients

The force that the flow exerts on a cylinder is basically a combination of two mechanisms, skin friction and pressure distribution. Integration of the wall shear stress τ_w and hydrostatic pressure p over the cylinder surface gives the total force

$$\vec{F} = \int_A \tau_w \vec{x}_t \mathrm{d}A + \int_A p\vec{x}_n \mathrm{d}A \,, \tag{5.3}$$

where $\vec{x}_t$ and $\vec{x}_n$ are the tangential and normal vectors to the surface. The total force vector is usually split up into its components normal and perpendicular to the mean flow direction giving the drag force F_D and lift force F_L , respectively. These forces can be non-dimensionalized by means of the dynamic pressure

$$q = \frac{1}{2}\rho u_\infty^2 \tag{5.4}$$

and the projected area normal to the force which is always Ld in case of a circular cylinder,

$$c_D = \frac{F_D}{1/2\,\rho u_\infty^2 Ld} \,, \tag{5.5}$$

$$c_L = \frac{F_L}{1/2\,\rho u_\infty^2 Ld} \,. \tag{5.6}$$

Both forces (and the coefficients) will oscillate due to the periodic eddy shedding. The lift force moves back and forth with the eddy shedding period while the drag force fluctuates twice as fast. The amplitude of the drag force is usually much smaller than that of the lift force which can induce significant swaying motions of the cylinder perpendicular to the flow. The mean of the lift force is always zero (except in the TrBL1 state) due to the symmetry of the mean flow field perpendicular to it. The mean pressure in front of the cylinder, however, is different from that at the cylinder back which imposes a mean drag force on the cylinder.

Like the Strouhal number the mean drag coefficient is quite constant around $c_D \approx 1$ over a wide range of flow states up to the onset of transition in the boundary layers aligned with the ‘drag crisis’ explained above. The mean drag coefficient obtained from various experimental data as compiled by Cantwell & Coles (1983) is shown in Figure 5.5. It can be seen that for $Re < 5{\cdot}10^3$ in the early Transition-in-Shear-Layers state the drag coefficient is slightly less than 1 and increases then to obtain a constant value in the range $1.1 < c_D < 1.3$. The scatter of the data suggests the drag

coefficient to be quite sensible to influencing parameters like e.g. the roughness of the cylinder surface. However, the drag crisis occurring due to the onset of turbulence in the boundary layers is clearly identified between the TrBL0 and TrBL2 states. If the Reynolds number further increases the drag coefficient will slightly recover a value of about $c_D \approx 0.4$.

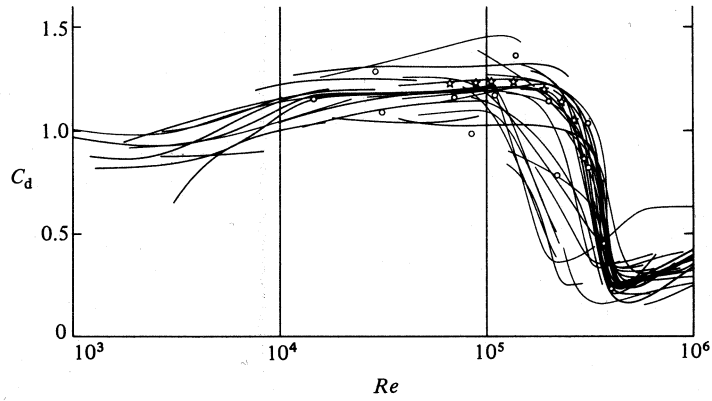

Figure 5.5: Drag coefficient as a function of Reynolds number for a circular cylinder (taken from Cantwell & Coles (1983)).

5.2.3 Triple decomposition

As shown above in most situations the flow around a circular cylinder will have a strong periodic component due to the alternating shedding of eddies from the cylinder surface. To gain an analytical access to the physics of the circular cylinder flow it is useful to extent the Reynolds decomposition introduced in chapter 3.4. Instead of decomposing the flow variables only into a mean and a turbulent fluctuating part a third component is added which reflects the periodic motion. Thus,

$$\phi = \overline{\phi} + \tilde{\phi} + \phi' , \tag{5.7}$$

where ϕ represents any flow variable and the overbar, tilde and prime denote the mean, periodic and turbulent components, respectively. Incidentally, this decomposition was introduced by Reynolds & Hussain (1972) where the first author is not to be confused with Osborn Reynolds who introduced the decomposition given by (3.24) already in 1895. However, the name seems to be obligatory.

To proceed further it is again necessary to define averages and the corresponding rules that apply to each of the components. Given a typical signal of N samples of a flow quantity that covers a few shedding cycles the global mean value is readily defined as

$$\overline{\phi} = \frac{1}{N}\sum_{n=1}^{N}\phi_n \,. \tag{5.8}$$

For the determination of the fluctuating components it is also necessary to define an ensemble average according to the definition in (3.25). To account for the periodic motion one shedding cycle is subdivided into M nominally equal sections each of which containing N_m samples. The ensemble average is then represented by a phase average, meaning an ensemble average at constant phase:

$$\langle\phi\rangle = \frac{1}{N_m}\sum_{i=1}^{N_m}\phi_i \qquad (m = 1,2,\ldots,M)\,. \tag{5.9}$$

Note that in chapter 3 the ensemble average was identified by an overbar which is here used for the global (temporal) mean while the ensemble (phase) average is marked by angled brackets.

The fluctuating part of the periodic component is then given by

$$\tilde{\phi} = \langle\phi\rangle - \overline{\phi}\,, \tag{5.10}$$

and the turbulent component accordingly,

$$\phi' = \langle\phi\rangle - \phi\,. \tag{5.11}$$

These definitions are subject to the following rules:

$$\begin{aligned} &\langle \bar{\phi} \rangle = \bar{\phi}; \qquad \langle \tilde{\phi} \rangle = \tilde{\phi}; \qquad \langle \phi' \rangle = 0; \\ &\langle \bar{\phi}\phi \rangle = \bar{\phi} \langle \phi \rangle; \quad \langle \tilde{\phi}\phi \rangle = \tilde{\phi} \langle \phi \rangle; \quad \langle \phi'\phi \rangle = \phi'\phi'. \end{aligned} \tag{5.12}$$

Ignoring external forces in form of gravity or Coriolis forces the momentum balance for the mean flow at constant phase can be written as

$$\frac{\partial \langle u_i \rangle}{\partial t} + \langle u_j \rangle \frac{\partial \langle u_i \rangle}{\partial x_j} - \nu \frac{\partial^2 \langle u_i \rangle}{\partial x_j \partial x_j} = -\frac{1}{\rho_0} \frac{\partial \langle p \rangle}{\partial x_i} - \frac{\partial \langle u_i' u_j' \rangle}{\partial x_j}, \tag{5.13}$$

which is exactly the same as the Reynolds averaged momentum balance (3.30) except for the neglect of gravity and Coriolis terms and the notation for the average. Hence, the mixing of momentum at constant phase is solely governed by the turbulent fluxes. However, inserting (5.10) into (5.13) and taking the global average yields the following momentum equation (cf. Reynolds & Hussain (1972)):

$$\bar{u}_j \frac{\partial \bar{u}_i}{\partial x_j} - \nu \frac{\partial^2 \bar{u}_i}{\partial x_j \partial x_j} = -\frac{1}{\rho_0} \frac{\partial \bar{p}}{\partial x_i} - \frac{\partial \left(\overline{u_i' u_j'} + \overline{\tilde{u}_i \tilde{u}_j} \right)}{\partial x_j}, \tag{5.14}$$

which shows that the global mean flow is additionally mixed by the fluctuations of the periodic motion.

5.3 Flow at Re = 140.000

The flow around a circular cylinder is one of the most difficult tasks in numerical modeling. Not only because the distinct flow features strongly vary with Reynolds number as shown above, but also the point of separation from the cylinder is not clearly defined and depends on the right prediction of the adverse pressure gradient. As pointed out by Breuer (2000) high Reynolds number circular cylinder flow is a challenging test case and can be considered as the paradigm of complex flows.

In view of the structure induced mixing of density currents, here, it is most important to accurately simulate the turbulence in the cylinder wake which is the major source for mixing as to be shown later. There have been very many laboratory

experiments on the flow around a circular cylinder most of which, however, exclusively concentrated on the bulk and mean effects like drag coefficient, shedding frequency or recirculation length. Moreover, the Reynolds numbers of the experiments were often limited by the laboratory facilities. One of the few experiments at moderate Reynolds number which concentrated on the turbulent flow field in the cylinder wake is that of Cantwell & Coles (1983). As such it has been chosen by the Advisory Group for Aerospace Research and Development (AGARD) to be a suitable test case for the validation of numerical models (AGARD (1998)). The complete well documented experimental data is provided on the internet (ftp://torroja.dmt.upm.es/AGARD) and has been used by several authors as a reference for their numerical models. For the present purposes this has the advantage that not only the laboratory measurements will serve for a comparison with the numerical model data but also the experience with other numerical simulations from the literature can help in the interpretation of the results in this work. These will be summarized next.

5.3.1 Experimental data and other numerical simulations

The experiments of Cantwell & Coles (1983) were carried out in a wind tank with a circular stainless-steel tubing of 2.97 m length and 10.14 cm diameter. Velocities were measured by a flying hot wire probe at various points in the wake of the cylinder. At each point measurements were taken over 1024 shedding cycles with a rate of 16 samples per period. Data was evaluated using the triple decomposition method described above and the presented results concentrated mainly on the mean velocity field and the correlations of the turbulent and periodic fluctuations at constant phase. The recirculation length behind the cylinder was determined from the mean velocity field averaging the results over all 16 distinct phases. Pressure measurements around the circumference of the cylinder showed a pressure distribution and a back pressure coefficient which is in a confidential range compared to the results of other experiments at similar Reynolds numbers.

The angle of separation from the cylinder was estimated from the pressure measurements and defined as the point of inflection of the pressure distribution

which led to a value of 77° measured from the stagnation point. Aschenbach (1968) found that in the Reynolds number regime between $Re = 1 \cdot 10^5$ and $Re = 2.6 \cdot 10^5$ the separation angle shows a very nonlinear behavior and varies between 72° and 94° with the minimum value at $Re = 1.5 \cdot 10^5$. Son & Hanratty (1969) give a value of 78° at $Re = 1 \cdot 10^5$ which confirmed the findings of Aschenbach (1968) and gives confidence to the value Cantwell & Coles (1983) which might have a small uncertainty of a few degrees. The Strouhal number of $St = 0.179$ determined by Cantwell & Coles (1983), however, is quite low compared to most other experimental data which suggest a value of $St \approx 0.2$ (see Figure 5.4). This fact is also discussed by the authors and should be kept in mind in the comparison with numerical experiments.

Recently, Djeridi et al. (2003) and Perrin et al. (2006) carried out PIV measurements of the flow around a circular cylinder at the same Reynolds number but in a confined channel with much smaller aspect ratios ($L/D = H/D = 4.8$). Even if these circumstances and the measurement techniques are quite different compared to those of Cantwell & Coles (1983) the presented results of the mean velocity field and particularly the turbulent quantities are very similar. This confirms the intrusive velocity measurements of Cantwell & Coles (1983) giving more confidence in their data and justifies using them as a reference for the validation of numerical models.

One of the first numerical simulations were presented by Franke (1991) who used a two-dimensional Finite Volume formulation in cylindrical coordinates of the RANS equations which were closed by the standard k-ε model and a Reynolds stress model with the model constants of Gibson & Launder (1978) (see chapter 3.6, Table 3.7). For the near wall treatment at the cylinder Franke (1991) used the two layer approach for both turbulence models. The major outcome of this work is that the standard k-ε model underestimates the turbulent fluctuations (data for the periodic fluctuations were not presented) which ultimately leads to an overestimation of the recirculation length attributed to the too small dissipation in the free shear layers. The Reynolds stress model on the other hand gives a too small recirculation length probably because of the overestimation of the fluctuations in the wake. Although both models provide very different mean and turbulent velocity fields and consequently different pressure distributions around the cylinder they predict quite

similar Strouhal numbers which are in good agreement with the experimental data. This might lead to the conclusion that the Strouhal number is not necessarily related to the turbulence in the cylinder wake.

Breuer (2000) has shown that LES is a very powerful tool in the simulation of the flow around a circular cylinder. He investigated the influence of different subgrid scale (SGS) models, different grid resolutions and different computational domain sizes on the numerical results and found a generally good agreement with the data of Cantwell & Coles (1983). A reduction of the SGS constant and hence the dissipating mechanism in the modeled portion of the turbulent flow field leads to a decrease of the backpressure and drag coefficients and an increase in the recirculation length. A similar behavior could be deduced from the results of Franke (1991) above.

Although the LES approach seems to be superior to models based on the turbulent viscosity assumption this has to be paid with a very much higher computational effort. As in a LES a significant part of the turbulent flow field is directly resolved by the numerical grid this must be much finer than in case of turbulent viscosity or Reynolds stress models. Moreover, variations along the cylinder span can no longer be neglected and all simulations require a three-dimensional grid to account for the vortex stretching and the energy cascade in the resolved part of the turbulence spectrum.

While the simulations of Franke (1991) were performed on an O-type grid with a radius of 20 cylinder diameters and 144 x 144 grid points, Breuer (2000) used also an O-type grid but with a smaller radius of 15 cylinder diameters and a finer resolution of 165 x 165 and 325 x 325 grid points, respectively. The cylinder span was always resolved with 64 grid points in these simulations such that the numerical effort was about 50 to 200 times larger than that for the simulations of Franke (1991).

Lübcke et al. (2001) made a direct comparison of the LES and the RANS approach. For the subgrid scale of the LES a dynamic model was chosen as the results of Breuer (2000) indicate a slightly better performance of this approach compared to that with the classical Smagorinsky constant. The RANS equations were closed by the standard k-ω model and an explicit algebraic stress model (EASM). While the

RANS simulations were performed on a two-dimensional grid with a total of 18 000 grid points, for the LES a three-dimensional grid was chosen with 64 layers along the cylinder span and a total of 2 600 000 grid points. The additional numerical effort for the LES, although not explicitly given in the paper, can be estimated to be two orders of magnitude bigger than that for the RANS simulations.

Lübcke et al. (2001) did not present results for the turbulent and periodic fluctuations but the mean streamwise velocity along the centerline for the LES compares fairly well to the results of Breuer (2000) and the laboratory data although the mean drag coefficient and the backpressure coefficient are significantly underestimated. The best results were achieved with the EASM which did not only give a good agreement of the mean streamwise velocity but also compared well with the bulk parameters. The standard k-ω model on the other hand can be regarded as the worst in this comparison as it showed the same behavior like the standard k-ε model used by Franke (1991). Not only the recirculation length is significantly overestimated (which might indicate an underestimation of turbulence) but also the drag coefficient is much too low. Interestingly the Strouhal number is much higher than that determined by Franke (1991) which is not commented by the authors but should be kept in mind for the interpretation of the present results to be followed.

The bulk parameters of the experiment of Cantwell & Coles (1983) and the numerical simulations from the literature presented above are compiled in Table 5.2. As mentioned above the Strouhal number of the experiment might be a bit too low and should be about $St \approx 0.2$ which is confirmed by the presumably best numerical data with the LES of Breuer (2000) and Lübcke et al. (2001). The background pressure coefficients and recirculation lengths of Franke (1991) were not explicitly given and were estimated from figures. From the data given in Table 5.2 and the more specific results in each of the papers it might be concluded that the turbulent viscosity approach together with a two-equation turbulence model is not the best choice for the simulation of the flow around a circular cylinder. However, it will be shown in the present model tests that this is only true for the standard formulations and slight modifications (RNG k-ε, SST k-ω) improve the performance significantly.

Reference	St	α_s [°]	$\overline{c}_D$	c_{pb}	L_r
Exp., Cantwell & Coles (1983)	0.18	77	1.24	-1.21	0.44
std. k-ε, Franke (1991)	0.22	–	0.72	≈ -0.4	≈ 1.9
RSM, Franke (1991)	0.23	–	1.55	≈ -1.5	≈ 0.3
LES, Breuer (2000)	0.20 – 0.22	92.6 – 95.2	1.22 – 1.45	-1.40 – -1.76	0.34 – 0.57
LES, Lübcke et al. (2001)	0.2	92	0.68	-0.65	0.40
std. k-ω, Lübcke et al. (2001)	0.3	–	0.41	–	1.19
ASM, Lübcke et al. (2001)	0.22	–	1.16	–	0.59

Table 5.2: Bulk parameters of the experiment of Cantwell and Coles (1983) and numerical simulations of other authors.

5.3.2 Model setup

The goal of the present analysis is to determine the numerical demands to predict the flow field around a circular cylinder as accurate as possible. These imply the necessary grid size and the appropriate turbulence model including the near wall treatment as explained in chapter 3.8. In view of the high Reynolds numbers associated with the simulations of a density current around a circular cylinder in a natural scale only turbulence models based on the turbulent viscosity assumption have been used as LES would require a too high numerical effort.

Thus, it is sufficient to use a two-dimensional grid here and neglect the variations along the cylinder span as they are suppressed by the turbulence models anyway. The cylinder with a unit diameter 1 is placed at $x = y = 0$ in a computational domain that extents 6 diameters left, right and in front of the cylinder and 20 diameters in the cylinder wake. Two different regular grids have been used which are shown in Figure 5.6. Note that the coordinates have been nondimensionalized by the cylinder diameter according to (5.15) (see below). However, as the diameter had been chosen to be unity this is not important in the present context but for consistency all coordinates will be given in non-dimensional form denoted by capital letters.

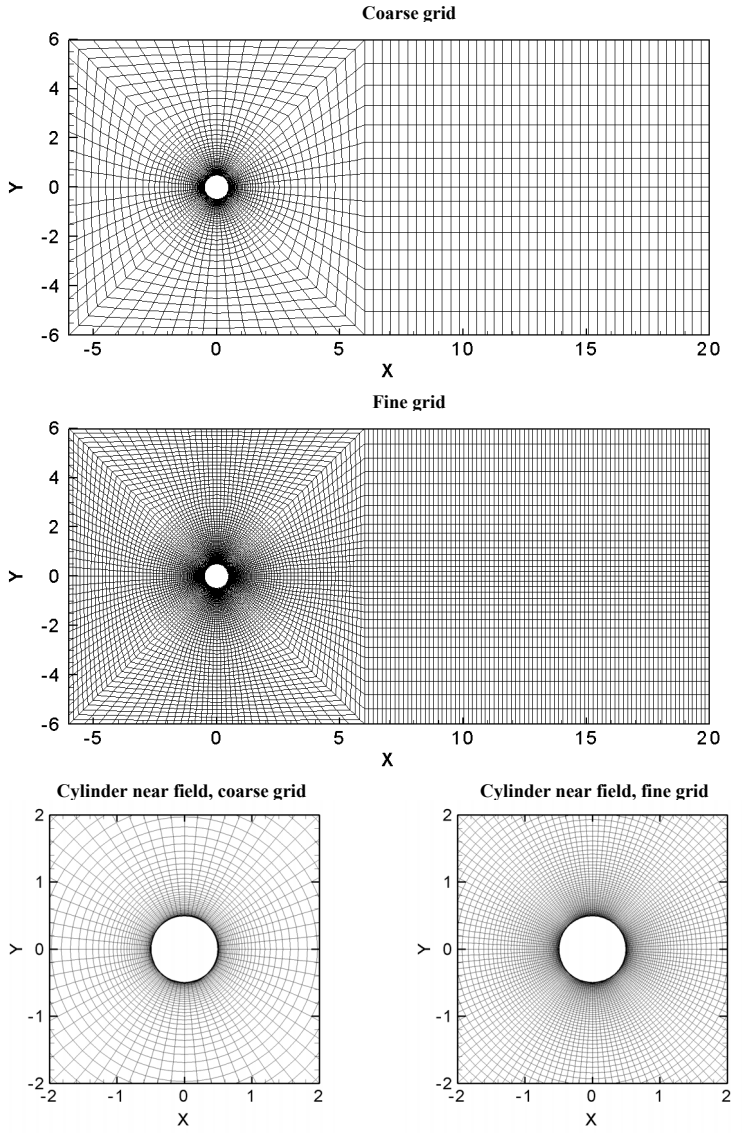

Figure 5.6: Coarse and fine numerical grids used for the present simulations.

The grid is circular up to 3 diameters around the cylinder and then converted to the rectangular shape of the numerical channel. The finest resolution is in the vicinity of the cylinder to account for the wall boundary layer and the free shear layers shed from the cylinder surface. With increasing distance from the cylinder the numerical grid gets successively coarser while the grid size is kept constant after 6 diameters behind the cylinder where the resolution in the wake along $Y = 0$ is kept more compact compared to the less important side regions.

The fine grid has twice the resolution of the coarse grid except in the near wall region where the distance of the closest grid point is governed by the near wall treatment method. Both the wall functions and the two layer approach as introduced in chapter 3.8 have been used. For the wall functions approach the non-dimensional wall distance should be slightly above $y^+ \approx 30$ while for the two layer approach it should be less than $y^+ \approx 5$. To fulfill these requirements on both grids identically the distance of the closest grid point to the cylinder surface has been chosen to be $2.1 \cdot 10^{-3}$ and $2.5 \cdot 10^{-4}$ cylinder diameters for the wall function and the two-layer approach, respectively. As mentioned above the grid is successively coarsened with increasing distance from the cylinder, the stretching factor for the coarse grid being about $f_w \approx 1.11$ and for the fine grid about $f_w \approx 1.06$. The main characteristics of the different grids used in this study are summarized in Table 5.3.

grid	N	y^+	$\Delta r_{\min}$	f_w
WF coarse	3840	32	$2.1 \cdot 10^{-3}$	1.109
WF fine	12800	32	$2.1 \cdot 10^{-3}$	1.0615
TL coarse	4992	3	$2.5 \cdot 10^{-4}$	1.116
TL fine	17280	3	$2.5 \cdot 10^{-4}$	1.0623

Table 5.3: Characteristics of the different grids used for the simulations. Total number of grid cells N, maximum non-dimensional wall distance y^+, minimum wall distance $\Delta r_{\min}$ in cylinder diameters and stretching factor f_w in the near wall region.

For the simulation of the turbulent flow field all two equation models as described in chapter 3.5 and the RSM as derived in chapter 3.6 with the coefficients of Gibson &

Launder (1978) have been used. It should been noted, that the distinction in the near wall treatment between the wall function and the two layer approach actually only applies to the k-ε models and the RSM. For the k-ω models the near wall region is always treated as depicted in chapter 3.8.2 but with different distances of the closest grid point to the cylinder.

The boundary conditions at the outer boundaries are a velocity inlet at $X = -6$, a pressure outlet at $X = 20$ and symmetry (slip) conditions at the sidewalls ($Y = \pm 6$). The turbulence parameters at the inlet are determined from an imposed turbulence intensity of $I = 0.1$ % and a turbulent viscosity ratio of $\mu_t/\mu = 1$. All simulations were started from scratch with zero velocities and turbulence and run so long until a periodic motion behind the cylinder established. Afterwards the runs were continued and statistics were accumulated over at least 40 shedding cycles.

5.3.3 Present results

The analysis of the present numerical results is basically split into three parts. First the bulk parameters like the Strouhal number, mean drag coefficient, recirculation length and separation angle shall give a first impression of the performance of each turbulence model and the influence of grid resolution and near wall treatment. The following comparison of the mean velocity field will help to confirm these first interpretations. Even if the bulk parameters and the mean flow field might be important in some applications the major interest here is on the right prediction of the turbulent and fluctuating flow field around the cylinder. Therefore this point will be discussed a bit more detailed at the end of this section.

Bulk parameters

The Strouhal number St is determined from the time series of the lift coefficient and given in Table 5.4 for all 24 model runs. It can be noted at first sight that this parameter is generally too high compared to the experimental data and the numerical results presented above. Only the simulations of Lübcke et al. (2001) with the standard k-ω model show a similarly high value. Concerning the near wall treatment or the grid resolution there is no clear tendency to be deduced from the Strouhal

numbers given in Table 5.4, but it is noteworthy that the SST *k-ω* model seems to perform even better than the RSM concerning this specific parameter. However, as the Strouhal number is of limited interest here, no more work has been put in a further investigation of the overall rather poor numerical prediction.

grid	std. *k-ε*	RNG *k-ε*	rel. *k-ε*	std. *k-ω*	SST *k-ω*	RSM
WF coarse	0.28	0.28	0.28	0.26	0.25	0.28
WF fine	0.33	0.29	0.32	0.29	0.26	0.31
TL coarse	0.27	0.31	0.31	0.27	0.26	0.29
TL fine	0.28	0.34	0.37	0.31	0.27	0.31

Table 5.4: Comparison of Strouhal number *St* for all 24 model runs.

Like the Strouhal number the angle of separation which is given in Table 5.5 is generally overestimated quite significantly compared to the 77° determined by Cantwell & Coles (1983). In case of the *k-ε* models and the RSM there is only a minor improvement if the two layer approach is used instead of wall functions which indicates that none of them is really capable to reflect the physics in the boundary layer correctly. This is supported by the fact that the *k-ω* models which are integrated down to the wall show values comparable to the LES data of Breuer (2000) and Lübcke et al. (2001) if the boundary layer is adequately resolved (last row in Table 5.5).

grid	std. *k-ε*	RNG *k-ε*	rel. *k-ε*	std. *k-ω*	SST *k-ω*	RSM
WF coarse	115.4	117.6	115.6	117.0	109.0	116.5
WF fine	114.8	118.2	114.7	120.0	111.1	116.7
TL coarse	111.1	114.2	112.3	111.3	105.5	115.2
TL fine	111.0	113.5	111.9	98.1	92.7	112.9

Table 5.5: Comparison of separation angle α_s for all 24 model runs.

As shown in chapter 5.2.2 the mean drag coefficient $\overline{c}_D$ is evaluated from the pressure and skin friction around the cylinder where the latter only makes a few

percent of the overall drag force at this high Reynolds number. Thus, the mean drag coefficient is representative for the pressure distribution around the cylinder and an additional analysis of the backpressure coefficient is dispensable as could already be deduced from Table 5.2 above. The $\overline{c}_D$ values of the present analysis are shown in Table 5.6.

grid	std. *k-ε*	RNG *k-ε*	rel. *k-ε*	std. *k-ω*	SST *k-ω*	RSM
WF coarse	0.49	0.73	0.54	1.40	1.10	0.75
WF fine	0.48	0.69	0.54	1.42	1.11	0.80
TL coarse	0.44	0.41	0.39	1.16	0.83	0.66
TL fine	0.48	0.40	0.39	1.20	0.87	0.70

Table 5.6: Comparison of mean drag coefficient $\overline{c}_D$ for all 24 model runs.

A comparison of the first and last two rows clearly shows that the overall grid resolution has rather no influence on the mean drag coefficient as might have been expected, because the pressure distribution is mostly governed by the near wall region. Accordingly, except for the standard *k-ε* model there seems to be a quite significant sensibility to the near wall treatment and corresponding grid resolution at the cylinder. The two layer approach and higher grid resolution in the boundary layer reduce the mean drag on the cylinder which is generally lower for the *k-ε* models and highest for the standard *k-ω* model.

While all parameters regarded so far are not important concerning the fluctuating motions in the cylinder wake the recirculation length L_r which is actually derived from the mean flow field will give a first idea about the mixing of momentum. In section 5.3.1 above it was found that the higher the turbulent and periodic fluctuations the shorter the recirculation length as the shedding free shear layers will roll in earlier with increasing turbulence level. Table 5.7 summarizes the recirculation lengths for the present model runs. Compared to the data of Cantwell & Coles (1983) the standard *k-ε* and the realizable *k-ε* model overestimate the recirculation length. This is consistent with the findings of Franke (1991) and Lübcke et al. (2001) even if the values here are closer to the laboratory reference.

grid	std. k-ε	RNG k-ε	rel. k-ε	std. k-ω	SST k-ω	RSM
WF coarse	0.86	0.41	0.79	0.10	0.32	0.46
WF fine	0.91	0.42	0.86	0.12	0.28	0.42
TL coarse	0.91	0.63	0.76	0.15	0.42	0.38
TL fine	0.95	0.66	0.80	0.16	0.45	0.40

Table 5.7: Comparison of recirculation length L_r for all 24 model runs.

The RNG modification of the k-ε model on the other hand is in good agreement with the reference data if wall functions are applied. With the two-layer approach, however, L_r gets significantly larger indicating an underestimation of the fluctuating motions. The same tendency can be found for the k-ω models if the resolution of the boundary layer is increased. However, while the standard k-ω model always seems to overestimate the fluctuations (too small L_r) the SST k-ω model performs fairly well on the finest grid.

Mean flow field

After the bulk properties have been analyzed, now the mean velocities will be compared to the experimental data. For this purpose all quantities are normalized first. Lengths are normalized by the cylinder diameter d and velocities are normalized by the free stream (inlet) velocity u_∞. Denoting the normalized mean quantities by capital letters, one obtains:

$$X = \frac{x}{d}; \qquad Y = \frac{y}{d}; \qquad U = \frac{\overline{u}}{u_\infty}; \qquad V = \frac{\overline{v}}{u_\infty}. \tag{5.15}$$

Figure 5.7 shows the normalized mean streamwise velocity U along the x-axis at the plane of symmetry ($Y = 0$). In each panel the results of all turbulence models for one specific grid are compared to the data of Cantwell & Coles which are represented by the open circles. At first sight it appears that all models, except for the standard k-ω model (to be discussed later), overestimate the velocity in the far field by about 10 % which might be attributed to the delayed separation which imports momentum in streamwise direction into the wake and accelerates the flow. This argument is supported by a faster increase of the velocity after the separation bubble.

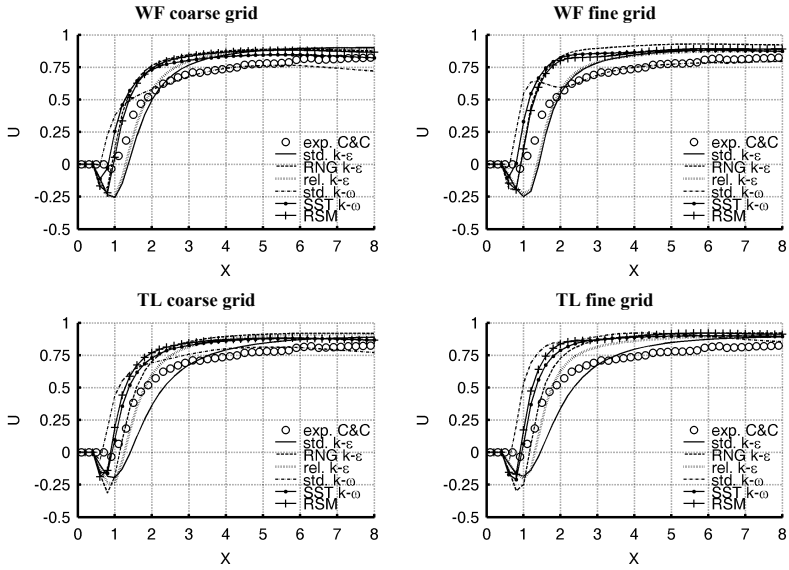

Figure 5.7: Normalized mean streamwise velocity U along the x-axis at $Y = 0$.

The overall grid resolution only slightly alters the mean flow in the wake as can be seen by comparing the left and right panels. The most obvious difference is the slightly lower acceleration behind the separation bubble on the coarse grids which might be attributed to a higher numerical dissipation. The near wall treatment and the resolution in the boundary layer, respectively, have more influence on the results, which will be discussed considering the individual turbulence models.

As could be expected from the analysis of the bulk parameters above the standard and the realizable k-ε model are very similar at least if wall functions are used. In case of the two-layer approach, however, they show a completely opposite behavior. While for the standard k-ε model the recirculation length increases (cp. Table 5.7) and the acceleration decreases, the recirculation length for the realizable model is almost constant and the velocity increase is slightly faster. The reason for that is an unrealistic high production of turbulent kinetic energy in front of the stagnation point which is a typical drawback of the standard k-ε model (cf. Bosch (1995)) and is especially severe with the two-layer approach. The realizable model also suffers

from this problem, but the effects are less extreme mainly due to the different formulation of the turbulent viscosity.

The results with the RNG k-ε model are somewhat better compared to those with the other two of this class of models. The main reason for this superiority is the additional term in the ε equation which compensates the overproduction of turbulent kinetic energy. As could already be seen in the analysis of the bulk parameters, with the wall function approach the RNG k-ε model provides very similar results to those of the RSM which might be designated as the most elaborate of all models. However, if the two-layer approach is applied the overproduction of turbulent kinetic energy gets stronger with a similar effect like for the standard k-ε model.

In contrast to the k-ε models neither the RSM nor the k-ω models tend to overestimate the production of turbulent kinetic energy in front of the cylinder. Therefore they seem to be better suited for the simulation of the flow around bluff bodies. Obviously the RSM and the SST k-ω model are in good agreement with each other and show almost similar results on all grids. The standard k-ω model, however, yet underestimates the turbulent kinetic energy which leads to increased periodic fluctuations and even an unrealistic reattachment of the free shear layers. This in turn causes the generally too short recirculation length and the somehow strange velocity profile in the upper right panel. As will be shown in the following section, due to the strong periodic motion the total fluctuating kinetic energy is significantly overestimated which again implies a higher momentum exchange and explains the lower velocity in the far field.

Further support for the findings up to now can be gained from the normalized mean cross-stream velocity V in the wake. Figure 5.8 shows the profiles in a cross section, 0.5 diameters behind the cylinder (X = 1) where the shear layers roll in and V is approximately at maximum. The standard and the realizable k-ε model clearly underestimate the maxima even if the two-layer approach shows some improvement for the realizable k-ε model. Again, the best agreement with the experimental data is found for the RSM and the SST k-ω model which slightly overestimate the maxima on the fine grids. The RNG k-ε model is comparable to the RSM if wall functions are used and underestimates the peak velocities in case of the two-layer approach.

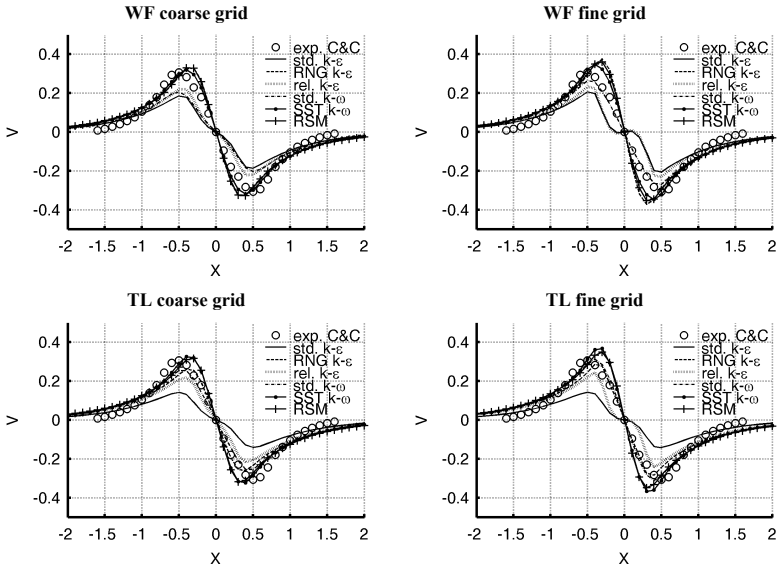

Figure 5.8: Normalized mean cross-stream velocity V along the y-axis at $X = 1$.

Due to the retarded separation all models predict a confined wake as can be seen by the velocity maxima which are closer to the line of symmetry than the experimental data. The higher velocities in the outer region are attributed to the acceleration of the flow in the wake that sucks in the surrounding fluid.

Up to now it can be summarized that the standard k-ε model, the realizable k-ε model and the standard k-ω model do not represent the best choice for the simulation of the flow around a circular cylinder. As might have been expected, the results for the RSM as the most elaborate model compare fairly well with the experimental data despite the retarded separation and the resulting effects which are, however, a problem for all models considered here. The results for the RNG k-ε model are almost identical to those of the RSM as far as wall functions are used for the near wall treatment. Finally, the SST k-ω model, which provides a very similar mean flow field compared to the RSM, can be considered as the best model for the circular cylinder flow as it is slightly superior concerning the bulk parameters compared to the laboratory data.

Turbulent and periodic flow field

As remarked in the introduction of this chapter the bulk properties and the mean flow field are of minor interest here, as it is the turbulence and fluctuating motion that will contribute to the additional mixing of density currents. The preceding discussion, however, provided a good insight into the general advantages and drawbacks of each turbulence model and will help in the interpretation of the following analysis of the turbulent and periodic flow field.

Cantwell & Coles (1983) used the triple decomposition technique described above for the evaluation of their data. The same procedure was followed here in the analysis of the numerical results even if it might not be expected that a turbulence model will exactly reproduce the break-up into turbulent and periodic fluctuations as measured in the laboratory. But this is of minor importance, anyway, as on average momentum is mixed by the sum of both components as shown in (5.14). Therefore a turbulence model must be able to predict this sum correctly and not each component individually. However, as already mentioned above, both components interact with each other, such that a higher turbulent kinetic energy will decrease the periodic motion and vice versa.

Following the naming convention in the preceding section the normalized mean total momentum fluxes are denoted by

$$u_i u_j = \frac{\overline{u_i' u_j'} + \overline{\tilde{u}_i \tilde{u}_j}}{u_\infty^2} \qquad i = j = 1,2 \tag{5.16}$$

and the normalized mean turbulent, periodic and total fluctuating kinetic energies are defined as

$$k_t = \frac{3}{4}\frac{\overline{u_i' u_i'}}{u_\infty^2}; \qquad k_p = \frac{3}{4}\frac{\overline{\tilde{u}_i \tilde{u}_i}}{u_\infty^2}; \qquad k = k_t + k_p = \frac{3}{4} u_i u_i \qquad i = 1,2\,. \tag{5.17}$$

Franke (1991) and Breuer (2000) compared their numerical results with the data of Cantwell & Coles (1983) for each of the individual momentum fluxes. However, due to the number of different grids and turbulence models that have been

investigated here, a detailed discussion of the momentum fluxes would go beyond the scope of this section. Thus, the present analysis is restricted to the fluctuating kinetic energy as its turbulent part is a direct outcome of all two equation models and, as can be seen from (5.17), this quantity is representative for the sum of the normal stresses.

Figure 5.9 shows the normalized mean total fluctuating kinetic energy k along the plane of symmetry at $Y = 0$.

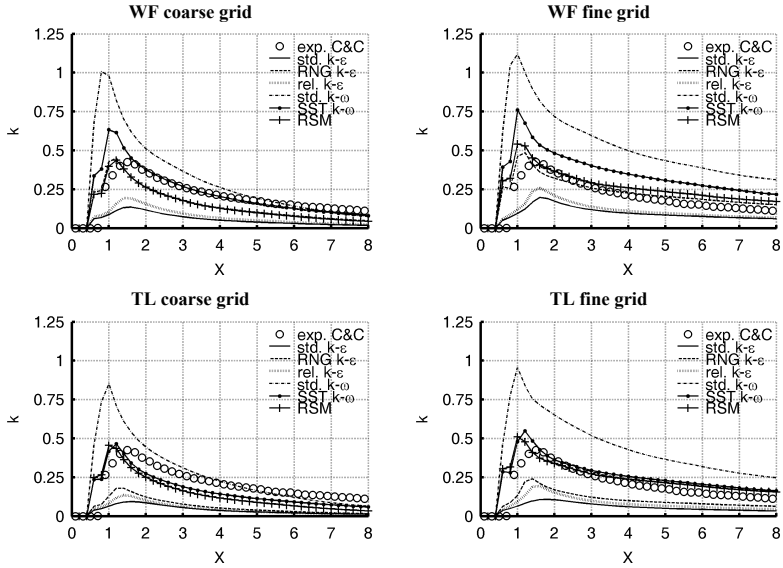

Figure 5.9: Normalized mean total fluctuating kinetic energy along the x-axis at plane of symmetry ($Y = 0$).

Several of the above findings can be approved here. The RSM and the SST k-ω model show the best agreement with the laboratory data while the results for the latter are improved by a refinement of the boundary layer. By contrast, the RNG k-ε model works best with a coarse boundary layer grid and the use of wall functions, as can be seen by the almost identical results compared to the RSM. All models show an increased amount of fluctuating kinetic energy on the fine grids due to the

reduced numerical dissipation. The retarded separation on the backside of the cylinder is reflected by the peak values which are always closer to the cylinder than the experimental data.

The overestimation of the recirculation length with the standard and realizable k-ε model was attributed above to an underestimation of the total dissipation which is approved by the significantly lower total fluctuating kinetic energy. On the other hand, the standard k-ω model showed a too short recirculation length and higher dissipation in the near wake leading to a reduced mean streamwise velocity compared to the other models. Also this argumentation is manifested by the fluctuating kinetic energy which is always significantly overestimated, especially in the near wake.

Although no significantly new insights might be expected from the lateral extent of the total fluctuating kinetic energy, it might be interesting to look at the overall distribution. This is shown as contour plots in Figure 5.10, where the top panel represents the laboratory reference of Cantwell & Coles (1983) and the panels below correspond to the presumably best numerical results for each turbulence model. The cross-stream extent is confined for all simulations, particularly very close to the cylinder, which nicely shows the impact of the point of separation. However, despite this fact the agreement of the experimental data with the results of the RNG k-ε model, the SST k-ω model and the RSM is very satisfactory. Qualitatively also the standard and realizable k-ε model and the standard k-ω model agree with the laboratory data as far as they at least show the right distribution. Anyway, the absolute values are clearly missed which above was assumed to be caused by an over- and underproduction of turbulent kinetic energy, respectively.

This assumption shall be confirmed by Figure 5.11 where the distribution of turbulent (left row) and periodic (right row) fluctuating kinetic energy is shown for the standard k-ε model (in representation of the realizable k-ε model), the standard k-ω model and the SST k-ω model as a reference. Indeed, in case of the standard k-ε model the severe overproduction of k_t in front of the cylinder is carried around the cylinder to yield much higher values than for the SST k-ω model.

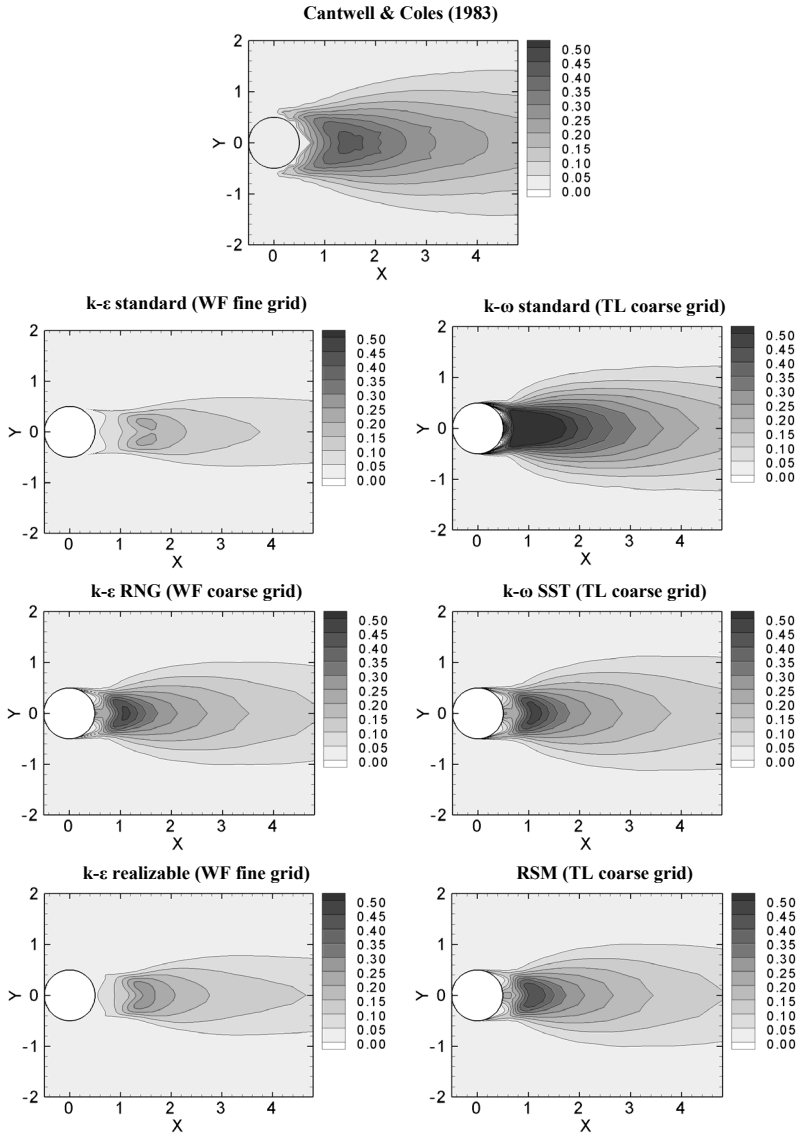

Figure 5.10: Comparison of normalized mean total fluctuating kinetic energy *k*.

In consequence, the periodic motion is significantly damped which results in an underestimation of the total amount of fluctuating kinetic energy. By contrast, the turbulent kinetic energy for the standard *k-ω* model is significantly lower such that the periodic kinetic energy is increased and the sum of both is overestimated.

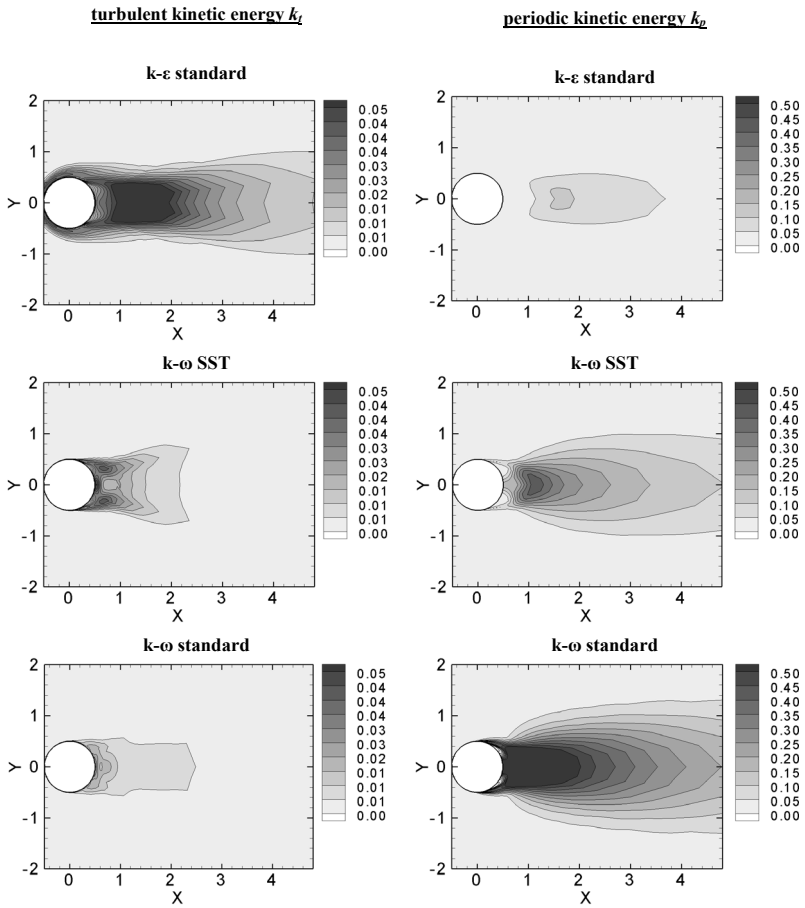

Figure 5.11: Comparison of turbulent (left) and periodic (right) fluctuating kinetic energy for three selected turbulence models.

It should be noted that Kato & Launder (1993) introduced a modification of the production term in the transport equation for turbulent kinetic energy to remedy the unrealistic overproduction in the stagnation point. This modification could be successfully applied by Bosch (1995) for the flow around a square cylinder and circular cylinder at lower Reynolds numbers. For the present analysis, however, only the realizable k-ε model with the two-layer near wall treatment showed major improvement if the production term was modified.

5.3.4 Concluding remarks

The study of numerical simulations from the literature showed that the best results for the flow around a circular cylinder are achieved with LES. However, this method is computationally to expensive if higher Reynolds numbers are considered and the present analysis therefore focused on turbulence models for the RANS equations. The standard and realizable k-ε model as well as the standard k-ω model suffer from a wrong production of turbulent kinetic energy which leads to significant deviations in the fluctuating and mean flow field. Thus, these models must be identified to be less suited for the flow around bluff bodies. Numerical results with the RSM, the RNG k-ε model and the SST k-ω model, on the other hand, agree fairly well with the laboratory reference data if the boundary layer at the cylinder is adequately treated.

However, for all models the angle of separation is significantly overestimated and the flow detaches partly far on the backside of the cylinder. In consequence, the mean drag force is reduced, the wake in cross-stream direction is confined and the mean streamwise velocity is higher compared to the experimental data. This might be attributed to the nature of the turbulence models which all assume a completely turbulent flow field while for the Reynolds number considered here, the boundary layer at the cylinder is actually laminar and transition to turbulence takes place in the free shear layers shortly after separation. Hence, it can be supposed that those models that already performed fairly well in the present case will even work better at higher Reynolds numbers when the boundary layer becomes turbulent and the angle of separation therefore moves to the back of the cylinder.

6 Density stratification and entrainment

In the preceding validation of the numerical model for the flow around a circular cylinder density was assumed to be constant throughout the fluid. However, the goal of this thesis is to investigate the influence of such cylinders on the evolution of a density current which is driven by differences in the density field. Hence, it is useful now to have a look at undisturbed density stratified fluids and introduce the main issues and parameters concerned with stratification and entrainment. At the end of this chapter a first validation of the numerical model will demonstrate its ability for the simulation of stratified flows.

6.1 Definitions

6.1.1 Gravity

Up to now gravity has been considered as a general external force per unit mass given by g_i in the momentum balance ((2.33)(b) or (3.38)(b)). In context with the flow around a cylinder discussed in the preceding chapter it is even negligible as it does not alter the solution of the problem. However, if density is not constant throughout the flow field the gravity term becomes very important as shown in chapter 2.3 where the Boussinesq approximation was introduced. Hence, for the further discussion, now it is convenient to define a coordinate system and the corresponding gravity vector g_i.

The gravitational acceleration on the earth can be approximated to be $g \approx 9.81$ m/s² (cf. chapter 2.4). Here the definition of the coordinate system which was introduced in context with the Coriolis forces is adopted. With the x- and y-axis spanning a horizontal plane and the z-axis pointing vertically upwards the external force vector is defined as

$$g_i = \begin{pmatrix} 0 \\ 0 \\ -g \end{pmatrix}. \tag{6.1}$$

Stratification is defined as the variation of the density field in the direction of the external force field. As shortly mentioned in context with the buoyancy production term (3.52) in chapter 3.4, a favorable (stable) stratification exists if density decreases upwards. Then the heavier fluid is below the lighter fluid and the driving force in the momentum equation (2.8) ($-\Delta\rho/\rho_0 g$) is directed to the bottom such that the situation remains stable. In the opposite case, for example in a thermal convection problem, the driving force will put the lighter (warmer) fluid upwards and increase the level of turbulence and mixing to return to a stable state. The issues of stability and mixing will be discussed next.

6.1.2 Gradient Richardson number

In chapter 3 the shear number (3.62) had been introduced as the ratio of the turbulent timescale (3.54) and the timescale of the mean flow field defined by the scalar strain rate (3.61) which can be interpreted as a shear frequency. Analogously the buoyancy number (3.129) was presented as the ratio of the turbulent timescale and a time scale characterizing the mean density field. This time scale is given by the inverse buoyancy frequency (or Brunt-Väisälä frequency) N given by

$$N^2 = -\frac{g}{\rho_0}\frac{\partial\rho}{\partial z}, \tag{6.2}$$

which is only a real number for a favorable density gradient.

The ratio of the buoyancy time scale and the shear time scale defines the gradient Richardson number which is given by

$$Ri_g = \frac{N^2}{S^2} = -\frac{g}{\rho_0}\frac{\dfrac{\partial\rho}{\partial z}}{\left(\dfrac{\partial\overline{u}}{\partial z}\right)^2 + \left(\dfrac{\partial\overline{v}}{\partial z}\right)^2}, \tag{6.3}$$

where in the middle term only the relevant components of the shear frequency S have been regarded. This simplification is based on the assumption that vertical velocities are very much smaller than horizontal velocities and that only vertical gradients are of relevance (cf. the boundary layer approximation used for the ASM in chapter 3.7). In relatively shallow waters, as in the coastal regions, this approximation is indeed justified and therefore also referred to as 'shallow water approximation'.

The gradient Richardson number is a measure for the stability of stratification. It is obvious that $Ri_g < 0$ represents an unstable situation as this case automatically implies an unfavorable density gradient (density decreasing with depth). Hence, only a positive gradient Richardson number is associated with a stabilizing effect when heavier fluid is below lighter fluid. However, it might not be expected that a positive gradient Richardson number implies unconditional stability. If the velocity gradient is large enough and the density gradient is small (i.e. small Ri_g) it is likely that the stabilizing density stratification will be broken up by the kinetic energy in the shear layer. With increasing Richardson number the stabilizing effect of stratification becomes more and more important and Howard (1961) and Miles (1961) showed by linear stability analysis that a necessary criterion for unconditional stability is $Ri_g > 0.25$.

This can be visualized by a simple example (Malcherek (2001)). Assuming linear distributions for velocity and density and taking a heavy parcel of fluid at z with $u(z)$ and $\rho(z)$ below a light parcel of fluid at $z + \Delta z$ with $u(z + \Delta z)$ and $\rho(z + \Delta z)$, the gain of potential energy and loss of kinetic energy when both parcels are exchanged is

$$\Delta E_p = \Delta z^2 g \frac{\partial \rho}{\partial z}, \qquad \Delta E_k = -\frac{1}{4}\rho_0 \Delta z^2 \left(\frac{\partial u}{\partial z}\right)^2, \tag{6.4}$$

where it has been assumed that the variation of density is negligible for the kinetic energy. Noting that the gain in potential energy cannot exceed the loss of kinetic energy

$$\frac{\Delta E_p}{\Delta E_k} = \frac{g\Delta z^2 \dfrac{\partial \rho}{\partial z}}{-\dfrac{1}{4}\rho_0 \Delta z^2 \left(\dfrac{\partial u}{\partial z}\right)^2} \quad < \quad 1, \tag{6.5}$$

and recalling the definition of the gradient Richardson number (6.3) the necessary condition for the fluid to be mixed is $Ri_g < 0.25$.

As the theory is based on linear assumptions in reality mixing can actually occur at still higher Richardson numbers as e.g. observed in laboratory experiments by Strang & Fernando (2001) or field measurements by Moum et al. (1989). However, the linear stability analysis at least provides a good estimation for the critical Richardson number and $Ri_g > 0.25$ is a widely accepted criterion for mixing to be negligible.

6.1.3 Flux Richardson number

While the gradient Richardson number above is defined by the ratio of mean density and velocity scales the flux Richardson number is defined by the relation of the corresponding turbulent quantities, namely buoyant production (3.52) and shear production (3.60). With the 'shallow water approximation' the flux Richardson number is given by

$$Ri_f = \frac{-G}{P} = \frac{\dfrac{g}{\rho_0}\overline{w'\rho'}}{-\left(u'w'\dfrac{\partial \overline{u}}{\partial z} + v'w'\dfrac{\partial \overline{v}}{\partial z}\right)} = \frac{-\dfrac{g}{\rho_0}\dfrac{\nu_t}{\sigma_t}\dfrac{\partial \rho}{\partial z}}{\nu_t\left(\left(\dfrac{\partial \overline{u}}{\partial z}\right)^2 + \left(\dfrac{\partial \overline{v}}{\partial z}\right)^2\right)} = \frac{1}{\sigma_t}\frac{N^2}{S^2} = \frac{1}{\sigma_t} Ri_g, \tag{6.6}$$

where the turbulent viscosity assumption has been applied to relate the flux Richardson number to the gradient Richardson number by the turbulent Prandtl number which will be discussed later. It should be noted that unlike the gradient Richardson number the flux Richardson number is also defined for shear-free flows or stagnant stratified fluids. In these cases turbulence is not produced by shear in the mean flow field as assumed in (6.6) but by other sources like breaking waves or ship impellers. However, her only sheared flows are regarded and Ri_f is defined by (6.6).

The flux Richardson number stems from the balance of turbulent kinetic energy (3.48) and gives the amount of the produced kinetic energy that is used to mix the fluid and gain its potential energy. In a steady state situation turbulence is in equilibrium, the left hand side of (3.48) vanishes and the balance is solely governed by the production and dissipation terms on the right hand side (e.g. Osborn (1980)). Thus, the remaining amount of the produced turbulent kinetic energy which is not used to increase the potential energy is dissipated to heat by ε. Therefore, the flux Richardson number is limited to a certain value less than 1 and in fact, as pointed out by Stewart (1959), should be considerably less than 1.

It is natural to expect Ri_f to depend on the stability of stratification and in turn on the gradient Richardson number (proportionality given by σ_t). In case of a neutral fluid (no stratification) $Ri_f = 0$ by definition, as the nominator in (6.6) vanishes. When the stabilizing effect of stratification increases turbulence will be more and more suppressed such that the denominator in (6.6) decreases. On the other hand, a certain amount of the remaining produced turbulent kinetic will be used for the buoyancy production resulting in a rise of Ri_f. However, as the maximum value of Ri_f is limited for the reasons above, it can be supposed that Ri_f increases most for weak stratification and then asymptotically approaches a maximum value at strong stratification until it becomes indefinite when turbulence and mixing are totally suppressed by stratification.

These assumptions are supported by laboratory experiments, numerical simulations and theoretical models as shown in Figure 6.1. The experimental data are taken from Rohr (1985), DNS simulations from Holt et al. (1992) and LES simulations from Schumann & Gerz (1995). The curves represent theoretical predictions from Schumann & Gerz (1995) and the Version A of the ASM of Canuto et al. (2001) (cf. chapters 3.6 and 3.7). The results of the numerical simulations are in fair agreement with the laboratory data except for some outliers around $Ri_g \approx 0.2$ which cannot be physically interpreted and should therefore be ignored. It should be stressed that the theoretical curves are no curve fittings to the data but are based on considerations of the relevant physical processes.

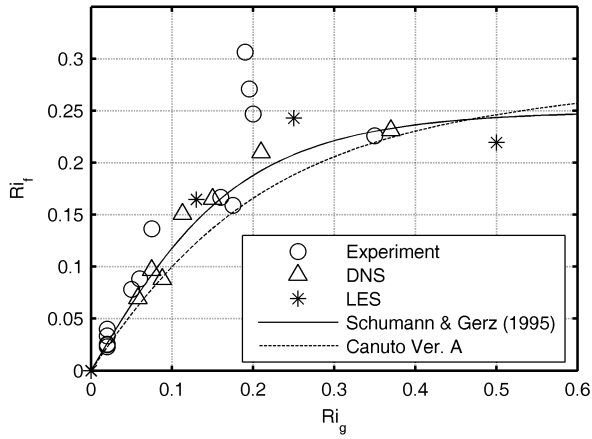

Figure 6.1: Flux Richardson number Ri_f as function of gradient Richardson number Ri_g.

Although both models are derived on different backgrounds they provide quite similar results with a maximum flux Richardson number of about $Ri_f \approx 0.25$ (for the model of Schumann & Gerz (1995) this is actually a tunable parameter, cf. (6.8) in the next section), which is supported by the laboratory and model data shown here. However, the maximum value of Ri_f is intensively discussed in the literature. Ivey & Imberger (1991), based on different laboratory experiments with air and water, have shown that Ri_f depends on the molecular Prandtl number Pr and varies between 0 and 0.2 for fluids with $Pr > 1$ (temperature in water: $Pr = 7$, salt in water $Pr = 700$) and between 0 and 0.15 for fluids with $Pr < 1$ (temperature in air $Pr = 0.7$). This dependence on the molecular Prandtl number could be confirmed by DNS results of Cortesi et al. (1999), or Shih et al. (2005) where the latter have shown slightly higher values ($Ri_{f,\max} \approx 0.25$) and less sensibility to the Prandtl number.

A very popular model in oceanography to estimate the turbulent diffusion from measurements of density and turbulent dissipation rate (see e.g. chapter 7.2.4) was proposed by Osborn (1980). The maximum flux Richardson number proposed by Osborn (1980) is $Ri_f = 1/6 \approx 0.167$ and therefore less than the values suggested above. Nevertheless, the model has been proven to work reasonably well for many field measurements which might be argued by patchy turbulence which generally

yields lower mixing rates (Arneborg (2002)). In laboratory experiments as well as numerical simulations and theoretical models turbulence is always assumed to be more or less homogenous while in nature patches of turbulence frequently occur and explain the lower flux Richardson numbers and the success of the Osborn model.

Anyway, the maximum flux Richardson number usually assumed in the oceanography community is $0.17 < Ri_f < 0.2$ and represents a reasonable range concerning the overall experience from field and laboratory measurements as well as numerical simulations and theoretical models.

6.1.4 Turbulent Prandtl number

The turbulent Prandtl number σ_t had been introduced in chapter 3.4.1 and is a central part of the turbulent diffusivity assumption as it relates the turbulent viscosity ν_t to the turbulent diffusivity ν_t' . The former is determined by the underlying more or less elaborate turbulence model while all the physics for turbulent diffusion are contained in σ_t. As the preceding discussion about the flux Richardson number has shown the turbulent Prandtl number cannot be constant in a stratified fluid as otherwise Ri_f would not asymptotically reach its maximum value. Hence, the turbulent Prandtl number must also be a function of the gradient Richardson number and in fact, the theoretical curves for Ri_f in Figure 6.1 are based on models for the turbulent Prandtl number rather than the flux Richardson number.

As shown in chapter 3.7 for an ASM the turbulent Prandtl number is not only a single function of the gradient Richardson number but more generally depends on the ratio of the turbulent buoyancy and shear numbers α_N and α_M, respectively. By definition the gradient Richardson number is given by $Ri_g = \alpha_N / \alpha_M$ and there are infinite possible combinations yielding the same gradient Richardson number but different turbulent Prandtl numbers. To compare the turbulent Prandtl numbers from an ASM to those predicted by other models that assume a dependence on Ri_g only a further constraint is needed. This can be achieved by the assumption of stationary turbulence where production and dissipation are in balance ($P + G - \varepsilon = 0$). Given the definitions of the single terms this can be transformed to $c_\mu \alpha_M + c_\mu' \alpha_N = 1$ and fixes the relation between the turbulent shear and buoyancy numbers.

Galperin et al. (1988) showed by scale analysis that it is no model inconsistency to apply the equilibrium turbulence assumption to the stability functions unless the fully dynamic equation for the turbulent kinetic energy is retained. This is supported by Burchard & Bolding (2001) comparing the full and the quasi-equilibrium versions of four different ASM.

One of the first simple models for the turbulent Prandtl number was proposed by Munk & Anderson (1948) based on a curve fit through available data. The functional relation between σ_t and Ri_g is given by

$$\sigma_t = \frac{\left(1+\frac{10}{3}Ri_g\right)^{\frac{3}{2}}}{\left(1+10Ri_g\right)^{\frac{1}{2}}}. \tag{6.7}$$

This model has been applied in oceanography for a long time due to the lack of alternatives. Schumann & Gerz (1995) were maybe the first to analytically derive a model equation for σ_t that also fitted reasonably well to experimental and numerical data as shown in Figure 6.1 in context with the flux Richardson number. The model of Schumann & Gerz (1995) is given by

$$\sigma_t = \sigma_{t0}\exp\left(-\frac{Ri_g}{\sigma_{t0}Ri_{f\infty}}\right)+\frac{Ri_g}{Ri_{f\infty}}, \tag{6.8}$$

where σ_{t0} and $Ri_{f\infty}$ are free parameters representing the neutral turbulent Prandtl number at zero stratification and the maximum flux Richardson number that was already discussed above. As with the maximum flux Richardson number there is slight controversy about the neutral turbulent Prandtl number. Schumann & Gerz (1995) derived a value of $\sigma_{t0} = 0.72$ for salt in water based on the measurements of Rohr (1985) and $\sigma_{t0} = 0.98$ for temperature in air based on wind tunnel data. Both are in the reasonable range suggested by many measurements and theoretical considerations as discussed by Schumann & Gerz (1995). The analytically derived quasi-equilibrium version of the ASM of Canuto et al. (2001), e.g. yields $\sigma_{t0} = 0.86$.

Figure 6.2 shows the turbulent Prandtl number against the gradient Richardson number for the models of Munk & Anderson (1948), Schumann & Gerz (1995) and the Version A of the ASM of Canuto et al. (2001) compared to laboratory and numerical data (cf. Figure 6.1).

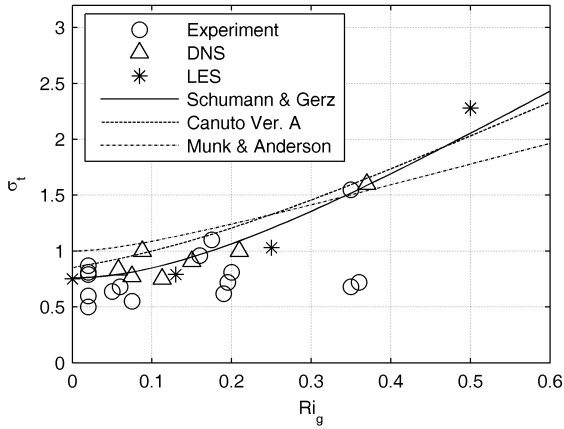

Figure 6.2: Prandtl number σ_t as function of gradient Richardson number Ri_g.

Although there is significant scatter in the reference data (especially for the measurements of Rohr (1985)) the increase of σ_t with increasing Ri_g is clearly observable. All theoretical models reproduce this increase whereas it seems to be slightly underestimated by the Munk & Anderson (1948) model. Anyway, for small Richardson number $Ri_g < 0.25$ all theoretical curves are within the data and the weak increase in that region even suggests the use of a constant turbulent Prandtl number as a reasonable approximation. This issue will be analyzed at the end of this chapter.

6.1.5 Stationary Richardson number

The stationary Richardson Ri_{st} number was first introduced by Holt et al. (1992) and describes the state for which turbulent kinetic energy is constant in time. Then the turbulent flow field is homogenous and the left hand side of the balance equation

(3.48) vanishes. Hence, production, buoyancy flux and dissipation must be in balance such that

$$\frac{dk}{dt} = P + G - \varepsilon = \nu_t S^2 + \frac{\nu_t}{\sigma_t} N^2 - \varepsilon = 0 \,, \tag{6.9}$$

where the third expression made use of the turbulent viscosity/diffusivity assumption.

A common practice in DNS and LES simulations of stratified homogenous turbulent shear flows is to fix the mean shear and density stratification (Ri_g = const.) and analyze the evolution of the turbulent flow field. The stationary Richardson number can then be found by varying the gradient Richardson number until the equilibrium for turbulent kinetic energy is achieved. Holt et al. (1992) found that the stationary Richardson number depends on the turbulence intensity given by the turbulent Reynolds number $Re_\lambda = \sqrt{2k}\lambda/\nu$, where λ is the Taylor micro scale. With increasing Reynolds number the stationary Richardson number also increases reaching a maximum value of Ri_{st} = 0.25 at high Reynolds numbers. These findings are corroborated by later DNS data of Shih et al. (2000) who showed that for low Reynolds numbers there is also a dependence on shear rate as proposed by Jakobitz et al. (1997).

As theoretically shown by Burchard & Baumert (1995) and supported by their numerical results, turbulence will exponentially grow if $Ri_g < Ri_{st}$ and for $Ri_g > Ri_{st}$ it will decay to zero. However, the idealized conditions of the numerical simulations only partly reflect reality as growing turbulence will actually increase mixing and so the gradient Richardson number. Hence, it can be anticipated that in shear layers far away from boundaries the stationary Richardson number will automatically be approached if $Ri_g < Ri_{st}$ initially. Interestingly, the upper limit for the stationary Richardson number as shown above is exactly the value proposed by Miles (1961) as a threshold for unconditionally stable stratification. However, as noted by Shih et al. (2000) this may be just a coincidence.

It should be expected from a turbulence model to reproduce the stationary Richardson number as otherwise mixing would be over- or underestimated. In case

of the two-equation models considered here this requirement is closely related to the buoyant production term in the second equation (for ε or ω). In a general form (cf. Umlauf & Burchard (2003)) this equation for stationary turbulence reads

$$\frac{d\psi}{dt} = \frac{\psi}{k}\left(c_{\psi 1}P + c_{\psi 3}G - c_{\psi 2}\varepsilon\right) = \frac{\psi}{k}\left(c_{\psi 1}\nu_t S^2 + c_{\psi 3}\frac{\nu_t}{\sigma_t}N^2 - c_{\psi 2}\varepsilon\right) = 0\,, \tag{6.10}$$

where ψ either stands for ε or ω and the third expression again made use of the turbulent viscosity/diffusivity assumption. It should be noted that (6.10) actually only applies to the standard k-ε model and the standard and SST k-ω models. In the realizable k-ε model the formulation for the production term is different and in the RNG k-ε model there is an additional term that is not recognized in (6.10). However, as mentioned in chapter 3.5 for homogenous turbulence both converge to the standard k-ε model which therefore will serve as a proxy for the class of k-ε models in the following discussion.

Combining (6.9) and (6.10) yields an expression for the stationary Richardson number in terms of the model constants in the ψ equation and the turbulent Prandtl number:

$$Ri_{st} = \sigma_t \frac{c_{\psi 2} - c_{\psi 1}}{c_{\psi 2} - c_{\psi 3}}\,. \tag{6.11}$$

As the model constants $c_{\psi 1}$ and $c_{\psi 2}$ are already assigned by the turbulence model Ri_{st} is only a function of $c_{\psi 3}$ and the model for the turbulent Prandtl number. It should be noted that the stationary Richardson number considered here corresponds to the gradient Richardson number and it is apparent from (6.11) that the efficiency of mixing as given by the flux Richardson number will only be a function of $c_{\psi 3}$.

Figure 6.3 shows the stationary Richardson number as function of $c_{\psi 3}$ for a constant turbulent Prandtl number $\sigma_t = 1.0$ and the three models discussed in 6.1.4, above.

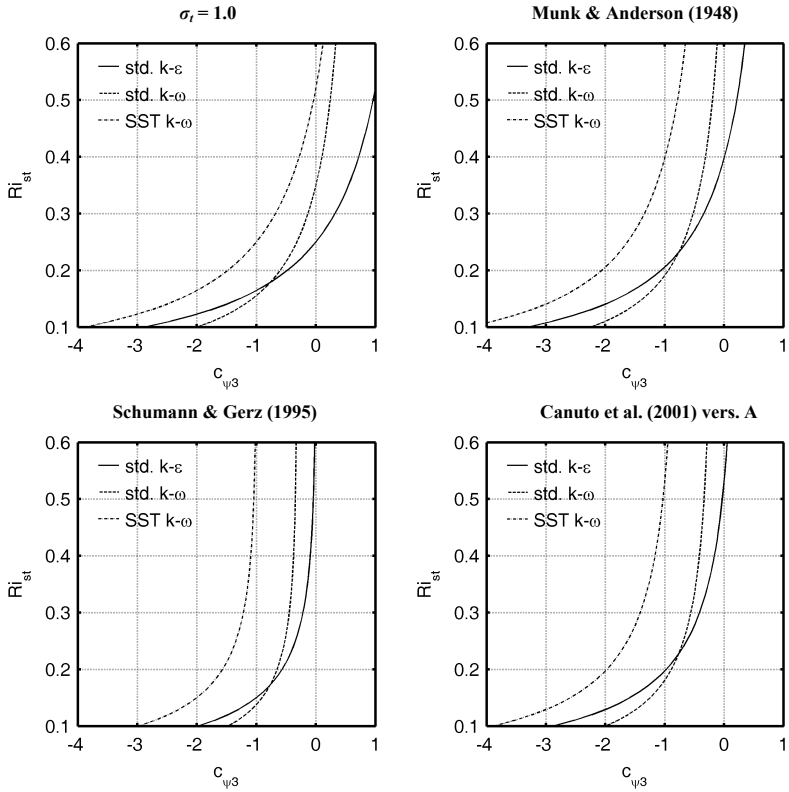

Figure 6.3: Stationary Richardson number as function of buoyant production constant $c_{\psi 3}$ for different models of turbulent Prandtl number.

Interestingly, with a constant turbulent Prandtl number σ_t = 1.0 the stationary Richardson number for the standard *k-ε* model exactly matches the alleged target-value $Ri_{st} = 0.25$. This might explain the idea of Rodi (1987) who suggested to neglect the buoyancy term in the ε-equation ($c_{\varepsilon 3} = 0$) in case of stable stratification. However, if σ_t = 1.0 is used with a *k-ω* model instead, the stationary Richardson number is significantly higher (std. *k-ω*: $Ri_{st} = 0.35$, SST *k-ω*: $Ri_{st} = 0.52$) and presumably overestimated. In case of the models of Schumann & Gerz (1995) and Canuto et al. (2001) a stationary solution is not even possible if $c_{\psi 3} \geq 0$. This

underlines the necessity to include the buoyancy term in the equation for turbulence length scale and points out its effect on the turbulent and specific dissipation rates, namely a reduction ($c_{\psi 3} < 0$) in case of stable stratification.

Although a definite value for the stationary Richardson number cannot be given, the maximum value of $Ri_{st} = 0.25$ suggested by the DNS data as shown above seems to be a reasonable approach that is further supported by the wind entrainment experiment of Kato & Phillips (1969) which will be discussed at the end of this chapter. The specific values of $c_{\psi 3}$ corresponding $Ri_{st} = 0.25$ for the different turbulence and turbulent Prandtl number models are given in Table 6.1.

turbulence model	σ_t **= 1.0**	**Munk & Anderson**	**Schumann & Gerz**	**Canuto A**
std. k-ε	0.00	-0.63	-0.34	-0.63
std. k-ω	-0.32	-0.69	-0.52	-0.69
SST k-ω	-1.00	-1.63	-1.34	-1.63

Table 6.1: Model constant $c_{\psi 3}$ for $Ri_{st} = 0.25$.

Surprisingly, the constants for the empirical model of Munk & Anderson (1948) and the theoretical model of Canuto et al. (2001) for this specific Richardson number are identical, as the actually quite different functions for the turbulent Prandtl number coincidently intersect at $Ri_g = 0.25$ (cf. chapter 6.1.4, Figure 6.2). It is further interesting to note, that the model constants for the standard k-ε model and the SST k-ω model are related by $c_{\varepsilon 3} = c_{\omega 3} + 1$, as pointed out by Umlauf et al. (2003). This, however, is no coincidence but stems from the model constants $c_{\omega 1}$ and $c_{\omega 2}$ that result from the transformation of the ε-equation into the ω-equation to arrive at the SST k-ω model (see chapter 3.5.2).

Before a first validation of the present numerical model for the simulation of mixing and entrainment in stratified fluids is made in section 6.3 it is useful first to shed some light on the nature of mixing and the idea behind the entrainment assumption.

6.2 Entrainment and mixing

In a laminar flow or a stagnant fluid at the limit mixing between regions of different properties (momentum, salinity, temperature, etc.) is caused by molecular motions parameterized by the molecular viscosity and diffusivities. In turbulent flows this approach can be adopted (see chapter 3.4.1) and mixing can be modeled with the assumption of turbulent viscosity and diffusivities. Even if this rather simple parameterization has the ability at least to work well for the mixing of momentum as could be demonstrated by the cylinder flow in the preceding chapter it does not tell anything about the actual mechanism of mixing. Hence, before the entrainment assumption will be discussed it is useful first to look at mechanisms of mixing.

For this purpose the flow is assumed to be turbulent and stratification is disregarded at first such that density is constant throughout and the flow is governed by the mass and momentum balance only. A very nice and classical example for entrainment and mixing in such a neutral situation is the turbulent jet which is ejected into a stagnant body of fluid as shown in Figure 6.4.

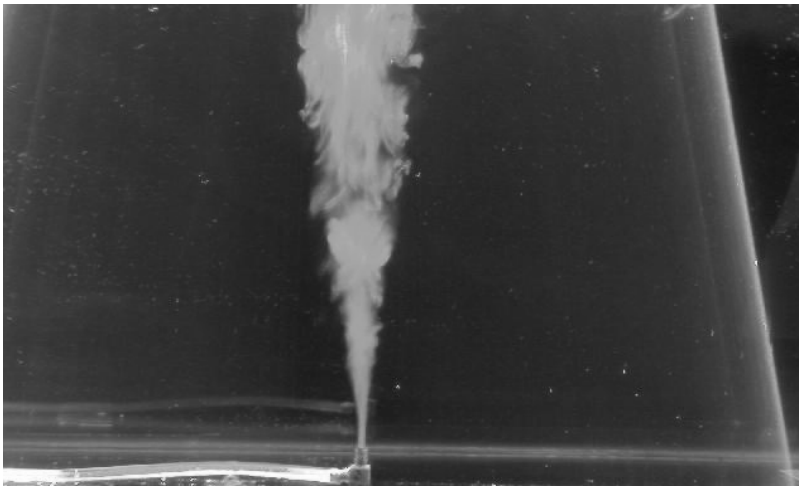

Figure 6.4: Snapshot from a laboratory experiment for a round vertical jet. Image source: http://www.amath.unc.edu/lab/

It is clearly seen that the initial size of the jet at the bottom corresponding to the nozzle diameter constantly grows with increasing distance from the point of injection. This spreading is caused by mixing of the turbulent core with the non-turbulent ambient fluid which is 'entrained' into the jet by large scale vortices at the interface induced by the shear between the jet and the stagnant surrounding. The large scale coherent structures denoted as Kelvin-Helmholtz waves are a distinctive feature of unstratified turbulent shear flows and can be detected to some extent from the snapshot in Figure 6.4.

It is believed, that mixing in an unstratified shear layer can be attributed to the growth of Kelvin-Helmholtz waves and the engulfing of ambient fluid which is finally incorporated into the turbulent core. This process has been extensively investigated in the past using both laboratory experiments and numerical simulations. One of the first applications of the latter was done by Corcos & Sherman (1984) who provided the nice representation of the engulfing process given in Figure 6.5.

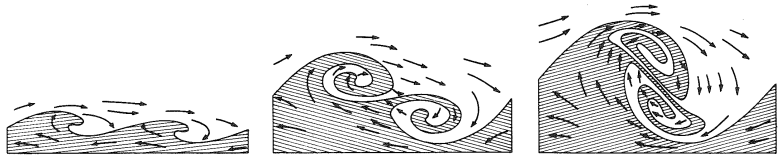

Figure 6.5: Visual record of 'engulfing' in an unstratified shear flow showing the successive positions of the interface at dimensionless times t = 1.0, 2.0, 2.5, with fluid on one side shaded and arrows of arbitrary length representing segments of the streamlines (adopted from Turner (1986)).

Although the instantaneous flow field in the jet is highly complex and chaotic as seen from Figure 6.4 the mean profiles averaged over some eddy turn-over times are steady, symmetric and self-similar after some distance from the injection. The self-similarity solution based on dimensional analysis (cf. e.g. Turner (1973) or Fisher et al. (1979)) can be used to parameterize the engulfing and entrainment of ambient fluid into the jet by a fictional entrainment velocity w_E. For a pure jet momentum can be assumed to be conserved while the mass flux (respectively

volume flux, as density is constant throughout) constantly increases with increasing distance from the injection point due to the entrainment of surrounding fluid:

$$\frac{\mathrm{d}q}{\mathrm{d}z} = \frac{\mathrm{d}}{\mathrm{d}z}\left(\int_A u \mathrm{d}A\right) = w_E A\,, \tag{6.12}$$

where q is the mass (volume) flux and u and A are the horizontal velocity profile and area of the jet at vertical distance z from the point of injection.

The entrainment velocity is a dimensional quantity and as such it depends on the distance from the injection and furthermore it strongly varies with the scales of the flow. To obtain a more general expression for the entrainment it is useful to scale the entrainment velocity by an appropriate velocity of the mean flow field which for example could either be given by the maximum or the average velocity of the jet at distance z from the injection. In the latter case the more general entrainment rate E is defined by

$$E = \frac{w_E(z)}{U_m(z)}\,, \tag{6.13}$$

where U_m is the mean velocity of the jet at distance z from the nozzle. It turns out that the entrainment rate is a universal constant which for the jet can be estimated from the similarity profiles and experimentally determined spreading rates (see e.g. Fischer et al. (1979)) to be $E \approx 0.054$. The spreading rate for jets is also a constant as could be expected from the snapshot given in Figure 6.4. It is directly related to the entrainment rate by $\mathrm{d}b/\mathrm{d}z = 2E \approx 0.108$ where b is the half-width of a planar jet or the radius of a round jet.

A more detailed discussion of the entrainment equations can be found in the review by Turner (1986) where a similar procedure is applied to vertical plumes. Unlike the jet, a plume is not driven by initial momentum but rather by the density difference between the light fluid making up the plume and the heavier ambient fluid. Hence, for a vertical plume not momentum but buoyancy is the conserved quantity and the resulting equations are slightly different. Considering small density difference such that the Boussinesq approximation can be applied (cf. chapter 2.3) the entrainment

rate for a plume can be estimated to be $E \approx 0.083$ which is significantly larger than the value suggested for the jet above. However, the spreading rate given by $db/dz = 6/5E \approx 0.100$ turns out to be interestingly of the same size although this value is based on much less precise data (Turner (1986)) as vertical plumes tend to oscillate and the meandering effects complicate a proper evaluation of the measurements (Pedersen (1986)).

Although there is a density difference in the vertical plume this kind of flow can still be regarded as unstratified because the density gradient is more or less perpendicular to the gravity force and stratification is unimportant. However, if the flow is bounded by an inclined wall such as in a light roof or dense bottom current stratification will have a damping effect on mixing and entrainment and the vertical plume can be regarded as the upper limit for these kinds of flow. The effect of stratification can be generally regarded in terms of a bulk Richardson number representative for the complete flow field, unlike the gradient Richardson given by (6.3) which is a local quantity. If the differential expressions in (6.3) are replaced by differences the bulk Richardson number can be written as

$$Ri_b = \frac{g}{\rho_0}\frac{\Delta\rho\Delta z}{\Delta U^2}, \tag{6.14}$$

where $\Delta\rho$ and ΔU are typical density and velocity differences for the specific kind of flow and Δz is a typical length scale which is not necessarily the distance over which the density or velocity difference occurs. Assuming for instance a density current of depth D with mean density ρ_c and speed U in a stagnant ambient fluid of density ρ_0 the corresponding differences are usually set to $\Delta\rho = \rho_c - \rho_0$, $\Delta U = U$ and $\Delta z = D$, where the current depth is most often used for the length scale rather than the thickness of the interface between the current and the surrounding fluid (see also chapter 7.1.5). Another typical example for stratified shear flow is the wind induced mixing of an initially stratified stagnant fluid which will be used in the next section as a first test case for the validation of the present numerical model. In this case $\Delta\rho$ and Δz make up the initial (linear) stratification and ΔU is set to the friction velocity u_τ caused by the wind blowing over the surface.

As stated above stratification will generally dampen mixing and entrainment. This can be explained by the fact that the energy needed to establish the engulfing Kelvin-Helmholtz waves by lifting up the heavier fluid in a dense bottom current or pushing down the lighter fluid in a light roof current increases with increasing density difference. The amount of available (kinetic) energy is given by the velocity difference and thus for sufficiently small bulk Richardson numbers (small density difference, large velocity difference) stratified shear flows are also governed by Kelvin-Helmholtz instabilities and mixing and entrainment just occur as sketched above ($Ri_b = 0$ for jets and plumes).

As the Richardson number increases, however, the growth of the Kelvin-Helmholtz waves will be inhibited by the restoring buoyancy forces and the basic entrainment assumption of engulfing ambient fluid seems to break down. From one of the first experiments on entrainment in stratified shear flows by Ellison & Turner (1959) it could be indeed concluded that there is no entrainment beyond $Ri_b > 0.8$. Based on their data Turner (1986) gave the following entrainment law for stratified shear flows depending on the bulk Richardson number:

$$E = \frac{0.08 - 0.1Ri_b}{1 + 5Ri_b} . \tag{6.15}$$

It is seen that for small Richardson numbers ($Ri_b \rightarrow 0$) the entrainment rate for a vertical plume given above is recovered and with increasing Richardson number entrainment gets smaller and smaller. At the limit for $Ri_b = 0.8$ the entrainment rate vanishes and for larger Richardson numbers this entrainment law looses validity.

However, in later experiments it could be shown that also for larger Richardson numbers significant entrainment may be present attributed to the occurrence of Holmboe waves (Holmboe (1962)) which are symmetric instabilities unlike the Kelvin-Helmholtz waves described above. A very nice visualization of both types of instabilities is shown in Figure 6.6 from which the roll-up and engulfing effect of Kelvin-Helmholtz billows is clearly identifiable. The Holmboe waves in the lower panel do not roll up and the whole entrainment process can be expected to much less violent.

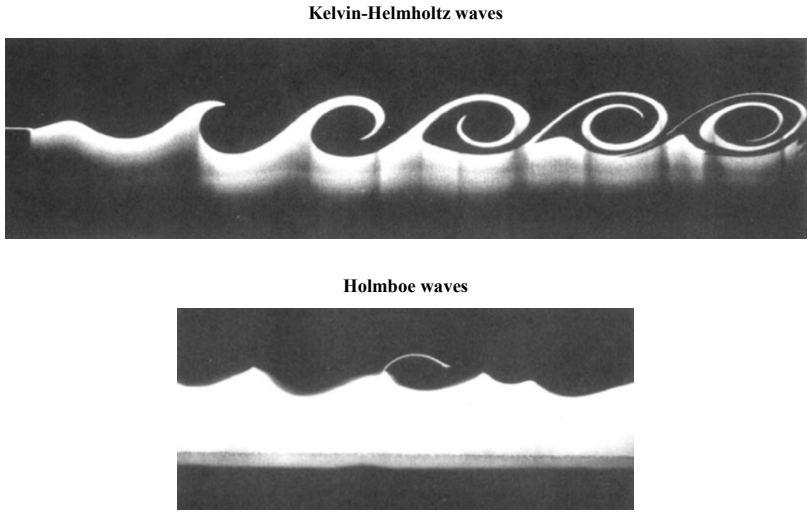

Figure 6.6: Visualization of Kelvin-Helmholtz waves and Holmboe waves in a laboratory experiment. Images are taken from Fernando (1991).

Pedersen (1980) conjectured that entrainment by Holmboe waves is associated with the ejection of small wisps of fluid from the cusp of the wave. The breaking of Holmboe waves actually occurs on both sides of the interface but due to lack of turbulence in the ambient fluid the entrained fluid is not further mixed there but will be forced back to the interface by buoyancy. Within the turbulent layer the entrained fluid is carried away from the interface and mixed with the surroundings causing the yet small but noticeable entrainment rates even at larger bulk Richardson numbers beyond $Ri_b = 0.8$.

It is not the goal of the present chapter to discuss all the aspects of mixing and entrainment in stratified fluids which are in fact not completely understood even by now (Strang & Fernando (2001)). Much more it was intended to explain the basic mechanisms of mixing and to introduce the idea behind the entrainment assumption. More details and a more thorough discussion about this topic can be found for example in the reviews of Turner (1986) and Fernando (1991) and the references therein. The present section shall be finished with a short presentation of the state of knowledge about entrainment and the entrainment laws reported in the literature.

Fernando (1991) provided a compilation of various measurements of entrainment in stratified shear flows all aiming to provide a more or less general entrainment law depending on the bulk Richardson number. As shown above in (6.15) the law given by Turner (1986) based on the data by Ellison & Turner (1959) breaks down for large Richardson numbers (Ri_b = 0.8). A more general expression which is defined for all (positive) Richardson number and was therefore used in almost all succeeding investigations is given by

$$E = mRi_b^{-n} , \tag{6.16}$$

where m and n are parameters to fit the function to the specific data. However, as well as there is some spread in the individual data the parameters suggested in the literature vary significantly. While the values for n are found to be still in quite narrow range between 0.5 and 2 the proposed values for m differ by several orders of magnitude ranging between $5 \cdot 10^{-4} < m < 160$ (cf. Table 1 in Fernando (1991)).

Figure 6.7 (adopted from Figure 15 in Fernando (1991)) shows a compilation of data from many different laboratory experiments and field measurements represented by the symbols compared to some selected entrainment laws displayed by the solid lines. The results from the recent experiments of Cenedese et al. (2004) and the field measurements of Baringer & Price (1997) have been added in order to show that they fall right within the scatter of the other data and therefore provide a reasonable reference for the simulation of natural density currents in the next chapter.

It can be seen that the law (6.15) based on the data of Ellison & Turner (1959) very nicely fits the data points from this specific experiment but obviously seizes to be valid for larger Richardson numbers, say Rib > 0.5, when the function starts to rapidly approach zero. Due to the exponential form given by (6.16) all other entrainment laws appear as straight lines in the logarithmic plot with the slope given by the exponent n. Especially noteworthy is the law given by Christodoulou (1986) who proposed to divide the entrainment rate versus Richardson number plot into three distinct regimes. For low Richardson numbers, say $Ri_b < 0.1$, he suggested $n = 0.5$, for intermediate Richardson numbers, say $0.1 < Ri_b < 10$, $n = 1.0$ and for high Richardson numbers $n = 1.5$. This is consistent with the data and the slope in

the intermediate regime (n = 1) was also assumed in many other entrainment laws (e.g. Kato & Phillips (1969) or Halpern (1974)). The law of Stigebrandt (1987) has been derived for subcritical density currents ($Ri_b > 1$) and assumes n = 1 throughout which seems to fit the data also for very high Richardson numbers.

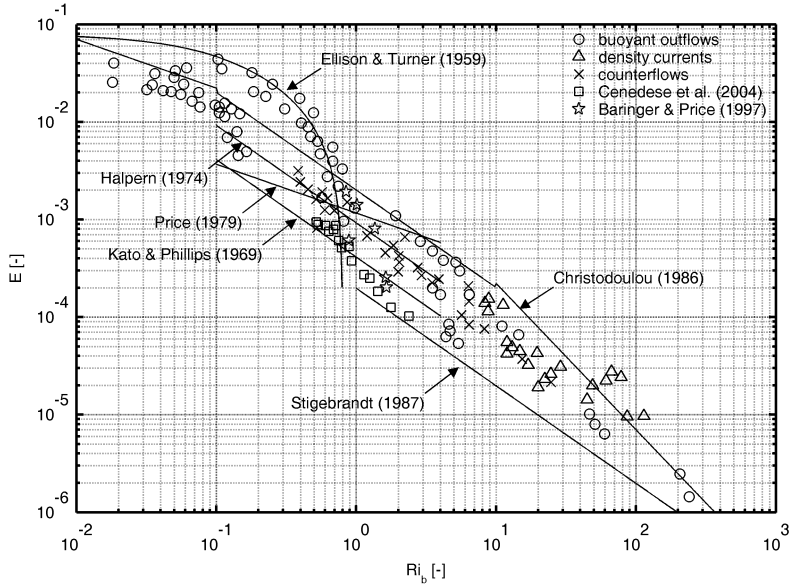

Figure 6.7: Entrainment rate versus bulk Richardson number. Comparison of different entrainment laws from the literature with laboratory and field measurements. Extension of *Figure 15* in Fernando (1991).

The major mechanism of mixing and entrainment discussed above might be a reasonable assumption, but the spread in the data shown in Figure 6.7 suggests that entrainment might be governed by several other processes, inhibiting the definition of a generally valid entrainment law. However, the power law given by (6.16) seems to be a good approximation which will be further discussed in chapter 7.1.5 where an entrainment law for density currents under the influence of Coriolis forces is theoretically derived. Before natural density currents are considered, however, the numerical model will at first be validated for the simulation of mixing in stratified fluids by the example of wind induced entrainment in a stratified body of water.

6.3 Wind induced entrainment

If wind blows over the surface of a stagnant water body, it will induce a shear stress on the surface which will produce turbulence and bring the water body in motion. At the very beginning only the upper part of the water is affected, but as the wind keeps blowing it will be felt in deeper and deeper layers. If the water is stably stratified the heavier water will be entrained into the lighter water above it by the wind induced turbulence. The effect of mixing grows constantly downwards over time and under stationary wind conditions this will finally cause the complete mixing of the whole water body.

Kato & Phillips (1969) carried out such a wind entrainment experiment in the laboratory that was later used by Price (1979) to derive an empirical formula for the temporal evolution of the mixed layer depth:

$$D_m(t) = \left(\frac{6}{5}\right)^{1/4} u_\tau \left(\frac{t}{N_0}\right)^{1/2}, \tag{6.17}$$

where D_m is the mixed layer depth, u_τ is the constant friction velocity at the surface and N_0 is the initial buoyancy frequency.

This experiment has often been used as a reference for the validation of numerical models (e.g. Deleersnijder & Luyten (1994), Burchard & Bolding (2001), Umlauf & Burchard (2005)) and will also serve here as a first test case for the present numerical model.

6.3.1 Model setup

For the numerical simulation of wind induced entrainment it is sufficient to apply a one dimensional model that only resolves the vertical domain (cf. references above). In the present simulations, however, the complete three dimensional equations had to be solved due to the requirements of the numerical model wich has been used here (Fluent (2005)). Therefore the horizontal domain is made up of only one grid cell and periodic boundary conditions are applied on the lateral boundaries. At the top

boundary a constant shear stress is applied that will bring the water body in motion and induce the turbulence for mixing. The boundary condition at the bottom is more or less arbitrary as the simulations are stopped before the mixed layer will reach the bottom. In the present case a symmetry boundary condition has been chosen.

The initial conditions conform to a stagnant constantly stratified water body with zero velocities and minimum turbulence ($k = 1{\cdot}10^{-7}$, $\varepsilon = 1{\cdot}10^{-9}$, $\omega = 0.1$) for which the stratification is given by a constant buoyancy frequency $N = 1{\cdot}10^{-2}$. The shear stress at the surface is given by a constant friction velocity $u_* = 1{\cdot}10^{-2}$. The total height of the domain is $H = 40$ m and, as found in preliminary model tests, the overall vertical grid resolution has been chosen to be $\Delta z = 0.25$ m which is refined in the upper 5 m to account for the steep gradients in the velocity and turbulence profiles.

Figure 6.8 shows the vertical profiles of the numerical grid resolution and the initial conditions for density anomaly and velocity as full lines. To give an idea about the evolution of the mixed layer in time also profiles of density anomaly and velocity after 10, 20 and 30 hours of mixing are shown.

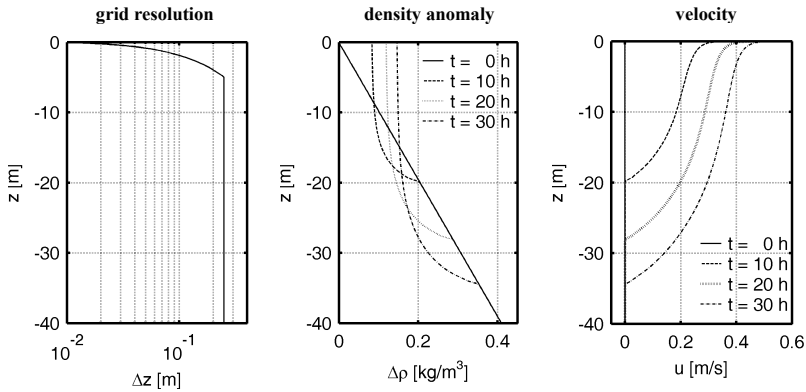

Figure 6.8: Model setup for the experiment of Kato & Phillips (1969).

It is obvious from these profiles that mixing is most intense at the beginning and exponentially decreases with time, as predicted by the formula (6.17) of Price (1979).

The velocity profiles indicate that the highest shear rate is in the upper and lower parts of the mixed layer. While the upper part has already been almost perfectly mixed (almost zero density gradients) the high shear below it contributes to the further erosion of the stable stratification.

6.3.2 Results

The main purpose of this test case is to approve the ability of the present numerical model to accurately account for the entrainment process in a stratified sheared fluid. Therefore all two-equation turbulence models that have been used in the preceding chapter for the unstratified flow around a circular cylinder have been reconsidered again. The RSM was not only neglected because of its significantly higher computational effort (that did not pay out for the flow around a cylinder) but much more because it showed such a strange behavior in the preliminary tests that for the present work no more effort has been put into this model.

As shown by Umlauf et al. (2003) it can be expected that the standard k-ε model and the standard k-ω model will yield quite similar results for mixing in a stratified shear layer provided the model parameters are adjusted to the specific problem (see also Umlauf & Burchard (2003)). The governing parameter for the present case is the stationary Richardson number discussed above. Its influence and correct adjustment will therefore be analyzed first and it will be shown that also the results for variations of the turbulence models (realizable, RNG, SST) mostly depend on this parameter. In chapter 6.1.4 it was suggested that the dependence of the turbulent Prandtl number on stratification is of minor importance for small Richardson numbers $Ri_g < 0.25$. Hence, in the subsequent section it will be examined if this argument really holds for a practical numerical simulation.

Partly the numerical results for the temporal evolution of the entrainment depth will be compared to the empirical formula (6.17) of Price (1979). According to other numerical studies, e.g. by Umlauf et al. (2003) or Burchard & Bolding (2001), in the numerical simulations the mixed layer depth is defined as the lower most point below the surface with a turbulent kinetic energy $k > 1 \cdot 10^{-5}$ m²/s².

Influence of stationary Richardson number

As shown in chapter 6.1.5 the right prediction of the stationary Richardson number can be a crucial aspect for the numerical simulation of mixing in a homogenous shear layer and is closely related to the effect of buoyancy on turbulence dissipation and turbulence time scale, respectively. By the example of a constant turbulent Prandtl number, $\sigma_t = 1.0$, it could also be shown that the neglect of the buoyancy production term ($c_{\psi 3} = 0$) in the transport equation for ε and ω, respectively, exactly yields the alleged target value $Ri_{st} = 0.25$ for the k-ε models and quite significantly higher values for the k-ω models.

For this case ($\sigma_t = 1.0$, $c_{\psi 3} = 0$) the numerically predicted temporal evolution of the mixed layer depth with all five turbulence models is compared to the empirical curve of Price (1979) in the left panel of Figure 6.9. The right panel shows the corresponding gradient Richardson number after 24 hours of mixing.

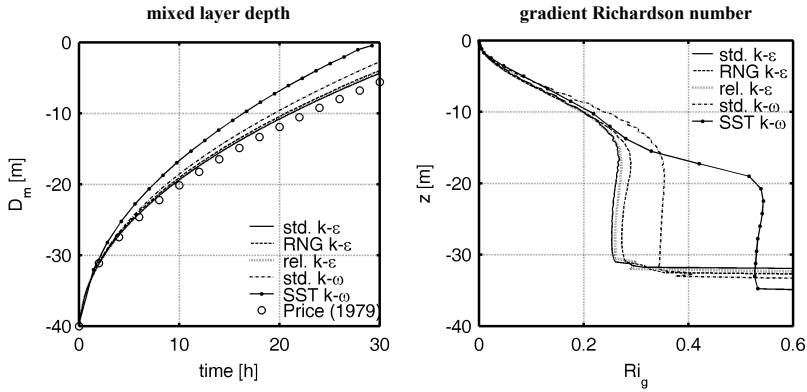

Figure 6.9: Temporal evolution of mixed layer depth and gradient Richardson number after 24 hours for the experiment of Kato & Phillips (1969). Different turbulence models with $\sigma_t = 1.0$ and $c_{\psi 3} = 0$.

In the well mixed region below the surface (cf. Figure 6.8) the gradient Richardson number increases constantly until it remains almost constant for a while and finally increases to infinity in the still unaffected stagnant stratified layer at the bottom. The

region of constant Ri_g indicates homogenous turbulence and a balance of production and dissipation where the stationary Richardson number is expected. Indeed, for the k-ε models $Ri_g \approx 0.25$, for the standard k-ω model $Ri_g \approx 0.35$ and for the SST k-ω model $Ri_g \approx 0.52$, just as predicted in chapter 6.1.5 (cf. Figure 6.3 and text below).

The comparison of the temporal evolution of the entrainment depth in the left panel shows good agreement of the theoretical curve and the results with the k-ε models, approving the proposed value of the stationary Richardson number, $Ri_{st} = 0.25$. The higher values of Ri_{st} for the k-ω models leads to an overestimation of mixing and a faster increase of the mixed layer depth, which is physically reasonable, as discussed above, and in agreement with other simulations, e.g. Burchard & Bolding (2001). The stationary Richardson number for the RNG k-ε model is also slightly higher than 0.25, due to the additional term in the ε-equation that is not recognized in the derivation of $c_{\psi 3}$. However, the resulting faster increase of the entrainment depth is not distinguishable from Figure 6.9 such that this slight deviation can be neglected.

Obviously, for the proper simulation of the entrainment the stationary Richardson number must be around $Ri_{st} = 0.25$. With a constant turbulent Prandtl number $\sigma_t = 1.0$ this was already the case for the k-ε models and can be achieved for the k-ω models if the corresponding values of $c_{\omega 3}$ are adopted from Table 6.1. The results for the entrainment depth and gradient Richardson number are shown in Figure 6.10.

As expected, for all turbulence models (except for the RNG k-ε model as discussed above) the profiles of the gradient Richardson number are almost identical with a stationary value of $Ri_g = 0.25$ in the homogenous turbulent layer. Although the Richardson numbers are quasi identical, the temporal evolution of the mixed layer depth is slightly slower for the k-ω models and therefore in perfect agreement with the empirical curve. It should be noted that a comparative analysis with the one-dimensional General Ocean Turbulence Model GOTM (Umlauf et al. 2005), which was also used in the above cited papers of Umlauf and Burchard provided identical results for the standard k-ε and k-ω models. The alleged better results for the k-ω models, here, are therefore only hardly explained and presumably an effect of the numerical model. However, as the general effect of the stationary Richardson

number and the required adjustment of the model constant $c_{\psi 3}$ are evident, this rather small discrepancy will be generously ignored.

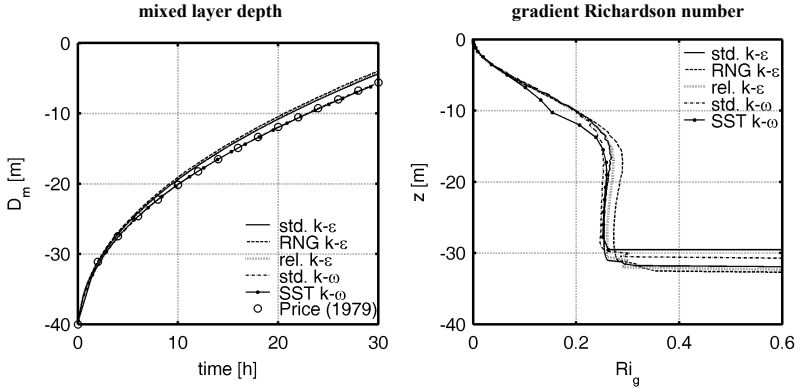

Figure 6.10: Temporal evolution of mixed layer depth and gradient Richardson number after 24 hours for the experiment of Kato & Phillips (1969). Different turbulence models with $\sigma_t = 1.0$ and $Ri_{st} = 0.25$.

Influence of turbulent Prandtl number

As the previous discussion has shown, the mixing process in a stratified shear layer is mainly governed by the stationary Richardson number. If the model constant $c_{\psi 3}$ is adequately adjusted the numerical simulations almost perfectly agree with the theoretical prediction, even with the crude assumption of a constant turbulent Prandtl number. However, as shown in chapter 6.1.4, the turbulent Prandtl number is actually a function of the gradient Richardson number which is empirically or theoretically estimated by different models. Even if the variation of σ_t is low for small Richardson numbers, $Ri_g < 0.25$, and the overall results for the mixed layer depths are almost perfect, it might be interesting to look at the effect of the turbulent Prandtl number on the specific mixing process. For this purpose Figure 6.11 shows the mixed layer depth, turbulent Prandtl number, flux Richardson number and buoyancy production for the different Prandtl number models used with the standard k-ε model (left column) and standard k-ω model (right column), respectively.

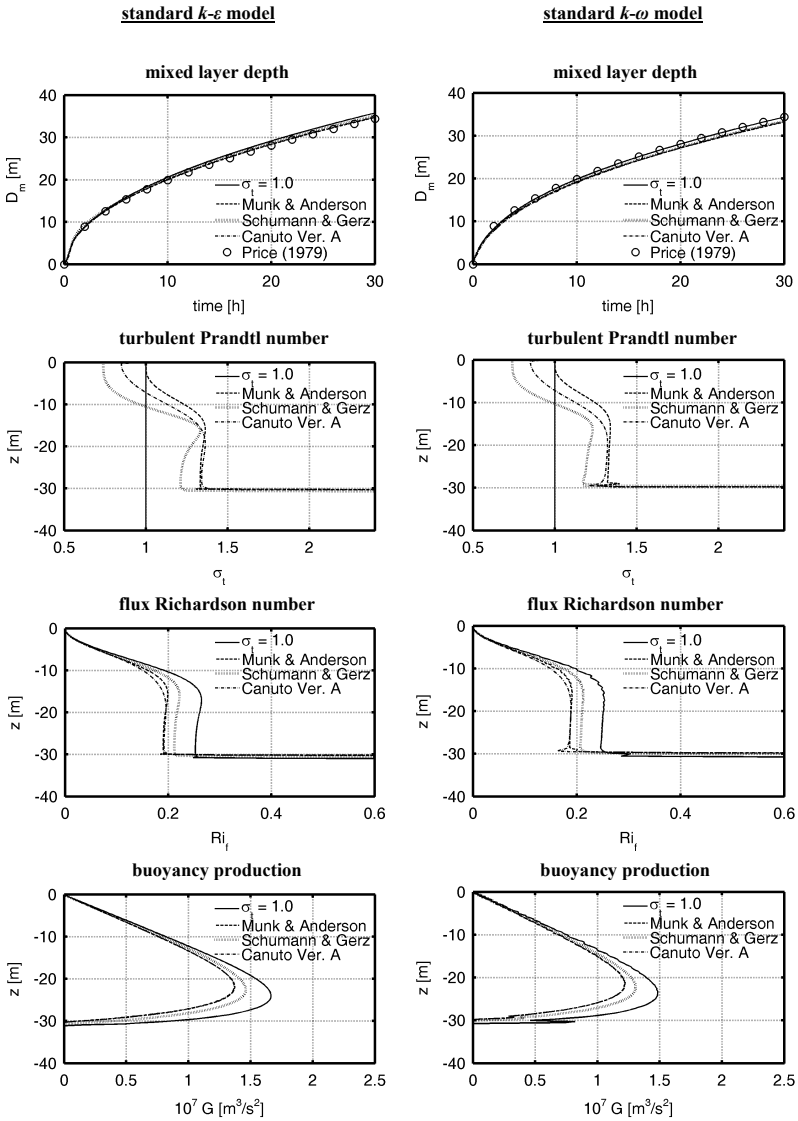

Figure 6.11: Influence of turbulent Prandtl number for the experiment of Kato & Phillips (1969). Standard k-ε model (left column) and standard k-ω model (right column) with $Ri_{st} = 0.25$.

As shown in the preceding section there is almost no difference between the specific models of the k-ε and k-ω type and the standard models serve as a proxy for each of the model classes. The choice of the standard models further allows for a direct comparison of the present results with those of Umlauf et al. (2003). They also used the standard models and presented profiles for turbulent kinetic energy which are in agreement with those of the present simulations which therefore have been omitted in Figure 6.11.

From the temporal evolution of the entrainment depth in the top panels it is apparent that the mixed layer grows slightly slower if the turbulent Prandtl number is not simply set to $\sigma_t = 1.0$. However, there is no distinguishable difference between either of the turbulent Prandtl number models. These effects become clear from the profiles of the turbulent Prandtl number in the second row. In the lower part of the mixed layer which is the most active zone for mixing, $\sigma_t > 1.0$ for all models. The empirical model of Munk & Anderson (1948) is even almost identical to the analytical model of Canuto et al. (2001) in accordance with the findings in chapters 6.1.4 and 6.1.5. Although the profile of the Prandtl number for the model of Schumann & Gerz (1995) is quite similar to that of the Canuto model its maximum is slightly less because of the smaller neutral value for $Ri_g = 0$ just below the surface.

In all simulations the model constant $c_{\psi 3}$ has been adjusted according to Table 6.1 to fix the gradient Richardson number to the desired stationary value of $Ri_g = 0.25$. For $\sigma_t = 1.0$ the flux Richardson number shown in the third row is also $Ri_f = 0.25$ while the higher Prandtl numbers predicted by the individual models reduce the flux Richardson number and by that the efficiency of mixing. This is very nicely approved by the buoyancy production in the bottom panels which is largest for $\sigma_t = 1.0$ and smaller for the Prandtl number models. It can also be seen that the buoyancy production for the k-ω model is generally less than that for the k-ε model which explains the slightly slower temporal evolution of the mixed layer depth. However, as discussed above this might be a numerical effect which is rather insignificant and can therefore be further neglected.

6.3.3 Concluding remarks

As shown in the previous discussion and approved by the validation of the present numerical model, entrainment in a stratified turbulent shear layer is mainly governed by the stationary Richardson number Ri_{st}. For the two-equation turbulence models considered here a reasonable value of $Ri_{st} \approx 0.25$ as found from idealized DNS of stratified homogenous turbulence can only be achieved if the effect of stratification (buoyancy production) is recognized in the balance equations for turbulence dissipation and specific dissipation rate, respectively.

The turbulent Prandtl number σ_t is also an important parameter as it provides the ratio between the turbulent viscosity and turbulent diffusion and so the gradient Richardson number Ri_g and the flux Richardson number Ri_f. Laboratory experiments and DNS suggest that the influence of stratification on the turbulent Prandtl number is rather small for Richardson numbers below the stationary limit $Ri_g < 0.25$ and indeed, the present validation of the numerical model showed only a marginal effect of the Prandtl number on the overall evolution of the mixed layer depth. However, a reasonable prediction of the maximum flux Richardson number $Ri_f \approx 0.2$ found from laboratory experiments and DNS requires to adequately account for the effect of stratification on σ_t.

All five turbulence models that have been considered in the present validation showed almost similar results that were in good agreement with the reference data (provided Ri_{st} is set accordingly). Alike, all the different models for the turbulent Prandtl number gave comparable results with a reasonable estimation of $Ri_f \approx 0.2$. It can therefore be concluded that for a proper simulation of wind induced entrainment in a stratified medium the choice of turbulence model is arbitrary and except for a constant turbulent Prandtl number the model for σ_t plays an insignificant role. Recalling the results of the preceding chapter on unstratified cylinder flow it follows for the planned simulations of entrainment in a density current induced by a circular cylinder that the best choice will be the SST k-ω model with either of the relations for σ_t.

7 Natural density currents

Before the influence of a cylindrical structure on the entrainment in a density current is investigated it useful first to study the undisturbed case. This chapter is therefore dedicated to the analysis and simulation of natural density currents. It will introduce a simple theory based on depth integrated equations and derive some simple parameterizations for the natural entrainment rates in density currents. These can be used as a reference for the analysis of the effect of a circular cylinder on the entrainment rates that will follow in the next chapter.

7.1 Theory

As mentioned before, gravity currents behave similar to open channel flows with the major difference being the reduced gravity that will cause all motions to slow down. Hence, some of the relations to be derived next might look familiar as they appear to be the same in open channel hydraulics except for the magnitude of gravity.

7.1.1 Problem definition

The main interest in this thesis lies on density currents as they typically occur in the Baltic Sea. The first characteristic being that the current advances in the ambient lighter fluid of the Baltic Sea which is assumed to be unstratified and stagnant. The second characteristic is that the density difference between the water from the North Sea and the water from the Baltic is only due to differences in salinity. Furthermore, the influence of wind or wave induced turbulence will be neglected as it is supposed that the bottom induced turbulence caused by the moving current is some orders of magnitude larger. However, this is only an assumption made here for simplicity and might be analyzed more thoroughly in the future. Last but not least the shallow water approximation, as introduced in chapters 3.7 and 6.1.2 will be made, assuming that vertical scales are very much smaller than horizontal scales.

A definition sketch of the density currents under investigation is given in Figure 7.1. The current moves along the x-axis on the floor of an ambient stagnant fluid of constant density ρ_0. The bottom is tilted by an angle α such that the driving force for the current is $g \cdot \sin(\alpha)$ − see (7.5), below. The total water depth is denoted by H and the depth of the density current − to be defined in the following − by D. As the current travels at a speed of U it will entrain a part of the surrounding lighter water which is sketched by the vectors above the interface indicating the entrainment velocity w_E − cf. chapter 6.2. According to equation (6.13) the rate of entrainment can then be defined as the ratio between w_E and U.

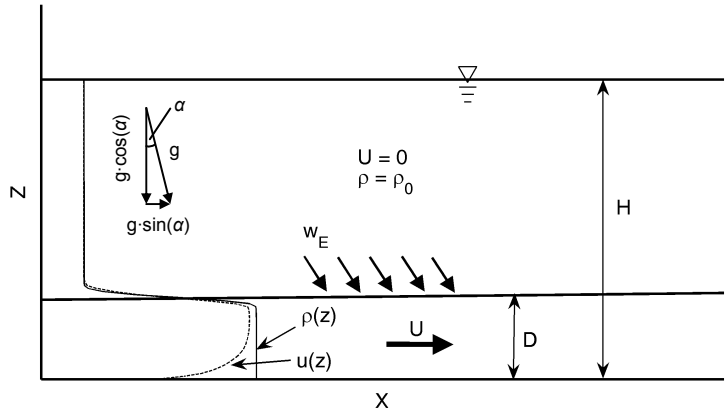

Figure 7.1: Definition sketch of a density current.

Before a theory can be derived it is necessary first to define the bulk speed and depth of the current. It seems evident that they are related to the density and velocity profiles that are given in the left part of the sketch. It is worth noting that both profiles resemble a natural state without the effect of Coriolis forces which will alter the velocity profile quite significantly as will be shown later. The question is how the depth dependent quantities can be used to define some bulk quantities. The way this is done here is adopted from Arneborg et al. (2007) where the succeeding theory is also given.

7.1.2 Depth integrated balance equations

In the general case where the current travels on the *x*-*y*-plane with the bulk velocity in *y*-direction given by *V*, the following depth integrated quantities can be defined:

$$g'D = \int_0^H \frac{\rho(z) - \rho_0}{\rho_0} g \mathrm{d}z \,, \tag{7.1}$$

$$\frac{1}{2} g'D = \int_0^H \frac{\rho(z) - \rho_0}{\rho_0} g z \mathrm{d}z \,, \tag{7.2}$$

$$UD = \int_0^H u(z) \mathrm{d}z \,, \tag{7.3}$$

$$VD = \int_0^H v(z) \mathrm{d}z \,. \tag{7.4}$$

Combining (7.1) and (7.2) defines the depth *D* as twice the distance between the bottom and the center of gravity of the current. The velocities *U* and *V* are obtained when (7.3) and (7.4) are divided by *D*. The same procedure applied to (7.1) yields the reduced gravity g' which represents the driving force for the current. As can be seen from the integrand in (7.1) the reduced gravity will only accelerate the denser fluid because it is zero where the depth dependent density equals the reference density ρ_0.

However, as long as the bottom is not tilted the dense layer will remain stagnant because then gravity is perpendicular to the bottom. Hence, the coordinate system will be tilted by an angle α, with the *x*-axis pointing downslope and the *y*-axis being parallel to the depth contours. This will also tilt gravity which becomes

$$g_i = \begin{pmatrix} g \sin\alpha \\ 0 \\ -g \cos\alpha \end{pmatrix} \approx \begin{pmatrix} g \tan\alpha \\ 0 \\ -g \end{pmatrix}, \tag{7.5}$$

where tan α is the bottom slope. The right hand side of (7.5) was simplified under the assumption that the bottom slope is small, hence cos $\alpha \approx 1$ and sin $\alpha \approx$ tan $\alpha \approx \alpha$.

Volume balance

The continuity equation which is a volume balance for the density current can be written in terms of the bulk quantities as

$$\frac{\partial D}{\partial t}+\frac{\partial UD}{\partial x}+\frac{\partial VD}{\partial y}=w_E\,. \tag{7.6}$$

It shows that in the stationary case the entrainment of lighter ambient water by the rate w_E will increase the volume flux of the current while if the current is followed with the speed (U,V) its depth will increase with time.

From here on only the latter case will be regarded further as it simplifies the derivation and the understanding of the following equations. The one-dimensional view simulates a vertical water column following the current and was also used in the preceding chapter. It is computationally much less expensive than a complete three dimensional model without loosing generality for the main physical aspects.

Momentum balance

The one-dimensional depth integrated momentum balance is derived from (3.38)(b) by neglecting the advective terms and combining the turbulent viscosity ν_t and the molecular viscosity ν to an effective viscosity ν_{eff}. Integrating over depth yields

$$\frac{\partial}{\partial t}\int_0^H u\mathrm{d}z-\int_0^H\frac{\partial}{\partial z}\left(\nu_{eff}\frac{\partial u}{\partial z}\right)\mathrm{d}z=\int_0^H\frac{\rho-\rho_0}{\rho_0}g\sin\alpha\mathrm{d}z+f\int_0^H v\mathrm{d}z\,, \tag{7.7}$$

$$\frac{\partial}{\partial t}\int_0^H v\mathrm{d}z-\int_0^H\frac{\partial}{\partial z}\left(\nu_{eff}\frac{\partial v}{\partial z}\right)\mathrm{d}z=-f\int_0^H u\mathrm{d}z\,, \tag{7.8}$$

where the overbar has been dropped for simplicity, keeping in mind that all equations contain the mean quantities. Recalling the assumptions made above with the problem definition these equations are subject to the boundary conditions

$$u\big|_{z=0}=v\big|_{z=0}=u\big|_{z=H}=v\big|_{z=H}=\left.\frac{\partial u}{\partial z}\right|_{z=H}=\left.\frac{\partial v}{\partial z}\right|_{z=H}=0\,. \tag{7.9}$$

With the definitions of the bulk quantities defined by (7.1) − (7.4) the depth integrated momentum equations in terms of bulk quantities can finally be written as

$$\frac{\partial UD}{\partial t} = g'D\sin\alpha + fVD - \frac{\tau_{bx}}{\rho_0}, \tag{7.10}$$

$$\frac{\partial VD}{\partial t} = -fUD - \frac{\tau_{by}}{\rho_0}, \tag{7.11}$$

where τ_{bx} and τ_{by} represent the bottom shear stresses defined by

$$\tau_{bi} = \nu_{eff}\rho_0 \left.\frac{\partial u_i}{\partial z}\right|_{z=0}. \tag{7.12}$$

Mass balance

The mass balance for the density current arises from the transport equations for temperature and salinity (3.38)(c) and (d). As density is a function of temperature and salinity the mass balance is basically a transport equation for density which can be derived from the according transport equations for temperature and salinity. Even if this is generally possible it is useful to make two more simplifications before. First, it will be assumed that density varies linearly with temperature and salinity (in case of salinity this assumption is justified indeed (cf. chapter 2.5). Hence,

$$\rho = \rho_0 + \beta_T\left(T - T_0\right) + \beta_S\left(S - S_0\right), \tag{7.13}$$

where β_T and β_S are the constant expansion coefficients. Secondly, the molecular diffusivities are neglected and the turbulent Prandtl numbers are supposed to be equal ($\sigma_T = \sigma_S = \sigma_t$), an assumption already made in the derivation of the turbulent buoyancy flux (3.51). Neglecting the advective terms the transport equation for density becomes

$$\frac{\partial \rho}{\partial t} - \frac{\partial}{\partial z}\left(\frac{\nu_t}{\sigma_t}\frac{\partial \rho}{\partial z}\right) = 0, \tag{7.14}$$

which is subject to the boundary conditions

$$\rho\big|_{z=0} = \rho\big|_{z=H} = \left.\frac{\partial\rho}{\partial z}\right|_{z=H} = 0\,. \tag{7.15}$$

However, as the ambient fluid is stagnant, (7.14) can also be written in terms of the density difference $\Delta\rho = \rho - \rho_0$ by simply subtracting the reference density ρ_0, giving

$$\frac{\partial\Delta\rho}{\partial t} - \frac{\partial}{\partial z}\left(\frac{\nu_t}{\sigma_t}\frac{\partial\Delta\rho}{\partial z}\right) = 0\,, \tag{7.16}$$

for which the same boundary conditions as (7.15) apply.

Multiplying (7.16) by g/ρ_0, integrating over depth and obeying the boundary conditions yields the mass balance in terms of bulk quantities which is given by

$$\frac{\partial g'D}{\partial t} = 0\,. \tag{7.17}$$

It states that buoyancy will decrease due to the entrainment of ambient fluid as it was found above that entrainment will cause an increase of D. The rate of decrease is given by

$$\frac{\partial g'}{\partial t} = -\frac{g'}{D}w_E\,, \tag{7.18}$$

which was found by combining (7.16) and (7.6). Recalling the definition of g' it turns out that mixing will cause a decrease of the density difference which is a logical consequence.

Kinetic energy balance

The depth integrated kinetic energy balance is obtained following the procedure described in chapter 3.1 (cf. equation (3.1)), by multiplying the momentum equations (7.7) and (7.8) with their respective velocities and summing up.

Integration over depth yields

$$\frac{\partial}{\partial t}\int_0^H \frac{1}{2}\left(u^2+v^2\right)\mathrm{d}z = \int_0^H \frac{\rho-\rho_0}{\rho_0} gu\sin\alpha\,\mathrm{d}z - \int_0^H \nu_{eff}\left(\left(\frac{\partial u}{\partial z}\right)^2+\left(\frac{\partial v}{\partial z}\right)^2\right)\mathrm{d}z\,, \tag{7.19}$$

where the Coriolis terms have canceled out. Introducing the form functions γ_k and γ_b, given by

$$\gamma_k = \frac{1}{D\left(U^2+V^2\right)}\int_0^H \frac{1}{2}\left(u^2+v^2\right)\mathrm{d}z\,, \tag{7.20}$$

$$\gamma_b = \frac{1}{g'UD}\int_0^H \frac{\rho-\rho_0}{\rho_0} gu\sin\alpha\,\mathrm{d}z\,, \tag{7.21}$$

and defining the total depth integrated bulk production of turbulent kinetic energy

$$P_b = \int_0^H \nu_{eff}\left(\left(\frac{\partial u}{\partial z}\right)^2+\left(\frac{\partial v}{\partial z}\right)^2\right)\mathrm{d}z = \int_0^H \nu_{eff} S^2\,\mathrm{d}z\,, \tag{7.22}$$

the depth integrated kinetic energy balance in terms of bulk quantities can be written as

$$\frac{\partial}{\partial t}\left(\frac{1}{2}\gamma_k D U_s^2\right) = \gamma_b g' DU\sin\alpha - P_b\,, \tag{7.23}$$

where U_s is the total speed of the current given by

$$U_s = \sqrt{U^2+V^2}\,. \tag{7.24}$$

It should be noted that the form functions γ_k and γ_b are equal to one in the ideal case of box profiles for velocity and salinity and close to one for natural profiles. However, the exact value is not important in the present context as the most important term in (7.23) is the bulk production of turbulent kinetic energy P_b which appears as a sink term in the mean kinetic energy balance and shows that by the production of turbulence the mean kinetic energy decreases.

Potential energy balance

The total potential energy (per unit area) of a water column is defined as

$$E_{p,tot} = \int_0^H \rho(z) g z \, \mathrm{d}z \ . \tag{7.25}$$

However, the total potential energy is based on the total density which will give a very huge number and is rather of limited interest as only the density difference between the ambient fluid and the current is subjected to mixing. Therefore a background potential energy given by the density of the ambient fluid

$$E_{p,amb} = \int_0^H \rho_0 g z \, \mathrm{d}z = \rho_0 g H \ , \tag{7.26}$$

is subtracted from (7.25) to give the available potential energy in terms of the density difference:

$$E_p = \int_0^H \Delta\rho(z) g z \, \mathrm{d}z \ . \tag{7.27}$$

In analogy to the kinetic energy balance above, the balance equation for the potential energy can be obtained from the mass balance (7.16), which when multiplied by gz, and integrated over depth gives

$$\frac{\partial E_p}{\partial t} = \frac{\partial}{\partial t} \int_0^H \Delta\rho g z \, \mathrm{d}z = -\int_0^H g \frac{\nu_t}{\sigma_t} \frac{\partial \Delta\rho}{\partial z} \mathrm{d}z \ . \tag{7.28}$$

Noting that the gradient of the density difference is the same as the gradient of the total density, the integrand on the right hand side of (7.28) turns out to resemble the buoyant production term (3.52). Hence, by dividing (7.28) by the reference density ρ_0, obeying the boundary conditions (7.15) and inserting (7.2) the potential energy balance in terms of bulk quantities can be written as

$$\frac{\partial}{\partial t}\left(\frac{1}{2} g' D^2 \right) = G_b \, . \tag{7.29}$$

In analogy to the bulk production of turbulent kinetic energy (7.22) the total depth integrated bulk buoyancy production is defined as

$$G_b = -\frac{g}{\rho_0}\int_0^H \frac{\nu_t}{\sigma_t}\frac{\partial \Delta\rho}{\partial z}\mathrm{d}z = -\frac{g}{\rho_0}\int_0^H \nu_t'\frac{\partial \Delta\rho}{\partial z}\mathrm{d}z\ , \tag{7.30}$$

which by definition makes a positive contribution for favorable stratification where density increases with depth. It is now seen what has been postulated a few times before, that mixing with the ambient fluid expressed by the production of buoyancy on the right hand side of (7.29) will increase the potential energy of a density current.

7.1.3 Momentum balance revisited

The balance equations presented in the preceding section are generally valid and already provided some theoretical insights into the physics of gravity currents. For the further discussion, however, it is useful to introduce some other definitions that mainly affect the momentum balance which will therefore be revisited now.

All balance equations above are written in terms of bulk parameters of the current. The momentum balance (7.10) and (7.11), however, still includes the bottom shear stress term on the right hand side which is not a bulk property yet. It can be transformed by applying a common parameterization used in open channel hydraulics where the bottom shear stress is assumed to be proportional to the square of the mean depth integrated velocity. The general quadratic friction law is given by

$$\tau_{bx} = C_D\rho_0 U_s U, \qquad \tau_{by} = C_D\rho_0 U_s V\ , \tag{7.31}$$

where C_d is the general drag coefficient and U_s is the total speed of the current given by (7.24). There are many similar forms of the general quadratic friction law the most famous being those of Darcy/Weisbach and Colebrook/White, Chézy and Manning/Strickler. The major difference between these friction laws stems from their derivation and the resulting coefficients which are related by:

$$\begin{array}{lll} \text{Darcy/Weisbach} \\ \text{Colebrook/White} & : & \lambda = 8C_D \\ \text{Chezy} & : & C = \sqrt{\dfrac{g}{C_D}} \\ \text{Manning/Strickler} & : & k_{St} = \sqrt{\dfrac{g}{C_D D^{1/3}}} \end{array} \quad . \tag{7.32}$$

The actual friction at the bottom depends on the roughness of the bottom which is conveniently expressed in terms of an equivalent sand roughness as introduced in chapter 3.8. Unfortunately, the relation between the friction coefficients and the sand roughness is nonlinear and depends on the current velocity and current depth. For a turbulent flow Colebrook/White gave the following implicit formula:

$$\frac{1}{\sqrt{\lambda}} = 2\log\left(\frac{2.51}{Re\sqrt{\lambda}} + \frac{k_s}{3.71 d_{hy}}\right), \tag{7.33}$$

with the Reynolds number of the flow given by

$$Re = \frac{U_s d_{hy}}{\nu}, \tag{7.34}$$

and the hydraulic diameter defined as

$$d_{hy} = 4D\,. \tag{7.35}$$

In oceanography it is common practice to consider bottom friction in terms of the general drag coefficient which takes values in the range of $0.002 < C_d < 0.003$. For a typical density current occurring in the Baltic Sea this implies an equivalent sand roughness of $0.02\ \text{m} < k_s < 0.10\ \text{m}$ which seems to be a reasonable range for the sea floor. It should be noted that bottom friction can be well parameterized by the equivalent sand roughness k_s but the law of Colebrook/White (7.33) is only an approximation to relate the bottom roughness to the bottom drag by the bulk speed and depth of the current. In the present numerical model the actual bottom drag stems from the wall functions approach given by (3.150) - (3.152) as described in

chapter 3.8. The difference between the real bottom drag and approximation in terms of bulk flow properties will be discussed later in section 7.2.3.

With the parameterization of the bottom shear stress the momentum balance can be completely written in terms of bulk parameters of the flow:

$$\frac{\partial UD}{\partial t} = g'D\sin\alpha + fVD - C_d U_s U \,, \tag{7.36}$$

$$\frac{\partial VD}{\partial t} = -fUD - C_d U_s V \,. \tag{7.37}$$

With the entrainment rate as introduced in chapter 6.2 and given in the present terminology as

$$E = \frac{w_E}{U_s} \,, \tag{7.38}$$

and the definition of the entrainment velocity given by the volume balance (7.6) the momentum balance can be rewritten as

$$\frac{\partial U}{\partial t} = g'\sin\alpha + fV - \frac{U_s U}{D}\left(C_d + E\right) \,, \tag{7.39}$$

$$\frac{\partial V}{\partial t} = -fU - \frac{U_s V}{D}\left(C_d + E\right) \,. \tag{7.40}$$

This form of the momentum balance gives a new insight in the interpretation of entrainment in a density current. The entrainment rate E acts like a drag coefficient and describes the effect of shear in the interface between the moving current and the stagnant ambient fluid. Furthermore, the effect of Coriolis forces as shown in chapter 2.4 on the current can be clearly identified from (7.40). Assuming the bottom slope is directed to the north such that the x-axis points northwards and the y-axis points westwards then the initial flow direction will be downslope (northwards) implying a positive velocity U. Through the first term on the right hand side of (7.40) this induces an acceleration in negative y-direction (eastwards) which means a deflection to the right just as postulated for the northern hemisphere.

A still better insight into the balance of forces can be gained if the coordinate system is rotated such that the principal axis points to the main flow direction rather than the main slope. Defining the new coordinate system with (m, n) and the rotation angle by

$$\beta = \arctan\left(\frac{V}{U}\right), \tag{7.41}$$

then the velocities in m- and n-direction are given by

$$U' = U\cos\beta + V\sin\beta = U_s\,, \quad V' = -U\sin\beta + V\cos\beta = 0\,, \tag{7.42}$$

showing that the streamwise velocity corresponds to the total speed of the current while the cross-stream velocity cancels out. In the rotated system there is now a slope in both coordinate directions with the respective angles given by

$$\sin\alpha_m = \sin\alpha\cos\beta\,, \quad \sin\alpha_n = -\sin\alpha\sin\beta\,. \tag{7.43}$$

Obeying these relations the momentum equations in the new coordinate system become:

$$\frac{\partial U'}{\partial t} = g'\sin\alpha_m - \frac{U_s^2}{D}\left(C_d + E\right), \tag{7.44}$$

$$\frac{\partial V'}{\partial t} = -fU_s - g'\sin\alpha_n\,. \tag{7.45}$$

It is interesting to note that the rotation of the reference system yielded a sorting of the relevant external forces on the right hand side. In main flow direction the Coriolis term vanished and only drag forces remained while in cross flow direction the latter disappeared and the Coriolis force remained. This becomes even clearer if some further simplifications are made. As will be shown later, for subcritical flows the entrainment rate is one to two orders of magnitude less than the bottom drag coefficient and can therefore be neglected in the momentum balance. In this case the inertia terms on the left hand side are also likely to be of minor importance and can

be ignored, too. Then the the current is in geostrophic balance and the momentum equations can finally be written as:

$$g' \sin \alpha_m = \frac{C_d U_s^2}{D}, \tag{7.46}$$

$$g' \sin \alpha_n = f U_s . \tag{7.47}$$

These relations show that in main flow direction the gravity force is balanced by the bottom drag while in cross-flow direction it is balanced by the Coriolis force. The simplification of the momentum equations by the assumption of geostrophic balance allows for the derivation of some more interesting facts which will be discussed next.

7.1.4 Froude number and Ekman number

The Froude number describes the ratio between inertia force and gravitational force and is the most important characteristic parameter in open channel hydraulics. The same applies to density currents with the only difference being the gravitational force which is given by the reduced gravity g'. To distinguish between the open channel Froude number and that for a density current, the latter is often referred to as 'densimetric Froude number'. Here, however, only density currents are regarded and the term 'densimetric' will be neglected in the following.

In the present terminology the Froude number in the most general form is given by

$$Fr = \frac{U_s}{\sqrt{g' D \cos \alpha_m}}, \tag{7.48}$$

where the bottom slope angle is not necessarily small. The nominator in (7.48) is the speed of long interfacial waves that will only propagate upstream in subcritical conditions if $Fr < 1$. Another interpretation of the Froude number can be gained from the combination of (7.48) with the geostrophic momentum balance in main flow direction (7.46), giving

$$Fr = \sqrt{\frac{\tan \alpha_m}{C_d}} \,. \tag{7.49}$$

This formulation shows that for subcritical flow conditions the bottom slope must be less than the drag coefficient which provides a good estimate for the slopes in a natural situation recalling the common range for C_d above. For supercritical flows, however, equation (7.49) loses its validity as the entrainment rate and the inertia terms become larger and the assumption of geostrophic balance breaks down.

The Ekman number for a density current can basically be defined as the ratio between the Ekman layer thickness and the depth of the current. In terms of the parameterized bottom friction this can be written as:

$$K = \frac{C_d U_s}{f D} \,. \tag{7.50}$$

Unlike the Froude number, the Ekman number does not depend on the density difference between the current and the ambient fluid and is mainly a measure for the influence of Coriolis forces. For small Ekman numbers when the Ekman layer is much thinner than the current depth the effect of Coriolis forces is large and the current will be strongly deflected and follow the contour lines of the slope. A large Ekman number in contrast implies an Ekman layer which is thicker than the current depth such that Coriolis forces become less important and the current will flow straight down the slope.

This interpretation of the Ekman number follows directly from the geostrophic momentum balance. Dividing (7.46) by (7.47) and applying the relations in (7.43) yields:

$$\tan \beta = -\frac{1}{K} \,, \tag{7.51}$$

which approves that $\beta \to 0°$ for large Ekman numbers and $\beta \to -90°$ for small Ekman numbers. Please recall that the present coordinate system had been defined with the x-axis pointing downslope and the y-axis pointing to the left along the depth

contours. A current following the slope therefore yields $\beta = 0°$ while a deflection to the right implies $\beta < 0°$.

Finally, the Froude number and the Ekman number can be formally related to each other by a combination of the momentum balance equations (7.46) and (7.47). In terms of the total slope and the bottom drag coefficient this functional relationship is given by:

$$Fr = \sqrt{\frac{\sin\alpha}{C_d}} K^{1/2} \left(K^2 + 1\right)^{-1/4} . \tag{7.52}$$

In the limits of small and large Ekman numbers (7.52) can be simplified. For large Ekman numbers the Froude number becomes independent of K and approaches

$$Fr = \sqrt{\frac{\sin\alpha}{C_d}} . \tag{7.53}$$

For large K, $\tan\alpha_m \approx \tan\alpha$ and for small α, $\tan\alpha \approx \sin\alpha$, which shows that (7.53) is identical to (7.49) if small bottom slopes are assumed.

For small Ekman number K < 1, the term in brackets on the right hand side of (7.52) approaches 1 and the Froude number can be expressed as

$$Fr = \sqrt{\frac{\sin\alpha}{C_d}} K^{1/2} . \tag{7.54}$$

Even if the theoretical relation between the Froude and Ekman number might be an interesting feature which will indeed be used in the following validation of the numerical model, the major interest here is on the entrainment.

7.1.5 Entrainment

The general idea of entrainment and the mechanisms involved have been discussed in chapter 6.2 where also some entrainment laws proposed in the literature have been presented. The scaling parameter for entrainment in stratified flows was

identified to be the bulk Richardson number which is a general quantity that applies to all the different entrainment situations. Although the entrainment in gravity currents can also be described in terms of the bulk Richardson number it seems more appropriate in the present context to use the Froude number. For small bottom slopes the Froude number and the bulk Richardson number are related by

$$Fr^2 = \frac{U_s}{g'D} = \frac{\rho_0}{g}\frac{U_s}{\Delta\rho D} = \frac{1}{Ri_b}\,, \tag{7.55}$$

such that all entrainment laws given in chapter 6.2 can in priciple also be given in terms of the Froude number. However, this is actually only meaningful in case of density currents for which a Froude number can be defined.

The entrainment rate as given by (7.38) is made up of the current speed and the entrainment velocity which within the context of the theory presented above can be determined in two different ways. The first directly stems from the volume balance of the current (7.6) where w_E is determined as the increase of the current depth and volume flux, respectively. In case of a one-dimensional model this simplifies to

$$w_E = \frac{\partial D}{\partial t}\,, \tag{7.56}$$

which relates the entrainment to the temporal evolution of the mixed layer depth. Indeed, the formula of Price (1979) for the temporal evolution of the mixed layer depth due to wind entrainment (6.17) is not explicitly given in the original paper but has been derived applying (7.56) to the presented entrainment law.

The second way to determine the entrainment velocity stems from the balance of potential energy (7.29) which by use of (7.56) can be rewritten

$$\frac{\partial}{\partial t}\left(\frac{1}{2}g'D^2\right) = \frac{1}{2}g'Dw_E = G_b\,, \tag{7.57}$$

and finally yields

$$w_E = \frac{2G_b}{g'D}. \tag{7.58}$$

This form of the entrainment velocity is more meaningful in terms of the actual source of mixing namely buoyancy production induced by turbulence. In chapter 6.1.3 the ratio between the total turbulence production and the amount that is used for buoyancy production was determined as the flux Richardson number. In the present depth integrated framework a bulk flux Richardson number can be established from the bulk production terms (7.22) and (7.30):

$$Ri_{f,b} = \frac{G_b}{P_b}. \tag{7.59}$$

Assuming weak slopes (subcritical flow) and quasi stationary conditions such that the entrainment rate is much smaller than bottom drag and the left hand side of (7.23) vanishes, (7.46) can be used to rewrite P_b as

$$P_b = \gamma_b g'DU_s \sin\alpha_m = \gamma_b C_d U_s^3. \tag{7.60}$$

This expression together with the buoyancy production given by (7.57) and the definition of the entrainment rate (7.38) can be used to rewrite the bulk flux Richardson as

$$Ri_{f,b} = \frac{1}{2}\frac{g'DU_sE}{\gamma_b C_d U_s^3}, \tag{7.61}$$

which finally provides an entrainment law derived analytically within the present depth integrated theory:

$$E = 2Ri_{f,b}C_d Fr^2. \tag{7.62}$$

It should be stressed that due to the assumptions made above in the derivation of (7.62) this entrainment law is only valid for subcritical flow conditions ($Fr < 1$), where bottom slopes are small, entrainment is much less than bottom drag and the inertia terms can therefore be neglected. Interestingly, most of the entrainment laws

presented in chapter 6.2 show the same Froude number squared dependence for this flow regime (cf. relation of Ri_b and Fr in (7.55)). However, all of these laws assume a constant factor in front of Fr^2 which is unlikely to be generally valid and explains the large scatter in the different factors proposed. For subcritical flows the bottom drag coefficient and the Froude number can be eliminated by substituting (7.53) into (7.62) to give

$$E = 2Ri_{f,b} \tan \alpha_m , \tag{7.63}$$

which shows that for subcritical flows entrainment is solely governed by the bottom slope (in flow direction) and the bulk flux Richardson number. Pedersen (1980) and Stigebrandt (1987) proposed very similar laws and assumed that for subcritical flows the ratio between entrainment and bottom slope is constant $E/\tan \alpha_m = 0.071$ which in the present theory implies a constant bulk flux Richardson number of $Ri_{f,b} \approx 0.035$. However, as shown by the numerical experiments of Arneborg et al. (2007) it is unlikely that $Ri_{f,b}$ is constant throughout the whole subcritical flow regime. Much more it can be assumed that bottom roughness and Froude number will have a certain influence on the efficiency of mixing. Indeed, Arneborg et al. (2007) found that all their data for the flux Richardson number could be collapsed onto a single curve dependent on Froude number and Ekman number which has been given by

$$Ri_{f,b} = 0.042 Fr^{0.65} K^{0.6} . \tag{7.64}$$

Inserting (7.64) into the present entrainment law (7.62) this can be rewritten in terms of Ekman number and bottom drag coefficient

$$E = 0.084 K^{0.6} C_d Fr^{2.65} . \tag{7.65}$$

Besides the dependence on Ekman number and bottom drag coefficient the entrainment rate now increases with $Fr^{2.65}$ which is interestingly just in between the laws proposed by Christodoulou (1986) with Fr^3 for very low and Fr^2 for intermediate Froude numbers (cf. chapter 6.2).

Using the relation between the bulk Richardson number and the Froude number given by (7.55) the data in Figure 6.7 can be recast in terms of the Froude number. These are shown in Figure 7.2 together with the present entrainment law represented by the thick line.

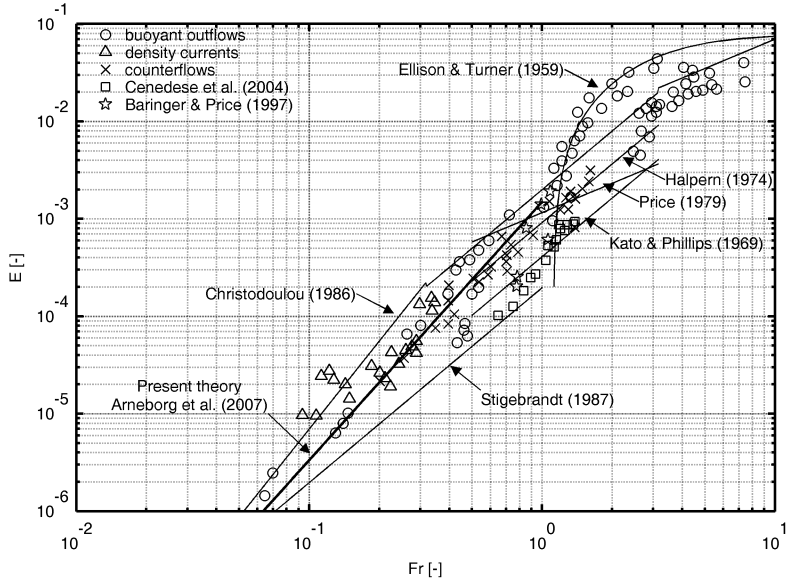

Figure 7.2: Entrainment rate versus Froude number. Comparison of entrainment laws and measurements from the literature (cf. Figure 6.7). Note that the present theory is actually not valid (see text).

The slope of 2.65 in the logarithmic plot seems to be a reasonable value which makes the present law lying in between the laws of Stigebrandt (1987) and Christodoulou (1986) and is a nice approximation of the measured data. Actually, the curve has been fitted to the data by adjusting the factor in front of the Froude number, but the chosen value of $1.5 \cdot 10^{-3}$ also seems to be quite reasonable. It results from $K^{0.6} C_d \approx 0.018$ or with $C_d = 0.003$, as assumed for the other laws, from $K \approx 20$ which is rather high and indicates a very small influence of Coriolis forces consistent with the data that have almost all been gathered from experiments in channels without rotation.

However, this very nice and at first sight absolute logically derived result is unfortunately not valid. The reason is that for large Ekman numbers say, K > 3, the present theory actually breaks down as the Froude number becomes independent of the Ekman number (cf. eq. (7.53)) and the entrainment law reads

$$E = 0.084 K^{0.6} C_d^{-0.325} \sin\alpha^{1.325} . \tag{7.66}$$

For constant bottom slope and bottom drag the entrainment rate thus only depends on the Ekman number and tends to infinity in the limit of a non rotating frame of reference. Nevertheless, it is interesting that the present theory yields a slope of 2.65 for the entrainment rate and the curve in Figure 7.10 has been included in order to visualize the good agreement of this result with entrainment data from non rotating laboratory experiments. The derivation of a valid theory supporting this slope could be a task for further research.

For smaller Ekman numbers as they are typically found in natural oceanic density currents like in the Baltic Sea the theory is definitely valid and for K < 1 the present entrainment law can be transformed by use of (7.54) giving

$$E = 0.084 \sin\alpha^{-0.6} C_d^{1.6} Fr^{3.85} . \tag{7.67}$$

This relation shows that entrainment is solely governed by the total bottom slope and bottom drag. The large exponent of the Froude number implies a much faster decrease of the entrainment rate than suggested by the data (from non-rotating experiments) in Figure 7.10. However, this is physically reasonable following a suggestion by Stigebrandt (1985) who argued that the bottom generated turbulence is restricted to the Ekman layer and for K < 1 is therefore hindered to reach the interface which will eventually reduce mixing. Furthermore, the field data of Baringer & Price (1997) and the rotating experiment data of Cenedese et al. (2004) included in Figure 7.10 also indicate a slightly steeper slope. This will be discussed in more detail in the next section when the influence of bottom friction and bottom slope on the entrainment rates is investigated.

7.2 1−D modeling of natural density currents

In the preceding chapter it was found that the choice of the turbulence model only marginally influences the wind induced entrainment in a stratified stagnant water body. Much more the governing parameter was identified to be the stationary Richardson number. Even if the wind induced mixing is a good test case for a numerical model the physical background of a density current moving on a sloping bottom is slightly different. The major difference lies in the stratification which is now mainly confined to the interface between the moving current and the stagnant ambient water. This configuration also alters the sources for turbulence which are now found at the bottom shear layer and the shear layer in the interface.

Therefore it is advisable first to apply all turbulence models again in a specific benchmark test to shortly identify their strengths and weaknesses. In the succeeding more detailed validation only the SST k-ω model is used, as it was found above to be the most suitable model for the simulation of cylinder induced entrainment.

7.2.1 Model setup

As for the wind entrainment experiment above it is sufficient to validate the numerical model for the simulation of undisturbed gravity currents with a one-dimensional model where only the vertical domain is resolved. Therefore a similar grid like above is used with the horizontal domain made up of only one grid cell and periodic boundary conditions applied on the lateral boundaries. To account for the effect of bottom roughness a wall boundary condition with k_s = 0.025 m has been used in all simulations and the free surface at the top is always simulated with a symmetry (slip) boundary condition.

Although the benchmark test has been arbitrarily defined it should at least approximately represent the natural conditions in the Baltic Sea. For this purpose the bottom roughness had been set to k_s = 0.025 m to account for realistic conditions at the sea floor. Coriolis forces correspond to a location 55° longitude North with a parameter $f \approx 1.19 \cdot 10^{-4}$ 1/s. The only driving force for the current stems from the bottom slope which has been chosen to be quite steep with tan $\alpha = 1.78 \cdot 10^{-3}$. The

total water depth is $H = 40$ m and the initial current depth is $D = 7.0$ m. The salinity difference between the current and the ambient fluid is $\Delta S = 10$ PSU which implies a density anomaly of $\Delta\rho = 7.85$ kg/m³ and a reduced gravity of $g' = 0.0765$ m/s². The global initial conditions for the benchmark test are compiled in Table 7.1.

tan α [‰]	k_s [m]	D [m]	ΔS [PSU]	Fr
1.78	0.025	7.0	10.0	0.8

Table 7.1: Initial conditions for the one-dimensional simulations of entrainment in an undisturbed gravity current.

The distribution of salinity is initially approximated by a simple box profile such that a realistic profile will evolve during the starting period of the simulation. In order to keep the initial settling time for the current as short as possible also box profiles for the velocities are applied that approximate the geostrophic balance. The initial profiles of density anomaly and velocity are displayed in Figure 7.3 where also the resolution of the numerical grid is shown in the left panel.

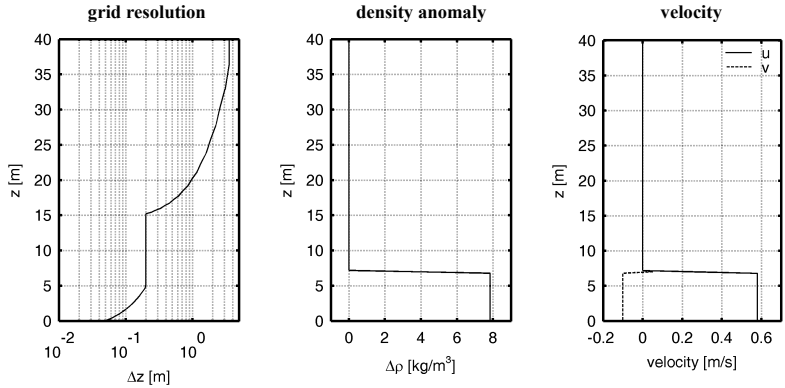

Figure 7.3: Grid resolution and initial conditions for the one-dimensional simulations of entrainment in an undisturbed gravity current.

As can be seen the grid is refined to the bottom in order to resolve the steep gradients of velocity and turbulence quantities in the boundary layer. The interface is

initially located at z = 7 m and will rise during the simulation due to entrainment. Therefore the region 5 m < z < 15 m has a constant resolution of Δz = 0.2 m in order to provide constant numerical settings during the evolution of the current. It should be noted, that the chosen resolution is comparably fine and preliminary tests have shown almost similar results for Δz = 0.5 m. However, as the numerical effort for the present grid size of 117 cells over the total water depth is relatively small the finest grid was chosen for the present validation. The region of the stagnant ambient fluid is numerically easy to treat and requires no specific resolution such that the grid for z > 15 m could be made increasingly coarser.

7.2.2 Comparison of different turbulence models

From the model validation in chapter 6 it could be concluded that for the simulation of entrainment in a stratified shear layer with two-equation turbulence models the choice of the specific model is rather unimportant as long as the governing parameters (Ri_{st} and σ_t) are adequately incorporated. This shall now be approved by the simulation of a gravity current. For all turbulence models the turbulent Prandtl number is given by the model of Schumann & Gerz (1995) and the constant $c_{\psi 3}$ has been adjusted to fix the stationary Richardson number to Ri_{st} = 0.25.

As shown in chapter 6, a unique definition of the stationary Richardson number is not possible for the RNG k-ε model due to the additional term in the ε-equation. For the wind induced entrainment simulations this had no significant effect although slightly different results compared to the other two k-ε models could already be noticed. However, for the present simulation of gravity current dynamics this discrepancy is obviously much more severe as the RNG k-ε model was susceptible to instabilities and the results showed very strange behavior compared to the other models. Therefore this model has not been regarded further and the following discussion is limited to the standard and realizable k-ε model and the standard and SST k-ω model.

All simulations were started with the initial conditions described above and run over 5 days. Figure 7.4 shows the temporal evolution of the current depth, entrainment rate, Froude number and Ekman number. It is obvious at first sight that the

difference between the individual turbulence models is marginal. From the current depth in the upper left panel it can be seen that the *k-ε* models and *k-ω* models are pairwise identical and that the *k-ω* models predict a slightly slower growth of the layer thickness. The same behavior could be observed in the wind entrainment experiment and is also here attributed to some kind of numerical error.

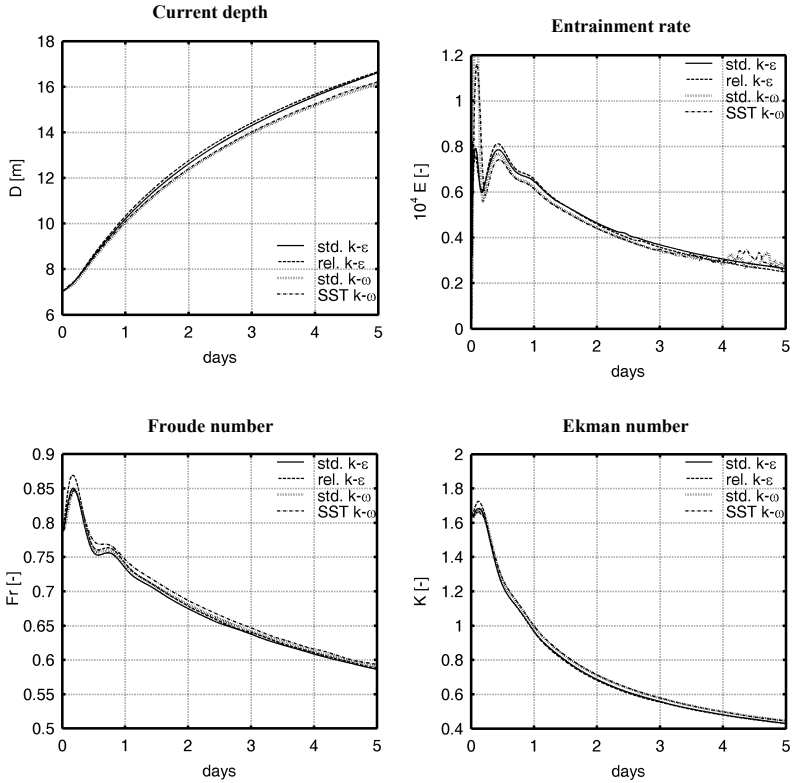

Figure 7.4: Comparison of different turbulence models. Temporal evolution of the gravity current.

From the strong variations in the Froude number and entrainment rate at the beginning of the simulation it can be followed that the initial settling time of the current is a bit less than 1 day. The *k-ω* models also show some random oscillations

in the entrainment rate at the end of the simulation for $t > 4$ days. These can be attributed to numerical problems in association with the grid resolution which changes for $z > 15$ m corresponding to the current depth at the beginning of the fluctuations. However, as long as the grid resolution is constant over the interface all models are stable and provide basically the same entrainment rates.

Due to entrainment the current depth increases with time as expected from (7.56). In this context it should be noted that the entrainment rate in the upper right panel was calculated from (7.58) and therefore is at first independent from the temporal evolution of the current depth. However, by definition both (7.56) and (7.58) should give the same entrainment rate, a fact that will be used in the validation of the numerical model in the next section.

The Froude number and the Ekman number decrease with time as shown in the lower panels of Figure 7.4. The latter indicates that the current is more and more deflected from the straight downhill path and turns into the slope. The temporal evolution of the Froude number together with the entrainment rate qualitatively supports the theoretical entrainment laws which predict reduced entrainment with decreasing Froude number. Also this point will be later discussed below.

The similarity of the different turbulence models concerning the depth integrated results is also found in the details. For a current depth of $D = 10$ m after about 1 day of entrainment in the present example Figure 7.5 displays depth profiles of density difference, buoyancy production, streamwise and cross-stream velocity (in the (m, n)-coordinate system), gradient Richardson number and flux Richardson number. As the stagnant ambient fluid is of limited interest only the lower 20 m of the total depth are shown.

Apart from some minor differences in the buoyancy production and Richardson numbers the profiles for all turbulence models are more or less identical. The initial density difference of $\Delta\rho \approx 8$ kg/m³ decreased by more than 25 % because of the entrainment of ambient fluid. The interface between the current and the ambient fluid is characterized by a more or less constant density gradient ($N^2 \approx 0.01$) which is found in the region 8 m < z < 12 m.

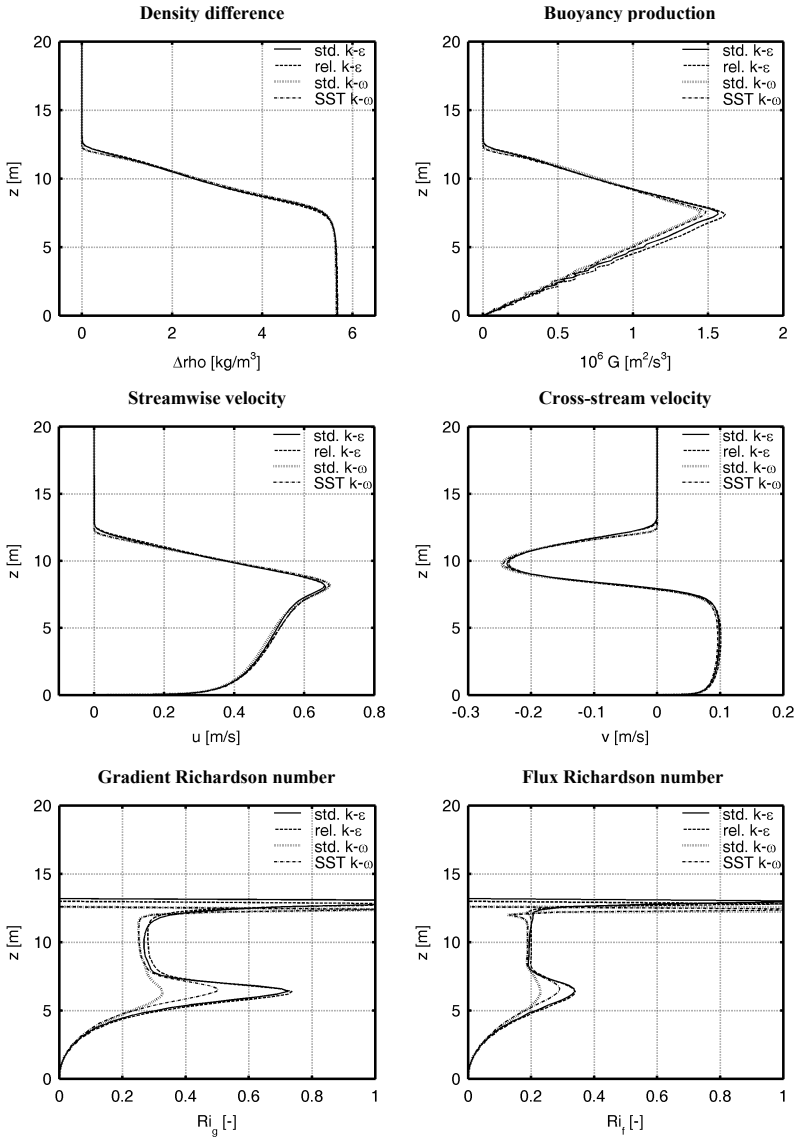

Figure 7.5: Comparison of different turbulence models. Vertical profiles for current depth $D = 10$ m.

A local mixing rate can be deduced from the buoyancy production in the upper right panel which increases linearly from $G = 0$ m^2/s^3 at the bottom to its maximum value $G \approx 1.5 \cdot 10^{-6}$ m^2/s^3 right below the interface and decreases to $G = 0$ m^2/s^3 again within the interface. This indicates the damping effect of stratification on turbulence and shows that mixing is most intense just below the interface where the ratio between turbulence intensity and stratification is at maximum.

The velocity profiles in the middle panels show the typical effect of a rotating frame of reference. At the bottom where friction forces are dominant both profiles have the characteristic logarithmic form with mean flow direction downhill. With increasing distance from the bottom, however, the influence of bottom drag decreases and Coriolis forces become dominant. These accelerate the flow in streamwise direction with the maximum velocity right below the interface. In cross-stream direction the flow is deflected to the right ($v < 0$) with the maximum velocity in the center of the interface.

From the profiles of the Richardson numbers in the lower panels it can be seen that within the interface the stationary values are reached indicating the validity of the equilibrium assumption in a stratified turbulent shear layer. At the top end of the interface density and velocity gradients tend to zero and the gradient Richardson number becomes ill-defined as indicated by the sudden increase for $z > 12$ m. Also below the interface both increase quite significantly before they approach zero at the bottom. This effect is most pronounced for the k-ε models and least significant for the standard k-ω model. However, the gradient Richardson number is a direct result of the density and velocity profiles which are apparently very similar. The alleged large differences stem from the fact that the velocity gradient enters squared into the nominator (cf. eq. (6.3)) such that small deviations in the velocity field can have a large effect on the gradient Richardson number. Hence, it still may be concluded that all turbulence models provide the same results.

For the following validation of the numerical model concerning the simulation of density currents it is therefore sufficient to regard only one turbulence model. In principle the choice of the turbulence model is arbitrary, but in view of the

subsequent simulations of the cylinder induced entrainment it seems most appropriate to use the SST k-ω model and ignore the other models from now on.

Before the model is validated against the depth integrated theory and field measurements in the next sections it is useful in context with the Richardson numbers discussed above to have a look at the kinetic energy balance. Figure 7.6 shows the individual profiles for production of turbulent kinetic energy P, buoyancy production G and dissipation ε in the left panel and the ratio of production to dissipation $R = P/(G + \varepsilon)$ in the right panel.

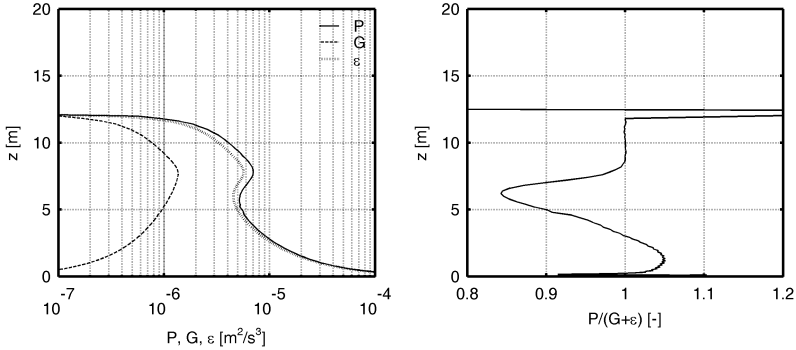

Figure 7.6: Balance of turbulent kinetic energy. Profiles of production and dissipation (left) and ratio of production and dissipation (right).

As discussed in chapter 6.1.5 for gradient Richardson numbers above the stationary value turbulence will decay while for values below it will increase. In case that the actual Richardson number corresponds to the stationary value production and dissipation are in balance which is nicely seen from their ratio in the right panel which is exactly $R = 1$ within the interface. Near the bottom it is expected that turbulence production outweighs dissipation which is indeed the case as $R > 1$ just above the bottom in agreement with the small gradient Richardson number in this region. In the intermediate region $R < 1$ as suggested above by the large gradient Richardson number. This means that in the core of the current turbulence is not in balance but produced at the bottom and then transported to higher levels.

7.2.3 Comparison with theory

After it has been shown by now that the numerical model is able to quite accurately predict the general features of entrainment in a stratified turbulent shear layer independent of the two equation turbulence model in the background the depth integrated theory derived above can be used as an ideal reference for further validation.

From the mass balance (7.17) it must be expected that the total buoyancy does not change with time. Furthermore the balance of potential energy requires that the entrainment rate given by (7.58) should be identical to that derived from the temporal increase of the current depth (7.56). Figure 7.7 shows the numerically evaluated and theoretical temporal evolution of the buoyancy in the left panel and the entrainment rates determined by (7.56) and (7.58) in the right panel.

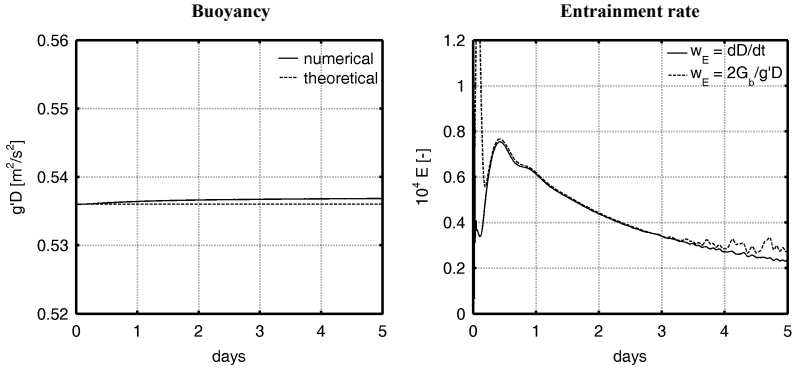

Figure 7.7: Evaluation of numerical errors. Temporal evolution of buoyancy (left) and entrainment rate (right).

The numerical model predicts a slight increase of buoyancy with time. However, after 5 days the difference to the theoretical value is less than 2 ‰ and can therefore be assumed to be negligible. Apart from the deviations at the beginning and the end of the simulation already argued above the entrainment rates in the right panel show

perfect agreement and approve the numerical balances of volume and potential energy.

The Ekman number as given by (7.50) depends on the bottom drag coefficient, current speed, current depth and the Coriolis parameter. While the latter three are uniquely defined the bottom drag coefficient can principally be determined in several ways. The actual bottom shear stress τ_b depends on the velocity profile (cf. chapter 3.8) and is a direct result of the numerical model. With the bottom shear stress given the actual drag coefficient can be easily calculated according to (7.31) from

$$C_D = \frac{\tau_b}{\rho_0 U_s^2} . \tag{7.68}$$

If the bottom shear stress is not explicitly known or if the velocity profiles are not suitable to calculate it the drag coefficient could be estimated from the bulk speed and depth of the current using the formula of Colebrook/White (7.33) together with (7.32) or if additionally the bottom slope is known from the geostrophic momentum balance given by (7.46) and (7.49), respectively.

The temporal evolution of the bottom drag coefficient obtained with all three methods is shown in the left panel of Figure 7.8. The different methods correspond to equations (7.68), (7.33) and (7.46), respectively where the slope in streamwise direction α_m for the latter has been determined from the total slope α using (7.43) and the deflection angle β given by (7.41). The drag coefficient derived from the depth integrated momentum balance (method 3) agrees fairly well with the actual bottom drag (method 1) and the difference between both could be explained by a slight overestimation of the bottom shear stress from the numerical model results. Apart from this difference both show identical trends and approach to a constant value of about $C_d \approx 0.002$ which shows that the bottom drag coefficient does not change if the flow is in geostrophic balance. The bottom drag coefficient obtained from the formula of Colebrook/White (method 2) also tends to a value of $C_d \approx 0.002$ at the end of the simulation. However, the temporal evolution is quite different from that of the other two methods and apparently this method also does not show an

asymptotic behavior with a constant drag coefficient in geostrophic balance. Even if the differences are not severe the determination of the bottom drag from the formula of Colebrook/White should be handled with care and was not further regarded in the present work.

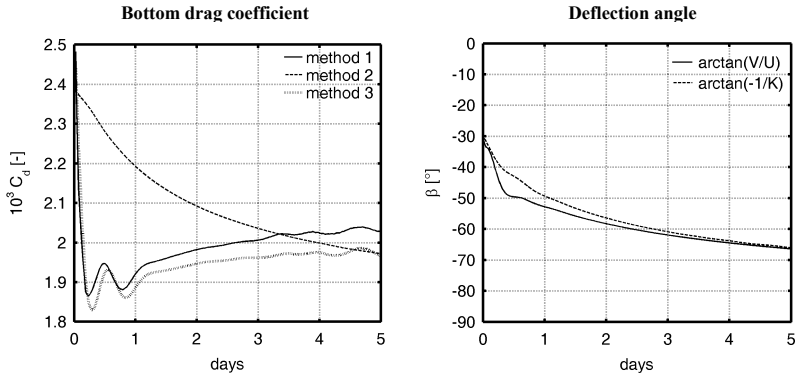

Figure 7.8: Temporal evolution of bottom drag coefficient (left) and deflection angle (right). The methods for the determination of C_d in the left panel correspond to: method 1 → eq. (7.68), method 2 → eq. (7.33), method 3 → eq. (7.46) and (7.49), respectively.

Whether the Ekman number is determined with the actual drag coefficient or the approximation given by (7.46) and (7.49), respectively is of minor importance as the results are almost identical. However, it might be interesting to compare the actual deflection angle of the current given by (7.41) to the theoretical angle predicted from the Ekman number by (7.51). The temporal evolution of the deflection angle β is shown in the right panel of Figure 7.8. At the very beginning of the simulation both are identical due to the initial conditions adjusted to geostrophic balance. As the velocity profiles evolve from the initial box profiles to the natural form the current turns more into the slope as predicted by the theory. However, after the initial settling time when velocity and density profiles have established the actual deflection angle tends back to the theoretical curve and the current is in geostrophic balance again.

The momentum balance suggests that the Froude and Ekman number are related by (7.52) if the flow is in geostrophic balance. This relation is shown in the left panel of Figure 7.9 where the theoretical curve is based on a constant bottom drag coefficient of C_d = 0.002. Apart from the deviations at higher Ekman numbers which are a result of the initial settling of the current the numerical results almost perfectly agree with the theoretical curve. This confirms both, the very good performance of the numerical model and that the current is indeed in geostrophic balance after an initial settling time.

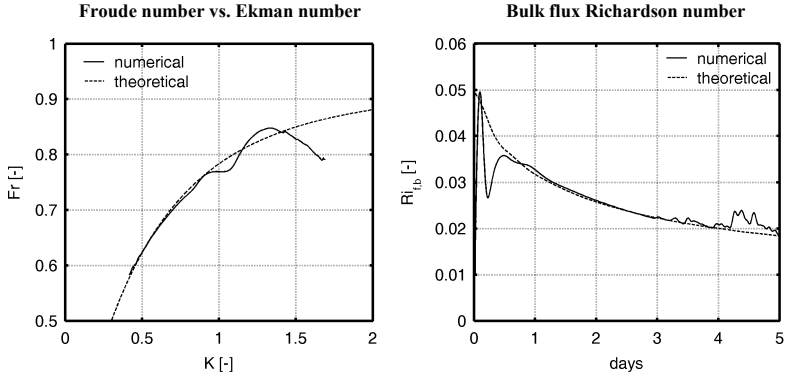

Figure 7.9: Froude-Ekman number relation (left) and temporal evolution of bulk flux Richardson number (right).

The right panel in Figure 7.9 shows the bulk flux Richardson number which is an important property concerning the efficiency of mixing and the prediction of the entrainment rate based on (7.62) and (7.63), respectively. The result of the numerical model stems from the ratio of the predicted buoyancy and turbulent kinetic energy production using (7.59) while the theoretical curve is based on the empirical formula (7.64) suggested by Arneborg et al. (2007). As (7.64) had been found by fitting a curve through numerical data the two curves shown basically provide a comparison between the present numerical model and that used by Arneborg et al. (2007). However, apart from the expected deviations at the beginning and the end the numerical results are in almost perfect agreement with the theoretical curve

supporting once more the performance of the present numerical model and the validity of the empirical formula (7.64).

The latter is important for the proposed entrainment law given by (7.62) and (7.63), respectively. For a given bottom slope and drag coefficient (tan α = $1.78 \cdot 10^{-3}$, $C_d \approx 0.002$ in the present example) the Froude and Ekman number are distinctly related by (7.52). Hence, for a specific range of Ekman and Froude numbers the bulk flux Richardson number is given by (7.64) and the entrainment rate can be computed from (7.62). This theoretical prediction is compared to the present numerically predicted entrainment rates in Figure 7.10. For further comparison the field data of Baringer & Price (1997), the laboratory data of Cenedese et al. (2004) and the entrainment law of Stigebrandt (1987) with $C_d = 0.002$ are also shown.

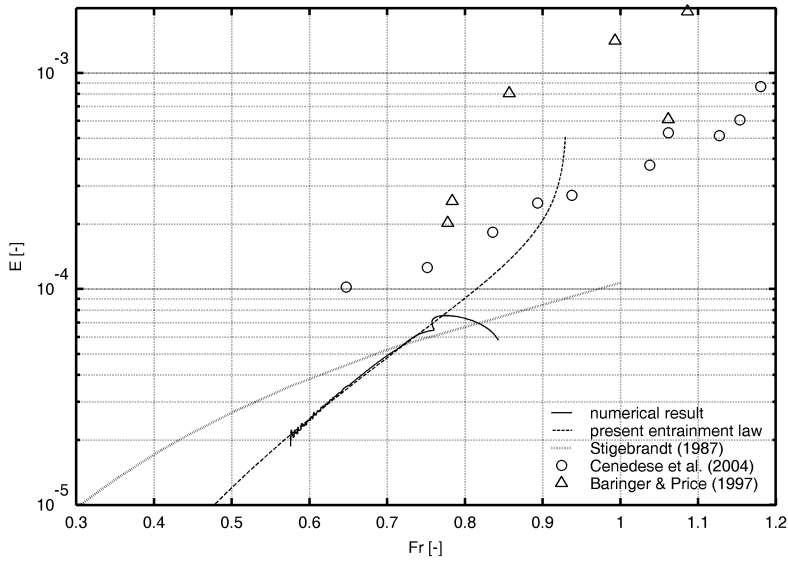

Figure 7.10: Entrainment rate versus Froude number. Comparison of present numerical model results with measurements and entrainment laws.

The agreement between the numerical model results and the present theory is expectedly striking and compared to the model of Stigebrandt (1987) entrainment decreases faster with decreasing Froude number (cf. eq. (7.70) and adjacent text). Note in this context that for the sake of better presentation the *x*-axis has been linearly scaled such that the entrainment laws do not appear as straight lines like in Figure 7.2 and Figure 6.7.

As mentioned in chapter 7.1 for large Ekman numbers the Froude number becomes independent of the Ekman number and the present theory will seize to be valid as indicated by the almost vertical increase of the entrainment rate for Fr ≈ 0.93. For density currents in the Baltic Sea which are of major interest here the Ekman number will usually be relatively small and the present entrainment law represents an ideal theoretical reference.

However, for the current example the numerically and theoretically predicted entrainment rates seem to be lower than those measured in the laboratory and the field, although the Ekman numbers in the experiments of Cenedese et al. (2004) were comparable to those found here. The reason for this alleged underestimation can therefore only be found in the steep slope and the relatively small bottom drag coefficient. This issue will be discussed in the following final validation of the numerical model against field measurements in the Baltic Sea.

7.2.4 Comparison with field measurements

The discussion in the previous two sections has shown that the present numerical model is very well suited to calculate the dynamics and entrainment rates of natural undisturbed density currents. Hence, the validation could actually be regarded as completed at this point. However, as there are very good current field measurements available which have also served as a reference for the numerical simulations of Arneborg et al. (2007) these data will now be used for a final validation of the present model and a discussion of the influence of bottom induced turbulence on the entrainment rates.

Description of the observed data

From January 26 to February 13, 2004 an extensive cruise was carried out within the framework of the QuantAS project in order to obtain measurements of medium-intensity saltwater inflows into the Baltic Sea. Luckily, such an event started on February 1 (Burchard et al. (2005)) entering the Baltic Sea over Drogden Sill and traveling down the sloping bottom into the Arkona Basin.

A map of the observed area is given in Figure 7.11 where the approximate pathway of the current is sketched by the thick lines. In front of Kriegers Flak the current splits up and passes the shoal on the northern and southern side. The dashed line indicates that only a minor portion of the current flows southward while the major part passes Kriegers Flak on the northern side (see Burchard et al. (2005)).

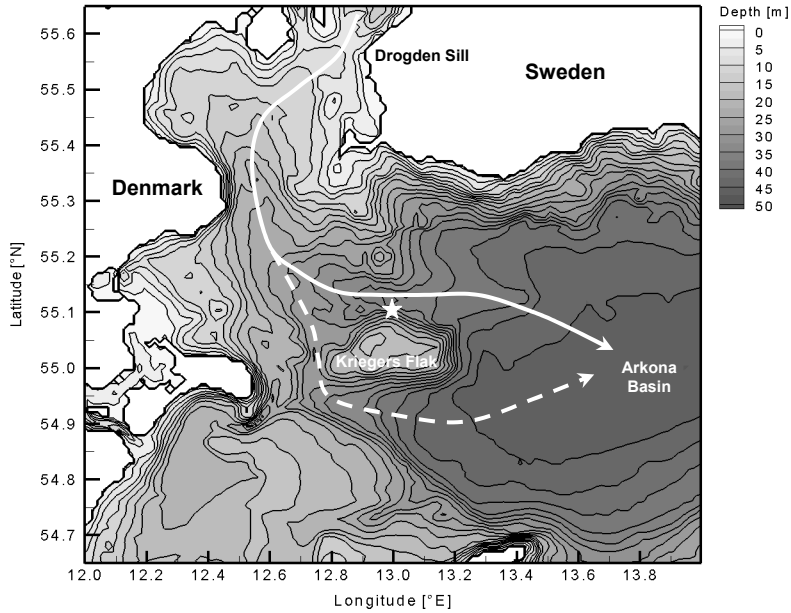

Figure 7.11: Contour map of the Baltic Sea between Drogden Sill and Arkona Basin. Pathway of the density current sketched by the full and dashed line and measurement station indicated by the star.

From February 6 to 7 velocities, temperature, salinity and turbulence dissipation rates were measured at a 38 m deep fixed location North of Kriegers Flak indicated by the star in Figure 7.11. A detailed discussion of the measurement equipment and the obtained data set is given in Arneborg et al. (2007) and will only briefly summarized here.

The current velocities were measured by an acoustic Doppler current profiler (ADCP) mounted in the sea chest of the ship at 3 m depth and taking a velocity profile with 1 m resolution every 1.4 s. The velocities can be regarded as quite reliable up to about 2 m above the ground where the ultra sonic signal can be contaminated by bottom echoes from side lobes of the downward looking ADCP. Furthermore, as pointed out by Arneborg et al. (2007) the mean gradient Richardson number within the current interface might be overestimated due to the finite depth resolution of the velocity profiles and the time averaging process to obtain the mean velocity gradients. A standard precision conductivity, temperature, depth (CTD) profiler was used to obtain data of the density stratification which can also be assumed to be quite reliable. Profiles of the turbulence dissipation rate as well as horizontal velocity fluctuations and thermal microstructures were measured with a microstructure (MST) profiler (Prandke (2005)) equipped with a pair of airfoil shear probes and a fast microthermistor.

From the profiles of velocities and density the bulk quantities of the current were obtained with (7.1) − (7.4) where a logarithmic velocity profile with an equivalent sand roughness of $k_s = 0.3$ m has been assumed to complete the missing velocities at the bottom. The comparably high bottom roughness is a result of the estimation of the bottom friction from the turbulence dissipation rate according to

$$\tau_b = \rho\left(\kappa z \varepsilon\right)^{2/3}, \tag{7.69}$$

where $\kappa \approx 0.41$ is the von Kármán constant (cf. eq. (3.145) in chapter 3.8) and z is the distance from the bottom. With (7.70) the bottom drag coefficient was determined to be $C_d = 0.0037 \pm 0.0015$ which is rather high as extensively discussed by Arneborg et al. (2007).

The entrainment rate was calculated from the bulk speed of the current U_s and the entrainment velocity w_E given by (7.58) where the bulk buoyancy production G_b is given by (7.30). The turbulent diffusion needed to evaluate G_b was estimated from the measured turbulent dissipation rate by the model of Osborn (1980):

$$\nu_t' = 0.2\frac{\varepsilon}{N^2}\,. \tag{7.70}$$

However, as argued by Arneborg et al. (2007) relation (7.70) is only valid within the interface such that the buoyancy flux below was assumed to linearly decrease towards the bottom implying a well mixed bottom layer with a depth independent rate of density change (cf. eq. (7.14)). Using this approach the bulk buoyancy production and the resulting entrainment rates were found to significantly change over the whole 19 hour observation period although the Froude number was almost constant. This is in contradiction to any theory and observation mentioned above and could not ad hoc be explained yet. For a comparison with numerical simulations it seems therefore advisable and was also done by Arneborg et al. (2007) to use the complete 19 hour average where at least short term fluctuations are smoothed out.

Table 7.2 summarizes these 19 hour averages of the bulk parameters, where the values of depth, velocity, bottom drag coefficient, Froude number, and entrainment rate have been taken from Arneborg et al. (2007). The values for reduced gravity and Ekman number have been computed from (7.48) and (7.50), respectively and slightly differ from the original paper. However, compared to the uncertainties in the measurements the difference is negligibly small and the values given here have only been chosen to be consistent with the present theory.

D [m]	U_s [m/s]	C_d	g' [m/s²]	Fr	K	E
11.6	0.49	0.0037	0.071	0.54	1.3	$6.6\cdot10^{-5}$

Table 7.2: Bulk parameters for a density current north of Kriegers Flak. 19 hour average of data observed from February 6 – 7, 2004.

Numerical simulations

As can be seen from the depth contours in Figure 7.11 at the measurement station the density current is restricted to a quite narrow channel and it can be expected that three dimensional effects which are not regarded in the one dimensional model will affect the current dynamics. Indeed, as shown by Burchard et al. (2005) the current interface slopes towards Kriegers Flak with the core of salinity being displaced towards the north. Furthermore the channel is widening downstream of the station which for subcritical flow conditions could lead to a deceleration of the current as argued by Arneborg et al. (2007). Hence, the one-dimensional model used here is actually not applicable to this case where the current is influenced in lateral and transverse direction by the varying topography. However, the results presented by Arneborg et al. (2007) encourage the use of such a simple model if the slope of the interface is assumed to be parallel to the bottom slope.

With the bottom drag coefficient and the Froude number given the slope in streamwise direction can be obtained from (7.49) which yields α_m = 1.08 ‰ in accordance with the value used by Arneborg et al. (2007). From the Froude number and Ekman number the total slope can be obtained from (7.52) and is tan α = 1.36 ‰ such that the slope in cross-stream direction must be 0.83 ‰ which is slightly more than the values used by Arneborg et al. (2007).

The numerical grid used for the present simulation is basically the same like that used in the previous sections with the density and velocity gradients within the interface resolved by Δz = 0.2 m. To realize the high observed bottom drag in the numerical simulation the bottom roughness has been chosen to be k_s = 0.40 m which seems to be unrealistically large and will be discussed in more detail later. Anyway, for numerical reasons the grid at the bottom had to be modified such that the distance of the closest grid point to the wall is in the range of the bottom roughness. As before the simulation was started with box profiles for salinity and velocity. In order to give the current enough time to stabilize the initial depth was chosen to be D = 5 m with a reduced gravity of $g' = 0.164$ m/s² corresponding to the observed total buoyancy of $g'D = 0.82$ m²/s².

The simulation was run for 7 days and after about 55.5 hours the current had reached the destination depth of 11.6 m. A comparison of the observed bulk parameters given in Table 7.2 with the results of the numerical simulation and the values predicted by the depth integrated theory is shown in Table 7.3.

	U_s [m/s]	C_d	Fr	K	E
observed	0.49	0.0037	0.54	1.3	$6.6 \cdot 10^{-5}$
simulation	0.48	0.0035	0.53	1.2	$6.0 \cdot 10^{-5}$
theory	0.49	0.0037	0.54	1.3	$7.1 \cdot 10^{-5}$

Table 7.3: Comparison of observed and modeled bulk parameters for a density current with $D = 11.6$ m and $g' = 0.071$.

Except for a slightly higher entrainment rate the theory is in perfect agreement with the observed data. Although the comparison of the numerical model with the theory in the previous section showed almost perfect agreement, the results here are slightly different. The main reason for this deviation lies in the comparably large bottom roughness that had to be applied in order to realize the observed high bottom shear stress and the resulting entrainment rates. With increasing bottom roughness the numerically computed bottom drag coefficient becomes less reliable as can be seen from the slightly lower simulated value in Table 7.3.

In fact the bottom roughness had been chosen in order to obtain the best agreement with the observed speed and Froude number of the current and the theoretical Froude Ekman number relation and entrainment rates. A comparison of the latter is shown in Figure 7.12 from which it is apparent that the numerical model needs some time before the results are in more or less perfect agreement with the theory. For $Fr > 0.52$ there are still some deviations explaining the different values given in Table 7.3. Interestingly, for $Fr = 0.54$ the numerically predicted entrainment rate corresponds exactly to the observed value of $E = 6.6 \cdot 10^{-5}$, which, however, might just be regarded as a coincident as the current speed and buoyancy are slightly different. Anyway, disregarding the slight model inconsistency in the bottom drag the overall agreement between the simulated and observed bulk parameters is very convincing and is even better than the results presented by Arneborg et al. (2007).

However, concerning the uncertainties in the measurements and assumptions that have been made for the present simulation a too detailed discussion about marginal deviations seems to be very academic, anyway.

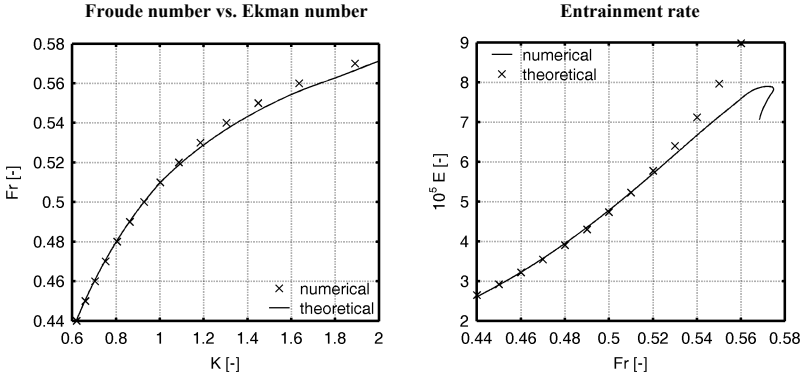

Figure 7.12: Comparison between numerical and theoretical results for Froude Ekman number relation and entrainment rate vs. Froude number.

For the sake of completeness Figure 7.13 shows vertical profiles of density anomaly, gradient Richardson number, velocities in streamwise and cross-stream direction, turbulence dissipation rate and buoyancy production over the lower 30 m of the total water depth. The thick lines represent the measurements averaged over the whole 19 hour period and the numerical results shown by the thin lines correspond to the instant when the current depth has reached the target value of $D = 11.6$ m. The present results are very comparable to those presented by Arneborg et al. (2007) and the following discussion therefore basically follows the same arguments.

The modeled density profile is in good agreement with the measurements and also the streamwise velocity profile conforms quite well with the observation although the numerical predicted maximum is slightly higher and the shear in the interface is somewhat larger. The modeled cross-stream velocity shows the typical form expected from Ekman theory while the observed profile has even a contrary shape. This can be attributed to the real topography which forces the current into a narrow channel, an effect that is disregarded in the one-dimensional numerical model.

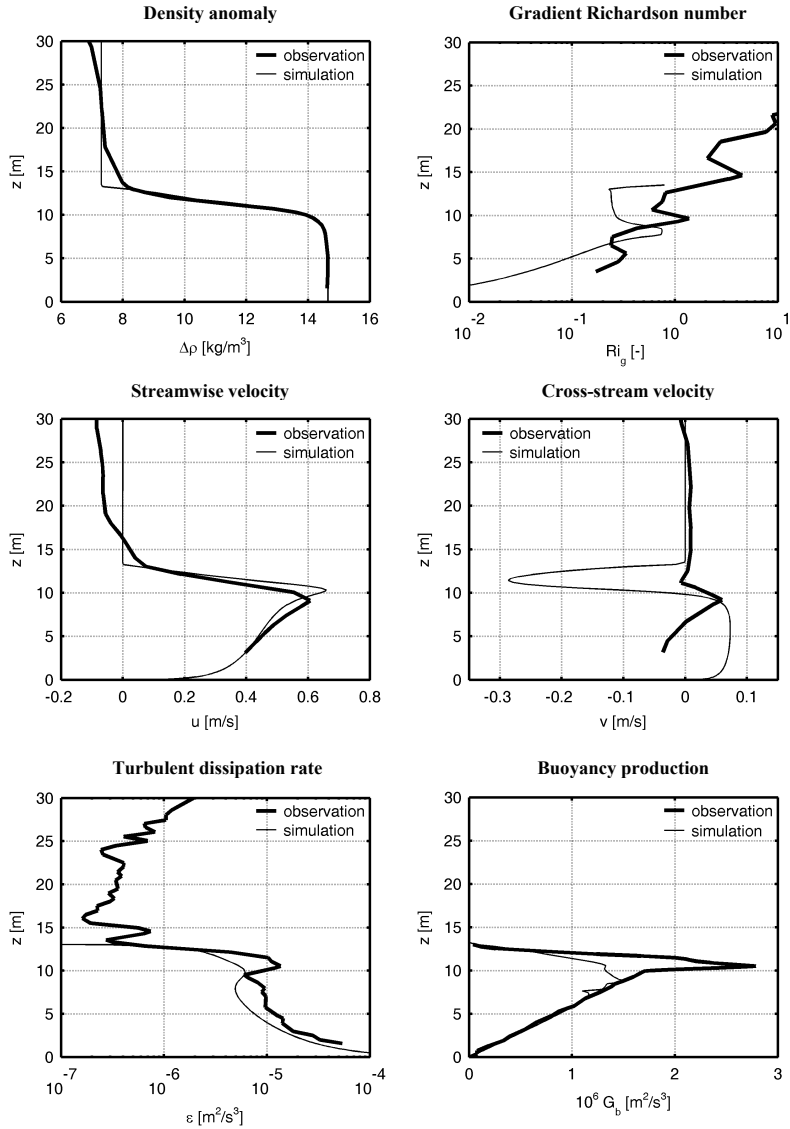

Figure 7.13: Vertical profiles of D, Ri_g, u, v, ε and G_b. Field observations compared to numerical simulation results with tan α = 1.36 ‰.

The gradient Richardson number shows similar features in the simulation and the observation with an increase from zero at the bottom to a maximum value below the interface and a constant local minimum within the interface. The numerical model predicts the desired stationary value of $Ri_g = 0.25$ while the observed value is about $Ri_g \approx 0.7$ which is significantly larger than the expected critical value and argued by Arneborg et al. (2007) with two points. First, it might be an effect of the vertical resolution of the velocity profile which is probably too coarse. Second, it could be an effect of intermittency with temporary very high values which are smeared out by the averaging process and are generally not regarded in the numerical model.

The observed and modeled turbulent dissipation rates are also quite similar and show the expected steep increase towards the bottom, a local minimum where the gradient Richardson is at maximum and a further increase to a local maximum within the interface. However, while the quantitative agreement is quite satisfying in the bottom boundary layer with increasing distance from the bottom the measurements show significantly larger values than the numerical model. As pointed out by Arneborg et al. (2007) there is a significant uncertainty in the measured dissipation rate profile and if the last hours are excluded from the average there would be a perfect correspondence between simulation and observation.

The turbulent dissipation rate can be regarded as a proxy for the production of turbulent kinetic energy and buoyancy. The profiles of the latter are compared in the lower right panel and indeed show the same pattern with a perfect agreement near the bottom and lower modeled values within the interface. Compared to the turbulent dissipation rate the absolute differences are much smaller and more locally restricted to the region of the interface. This explains the fair agreement between the observed and simulated entrainment rates rate which depend on the depth integrated bulk buoyancy production as defined by (7.58).

This also shows that a large part of the total entrainment is governed by the bottom induced turbulence, at least as long as the Ekman number is larger than 1 as in the present case. Therefore it might be interesting to have a final look at the influence of bottom drag and bottom slope on the dynamics and entrainment rates of a density current. For this purpose four additional scenarios based on the above presented

setup have been investigated. The chosen bottom slope and the theoretical and actual bottom drag coefficients (as discussed above) are summarized in Table 7.4.

	case 1	**case 1a**	**case 1b**	**case 2**	**case 3**
tan α [‰]	1.36	1.36	1.36	0.74	1.84
$C_{d,\,\text{theoretical}}$	$3.7\cdot10^{-3}$	$2.0\cdot10^{-3}$	$5.0\cdot10^{-3}$	$2.0\cdot10^{-3}$	$5.0\cdot10^{-3}$
$C_{d,\,\text{numerical}}$	$3.5\cdot10^{-3}$	$2.0\cdot10^{-3}$	$4.6\cdot10^{-3}$	$2.0\cdot10^{-3}$	$4.6\cdot10^{-3}$

Table 7.4: Definition of the five test cases to investigate the influence of bottom slope and bottom drag on the dynamics of a density current.

Case 1 represents the above analyzed scenario and cases 1a and 1b have the same bottom slope but different bottom friction. In cases 2 and 3 both bottom slope and bottom drag coefficient have been changed but their ratio ($\tan\alpha/C_d$) is held constant in order to keep a fixed relation between Froude and Ekman number (cf. eq. (7.52), assuming $\sin\alpha \approx \tan\alpha$). A first result concerning the performance of the numerical model can already be deduced from Table 7.4. For small bottom friction ($k_s < 0.1$ m) the numerically predicted bottom drag exactly matches the theory while it is smaller for larger bottom roughness as already found above. The deviations increase with increasing bottom roughness but seem to be independent of the bottom slope (current speed) at least in the range chosen here.

In order to cross-check with the results above the present simulations are evaluated when the current depth reached $D = 11.6$ m and the total buoyancy is $g' = 0.071$ m/s^2, accordingly. The respective vertical profiles of density anomaly, gradient Richardson number, velocities in streamwise and cross-stream direction, turbulence dissipation rate and buoyancy production are shown in Figure 7.14. Apparently, on a constant slope (cases 1, 1a and 1b) the bottom drag coefficient has only marginally influence on the depth structure of the current. As might have been expected from the momentum balance (7.46) the major differences are found in the streamwise velocity profiles which directly depend on the friction at the bottom. Although the streamwise velocities significantly differ this has obviously no effect on all other quantities as their profiles are almost identical.

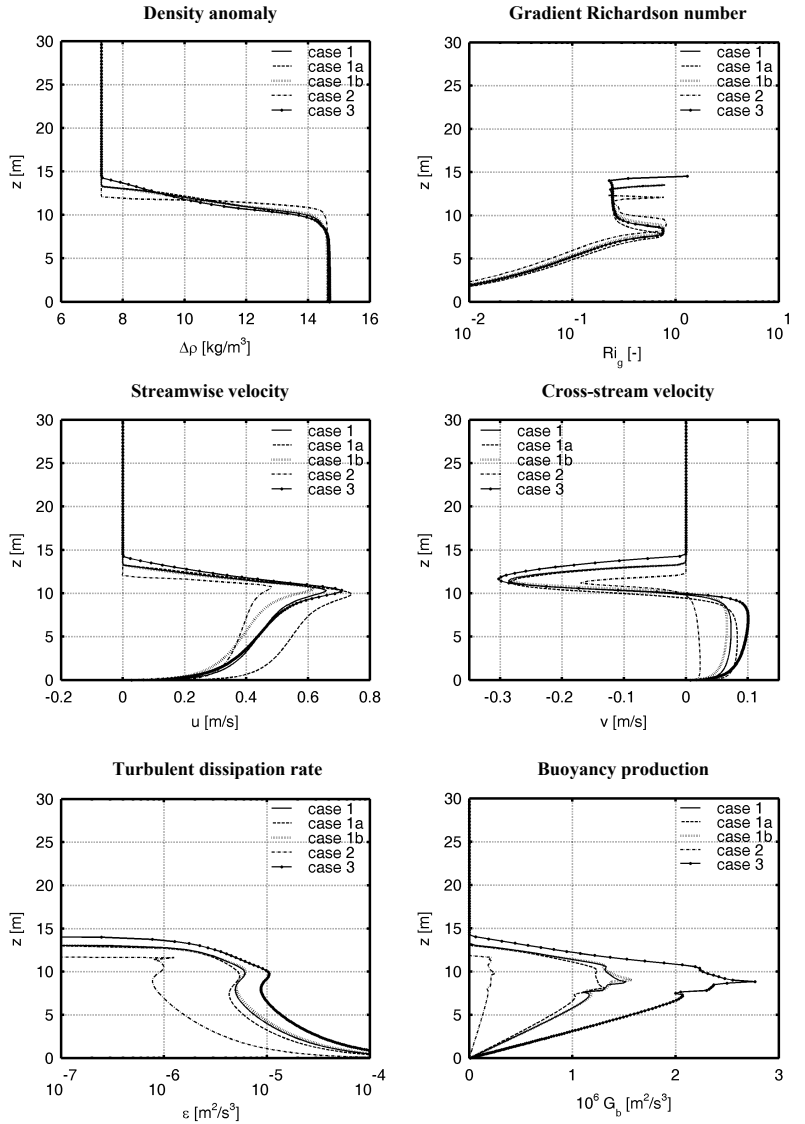

Figure 7.14: Vertical profiles of $\Delta\rho$, Ri_g, u, v, ε and G_b. Comparison of the five test cases to investigate influence of bottom drag and bottom slope.

However, actually this agreement is just a coincidence as the three different cases behave quite similar for about 5 days of entrainment and the destination depth is reached after about 2 days already. The profiles of the cross-stream velocity and the turbulent quantities yet indicate what will happen if the currents further evolve. Due to the Coriolis forces the different streamwise velocity profiles will induce different cross-stream velocities and due to the different drag at the bottom the turbulent dissipation rate and buoyancy production will be reduced and augmented, respectively. However, the differences are comparably small and the profiles for density and gradient Richardson number remain identical throughout indicating that the interface behaves proportional to the bottom slope rather than bottom drag.

This is supported by cases 2 and 3 which have the same bottom drag coefficients like cases 1a and 1b, respectively, but different slopes. A comparison of the profiles of density and gradient Richardson number shows that the thickness of the interface decreases with decreasing bottom slope. Although the profiles of streamwise velocity for case 1 and case 3 are almost identical the turbulent dissipation rates and the resulting buoyancy production significantly differ with much higher values on the steeper slope. On the other hand, due to the shallow slope in case 2 the velocity is generally smaller, reducing the turbulent dissipation rate and buoyancy production and in consequence leading to very small entrainment rates. It can therefore be concluded that the bottom drag has a certain effect on the entrainment rates but the influence of the bottom slope (or at least a combination of both) seems to be much more significant. This becomes clearer from the bulk parameters given in Table 7.5.

	case 1	**case 1a**	**case 1b**	**case 2**	**case 3**
Fr	0.53	0.65	0.47	0.42	0.55
K	1.19	0.82	1.42	0.55	1.68
U_s	0.48	0.58	0.43	0.38	0.50
E	$6.0 \cdot 10^{-5}$	$4.4 \cdot 10^{-5}$	$6.8 \cdot 10^{-5}$	$1.1 \cdot 10^{-5}$	$9.9 \cdot 10^{-5}$

Table 7.5: Bulk parameters for the five test cases when the current depth reached $D = 11.6$ m and $g' = 0.071$.

A sole dependence of the entrainment rate on the Froude number as suggested by some entrainment laws is clearly not given, at least not for the subcritical flow conditions regarded here. A much better approach is to consider the bottom drag coefficient as e.g. in the law of Stigebrandt (1987) or the present law given by (7.62). However, as discussed in section 7.1.5 the dependence of the bulk flux Richardson number remains which can be expressed by (7.64) introducing the Ekman number. This dependence is clearly justified through Table 7.5 and can be interpreted physically by the assumption that for $K < 1$ the bottom induced turbulence will not reach the interface and overall mixing must be small. On the other hand with increasing Ekman numbers $K > 1$ bottom turbulence spreads over the current, increasing the interface thickness and entrainment rates.

Finally, Figure 7.15 shows the entrainment rate versus Froude number comparing the results of the five test cases to measurements in the field and laboratory. In accordance to Figure 7.10 the measurements of Cenedese et al. (2004) and Baringer & Price (1997) have been included for reference and are represented by the open circles and triangles, respectively. The other symbols correspond to the numerical results and the lines show the theoretical solutions of the present theory. They have been added in order to extend the Froude number range and to once more approve the agreement of the numerical model with the depth integrated theory.

Due to the different bottom slopes and drag coefficients there is a remarkable spread in the numerical data. Although most of the measured entrainment rates were found for higher Froude numbers the present numerical results seem to be a reasonable extension of the observed entrainment rates to lower Froude numbers. Comparing cases 1, 1a and 1b it can be seen that for a constant bottom slope the Froude number decreases and entrainment rates increase with increasing bottom drag. This might have been expected by intuition as a larger bottom shear stress retards the current while the Ekman number is augmented. Furthermore, it is analytically supported by the simplified entrainment law (7.70) which for a constant slope predicts an increase of entrainment by $C_d^{1.6}$. On the other hand for constant bottom drag (7.70) suggests a decrease of entrainment with increasing bottom slope also in accordance with the simulations comparing cases 1a and 2 or cases 1b and 3 at the same Froude number.

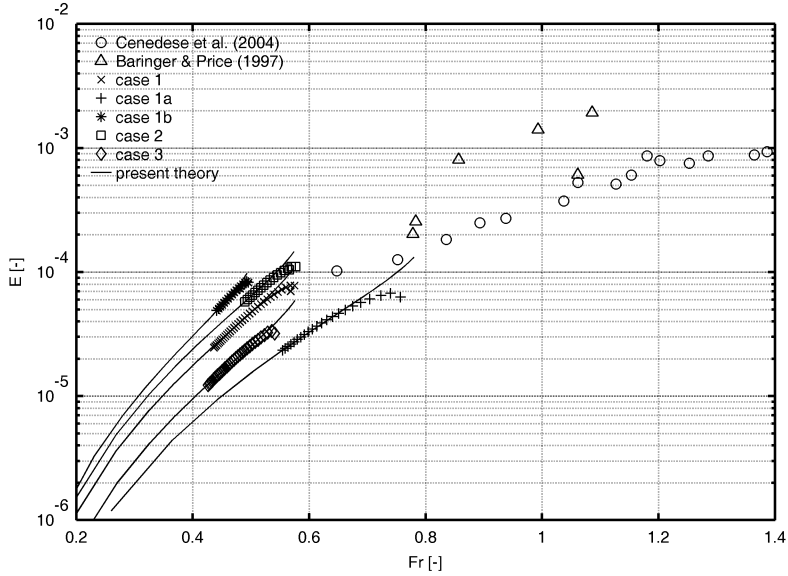

Figure 7.15: Entrainment rate versus Froude number. Results of the five test cases compared to different measurements.

The theoretical upper limit of the Froude number as given by (7.53) is also found in the simulation data. The slightly higher values for cases 1 and 3 compared to case 2 reflect the numerical underestimation of the bottom drag coefficient for large bottom roughness. To arrive in the higher Froude number range of the measurements the ratio of bottom slope and bottom drag coefficient must be in the order of 1 which is much higher than the values used in the present example. However, as indicated by the results of case 1a and suggested by the simplified entrainment law (7.70) the high entrainment rates of the measurements imply large bottom drag coefficients. Indeed, for the Mediterranean outflow where the mean bottom slope can be estimated by $\tan\alpha \approx 6$ ‰, Baringer & Price (1997) found the bottom drag coefficient to be in the range of $2\cdot10^{-3} < C_d < 12\cdot10^{-3}$. Even though the large spread poses some questions on this estimate and at first these values seem to be unrealistically huge, they are definitely supported by the present theory.

However, as shown by the friction law of Darcy/Weisbach (7.33) and (7.32) such high bottom drag coefficients require in fact unrealistically high 'physical' bottom roughness which consequently led to the numerical problems mentioned above. Hence, much more the question arises whether the bottom drag coefficient should be interpreted as a result of the bottom roughness alone or if it should more generally be regarded as a proxy for the turbulence in the bottom boundary layer. What indeed speaks in favor of the latter is that in a density current convective overturns may appear in the bottom boundary layer (Moum et al. 2004) which induce additional turbulence. This could explain the high dissipation rates found in the current north of Kriegers Flak as argued by Arneborg et al. (2007) and furthermore it would be a good argumentation for the high bottom drag coefficients estimated by Baringer & Price (1997). In any case it remains still an assumption that has to be investigated more thoroughly in future work.

7.2.5 Neglect of Coriolis forces

Though the present numerical model has now been extensively validated against theory and field data all the cases regarded so far were influenced by earth rotation and the effect of the resulting Coriolis forces. This is justified in so far as the density currents in the Baltic Sea which are of major interest here underlie these effects in fact. However, in view of the forthcoming fundamental investigation of the influence of a circular cylinder on a density current it might be desirable to start with a more basic configuration without the effect of secondary currents induced by a rotating frame of reference.

The next logical step is therefore to neglect the Coriolis forces and to regard purely two dimensional currents flowing straight down the hill. However, it turned out that it is not possible to achieve reasonable results with the one-dimensional model if the Coriolis factor is too small or even zero at the limit. The present section is therefore dedicated to a short analysis of the cause and effect of the rather unphysical behavior of the numerical model. For this purpose the simulations presented in section 7.2.1 have been repeated but with the Coriolis terms switched off.

Figure 7.16 shows depth profiles of density difference, velocity, gradient Richardson number, turbulence production, turbulent diffusion and buoyancy production 5, 10 and 15 hours after the beginning of the simulation. From the maximum values of density it is seen that obviously some amount of less saline water is entrained into the bottom layer as the density difference between the current and the ambient fluid is constantly reduced. However, compared to the profiles after about 24 hours shown in Figure 7.5 the reduction is much smaller which can be explained by the strange form of the interface found here. Apparently, the core of the current is more or less unchanged while the region above it is extensively mixed. From the profiles of velocity and gradient Richardson number it can be deduced that the mixed region is constantly growing and turbulence is in equilibrium (Ri_g = 0.25). However, even without Coriolis forces it should be expected that due to the stabilizing effect of stratification the interface will reach a quasi-stationary state just as those shown in Figure 7.5. In the present case the upper part of the current behaves more like a neutral jet and there is evidence that the interaction of the mean stratified and turbulent flow fields is unbalanced.

Indeed the unphysical model behavior arises due to a wrong prediction of turbulence production and is an inherent problem for all models based on the turbulent viscosity/diffusion assumption. For these models the production of turbulent kinetic energy is proportional to the shear of the mean flow field (cf. eq. (3.49)) and if the current is purely two-dimensional there is no production in height of the velocity maximum as the only gradient in the flow field vanishes. The minimal turbulence production inevitably yields a minimum of turbulent viscosity and diffusion which in turn precludes mixing of momentum and salinity and consequently results in the unphysical peak in the velocity profile and the steep gradient in the density profile. Due to the latter the core of the current is somewhat protected against entrainment while the upper part becomes more susceptible to mixing. The currents with Coriolis forcing above show a similar behavior during the adjustment of the profiles from the initial box shape, but the maxima of streamwise and cross-stream velocity in the balanced state are found in different heights limiting the minimum of turbulence production to finite values. Thus there is no unphysical suppression of mixing, the profiles stabilize and the numerical model provides reasonable results.

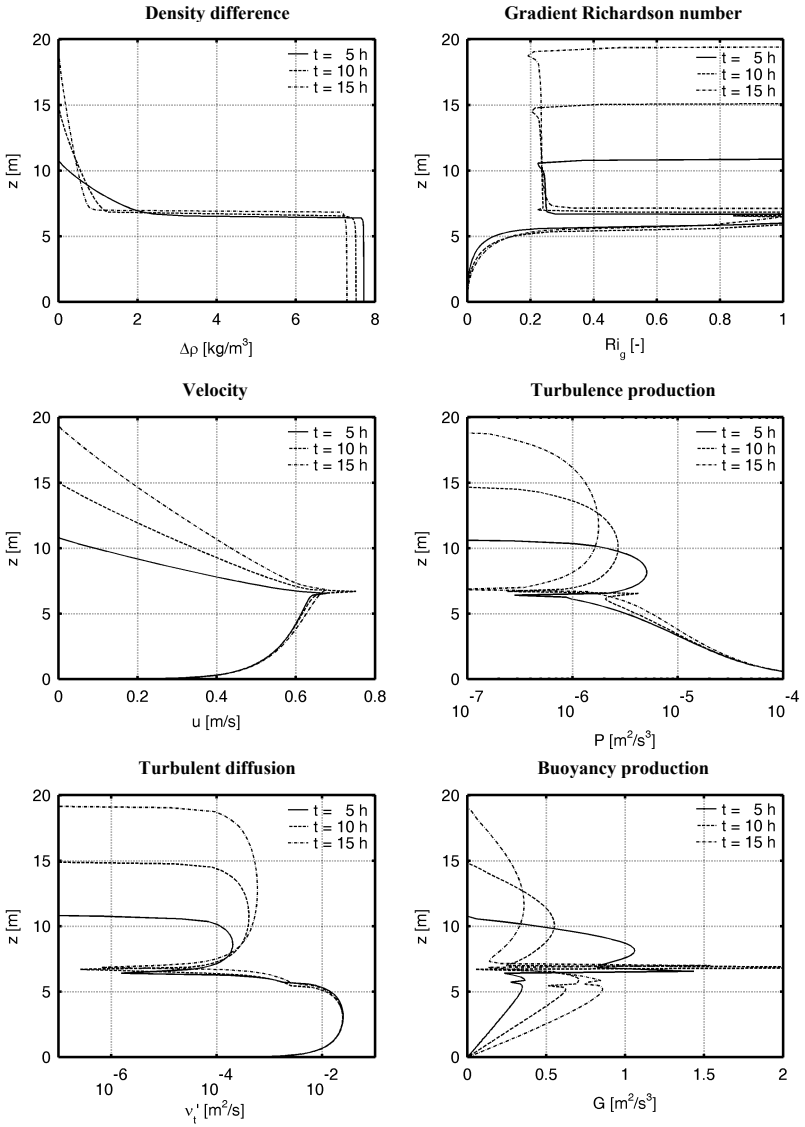

Figure 7.16: Simulation results for a density current without Coriolis forces. Vertical profiles of relevant quantities at different times.

One might argue that in a real current there is also a zero gradient in the mean velocity profile at the maximum and production of turbulence should vanish at this point leading to similar phenomena like above. However, while the first can be assumed to be more or less correct the conclusion is definitely wrong as there is evidence for currents without the effect of rotation to be stable. The reason is found in the nature of turbulence which is always a three dimensional process and in the case of stratified flows is not only produced by shear but also by breaking of internal waves. Simulations based on simple two-equation turbulence models like the one above must inevitably fail as the relevant processes are neither resolved nor adequately incorporated into the model assumptions.

One way out of this dilemma could be the use of another turbulence closure which is not based on the turbulent viscosity/diffusivity assumption. LES for instance might be an excellent candidate as a great part of the turbulent scales are resolved by the numerical grid and there is justified hope that this will solve the problem of zero production at the velocity maximum. However, as already discussed before for the simulation of natural currents LES is still computationally too expensive and is limited to laboratory scales with smaller dimensions and lower Reynolds numbers.

Another way to solve the problem could be found in a modification of the turbulence production term in analogy to the modification suggested by Kato & Launder (1993) for the flow around bluff bodies (cf. chapter 5.3) or the splitting of the buoyancy production term into the ordinary part and a portion going into internal waves as proposed by Baumert & Peters (2004). This approach however, was not further followed as it is supposed that the discrepancy of the model used for the present work only applies to undisturbed density currents which are of minor interest here. If the current is disturbed by a cylinder or any other obstacle additional shear will be induced and it can be assumed that the inherent drawback of the model is negligible in this case. Anyway, the singularity in turbulence production in an undisturbed density current without secondary flows puts a great challenge onto turbulence models based on the turbulent viscosity/diffusivity assumption and remains an open task for further research.

7.3 2-D/3-D modeling of natural density currents

The one-dimensional setup used in the preceding chapter was ideally suited to validate the numerical model for the simulation of undisturbed density currents. However, the influence of a circular cylinder on these currents can only be simulated in a fully three-dimensional domain and it should first be shown that the model also works for this configuration. Furthermore it is hoped that the discrepancies of the applied two-equation turbulence models for simulating purely two-dimensional currents without Coriolis forces are tolerable in a finite channel with boundary conditions approximately matching the expected properties.

In the one-dimensional model above no real boundary conditions in the horizontal domain exist and assuming the surface boundary conditions to be unimportant the solution of the problem only depends on the bottom boundary and initial conditions, as well as global settings like bottom slope and system rotation. In a two- or three-dimensional channel, however, streamwise inflow and outflow conditions have to be applied which can have a significant effect on the final result. In the following simulations it has been tried to keep the along channel conditions as stationary and steady as possible. The corresponding inflow and outflow conditions will be discussed more detailed below.

7.3.1 Model setup

For the following tests a channel with a total length of L = 1000 m and a total depth of H = 40 m is regarded. As indicated by the title of this chapter the final goal is to show the validity of the model for fully three-dimensional simulations. With the chosen turbulence models here, however, there will be no lateral variations as long as the global conditions remain constant which is assumed here for simplicity. Hence, it is sufficient to demonstrate the model behavior for a two-dimensional model with only one grid cell in lateral direction as the results in the fully three-dimensional case are identical.

The numerical grid is similar to that used for the one-dimensional model above (cf. left panel in Figure 7.3) with a fine resolution near the bottom to resolve the

boundary layer, a constant resolution between 5 m < z < 15 m to account for the gradients in the interface and a coarser resolution towards the top where the stagnant ambient fluid has no specific requirements. Even if the computational requirements for the two-dimensional model here can still be easily handled, the grid has been tried to be chosen as coarse as possible in view of the much higher computational demands in the forthcoming fully three dimensional simulations. By several test runs it was found that for the present simulations a horizontal resolution of $dx = 5$ m and a vertical resolution of the interface of $dz = 0.5$ m is necessary and sufficient.

As the simulations here serve as a first test for the fully three-dimensional simulations with a circular cylinder included it is useful to investigate boundary and global conditions that will also be used in the next chapter. In order to more or less reflect realistic conditions found in the Arkona basin the current depth is chosen to be $D \approx 10$ m with a salinity difference of $\Delta S \approx 10$ PSU, a target current speed of about $U \approx 0.5$ m/s and a resulting Froude number of $Fr \approx 0.57$. The bottom slope is $\alpha = 1.06$ ‰ and the bottom roughness has been set to $k_s = 0.025$ m which is rather smooth compared to the discussion in the preceding chapter. However, at least it is supposed to reflect the natural roughness quite well and indeed is numerically more reliable as shown above.

The inflow boundary is made up of Dirichlet conditions with fixed profiles for velocity, salinity and turbulent quantities making this boundary reflective. At the outflow boundary the current should leave the domain without reflection and velocity, salinity and turbulent quantities are treated by Neumann conditions. For numerical reasons a Neumann condition can not be used for pressure which has to be prescribed by a fixed profile. Assuming that the current depth does not change significantly over the channel length the excess pressure profile resulting from the current depth at the inlet has been used. At the top boundary also a pressure condition is applied but with zero excess pressure over the complete channel length. This allows fluid to enter the computational domain through the top in order to supply the mass deficit in the upper stagnant layer resulting from the entrainment of ambient fluid into the current. The rigid lid condition chosen for the one-dimensional model above could be applied as well but then the overall mass balance requires fluid to enter through the outflow boundary inducing a backflow current in

the upper ambient fluid. Although the resulting velocities are very small and there is almost no difference in the overall results the pressure boundary condition has been chosen as it is felt that it better reflects the natural conditions.

The simulations could either be started from scratch or with velocity, salinity, and turbulent fields approximately matching the final conditions. In both cases the current will need some time to adjust to the stationary state. However, with the latter choice the initial settling time can be significantly reduced and therefore the initial conditions are adopted from the inflow boundary.

7.3.2 Density currents in a channel with Coriolis forces

Like for the one-dimensional model above it is useful to start with a channel in a rotating frame of reference where the current underlies the effect of Coriolis forces. In this case the boundary (and initial) conditions can be gained from a preliminary run of the one-dimensional model which is evaluated when the current reached the target depth of 10 m. The lower 20 m of the corresponding vertical profiles for streamwise and cross-stream velocity, salinity, turbulent kinetic energy, specific dissipation rate and excess pressure are shown in Figure 7.17.

Boundary conditions

All profiles show the expected patterns that have been discussed in detail above. The pressure profile which was not regarded up to now also shows the expected behavior and linearly increases towards the bottom with the maximum value given by the hydrostatic balance $p_{bot} = \rho_0 \cdot g' \cdot D \approx 770$ N/m². Though within the interface the density difference and by that g′ decrease leading to a reduced gradient in the excess pressure observed between 8 m < z < 11 m, a pure linear functional relation could be assumed to be a good approximation. From the salinity profile the thickness of the interface can be estimated to be about 3 m justifying the chosen vertical resolution of the numerical grid with which the interface is resolved by 6 grid cells. The deflection of the current to the right is about 48 ° and in order to apply the velocities given in the upper left panel with zero volume flux in cross-stream direction the

channel is aligned in main flow direction such that the bottom slopes in streamwise and cross-stream direction are $\alpha_m = 0.70$ ‰ and $\alpha_n = 0.78$ ‰, respectively.

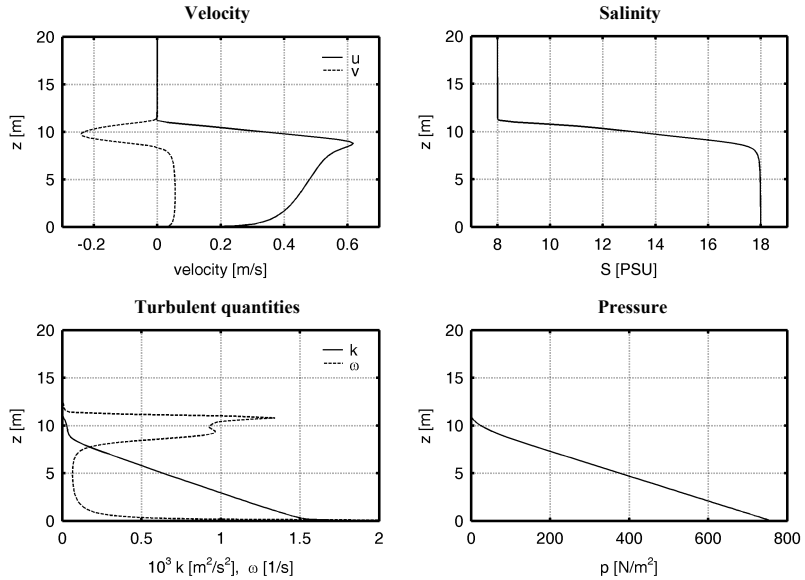

Figure 7.17: Boundary conditions for a density current in a channel with Coriolis forces.

Results

The entrainment rate in the present case found from the one-dimensional simulation and suggested by the depth integrated theory is about $E \approx 3.2 \cdot 10^{-5}$ with an entrainment velocity being only about half of that. The variations of the current along the channel can therefore assumed to be small and the vertical profiles given in Figure 7.17 which are imposed as boundary conditions indeed remain quasi identical over the whole length of the channel and are dispensable to be shown. Further support for the steadiness of the current is given by the along channel profiles of current depth, Froude number, volume flux and entrainment rate displayed in Figure 7.18.

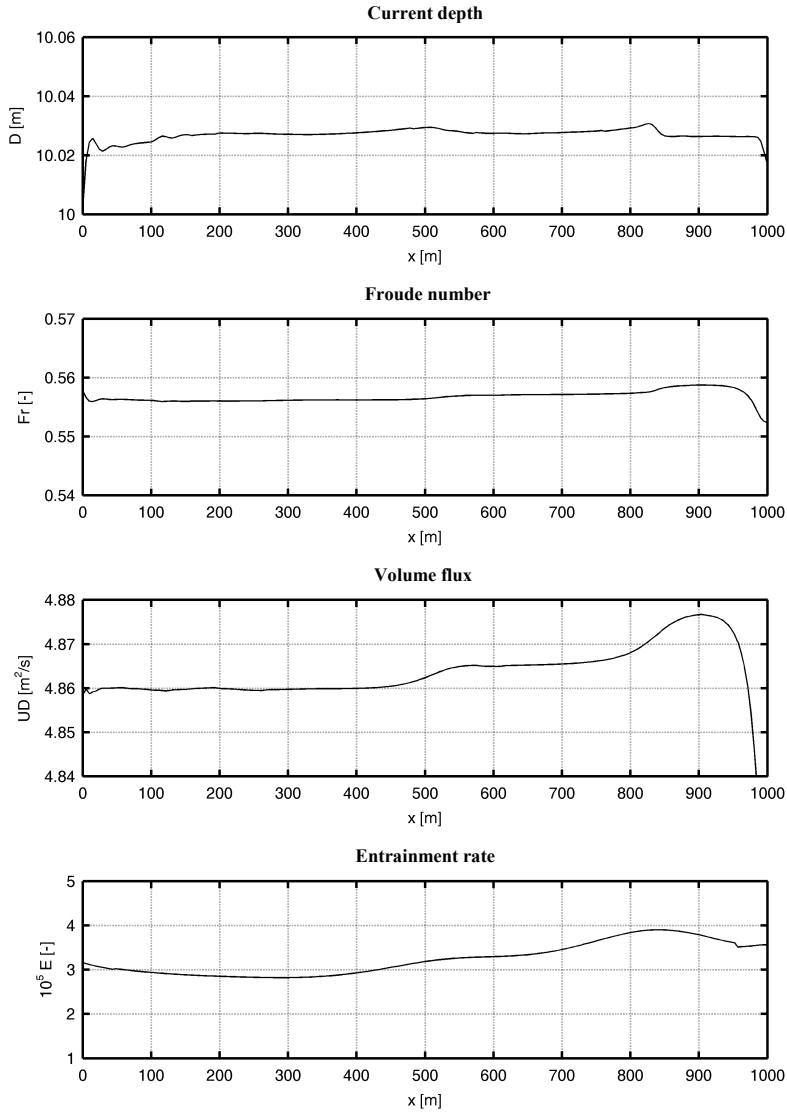

Figure 7.18: Along channel profiles of current depth, Froude number, volume flux and entrainment rate for a density current with Coriolis forces.

As expected, the current depth and Froude number remain constant over almost the complete channel length with the strongest variations found at the inflow and outflow boundaries. The influence of the outflow boundary is most apparent from the volume flux which significantly decreases about 50 m in front of the end of the channel. This intense variation stems from the top pressure boundary condition that produces a short cut current and sucks water from the outflow boundary. Though the resulting velocities are actually quite small they remarkably alter the depth integrated volume flux. However, this erroneous effect on the current is restricted to a narrow region at the end of the channel and the overall results seem to be reasonable if the inflow and outflow area, say the first and last 50 m of the channel, are disregarded.

The entrainment rate shown in the lower panel has been evaluated from the bulk buoyancy production as given by (7.58) and is in the expected order of magnitude of about $E \approx 3 \cdot 10^{-5}$ implying an entrainment velocity of $w_E \approx 1.5 \cdot 10^{-5}$ m/s. In principle the latter could also be determined from the volume balance (7.6) which reduces in the present stationary streamwise oriented case to

$$w_E = \frac{\mathrm{d}UD}{\mathrm{d}x} . \tag{7.71}$$

The expected increase of volume flux over the whole channel length of 1000 m should therefore be about $\mathrm{d}UD = 1.5 \cdot 10^{-5}$ m/s · 1000 m = 0.015 m²/s, which is relatively small but can indeed be estimated from Figure 7.18. However, due to these really small values a local evaluation of (7.71) requires a very precise determination of the volume flux which is notably precluded from the present data as can be seen from the along channel profile shown in the second panel from below. Anyway, the overall balances are obviously satisfied and a prediction of the local entrainment rate can be reliably gained from (7.58).

Without doubt the numerical model can be regarded as validated for the simulation of an undisturbed density current in a channel with Coriolis forces and is clearly suited for the investigation of the influence of a circular cylinder on these currents in the next chapter. However, as already mentioned above for an analysis of the

fundamental effects it is desirable to start with a simplified configuration and disregard the secondary currents in cross-stream direction induced by a rotating frame of reference. Therefore, first the model performance for simulating density currents in a channel without Coriolis forces will be demonstrated in the next section.

7.3.3 Density currents in a channel without Coriolis forces

As shown in chapter 7.2.5 the simulation of a density current without Coriolis forces using two-equation turbulence models, like here, suffers from an underestimation of turbulence production at the velocity maximum. If the current is left to freely evolve as in the one-dimensional model above this model failure will produce unphysical results and a prediction of the current dynamics and entrainment is actually not possible. In a finite channel the singularity in turbulence production is still present but its effect is less severe since the current dynamics are also governed by the inflow and outflow boundary conditions like in the case with Coriolis forces above. However, unlike in the case above, here it is unfeasible to generate boundary conditions by a preliminary one-dimensional simulation. Thus, these have rather to be provided by theoretical considerations.

Boundary conditions

The mean velocity and salinity (density) profiles within the interface are estimated to be of hyperbolic shape as suggested by experimental evidence (e.g. Thorpe (1987)) and assumed in many other numerical simulations on stratified shear layers (e.g. Caulfield & Peltier (1994, 2000), Cortesi et al. (1998, 1999)). In terms of the local vertical coordinate z' the profiles for velocity and salinity read

$$u(z') = u_{\min} + \frac{1}{2}\left(\tanh\left(-3\frac{2z'}{\delta}\right)/\tanh(3)+1\right)\Delta u \qquad \text{for} \quad -\frac{\delta}{2} < z' < \frac{\delta}{2}, \tag{7.72}$$

$$S(z') = S_{\min} + \frac{1}{2}\left(\tanh\left(-3\frac{2z'}{\delta}\right)/\tanh(3)+1\right)\Delta S \qquad \text{for} \quad -\frac{\delta}{2} < z' < \frac{\delta}{2}, \tag{7.73}$$

where δ is the thickness of the interface given by

$$\delta = 3Ri_{st}\frac{\rho_0 \Delta u^2}{g\Delta\rho}\,. \tag{7.74}$$

Below the interface from z = 0 to z = $D - \delta/2$ salinity is assumed to be constant and a logarithmic velocity profile as described in chapter 3.8 is applied. While the salinity difference ΔS is explicitly given the velocity difference Δu must be found in an iterative process until the depth integrated velocity corresponds to the target value.

Turbulent kinetic energy and specific dissipation rate are also determined from the definitions made for the turbulent logarithmic boundary layer in chapter 3.8. Turbulent kinetic energy is assumed to linearly decrease from its maximum value at the bottom given by (3.153) to a minimum value $k_{\min} = 10^{-6}$ m²/s² at $z = D$ which has been chosen in order to provide at least little initial turbulence within the interface:

$$k(z) = \max\left(\frac{u_\tau^2}{\sqrt{c_\mu}}(D-z),\, k_{\min}\right) \quad \text{for} \quad 0 < z < D\,. \tag{7.75}$$

The friction velocity u_τ is given by the logarithmic velocity profile and $c_\mu = 0.09$. The specific dissipation rate in the logarithmic boundary layer is given by (3.173) and within the interface a maximum constant value of $\omega_{\max} = 1.0$ is assumed as suggested by the simulations above (cf. lower left panel in Figure 7.17):

$$\begin{aligned} \omega(z) &= \frac{u_\tau}{\sqrt{c_\mu}\kappa z} && \text{for} \quad 0 < z < D - \delta/2\,, \\ \omega(z) &= \min\left(\frac{u_\tau}{\sqrt{c_\mu}\kappa z}, \omega_{\max}\right) && \text{for} \quad D - \delta/2 < z < D + \delta/2\,, \end{aligned} \tag{7.76}$$

where $\kappa = 0.4$ is the von Kármán constant and u_τ and c_μ are defined above.

Finally, the hydrostatic excess pressure needed for the outflow boundary condition can be either obtained by integrating the density profile or assuming a linear increase from $\Delta\rho \cdot g \cdot D = \rho_0 \cdot g' \cdot D$ at the bottom to 0 at $z = D$. Both alternatives yield very similar results but the former has been chosen here for consistency. The according profiles are shown in Figure 7.19.

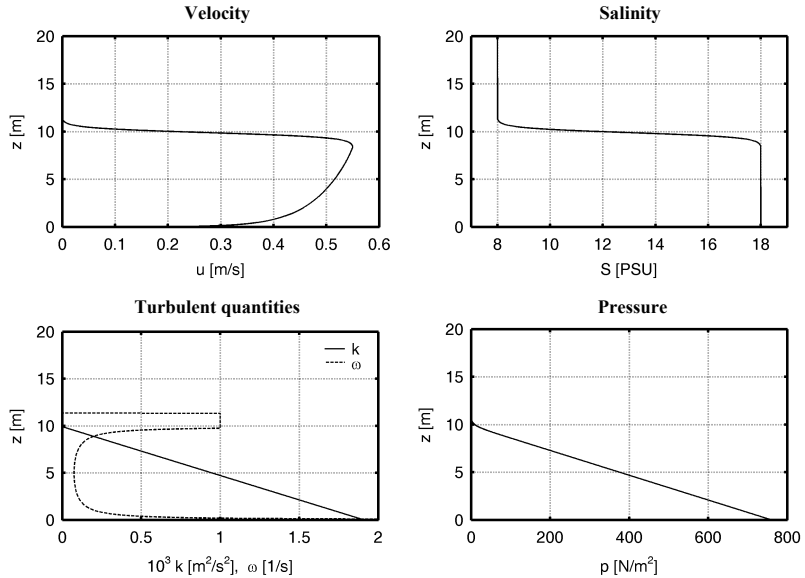

Figure 7.19: Boundary conditions for a density current in a channel without Coriolis forces.

Results

It is supposed that the boundary conditions approximately match the final solution and therefore the profiles will not change very much over the channel length. To verify this assumption the simulation has been run for 5000 s until the current passed the channel about 2.5 times such that all initial disturbances disappeared and stationary and steady conditions have established. The corresponding profiles of velocity, salinity, gradient Richardson number, buoyancy production, turbulent kinetic energy and specific dissipation rate at the beginning (x = 0 m), in the middle (x = 500 m) and near the end of the channel (x = 990 m) are shown in Figure 7.20.

From the profiles of velocity and salinity in the upper panels it is seen that the current indeed only marginally changes with the differences in salinity being even quasi undistinguishable.

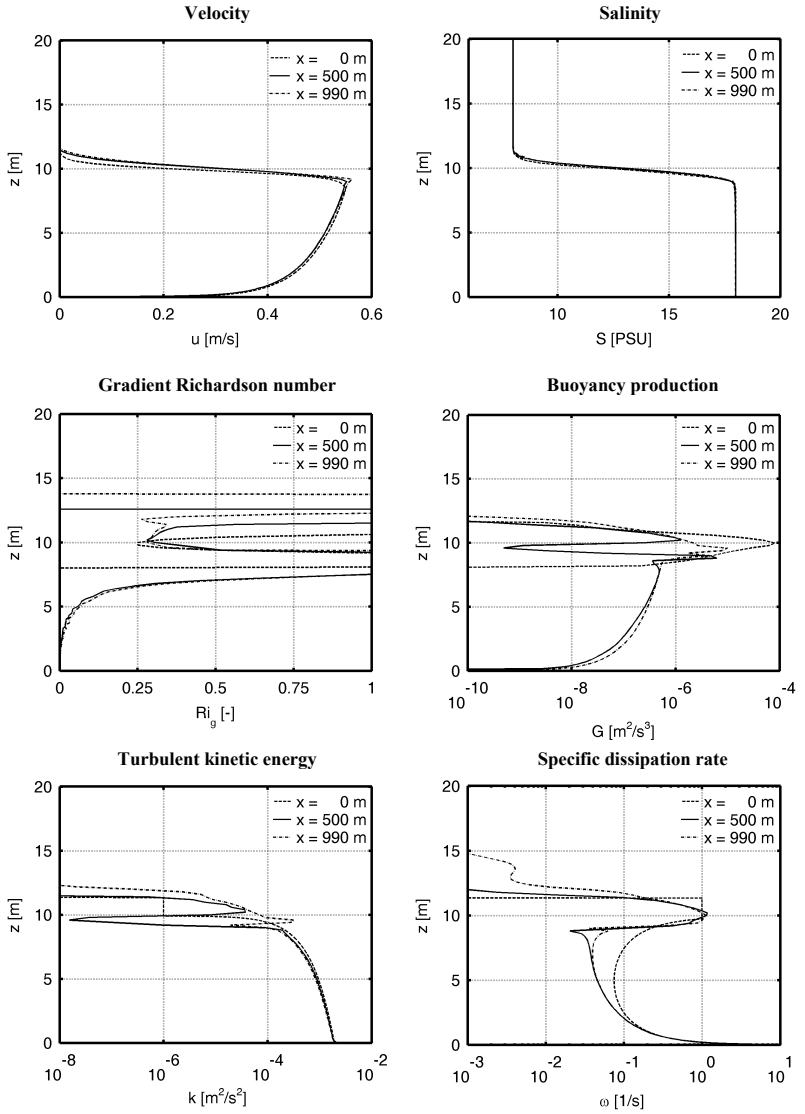

Figure 7.20: Vertical profiles of various quantities at the beginning, the middle and near the end of the channel for a density current without Coriolis forces.

The velocity profiles indicate a slight thickening of the interface which can also be deduced from the gradient Richardson number in the middle left panel. There it is further seen that the preset value of $Ri_g = 0.25$ is exactly matched at the inlet but is slightly higher at the other stations signifying some imbalance in turbulence (cf. chapter 6.1.5). This might have been expected from the difficulties in turbulence production which are reflected by the profiles of buoyancy production and turbulent kinetic energy in the middle right and lower left panels, respectively.

Buoyancy production at the inlet is restricted to the interface because of the zero density gradient which has been assumed in the core of the current (see boundary conditions above). As the current travels down the channel a density gradient establishes due to entrainment. Buoyancy production in the core shows the expected increase from the bottom which is a stable condition up to the end of the channel. However, at the middle station which is representative for the whole center part of the channel the minimum peak in buoyancy production and turbulent kinetic energy within the interface visualizes the erroneous turbulence production. Unlike in the one-dimensional model above this has no significant influence on the overall current dynamics due to the finite length of the channel but it can be expected that entrainment rates based on the integrated bulk buoyancy production will be underestimated.

The minimum peak is present throughout the major part of the channel but interestingly it disappears near the end. This is due to the actually unwanted short cut current at the outlet (see previous section) which induces additional shear such that the production terms stabilize. Even though this effect is spurious in the present case it approves that the turbulence model is well suited for situations in which shear is not restricted to only one dimension. For the following simulations of density currents in a channel with a cylinder it can be supposed that the numerical model will provide reasonable results due to the additional shear in the wake induced by the eddies separating from the cylinder.

Before continuing further, however, it is worth to have a look at the along channel profiles of depth integrated quantities given in Figure 7.21 to approve the steadiness of the current in the center part of the channel and show the effects at the boundaries.

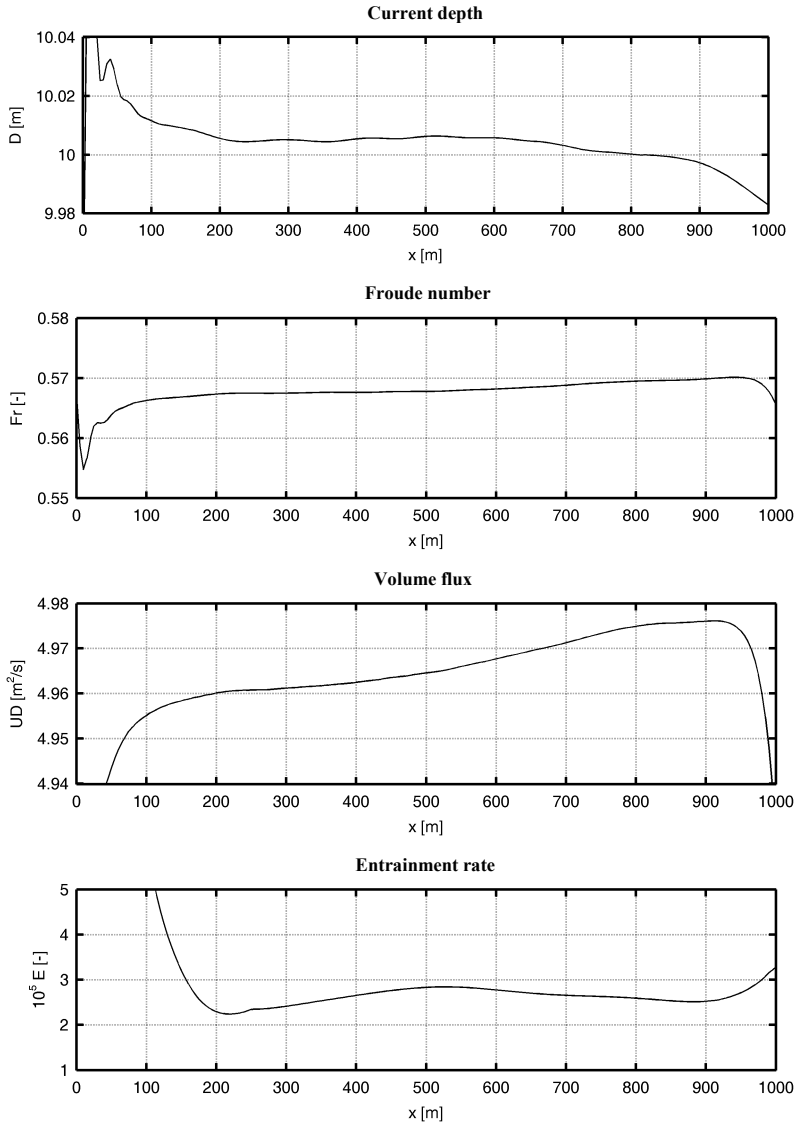

Figure 7.21: Along channel profiles for a density current without Coriolis forces. Current depth, Froude number, volume flux and entrainment rate.

Like in the simulations with Coriolis forces above, the current depth and Froude number remain constant over a large part of the channel and the strongest variations are found at the inflow and outflow boundaries. Especially at the inlet the deviations from the steady state are most significant and much stronger than those to be observed in Figure 7.18. This could be expected as the inflow boundary conditions here were only guessed and the current adjusts to the quasi-equilibrium state over about the first 200 m (cf. the discussion about the vertical profiles in Figure 7.20).

The strong transformation in the inflow region is associated with large entrainment rates as can be seen from the bottom panel in Figure 7.21 where entrainment within the first 100 m is even beyond the displayed range. The volume flux is qualitatively consistent with the entrainment rates and shows a large increase in the inflow region. However, in the center part of the channel, say between 100 m and 900 m the entrainment rate deduced from the volume flux is about $E \approx 5 \cdot 10^{-5}$ and hence almost twice of that based on the bulk buoyancy production.

Compared to the entrainment rate found for the current with Coriolis forces above ($E \approx 3 \cdot 10^{-5}$) for the present case without Coriolis forces the entrainment rate can be assumed to be higher following the argumentation by Stigebrandt (1985) already mentioned at the end of section 7.1.5. Thus, the entrainment rate shown in the bottom panel of Figure 7.21 is obviously underestimated which might have been expected from the unphysical minimum in buoyancy production below the interface (cf. Figure 7.20).

Summing up it can be concluded that in principle density currents in a channel without Coriolis forces can be simulated with the present numerical model. The mean flow field is quasi not affected by the discrepancy of the turbulence model and the results seem to be reasonable although a local determination of the entrainment rate is precluded by the erroneous prediction of turbulent quantities near the interface. However, entrainment in undisturbed density currents is only of minor interest here and it can be assumed that for the flow around a cylinder this drawback disappears due to the presence of secondary currents in the wake.

7.3.4 Concluding remarks

The present chapter was concerned with the theoretical and numerical prediction of undisturbed natural density currents. By a comparison with theoretical results and field measurements the numerical model could be shown to provide reasonable results at least in situations where Coriolis forces are present. As well as the theory breaks down for large Ekman numbers the numerical model coincidently fails if Coriolis force become small or even vanish. For two-equation turbulence models as used here the resulting velocity profile yields a singularity in turbulence production which inevitably leads to an erroneous prediction of the overall current dynamics.

In a one-dimensional model where only the vertical domain is resolved and the current is left to freely evolve the discrepancies of the turbulence model provide completely unphysical results for the evolution of a density current without Coriolis forces. However, in a two- or three-dimensional channel of finite size though the singularity in turbulence production is still present its effect on the mean flow field is less severe as the current is restricted by the inflow and outflow boundary conditions.

Despite the drawback in turbulence modeling it can thus be assumed that the following investigations of additional entrainment induced by circular cylinders can be promptly carried out with the present numerical model even if Coriolis forces and the resulting secondary currents are neglected. It can well be expected that the simulations will provide reliable results not only due to the finite channel length but much more because the flow around the cylinder induces secondary currents which inhibit the singularity in turbulence production at least for the most relevant part in the wake. Therefore the entrainment rates can be locally evaluated based on the bulk buoyancy production permitting a basic investigation of the influence of circular cylinders on mixing and entrainment of density currents to be followed now.

8 Entrainment induced by a circular cylinder

The preceding three chapters were dedicated to the discussion of the individual aspects and present knowledge about the flow around a circular cylinder and mixing and entrainment in stratified fluids like density currents. The influence of structures on these currents, however, is still an unresolved problem[1] and poses the major issue of the present thesis which will be worked out now by means of detailed numerical simulations.

Due to the lack of measurement data for the flow of density currents around a cylindrical structure the numerical model to be used here had to be validated for each of the involved processes separately. Unstratified flow around a circular cylinder was investigated in chapter 5.3, mixing in a stratified fluid in chapter 6.3 and finally entrainment in undisturbed natural density currents in chapter 7.2 and chapter 7.3. It could be shown that the specific features of the individual flows are well predicted by the model which is therefore assumed to be equally suited for the following simulations where all processes are combined. However, a validation of the model against measurements of the actual flow configuration either in the laboratory or in the field would gain final confidence in the results presented in the following and remains an open task for future work.

8.1 Methodology

As mentioned in the introduction in chapter 1.2 the present work is motivated by the intended construction of offshore wind energy devices in the Baltic Sea and the interest to determine the induced dilution of density currents passing these structures. All simulations here were therefore made on a 1:1 natural scale with velocities,

[1] To the author's knowledge the laboratory experiments of Jürgensen (1989) motivated by the planning of the Great Belt bridge are the only investigation on entrainment introduced by piers. However, his analysis based on overall budgets was rather crude and the results showed such a huge spread that the problem is basically regarded to be unresolved by now.

salinities and length scales varied in a realistic range representative for density currents in the Baltic Sea and possible foundations of the wind energy devices. However, in order for the results to be of general matter and to be applicable to other situations on different scales, it is useful to define the governing parameters of the flow and to express the results in terms of non-dimensional quantities.

In chapter 7 it was shown that for undisturbed density currents the densimetric Froude number is the governing parameter for mixing and entrainment (see e.g. Figure 7.10 or Figure 7.15). Even if other parameters like bottom drag, bottom slope and Ekman number, respectively, might have a certain influence on entrainment rates (at least for undisturbed currents) the Froude number turns out to be the most important and is therefore assumed to be also a governing parameter for the present flow of a density current around a circular cylinder.

The flow around the cylinder was found to be governed by the cylinder Reynolds number (cf. chapter 5.1) which in the present natural scale is usually in the order of 10^6 even if it slightly varies along the cylinder span due to the shape of the incoming velocity profile. Following the discussion in chapter 5.1 it can be assumed that a variation of the Reynolds number in this order of magnitude will only have a minor influence on the flow field around the cylinder as it is always in the supercritical to post-critical Transition-in-Boundary-Layers regime (cf. Table 5.1). However, in general the Reynolds number can be expected to have a certain influence on the results and therefore it has been chosen as the second governing parameter. In the present context it will only be used to approve the above assumption that the Reynolds number has more or less no effect on the flow topology and entrainment rates as long as there is no significant change in the flow regime.

Much more important than the Reynolds number might be the ratio between the current depth and cylinder diameter as the mean flow field behind the cylinder is governed by large three-dimensional vortical structures leading to strong advective transport in vertical direction which is a potential source for entrainment. For small aspect ratios, say $D/d = 1$, the vortices span over the whole current depth carrying fluid from the interface to the bottom and vice versa. This can be expected to be in association with rather large entrainment rates in contrast to situations with large

aspect ratios, say $D/d = 10$, where coherent structures in the wake are of size of the interface and mixing is restricted to the upper part of the current only leading to comparably smaller entrainment rates. The ratio of current depth to cylinder diameter is chosen as the third governing parameter for the present investigation and as explained above it is expected that its effect on the flow topology and entrainment is stronger than that of the Reynolds number due to the natural scale.

Although density currents in the Baltic Sea are influenced by Coriolis forces as shown in chapter 7 it is desirable for the investigations on cylinder induced entrainment to neglect this effect at first. The secondary currents due to Coriolis forces would complicate the flow field behind the cylinder and hamper the interpretation of the results. Their neglect facilitates the analysis and furthermore improves the significance of the results for cases in which rotation plays no role − whatever these cases might be. Thus, Coriolis forces will be regarded only briefly at the end of this chapter and the basic analysis to be followed is focused on purely two-dimensional incoming currents.

The major goal is to analyze the flow field around the cylinder and to quantify the additional entrainment induced by the structure. For this purpose fully three-dimensional simulations were carried out in which the governing parameters were varied in order to identify their influence on the results. Although the configuration of the whole problem is rather simple the computational costs are very extensive due to the required resolution of the numerical grid which will be described in the next section. Even if only the three major parameters above (Fr, Re, D/d) are regarded it is impossible to cover the full range of combinations, owing to the immense effort for one single simulation. It has been tried instead to focus on only a few cases which allow for an extension to a more general interpretation. As it is the first time that mixing of density currents due to cylindrical structures is investigated in detail the present work should not be understood as being complete but much more as showing the way how to get access to the problem, giving first quantitative results and providing suggestions for future work.

As mentioned above the governing parameters are varied in a range representative for density currents in the Baltic Sea being disturbed by the foundations of wind

energy devices. All currents investigated here are subcritical with the Froude number being less than 1. This is not only realistic for the currents in the Baltic Sea but much more the inherent entrainment of subcritical currents is comparably small (cf. chapter 7.1.5) and it can be assumed that the additional entrainment induced by a structure is much more significant for these currents than for supercritical ones. However, the proof for this assumption could be a task for future research.

The individual parameters of all cases are compiled in Table 8.1 where the first three columns show the dimensionless governing parameters and the actual dimensional quantities that have been used are found in the last four columns.

case	***Fr***	***Re***	***D/d***	**ΔS [PSU]**	**U_s [m/s]**	***D*** **[m]**	***d*** **[m]**
1111	0.57	$1.0 \cdot 10^6$	2	1.6	0.20	10	5
1121	0.57	$2.5 \cdot 10^6$	2	10.0	0.50	10	5
1131	0.57	$4.0 \cdot 10^6$	2	25.5	0.80	10	5
2121	0.92	$2.5 \cdot 10^6$	2	3.9	0.50	10	5
2131	0.92	$4.0 \cdot 10^6$	2	10.0	0.80	10	5
3111	0.36	$1.0 \cdot 10^6$	2	4.1	0.20	10	5
3121	0.36	$2.5 \cdot 10^6$	2	25.5	0.50	10	5
1212	0.57	$0.2 \cdot 10^6$	10	1.6	0.20	10	1
1222	0.57	$0.5 \cdot 10^6$	10	10.0	0.50	10	1
1232	0.57	$0.8 \cdot 10^6$	10	25.5	0.80	10	1
1313	0.57	$2.0 \cdot 10^6$	1	1.6	0.20	10	10
1323	0.57	$5.0 \cdot 10^6$	1	10.0	0.50	10	10
1112	0.57	$0.2 \cdot 10^6$	2	10.0	0.22	2	1
1133	0.57	$7.0 \cdot 10^6$	2	10.0	0.70	20	10

Table 8.1: Parameters of the 14 test cases for the basic analysis of additional entrainment in density currents induced by a circular cylinder.

The naming of the cases was chosen with the intention to more easily identify the specific issues of a case. The first index corresponds to the Froude number, the

second index to the current depth to cylinder diameter ratio, the third index to the current speed and the last index to the cylinder diameter both making up the Reynolds number.

From the discussion of the measurements in the Arkona basin in chapter 7.2.4 it can be deduced that case 1121 corresponds most closely to these conditions. It will therefore serve as the case of reference which will be discussed in most detail in section 8.3.1 and the influence of the governing parameters will be shown by a comparison with the other cases afterwards. Most cases are based on a current depth of D = 10 m and the variation of Froude and Reynolds number was achieved by adjusting the salinity difference and speed of the current. By that the first seven cases are focused on the effect of Froude and Reynolds number at a constant cylinder diameter of d = 5 m.

The next five cases 12xx and 13xx have been defined to investigate the effect of current depth to cylinder diameter ratio using the same currents as in cases 11xx and changing only the diameter of the cylinder by scaling the actual (dimensional) horizontal domain size while keeping the vertical size. The last two cases were added to prove that the different behavior found for cases 12xx and 13xx are really an effect of depth to diameter ratio and not of the Reynolds number. For this purpose the whole (dimensional) domain has been scaled such that both cylinder diameter and current depth were changed accordingly. While length scales linearly change with the scaling ratio velocities change with the square root of the scaling ratio leading to the slightly different values than in the other cases.

As seen from Table 8.1 much effort was put on the variation of the Reynolds number which later turned out to be in fact rather insignificant for the present order of magnitude, as will be shown later. For this reason the analysis here is actually not complete and the simulations for D/d = 1 and D/d = 10 should also be made with Fr = 0.36 and Fr = 0.92, respectively, to round up the work. It might also be desirable to accomplish the data with another depth to diameter ratio, say D/d = 5, in order to provide even more confidence in the interpretation of the presented results. However, these additional simulations could not be made within the schedule of the present thesis and are left as an open task for future work.

Unless not otherwise mentioned all results shown in the next sections are presented in normalized quantities. Following the procedure in chapter 5.3 length scales are normalized by the cylinder diameter d and expressed as capital letters (cf. eq. (5.15)), the only exception being in the presentation of the model setup in the next section where the vertical scale is normalized by the current depth. According to this course of action velocities are scaled by the current speed U_s just as in the definition of the entrainment rate (7.38) and time scales are normalized by d/U_s.

The normalized time step for all simulations was $\Delta t = 0.04$, which means that the complete domain (to be shown in the next section) is passed within 2000 time steps. In order to obtain quasi-stationary conditions with initial disturbances vanished all simulations were run for 4000 time steps initially. Subsequently, over another 4000 time steps which corresponds to about 30 shedding cycles mean values for all flow quantities including turbulent fluxes were gained. Due to the relatively high Reynolds numbers for most of the cases the directly simulated periodic motion is rather small and most of it falls within the turbulence modeling. Therefore the averaging time might have been taken smaller, but was chosen to cover 30 cycles in order to gain more confidence into the statistics.

In chapter 5.2.3 it was shown that the flow field around a bluff body can be decomposed into three portions, a global mean, a fluctuating turbulent and a fluctuating periodic part. From (5.14) it can be seen that on average momentum is mixed by both turbulent fluxes and fluxes due to the periodic motions. The same applies to the mixing of transported quantities like salinity or the resulting density field. Therefore the buoyancy production term which is needed to determine the entrainment rate can be decomposed into a turbulent and periodic fluctuating part:

$$G = G' + \tilde{G}\,, \tag{8.1}$$

where

$$G' = -\frac{g}{\rho_0}\overline{w'\rho'} = \frac{g}{\rho_0}\overline{\frac{\nu_t}{\sigma_t}\frac{\partial \rho}{\partial z}} \tag{8.2}$$

is the production of buoyancy by random fluctuations and

$$\tilde{G} = -\frac{g}{\rho_0}\overline{\tilde{w}\tilde{\rho}} \tag{8.3}$$

denotes the periodic part. Note that the overbar has been omitted on the left hand side for simplicity as all quantities here are time averaged values and an extra indication is unnecessary. According to the decomposition of the local buoyancy production the bulk buoyancy production given by (7.30) can be written as

$$G_b = G_b' + \tilde{G}_b = -\int_0^H G' \,\mathrm{d}z - \int_0^H \tilde{G} \,\mathrm{d}z = -\int_0^H G \,\mathrm{d}z \,, \tag{8.4}$$

and the entrainment rate given by (7.38) is redefined as

$$E = E' + \tilde{E} = \frac{2G_b'}{g'DU_s} + \frac{2\tilde{G}_b}{g'DU_s} = \frac{2G_b}{g'DU_s} \,. \tag{8.5}$$

The same procedure can be applied to the production of turbulent kinetic energy and the corresponding depth integrated bulk production which can then be used to obtain the bulk flux Richardson number as given by (7.59).

The following analysis of the simulation results will be started with a detailed analysis of the mean flow field around the cylinder which is responsible for the advective transport of salinity (density) to levels at which it is mixed with the surrounding fluid. The amount and efficiency of mixing will then be quantified by an analysis of the local entrainment rates and bulk flux Richardson numbers as defined above. As mentioned before this procedure is followed in detail for case 1121 which corresponds most to the actual situation in the Arkona Basin and will serve as a reference for the succeeding less extensive comparison with the other cases in order to work out the effects of the governing parameters. Finally it will be tried to assess the total entrainment induced by the cylinder and to estimate its dependence on the governing parameters based on the available simulation data. These results could then be used for a parameterization of global models or as a rule of thumb for preliminary planning of offshore wind energy devices in the Baltic Sea. First, however, the computational grid and the specific boundary conditions used for the simulations should be addressed.

8.2 Model setup

All simulations were carried out on the same computational domain which is sketched in Figure 8.1 with the cylinder in the center. The shaded plane is the result of one simulation and denotes the current depth which has been added to better visualize the model setup. Horizontal length scales are normalized by the cylinder diameter and the vertical scale is normalized by the current depth. The coordinate system is placed on the bottom in the center of the cylinder with the z-axis pointing vertically upwards, the x-axis pointing in streamwise direction and the y-axis pointing to the left.

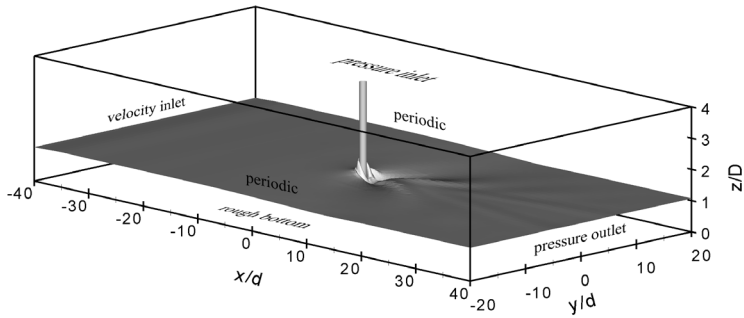

Figure 8.1: Definition sketch of the computational domain with the cylinder in the center. Boundary conditions are assigned by the text and current depth indicated by the shaded plane.

The vertical extent of $z/D = 4$ was motivated by the simulations in chapters 7.2 and 7.3 as it reflects the actual situation in the Arkona Basin with a total depth of about 40 m and current depth of about 10 m. A more confined extent, say $z/D = 2$, would not have changed the results, but due to the successively coarser grid above the current (see below) the computational savings by that reduction are only small and the present extent was kept for consistency. In lateral direction the size of the domain is $y/d = \pm 20$ which is assumed to be more than sufficient for the cylinder flow not to be influenced by the lateral boundaries (cf. chapter 5). The domain size in streamwise direction is $x/d = \pm 40$ where the extent behind the cylinder is assumed

to be enough to capture the most active part of the wake and the extent in front of the cylinder is so large in order to give the incoming undisturbed current sufficient space not to be influenced by always imperfect boundary conditions (cf. chapter 7.3).

The boundary conditions correspond basically to those used for the simulation of undisturbed density currents in a channel in chapter 7.3.1. The major difference comes from the new lateral boundaries at which periodic conditions are applied. Like for the top boundary also here symmetry (slip) conditions could have been chosen without significantly changing the results at least for purely two-dimensional currents. However, if Coriolis forces are regarded the resulting secondary flow in y-direction can only be realized with periodic conditions which have then always been used even if they are not the only alternative in cases without Coriolis forces.

The profiles for velocity, salinity, turbulent quantities and pressure needed for the inflow and outflow boundary conditions as well as initial conditions were gained from preliminary simulations of undisturbed currents. Just as in chapter 7.3.2 for currents with Coriolis forces a one-dimensional model has been used to obtain the corresponding profiles. In cases without Coriolis forces, however, this is not possible for reasons mentioned above and the boundary profiles were gained from simulations in a two-dimensional channel as shown in chapter 7.3.3.

The bottom roughness is always set to k_s = 0.025 m corresponding to a drag coefficient of $C_d \approx 0.0022$ for all cases where D ≥ 10 m. The slope of the channel is then found from the definition of the Froude number (7.49) with tan α_m = 0.72 ‰ for Fr = 0.57, tan α_m = 0.28 ‰ for Fr = 0.36 and tan α_m = 1.85 ‰ for Fr = 0.92. Please note that these slopes correspond to the inclination in streamwise direction which is identical to the total slope of the channel for currents without Coriolis forces. If Coriolis forces will be regarded later the channel must also be tilted in lateral direction and the respective slopes can be determined from the total slope given by the Ekman number (7.50), Froude-Ekman number relation (7.52) and the angle of deflection which can be determined from (7.51).

While the (normalized) size of the computational domain is the same for all cases the grid resolution had to be adjusted somehow to account for the peculiarities of the

individual cases. The grid is block-structured and the basic resolution is based on the experiences gained with the validation of the numerical model in chapters 5 and 7. The combination of a density current flowing around a cylinder requires a high resolution in both vertical as well as horizontal domain such that the whole problem demands a high computational effort especially because the horizontal domain size must be large for reasons mentioned above. The total number of grid cells N_{tot}, the number cells in the vertical N_z and the normalized minimum grid sizes at the cylinder Δr_{min} and within the interface Δz_{int} are compiled in Table 8.2.

case	*Fr*	*D*/*d*	N_{tot}	N_z	Δr_{min}	Δz_{int}
11xx	0.57	2	338192	47	$5.0 \cdot 10^{-4}$	0.050
21xx	0.92	2	338192	47	$5.0 \cdot 10^{-4}$	0.050
31xx	0.36	2	507288	70	$5.0 \cdot 10^{-4}$	0.025
12xx	0.57	10	299920	47	$2.5 \cdot 10^{-3}$	0.050
13xx	0.57	1	358800	47	$2.5 \cdot 10^{-4}$	0.050

Table 8.2: Grid characteristics for the different test cases.

In the vertical it is necessary to adequately resolve the steep gradients of velocity and turbulence quantities in the bottom boundary layer and of velocities and salinity (density) in the interface. In the range $0.5 < z/D < 1.5$ the resolution of the latter in terms of current depth was chosen to be $\Delta z_{int} = 0.05$ corresponding to 0.5 m for a current depth of 10 m which was found to be sufficient for the simulations in chapter 7.3. However, the thickness of the interface decreases with decreasing Froude number and the resolution has been doubled for the lowest Froude number investigated here to account for this effect.

The horizontal grid topology is the same for all cases and adopted from that used in chapter 5.3 for the simulations of unstratified flow around a circular cylinder. The grid is circular up to 3 diameters around the cylinder and then converted over the next 3 diameters to the rectangular shape of the channel. The finest resolution at the cylinder Δr_{min} as given in Table 8.2 corresponds to the wall function approach with y^+ being in the order of 10^2 or slightly below (cf. chapter 5.3.2). To reduce the

computational effort the resolution in the far field has been chosen much coarser with $\Delta x/d = \Delta y/d = 1$ which is slightly condensed in the wake region. Figure 8.2 shows a side and top view of the complete numerical grid with details at the bottom and cylinder displayed in the small panels.

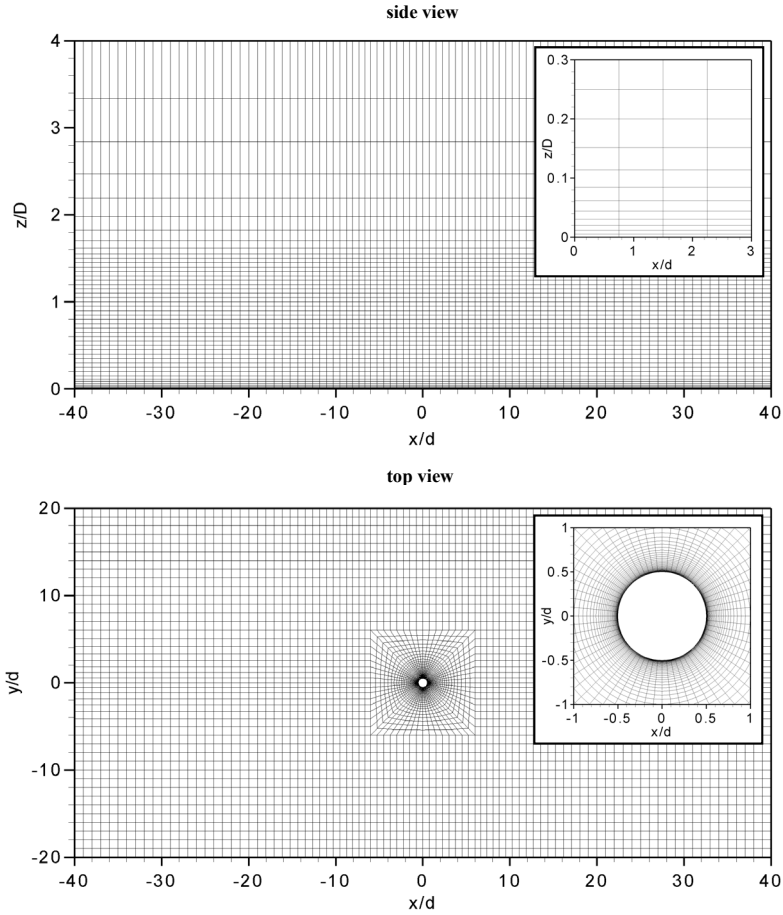

Figure 8.2: Side view and top view of the numerical grid. Small panels showing the refined resolution at the bottom and cylinder, respectively.

8.3 Results

As illustrated at the end of section 8.1 the analysis of the simulation results will focus on the mean flow field, entrainment rates and flux Richardson number. It will be started with a detailed discussion of the individual flow features for case 1121 which is assumed to most realistically reflect a typical situation in the Arkona Basin (cf. Table 8.1). An evaluation of depth profiles at specific single points in the current as always done before seems to be inappropriate here, due to the three-dimensional nature of the flow field behind the cylinder. The present analysis is thus based on the discussion of the individual quantities within specific longitudinal and cross-sections as this view is supposed to provide a better insight into the flow characteristics. entrainment rates and efficiency of mixing given by the bulk flux Richardson number are depth integrated quantities which will also be analyzed globally within the whole flow plane. After the influence of the governing parameters has worked out by a comparison of individual features the integration of the entrainment rate over the flow plane will finally provide an estimate of the total amount of additional mixing induced by a circular cylinder. These values can then be plotted in terms of the governing parameters to provide a kind of entrainment law for this specific flow.

8.3.1 Case of reference

The following discussion of a current with $Fr = 0.57$, $Re = 2.5 \cdot 10^6$ and $D/d = 2$ is intended to introduce the peculiarities of the flow and to provide a reference for the succeeding analysis of the influence of the governing parameters. To get a general feeling for the effect of the cylinder on the density current it is useful to have a look at the distribution of the density (salinity) field and the buoyancy production as a measure for mixing intensity. For this purpose Figure 8.3 shows a contour plot of (dimensional) buoyancy production in four different longitudinal sections in the vicinity of the cylinder at $Y = 0$, $Y = 0.5$, $Y = 1$ and $Y = 5$. The contour lines mark salinity concentrations at 0.5 %, 25 %, 50 % , 75 % and 99.5 % of the complete salinity difference and indicate the interface. The time averaged flow around the cylinder is symmetric and the sections shown here are identical to those for the corresponding negative values of Y.

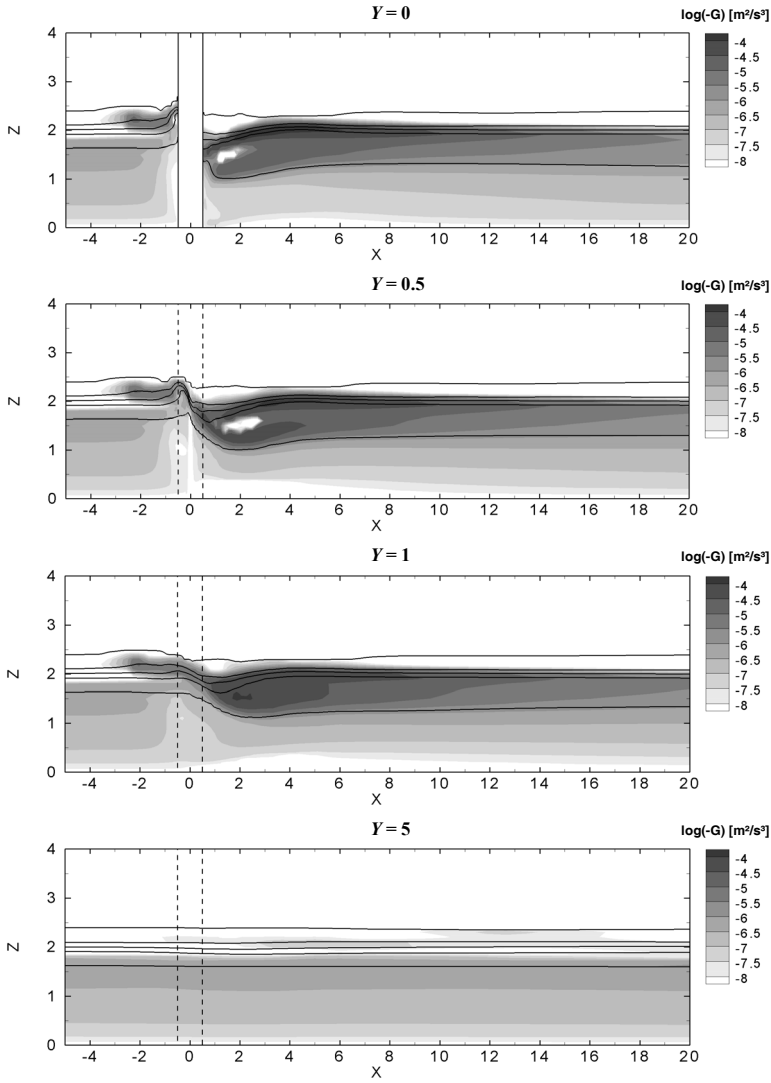

Figure 8.3: Salinity and buoyancy production at different longitudinal sections for the reference case with $Fr = 0.57$, $Re = 2.5 \cdot 10^6$, $D/d = 2$. Contour lines indicating salinities at 0.5 %, 25 %, 50 %, 75 % and 99.5 % of ΔS. Buoyancy production is given in logarithmic format.

In the bottom panel at $Y = 5$ buoyancy production and density field are both constant over the whole length of the section and more or less no disturbance of the current is detectable. This indicates that the influence of the cylinder on the current is restricted to the very near field of the structure (at least in lateral direction) and moreover it allows for using this section as a reference. From the contour lines of salinity the vertical structure of the interface can be detected to be of the typical hyperbolic form as found for undisturbed currents in chapters 7.2 and 7.3. The large density gradients in the core of the interface as reflected by the small distances behind the contour lines at 25 %, 50 % and 75 % ΔS indicate strong stability against local mixing while the upper and lower part where stratification is weak can be assumed to be more susceptible to mixing. From the distance of the outer contour lines the thickness of the interface can be estimated to be about $0.6d$ corresponding to 3 m for the present case which is consistent with the findings in chapter 7.3 for a similar undisturbed current.

Also the buoyancy production shows the expected behavior with an increase from the bottom to a maximum value of $G \approx 10^{-6}$ m^2/s^3 at the lower part of the interface and a decrease within the interface which, however, is presumably not very well predicted due to the inconsistency of the turbulence model discussed in chapter 7.2.5. However, as argued there, this discrepancy of the model can be assumed to be unimportant in the wake of the cylinder where secondary currents prevent a singularity in turbulence production. Much more these currents produce a significant amount of additional turbulence in the wake region which is the source for increased mixing as reflected by the high buoyancy production rates behind the cylinder found in the sections at $Y = 0$, $Y = 0.5$ and $Y = 1$.

The spatial evolution of buoyancy production along these sections shows that after 20 diameters behind the cylinder the undisturbed profile as given in the lower panel at $Y = 5$ is almost completely recovered suggesting that the effect of the cylinder on entrainment is restricted to only a few diameters also in streamwise direction. This is supported by the contour lines of salinity which most remarkably change in the near wake, say up to 10 diameters behind the cylinder, and than remain almost constant indicating that entrainment rates recovered to small values.

The evolution of the density field also supports the above assumption that mixing is most efficient in those parts of the interface that are only weakly stratified. The core of the interface where density gradients are large and the upper part where density gradients are small but shear is insignificant remain both basically constant and are only moved up and down by the currents around the cylinder to be discussed below. However, the lower part of the interface where stratification is weak and shear is large is significantly affected by mixing. This is indicated by the distance between the lowest salinity contours which drastically increases behind the cylinder visualizing the decreasing density gradient due to entrainment of lighter fluid. The white spots in the buoyancy production field found in the near wake at $Y = 0$ and $Y = 0.5$ represent areas of negligible or even negative buoyancy production. In these regions the fluid has either completely been mixed or even convection set in.

Without doubt the most active region for entrainment and mixing is found in the wake behind the cylinder. However, the flow field in the wake is strongly affected by the situation in front of the cylinder which should therefore not be disregarded in the present discussion. The flow in the section along the cylinder axis at $Y = 0$ is completely blocked by the cylinder which induces a downward current forming a small vortex at the bottom and an upward current lifting the interface. The latter causes an excess pressure to the surroundings driving a backflow current within the interface in front of the cylinder which is the source for turbulence production and explains the higher buoyancy production found in the upper part of the interface in front of the cylinder. The excess pressure caused by the lifted interface also induces a strong downward current in streamwise direction which causes an advective transport of the interface as can be deduced from the contour lines of salinity. In the wake upward currents lift the interface again to a maximum level about 5 diameters behind the cylinder before it finally settles to a slightly lower height when secondary currents and mixing rates have diminished.

To get a better idea about the three dimensional flow field around the cylinder Figure 8.4 shows the velocity field, buoyancy production and salinities at different cross-sections in front of and behind the cylinder. Buoyancy production and salinity are given as in Figure 8.3 and the velocity field is represented by the vectors which are differently scaled in the individual panels (see reference vector).

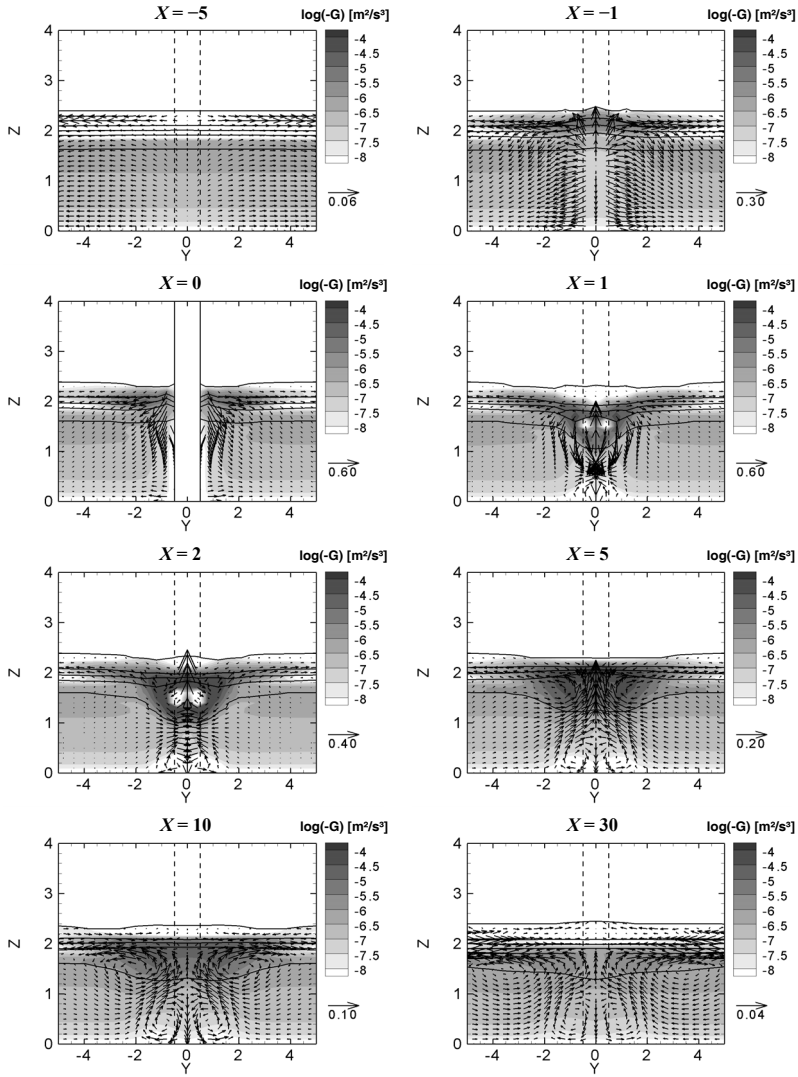

Figure 8.4: Flow field at different cross-sections in front of and behind the cylinder for the reference case with $Fr = 0.57$, $Re = 2.5 \cdot 10^6$, $D/d = 2$. Salinity and buoyancy production are displayed as in Figure 8.3. Note the different scaling of velocity vectors.

The expected symmetry of the (time averaged) flow field can be found in all sections justifying the restriction of the above discussion to longitudinal sections at positive Y only. Moreover it is obvious at first sight that the influence of the cylinder in lateral direction is indeed limited to a few diameters as directly seen from the pattern of the velocity field and further reflected by buoyancy production and salinity at $Y = \pm 5$ which are identical in all sections, except for $X = 30$. This is an effect of the increasing width of the wake which is reflected by the velocity and salinity fields in the last four panels and exceeds the width of the section at $X = 30$. The spreading of the wake is associated with a loss of local intensities equalizing high gradients in the flow field and smoothing the local effects of entrainment in lateral direction. Before continuing further it seems to be more useful to align the discussion of the flow field with the pathway of the current around the cylinder starting in the upper left panel of Figure 8.4 and then going from left to right and top to bottom.

Some distance in front of the cylinder at $X = -5$ a clear divergence of the current to the left and right can already be noticed. The highest velocities are found within in the interface although they only amount a few percent of the current speed. Moving closer to the cylinder at $X = -1$ lateral velocities close to the cylinder have significantly increased and the upward and downward current at the cylinder axis is clearly identified from the vectors at $Y = 0$ with the point of inflection being at about $Z \approx 1.3$ (i.e. $2/3D$). The lifting of the interface caused by the upward current can be deduced from the salinity contours and the increased buoyancy production within the interface can be associated with the currents induced by the resulting excess pressure.

Right next to the cylinder at $X = 0$ the downward component of the excess pressure induced current is at maximum and of the same order as the current speed. The interface has been transported back downwards by this current to reach its minimum level behind the cylinder at $X = 1$. Although a significant vertical downward component is still present left and right of the cylinder in this cross-section the highest velocities are found at the cylinder axis and are directed upwards. They cause the transport of the interface in the wake back upwards and induce large vortices which are more clearly identifiable in the following cross-sections farer

away from the cylinder. At the bottom another vortex pair is formed which mixes the very low bottom part of the current as can be deduced from the slightly higher levels of negligible buoyancy production at the bottom indicating that density gradients have vanished in that region. However, these vortices are rather unimportant concerning the overall mixing process.

Much more important is the buoyancy production within the interface from which the white spots of negligible or negative production are found again right behind the cylinder at $X = 1$ and $X = 2$. The highest levels of buoyancy production within each cross-section are located just around these spots with the overall maximum values found at $X = 2$. It can therefore be assumed that the maximum entrainment rates will be found about 2 diameters behind the cylinder and about 1 diameter moved to the left and right, respectively.

Following the current further along the wake at $X = 5$, $X = 10$ and $X = 30$ it can be seen that buoyancy production more and more decreases such that at $X = 30$ additional mixing by the cylinder is no longer detectable and the natural state found in front of the cylinder is recovered. Within the mean flow field, however, the influence of the cylinder remains present much longer as clearly identifiable by the large vortices. This is clear from the fact that mixing induced by the cylinder is actually restricted to a rather small region in the wake which causes quite significant lateral density gradients. These gradients induce lateral currents driving the vortices and compensating the density difference, a process which will naturally take much longer than the actual local entrainment of ambient fluid.

This homogenization process can be well identified from a comparison of the two cross-sections in the far wake at $X = 10$ and $X = 30$. Below the interface there is a current directed to the cylinder carrying denser fluid from the lateral far field to the wake region where the lowest salinity contour line is lifted while it is lowered at the sides. A similar pattern is found within the interface where denser fluid in the lower part is transported away from the cylinder while above lighter fluid is added from the sides increasing the amount of low salinity as indicated by the lifted uppermost contour line.

From the last cross-section at $X = 30$ it can be guessed that the restabilization of the current is not completely finished within the present computational domain. However, it is unnecessary to cover the whole course of homogenization which is a mass conserving process and the major interest here is on the dilution of the current caused by entrainment of lighter ambient fluid rather than the final restabilized pattern of the current. The remaining lateral currents might play a role if more than a single cylinder is regarded and structures are arranged in a row, but this is not the issue of the present thesis and could be a task for future work. Anyway, concerning wind energy devices in the Baltic Sea the effect of these currents on the flow field around an adjacent structure can be assumed to be negligible as the distance between the constructions can be expected to be at least $20 - 30$ diameters and the remaining velocities at that distance are very small.

The actual process of mixing and entrainment, i.e. the adding of mass from the ambient fluid to the current, is associated with the level of turbulence and the amount of buoyancy production which was found above to be restricted to a comparably small region around the cylinder. To assess the overall effect of the cylinder on the dilution of the current it is useful to analyze the spatial distribution of entrainment rates and efficiency of mixing given by the flux Richardson number. Both are directly associated with the depth integrated bulk buoyancy production which should therefore be shortly discussed first.

As elucidated in chapter 5.2.3 the time averaged mixing rate behind a bluff body is governed by two processes, random turbulent fluctuations and periodic fluctuations. The total time averaged bulk buoyancy production can be split up accordingly into a turbulent and a periodic part as shown above in chapter 8.1. The former is determined by the turbulence model and the latter by the remaining motions in the mean flow field. Figure 8.5 shows the spatial distribution of the individual components in the upper and middle panel and the sum of both in the lower panel.

Compared to the turbulent part of buoyancy production the periodic portion is very small (also note the different scaling of contour levels) and restricted to the very near field of the cylinder. Most of the total production is simulated by the turbulence model which might have been expected as the high Reynolds number implies that a

large part of the flow field is governed by isotropic small scale fluctuations. This is the basic assumption of the turbulent viscosity/diffusivity approach on which the present turbulence model is founded and it can therefore be assumed that the high turbulence portion of the flow is well predicted by the model.

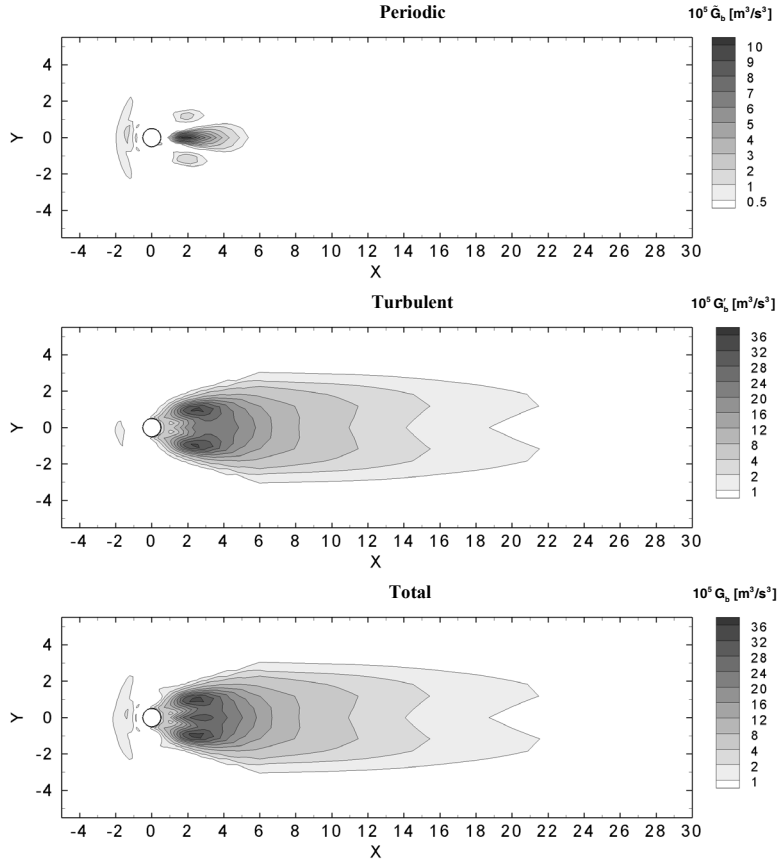

Figure 8.5: Periodic, turbulent and total amount of bulk buoyancy production for the reference case with $Fr = 0.57$, $Re = 2.5 \cdot 10^6$, $D/d = 2$. Note the different scaling of the contour levels.

The total entrainment rate, i.e. the relative amount of added mass to the current, can be determined from the bulk buoyancy production using (8.5). The efficiency of mixing, i.e. the rate of total produced energy that is used for production of buoyancy, however requires the knowledge of the bulk production of turbulent kinetic energy which is determined in a similar way as shown above for the bulk buoyancy production (cf. eq. (8.1) - (8.4)). For the sake of completeness the spatial distribution of total bulk production of turbulent kinetic energy is shown in Figure 8.6. Note that the contour levels are 20 times higher than that of bulk buoyancy production above, indicating that (as expected) only a few percent of the produced turbulent kinetic energy is used for the production of buoyancy.

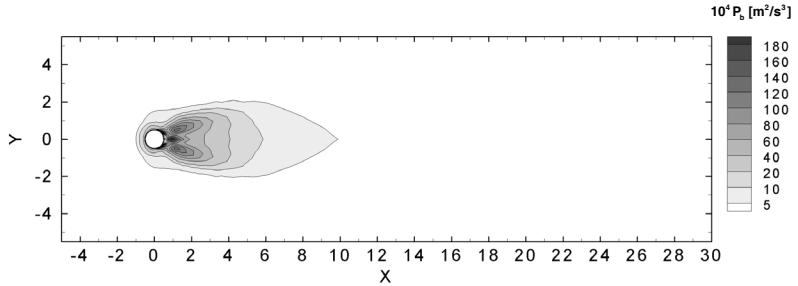

Figure 8.6: Total bulk production of turbulent kinetic energy for the reference case with $Fr = 0.57$, $Re = 2.5 \cdot 10^6$, $D/d = 2$.

Finally, the spatial distributions of the total entrainment rate and the bulk flux Richardson number are given in Figure 8.7. As explained in chapter 7.3.3 the entrainment rate of the undisturbed current cannot be determined from the buoyancy production due to the discrepancy of the turbulence model. However, from the volume flux it could be reasonably estimated to be about $E \approx 5 \cdot 10^{-5}$ for the present case (cf. chapter 7.3.3) which was therefore chosen as the lowest level for the entrainment rate and is the threshold value to determine the effective entrainment induced by the cylinder. The same problem applies to the flux Richardson number which can also not be determined for an undisturbed density current without Coriolis forces. A reasonable value seems to be about $Ri_{f,b} \approx 0.03$ (cf. discussion in chapter 7.1.5 and Figure 7.9) which has therefore been chosen here as the threshold value to identify the influence of the cylinder.

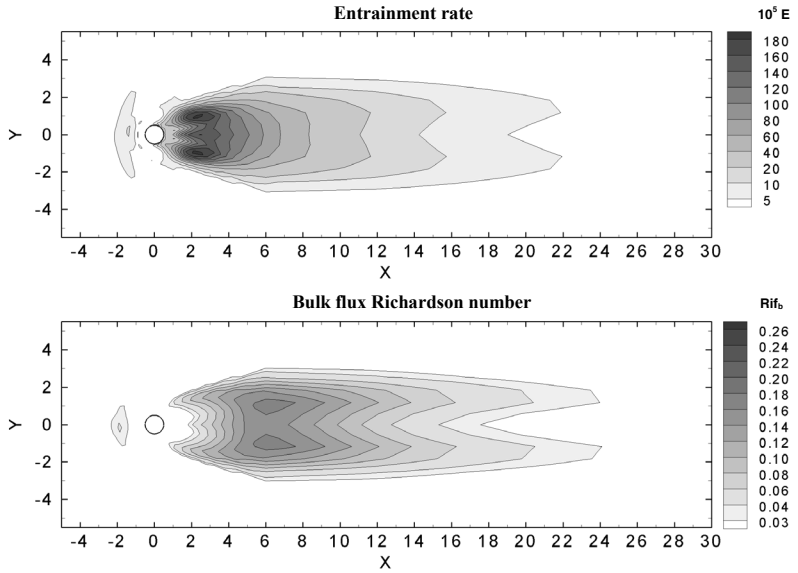

Figure 8.7: Total entrainment rate and bulk flux Richardson number for the reference case with $Fr = 0.57$, $Re = 2.5 \cdot 10^6$, $D/d = 2$.

The distribution of the entrainment rate is almost identical to that of the bulk buoyancy production above which might have been expected from (8.5) where the denominator is quasi constant except for some slight deviations of $g'D$ in the rapidly varying region very close to the cylinder. Although there is also some entrainment in the bow wave in front of the cylinder most mixing takes place in the wake where the highest entrainment rates are found at $X = 2$, $Y = \pm 1$ which was already assumed above in the discussion about the depth resolved buoyancy production in Figure 8.4.

The spatial distribution of the entrainment rate allows for an estimate of the area of influence of the cylinder which can be assessed to be about 20 diameters long and 6 diameters wide. Although locally the cylinder induced mixing is very intense with entrainment rates being more than 2 orders of magnitude higher it can be assumed that the overall effect of an offshore wind energy farm on the current is small as long as the structures are not very close to each other. However, this will be discussed in more detail in section 8.3.5.

From the bulk flux Richardson number it is seen that mixing is not necessarily most efficient where the entrainment rates are largest. In contrast the highest efficiency of mixing is found where entrainment rates already decay although the pattern of both is quite similar at least in the far wake. It is beyond the scope of the present work to analyze the mixing process in form of the flux Richardson number in more detail as the major interest is on the actual effect which is represented by the entrainment rate. However, it can be concluded that entrainment induced by a cylinder is generally associated with higher bulk flux Richardson numbers than that found in an undisturbed current. For the present case the maximum values of the bulk flux Richardson number are found left and right of the middle axis and show that buoyancy production can be up to about 16 % of the total produced turbulence.

Now that the principal effect of the cylinder on a density current has been thoroughly discussed it is time to investigate the influence of the governing parameters on the flow field and especially on the entrainment rates. This analysis should be started with the Reynolds number which is expected to have the least influence on the results as within the present order of magnitude ($Re \approx 10^6$) the flow field in the wake will not significantly change.

8.3.2 Influence of Reynolds number

The effect of the Reynolds number will be studied by a comparison of the reference case 1121 above with three other cases, case 1112, case 1131 and case 1133, for which the Reynolds number changes between $Re = 0.2 \cdot 10^6$ and $Re = 7 \cdot 10^6$ while the other governing parameters are constant ($Fr = 0.57$, $D/d = 2$). As can be seen from Table 8.1, the dimensional quantities are significantly different with current depths ranging between 2 and 20 m and cylinder diameters ranging between 1 an 10 m. If the Reynolds number has no influence, which might be expected at least for $Re > 1 \cdot 10^6$ as argued above, this would support the assumption that the flow of a density current around a cylinder is indeed only governed by the other parameters.

Figure 8.8 shows the flow field for the four cases at two cross-sections in the wake with increasing Reynolds number from top to bottom and the left and right column representing the results at $X = 2$ and $X = 10$, respectively.

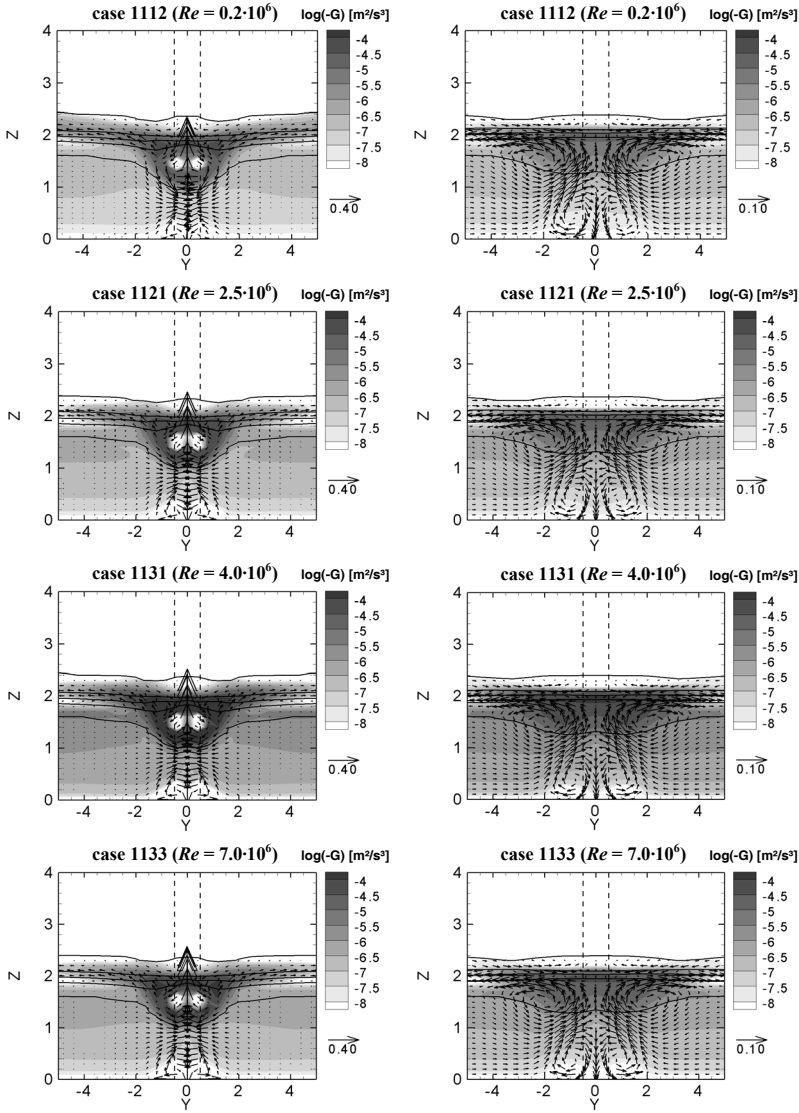

Figure 8.8: Influence of Reynolds number on flow field behind the cylinder for cases with constant $Fr = 0.57$ and ratio $D/d = 2$. Left column: $X = 2$; right column: $X = 10$.

From the discussion about the characteristics of unstratified flow around a circular cylinder in chapter 5.1 it is seen that all cases belong to the Transition-in-Boundary-Layers regime and from Table 5.1 it can be expected that the wake pattern should not significantly change for cases 1121, 1131 and 1133, which belong to the very similar supercritical and post critical subregimes. However, with a Reynolds number of just $Re = 0.2 \cdot 10^6$, case 1112 belongs to the precritical subregime and might show some differences or maybe even asymmetries due to the proximity of the single bubble regime. In fact, Figure 8.8 shows that the velocity and salinity fields are quasi identical for all cases indicating that the vertical shear in the velocity field of the incoming current and the strong vertical currents in the wake as a consequence of the 'free surface' obviously alter the range of the distinct flow states.

As will be shown in the next section the intensity of the vertical currents are a clear function of the depth to diameter ratio and almost vanish for large D/d. Due to the relatively small cylinder diameters the Reynolds number in these cases is also smaller and the flow again falls into the precritical to single-bubble subregimes, but then indeed leads to a clear asymmetry in the wake (cf. Figure 8.10). This shows that the Reynolds number has a certain effect (at least on the flow field in the wake) but the distinction of the different regimes depends on the depth to diameter ratio. A comparison (not explicitly presented here) of case 1212, 1222 and 1232, all belonging to the single-bubble regime for $D/d = 10$, shows that the results are more or less identical in analogy to those presented in this section. This leads to the final conclusion that the Reynolds number is an unimportant parameter as long as the flow belongs to a distinct regime.

The discussion about the influence of the Reynolds number might thus be stopped at this point with the assumption that the similarity in the flow field implies identical entrainment rates. At first sight this would be supported by the buoyancy production field showing exactly identical patterns for all cases, but looking more closely it is seen that the absolute values are different for the individual cases. However, this is neither an effect of the Reynolds number nor a numerical error but indeed a realistic result as buoyancy production has not been normalized and represents the actual dimensional values which depend on depth, salinity and speed of the current. This can be best explained by the entrainment rate given by (8.5). As the Froude number

is constant the entrainment rate must also be constant (at least in the unaffected regions at the sides) and the bulk buoyancy production scales with U_s^3 only. For low current speeds it is therefore natural to expect lower values of buoyancy production which is indeed approved comparing the different cases.

Although the flow field is independent of the Reynolds number the different buoyancy production for the individual cases suggests to proof that the entrainment rates in the wake are also identical. For this purposes Figure 8.9 shows the spatial distribution of the entrainment rates for the four cases with increasing Reynolds number from top to bottom. It is seen that the entrainment rates behind the cylinder are indeed identical, but the entrainment induced by the bow wave in front of the cylinder shows significant differences. The increasing entrainment rate could be explained by the higher speed of the current which is 0.5 m/s for case 1121 and 0.8 m/s for case 1131. This assumption would be supported by case 1133 where the speed of the current is 0.7 m/s and entrainment rates are slightly less than in case 1131. However, the most intense entrainment rates in front of the cylinder are found for case 1112 with the lowest current speed of 0.22 m/s such that the above assumption no longer holds. Anyway, more than 90 % of the total entrainment of ambient fluid is found in the wake and the ambiguous behavior in front of the cylinder can be assumed to be of minor importance for the major issue of this work. Therefore it has not been tried to investigate this effect further within this thesis but it might pose an interesting question for future work.

It can be concluded that the flow field in the wake changes with different flow regimes which are basically governed by the Reynolds number but for the present problem further depend on the current depth to cylinder diameter ratio. Disregarding the differences in front of the cylinder the Reynolds number could be shown to have no influence on the flow field and entrainment rates in the wake as long as the current is in the same flow regime. This can be assumed to be at least the case for realistic conditions in the Baltic Sea and the Reynolds number is regarded as an unimportant parameter for the present investigation. From a scientific point of view, however, it might be interesting to further investigate the Reynolds number effect by small scale simulations at low Reynolds numbers which would then also allow for a comparison with laboratory measurements. But this is also a task for future work.

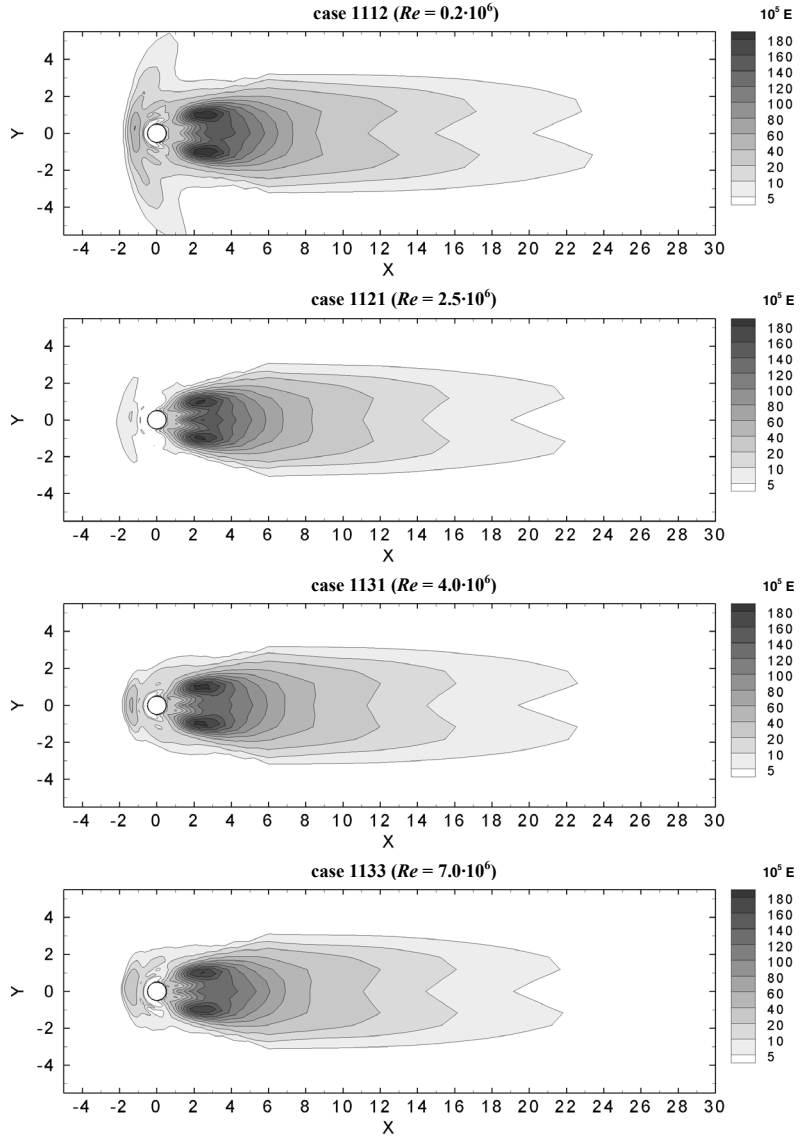

Figure 8.9: Influence of Reynolds number on entrainment rates for cases with constant $Fr = 0.57$ and ratio $D/d = 2$.

8.3.3 Influence of aspect ratio

The influence of current depth to cylinder diameter ratio will be analyzed in a similar fashion like the Reynolds number above by comparing the reference case 1121 with two other cases, case 1323 and case 1222 at the same Froude number $Fr = 0.57$. The current depth was kept constant such that the incoming current is absolutely identical for all cases and only the diameter of the cylinder has been changed. This implies a significant change of the Reynolds number which, however, was found above to be unimportant as long as the flow is in the same regime.

Again the discussion will be started with the flow field in the wake of the cylinder represented by the results in the cross-sections at $X = 2$ and $X = 10$ which are shown in Figure 8.10 in the left and right column, respectively. The aspect ratio increases from top to bottom and it should be noted that the vertical scale changes with aspect ratio due to the normalization of current depth with cylinder diameter. As the incoming current is identical for all cases buoyancy production in the unaffected regions at the sides is seen to be also the same for all cases. The flow field within the wake, however, is significantly different. It can be followed that the maximum velocities increase with increasing diameter which seems natural as the more of the current is blocked the higher are the velocities around the cylinder and the more intense is the upward current in the center at $X = 2$.

As pointed out in section 8.3.1 this current induces large vortices within the interface which therefore gain more energy with increasing diameter and for $D/d = 1$ they are so large that they reach down to the bottom where the smaller vortices found for $D/d = 2$ completely disappear. On the other hand for $D/d = 10$ the cylinder has almost no effect on the density current and upward velocities in the middle plane and the resulting vortices can quasi not be noted at all. Due to the large aspect ratio this flow even more resembles the unstratified flow around an infinite cylinder discussed in chapter 5 and therefore an asymmetry in the wake flow is found as to be expected for the present Reynolds number defining the asymmetric one-bubble regime. However, as the impact of the cylinder on the flow field and especially the buoyancy production rates within the interface is negligible this case needs no further discussion.

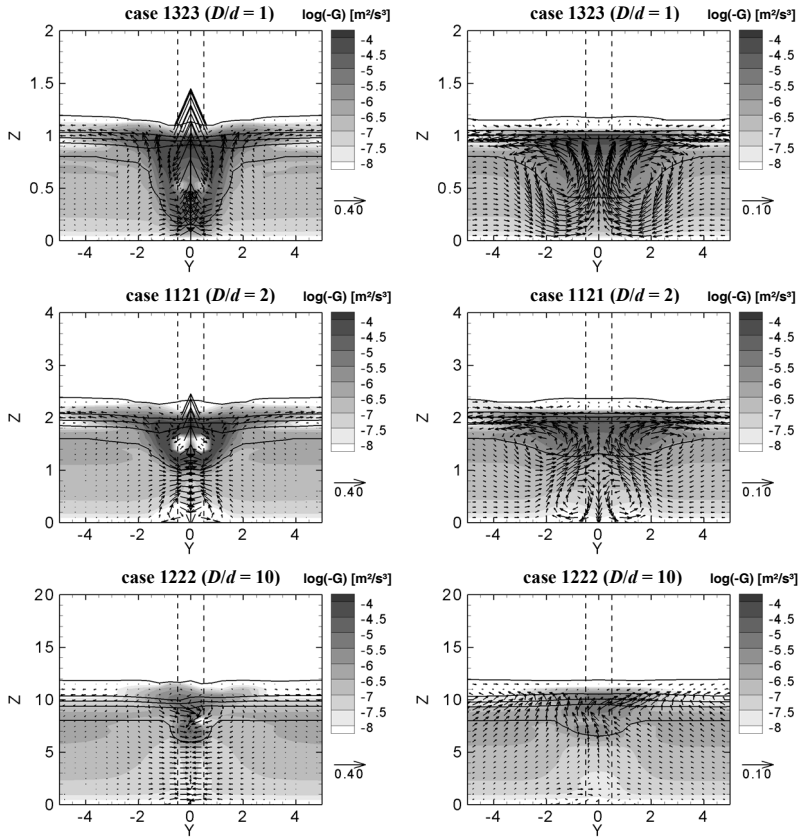

Figure 8.10: Influence of depth to diameter ratio on flow field for identical currents with $Fr = 0.57$. Left column: $X = 2$; right column: $X = 10$.

The higher velocities for the smallest aspect ratio $D/d = 1$ are likely to be associated with a stronger impact on the advective transport of the interface which is indeed reflected by the contour lines of salinity. Especially the lowest contour line is found much deeper than for $D/d = 2$ suggesting that also mixing is more intense. This is supported by the buoyancy production field which has a similar pattern for both cases but for the smaller aspect ratio the levels within the interface are higher, indicating a larger bulk production and by that higher entrainment rates.

Figure 8.11 shows the spatial distribution of the corresponding entrainment rates for the three cases with increasing aspect ratio from top to bottom. In fact, it is seen at first sight that the entrainment rates are largest for D/d = 1 and decrease with increasing depth to diameter ratio. For D/d = 10 the effect of the cylinder can be quasi neglected as the maximum values are more or less in the order of the natural entrainment rates of the current. So again this case needs no further discussion.

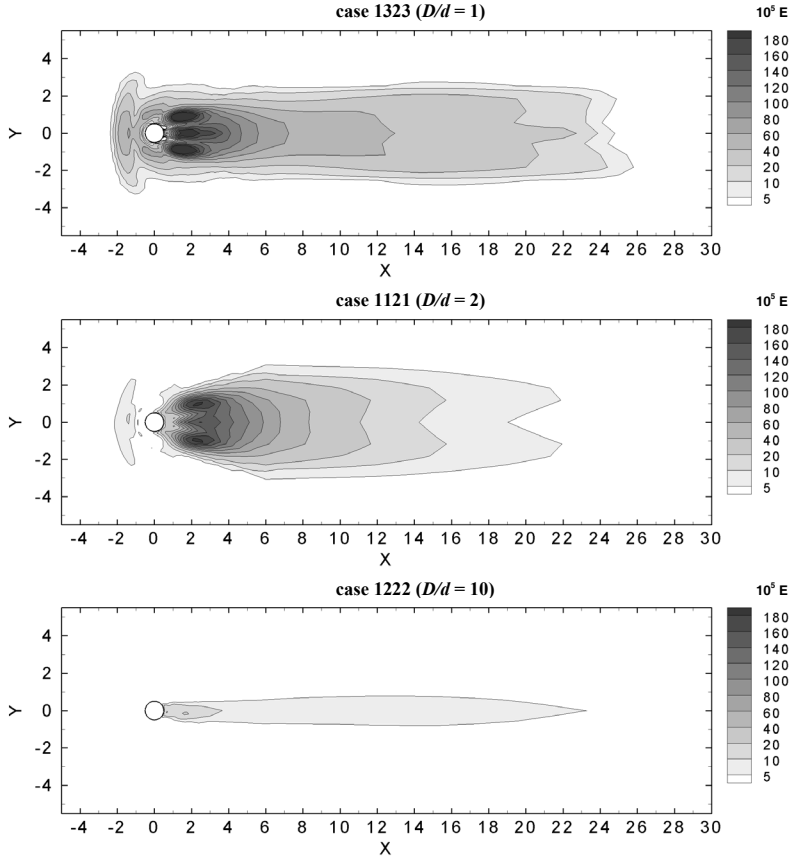

Figure 8.11: Influence of depth to diameter ratio on entrainment rate for identical currents with Fr = 0.57.

The pattern of the entrainment rates behind the cylinder for the other two cases is very similar especially in the near wake. Apart from the absolute higher entrainment rates for the smaller aspect ratio there is also a tendency to increased mixing in the middle plane along the cylinder axis which is less pronounced for $D/d = 2$. This might be the result of the flow field in the wake which had not only higher velocities but was also more concentrated at the cylinder axis for $D/d = 1$ (cf. Figure 8.10). Due to the higher intensities in the flow field the area of influence of the cylinder is seen to be longer for the lower aspect ratio but the lateral extent is slightly less than for $D/d = 2$. This could also be expected from Figure 8.10 where the deformation of lowest salinity contour, especially at $X = 10$, is seen to be more confined for $D/d = 1$.

With decreasing aspect ratio entrainment rates not only increase in the wake but also around and in front of the cylinder. While the strong intensities in the bow wave found for the lowest Reynolds number in the preceding section could not be given a proper explanation here it might be argued by the higher blocking ratio and the resulting velocity field around the cylinder. However, also this is just an assumption which has not been further verified as again the higher rates in front of the cylinder are clearly visible but make up less than 10 % of the total entrainment. Thus, the conclusions of the present thesis are not severely affected by this effect and the investigation of the processes involved is left for future work.

Now, after it was found that the depth to diameter ratio has a quite significant effect on the entrainment rates it might be finally worth to have a look at its influence on the efficiency of mixing. This is reflected by the spatial distribution of the bulk flux Richardson number shown in Figure 8.12 where the aspect ratio again increases from top to bottom. As expected the results for $D/d = 10$ in the bottom panel are in an order of magnitude which needs no further discussion and this case is only shown for the sake of completeness. The other two cases, however, point out the interesting fact that the larger entrainment rates found for $D/d = 1$ are the result of higher flux Richardson numbers and more effective mixing rather than a higher amount of turbulence production. This might not have been expected at first but indeed the bulk production of turbulent kinetic energy (not shown) is more or less the same for both cases and even tends to be slightly higher for $D/d = 2$.

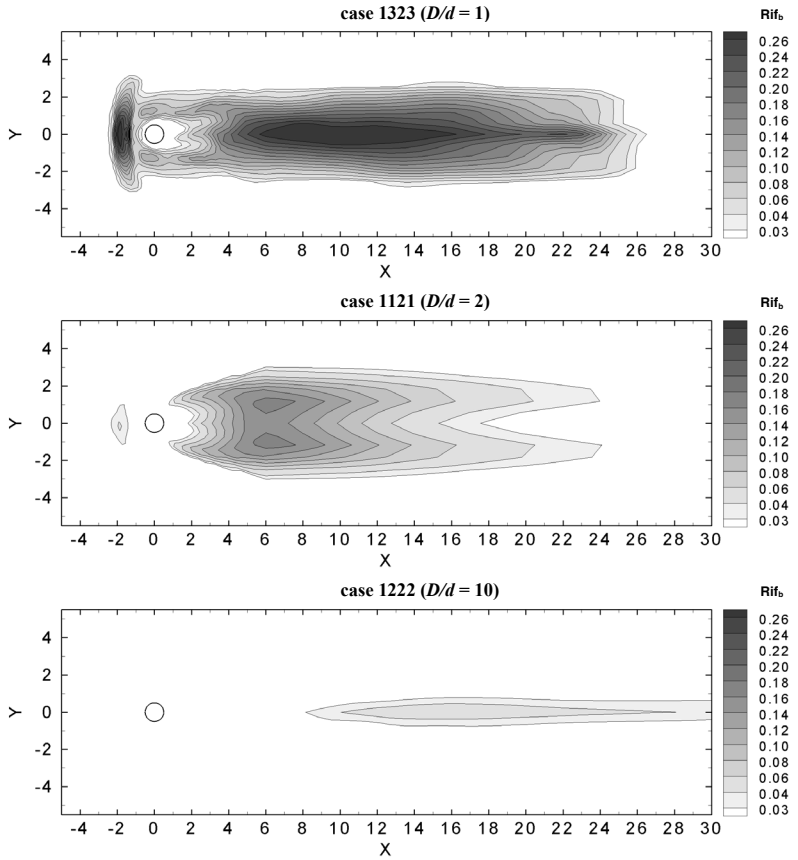

Figure 8.12: Influence of depth to diameter ratio on bulk flux Richardson number for cases with constant $Fr = 0.57$.

Apart from the lower absolute values for $D/d = 2$ it is also seen that the pattern is different to that for $D/d = 1$ where the maximum values are found right in the center of the wake while they are slightly moved to the left and right for the lower aspect ratio. This is consistent with the above findings for the entrainment rate and might therefore also be explained by the structure of the flow field in the wake which was found to be more concentrated along the cylinder axis for $D/d = 1$. However, as already argued in section 8.3.1 it is beyond the scope of the present work to analyze

the flux Richardson number in more detail as the major interest here is actually on the entrainment rates.

It can be concluded that unlike the Reynolds number above the depth to diameter ratio has a significant influence on the flow field, entrainment rates and also mixing efficiencies. As might have been expected the more of the current is blocked the larger is the impact of the cylinder on its dilution. It could be well shown that the influence of the cylinder decreases with increasing aspect ratio and more or less vanishes for D/d = 10. However, for this case the flow changes to another regime and the effect of the Reynolds number can no longer be neglected. Therefore it might be desirable to complement the present analysis with another aspect ratio, say D/d = 5, to exclude the Reynolds number effect and to get an even better idea about the influence of the current depth to cylinder diameter ratio.

8.3.4 Influence of Froude number

As seen from the first seven cases in Table 8.1 three different Froude numbers have been simulated for a constant depth to aspect ratio D/d =2 and varying Reynolds numbers. Although the Reynolds number was found above to be an insignificant parameter, for the present analysis of the influence of the Froude number the Reynolds number is kept constant for consistency and the reference case 1121 will be compared with case 2121 and case 3121.

The natural effect of the Froude number on the density current is an increase of the thickness of the interface with increasing Froude number. It might be therefore interesting first to investigate the evolution of the salinity field before the flow field in the wake is regarded in detail. Figure 8.13 shows the buoyancy production and salinity fields in a longitudinal section along the cylinder axis at $Y = 0$ for the three cases with increasing Froude number from top to bottom. In front of the cylinder the salinity contours clearly reflect the thickness of the interface increasing with Froude number. From the lowest Froude number in the upper panel it is now clear why the vertical resolution of the numerical grid had to be refined for this case as the complete salinity difference of $\Delta S = 25$ PSU takes place over a very small distance .

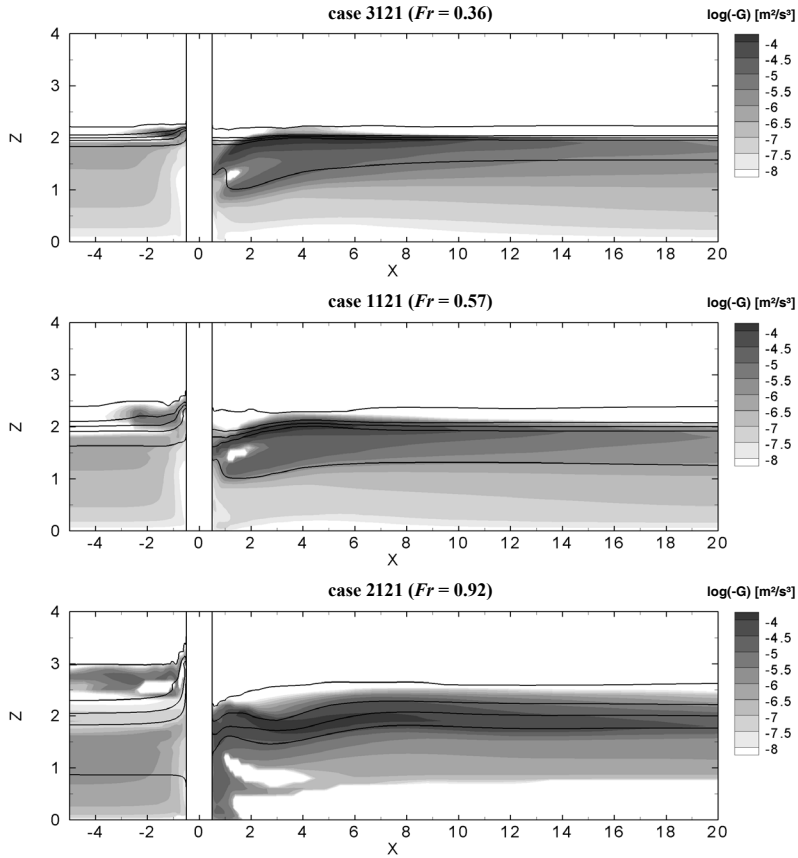

Figure 8.13: Influence of Froude number on buoyancy and salinity fields along a section at $Y = 0$, for cases with constant $Re = 2.5 \cdot 10^6$ and $D/d = 2$.

The decreasing density gradients for the other cases as reflected by the larger distance of the contour lines provide increasing susceptibility to mixing which explains the increasing occurrence of white areas in the buoyancy production field. For the largest Froude number the lowest contour line even completely disappeared in the wake and within the lower third of the current density gradients vanished or even became negative. It should be kept in mind that the absolute salinity difference decreases significantly with increasing Froude number (Table 8.1) and the total

amount of energy needed to locally mix the fluid gets less with increasing Froude number. Moreover Figure 8.13 only reflects the situation along the cylinder axis which is not necessarily representative for the lateral extent. To get a better idea about the flow field in the wake Figure 8.14 shows the results for the three cases in cross-sections at $X = 2$ and $X = 10$, in analogy to the preceding sections.

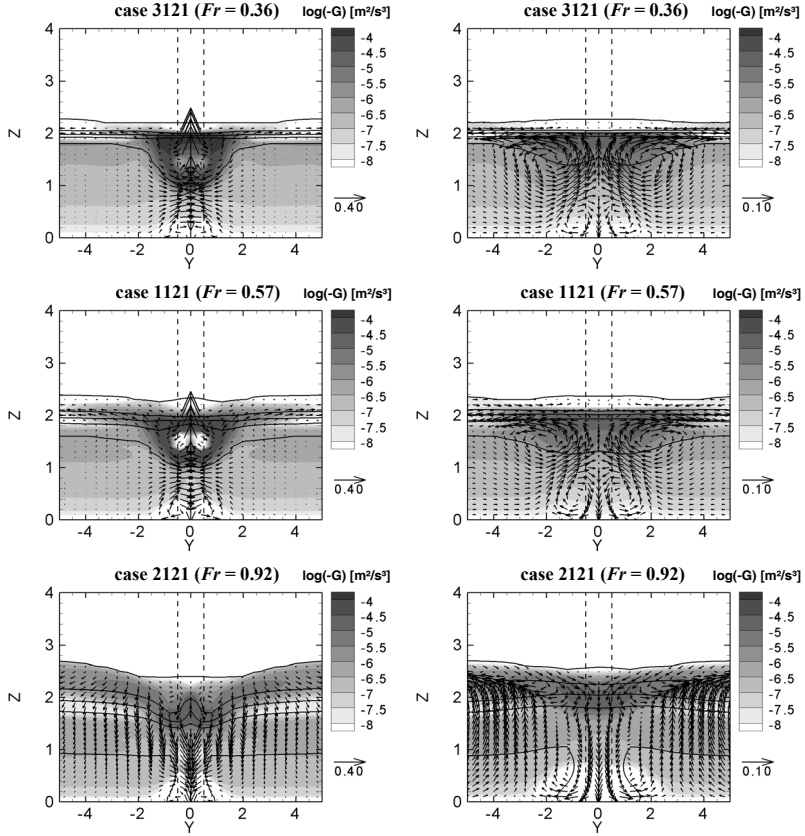

Figure 8.14: Influence of Froude number on the flow field in the wake for cases with constant $Re = 2.5 \cdot 10^6$ and $D/d = 2$. Left column: $X = 2$; right column: $X = 10$).

The wake patterns for the smaller Froude numbers $Fr = 0.36$ and $Fr = 0.57$ are very similar and show the typical features discussed in section 8.3.1, with strong upward velocities in the center plane at $X = 2$ and two clearly identifiable counter-rotating vortex pairs at $X = 10$. However, the flow field for $Fr = 0.92$ is significantly different. At $X = 2$ still a strong downward current in the center of the wake can be observed and there are only relatively low upward velocities in the core of the interface as indicated by the slightly lifted salinity contours. This does not imply that the upward current completely disappears for larger Froude numbers, but actually it is found further downstream and becomes most pronounced at $X = 4$ (not explicitly shown here). The tendency that all processes move downstream for higher Froude numbers could also be detected in Figure 8.13 where the minimum of the interface for $Fr = 0.92$ is found at $X \approx 3$ compared to $X \approx 1$ for the other cases. This behavior can be explained by the fact that the velocity is in the order of the propagation speed of disturbances which therefore are transported farer downstream and at the limit for $Fr > 1$ waves should be totally inhibited to travel upstream.

Another interesting effect of the Froude number is a smoothing of the flow field for $Fr = 0.92$ as very well seen in the cross-section at $X = 2$ but also for $X = 10$. This can be argued by the low stability of the interface which only offers a small resistance against disturbances to spread in cross-stream direction such that the whole flow field for the larger Froude number is much more uniform than for the smaller ones. By that the formation of the vortex pairs is inhibited and they can only hardly be detected in the lower right panel at $X = 10$. Finally, the field of (dimensional) buoyancy production supports the above findings that the amount of energy needed for mixing increases with decreasing Froude number and it suggest to investigate the effect on the entrainment rates.

Before the spatial distribution of the entrainment rates is discussed it should be recalled that the Froude number for all cases regarded in the preceding sections was $Fr = 0.57$ for which the natural entrainment rate of the undisturbed current was guessed to be $E \approx 5 \cdot 10^{-5}$. Now the Froude number is changed in the different cases and by that also the natural entrainment rates will change. Hence, for the presentation of entrainment induced by the cylinder it is useful to define other threshold values which are oriented at the natural rates. As these rates cannot be

accurately determined with the present numerical model they were guessed from available data in the literature which were compiled in Figure 7.2. Assuming the lowest limit the corresponding values could be assessed to be $E \approx 2 \cdot 10^{-5}$ for $Fr = 0.36$ and $E \approx 15 \cdot 10^{-5}$ for $Fr = 0.92$. Figure 8.15 shows the corresponding representation of the entrainment rates for the different cases with increasing Froude number from top to bottom.

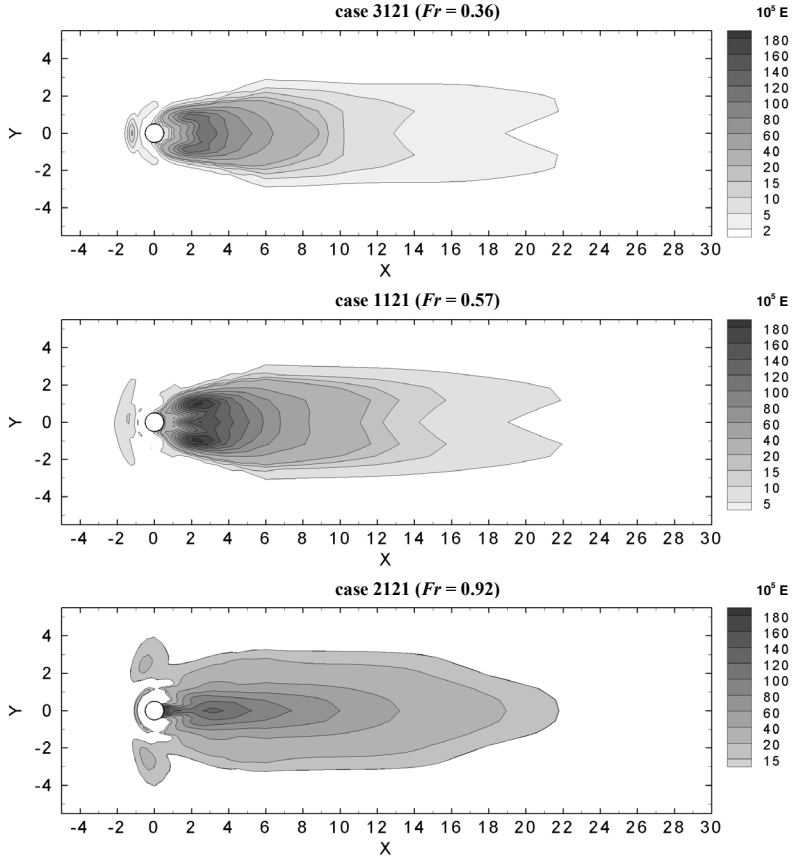

Figure 8.15: Influence of Froude number on entrainment for cases with constant $Re = 2.5 \cdot 10^6$ and $D/d = 2$. Note the different lowest contour levels.

As might have been expected from the similar flow fields in the wake for $Fr = 0.36$ and $Fr = 0.57$ also the patterns of the entrainment rates in the upper and middle panel are quasi identical except for slightly stronger maxima in the center of the near wake for $Fr = 0.57$. The absolute values, however, are different and suggest that in analogy to undisturbed currents entrainment induced by a cylinder also increases with Froude number. This tendency seems logical at first sight but is actually not supported by the results for $Fr = 0.92$ where the maximum values are clearly less than for $Fr = 0.57$ and also the pattern has changed. The highest rates are found right in the center of the wake rather than left and right of it and due to the homogeneity of the flow field discussed above the spatial distribution of the entrainment rates is much more uniform for $Fr = 0.92$.

The area of influence of the cylinder is more or less the same for all Froude numbers which is the result of the different threshold values based on the natural entrainment rates defined above. Also the pattern in the bow wave in front of the cylinder is relatively similar for all cases with the tendency to a larger lateral extent with increasing Froude number. This seems logical from the above argumentation that the potential of a local disturbance to laterally spread increases with decreasing stability of the interface and by that with increasing Froude number. Moreover, the comparable patterns support the preceding findings that the dynamics of the bow wave are presumably associated with the cylinder rather than the current itself.

As the Reynolds number is the same for all cases the bulk production of turbulent kinetic energy is also more or less identical. The difference in the entrainment rates above suggest to investigate how much of the total amount of turbulence production is used to mix the fluid. This is reflected by the spatial distribution of the bulk flux Richardson shown in Figure 8.16 where the Froude number again increases from top to bottom. At first sight it can be noted that the patterns correspond to those for the entrainment rates shown above and the flux Richardson number increases with decreasing Froude number. For the lowest Froude number regarded here, locally more than 30 % of the produced turbulent kinetic energy is used for mixing while the highest values found for $Fr = 0.92$ are only around 10 % although the entrainment rates in that region are larger than for $Fr = 0.36$.

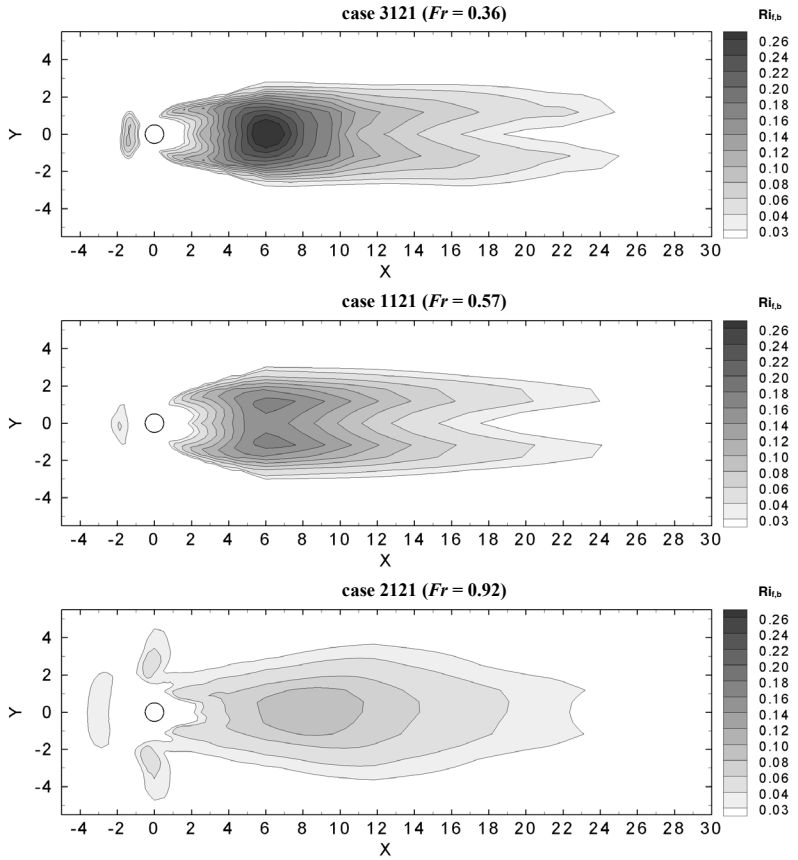

Figure 8.16: Influence of Froude number on bulk flux Richardson number for cases with constant $Re = 2.5 \cdot 10^6$ and $D/d = 2$.

As shown above the depth to diameter ratio has a comparably significant influence on entrainment rates and mixing efficiencies like the Froude number considered here. Therefore it might be interesting to investigate the Froude number dependence of the results also for other aspect ratios. As mentioned above this was not be done for the present thesis and poses a task for future work to support (or reject?) the present local results and to complement the dataset for the determination of the overall impact of the cylinder to be discussed in the following section.

8.3.5 Total entrainment

In the preceding sections the principal effect of a circular cylinder on the flow field, entrainment rates and mixing efficiencies of a density current has been analyzed and the influence of the individual parameters governing the flow has been thoroughly investigated. It seems useful now to analyze the overall impact of the cylinder on the dilution of the current first, before the influence of Coriolis forces is finally regarded in the next section.

The total entrainment induced by the cylinder is found by integrating the local entrainment rates over the area of influence of the cylinder indicated by the contour plots shown in the preceding sections (cf. Figure 8.9, Figure 8.11, Figure 8.15). The lowest contour levels were chosen by intention to correspond to the natural entrainment rates of the undisturbed current such that the additional amount due to the presence of the cylinder is clearly identified. However, without the presence of the cylinder the current would still be diluted by the natural entrainment rates which have therefore first to be subtracted from the results presented above before integrating. The corresponding total additional entrainment rates due to the cylinder are shown in Figure 8.17 as a function of the Froude number. Each of the individual points corresponds to one specific case and the results for the different aspect ratios can be distinguished by the various symbols. The curves represent some kind of entrainment law which will be discussed below. They have been added primarily in order to better visualize the results and to simplify their interpretation.

The clustering of the individual points reflects the negligible influence of the Reynolds number discussed in section 8.3.2. However, also one outlier can be noted giving $E \approx 0.04$ for $Fr = 0.57$ and $D/d = 2$ which is slightly higher than the values suggested by all other cases for this Froude number and aspect ratio. It corresponds to case 1112 which was found to show an ambiguous behavior with very high entrainment rates in front of and around the cylinder leading to the larger total amount compared to the other cases. However, as mentioned above, this strange behavior cannot be easily explained and could also be a numerical artifact. Therefore it seems justified and advisable to exclude this case from the further discussion.

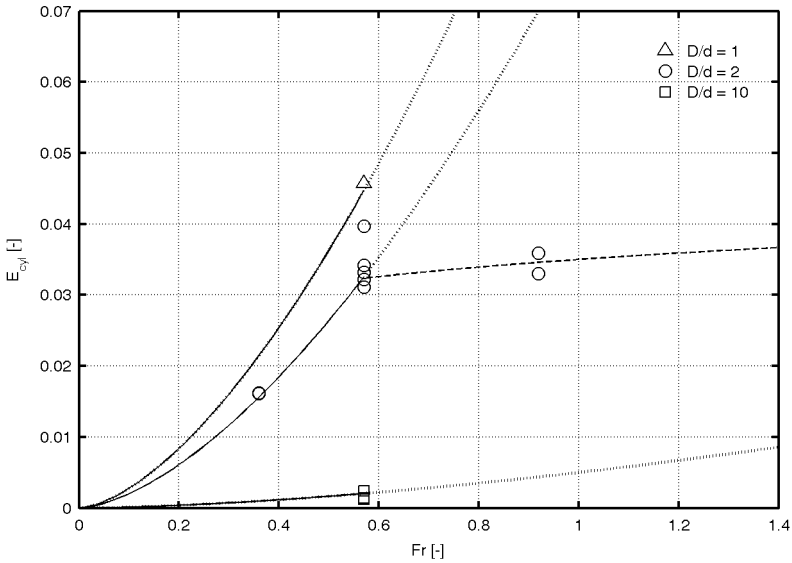

Figure 8.17: Total entrainment induced by a circular cylinder as function of the Froude number.

As mentioned above the curves represent the attempt to provide some kind of entrainment law. However, due to the sparse data set this law still suffers from many uncertainties and might be assumed to be only valid in the lower Froude number range represented by the full lines. The data suggest the entrainment law for the cylinder to be of the same form like the general entrainment law for undisturbed density currents given by (6.16) which in terms of the Froude can be written as:

$$E_{cyl} = m_1 Fr^{n_1} \,. \tag{8.6}$$

From the data for D/d = 2 (disregarding case 1112) the parameters could be determined to be $n_1 = 1.6$ and $m_1 = 0.08$. For the lack of further data the exponent n_1 was assumed to be independent of the aspect ratio and the other curves were fit through the (single) data points by adjusting the parameter m_1 only, which is found to be $m_1 = 0.11$ for $D/d = 1$ and $m_1 = 0.005$ for $D/d = 10$.

At first sight the curves seem to be a reasonable approach showing that the total additional entrainment induced by the cylinder increases with Froude number. This is consistent with the local entrainment rates discussed in section 8.3.4 above which also increased from $Fr = 0.36$ to $Fr = 0.57$ (cf. Figure 8.15). However, it was also found that for the higher Froude number $Fr = 0.92$ the maximum local entrainment rates in the near wake decrease again while the rates farer away are higher due to a more homogenous flow field. In consequence, the integrated total entrainment rates do not increase further as suggested by the power law. Much more they seem to approach a maximum value which has been tried to visualize by the dashed line.

While the increase of the cylinder induced entrainment for low Froude numbers seems comprehensible, justifying the appliance of (8.6), the background of the effect found for higher Froude numbers is less clear. It might as well be the case that the assumption of an asymptotic behavior for higher Froude numbers is wrong and the entrainment rates will even decrease which, however, can only be clearly judged with additional data. It is therefore inadvisable to provide a mathematical relationship for this effect at this point but in any case it can be concluded that the increase of the cylinder induced entrainment with the Froude number is limited to the lower Froude number range and will quickly approach a maximum value.

It can be expected that the same behavior also occurs for the other aspect ratios even if this assumption cannot be verified here due to the lack of data. By now the suggested entrainment law (8.6) was assumed to be valid also for higher Froude numbers, simply for reasons of presentation, but to reflect the uncertainty of the law in the range beyond $Fr = 0.57$ the lines have been dotted. In any case, Figure 8.17 emphasizes the strong need for a complementation of the present dataset.

However, the present data suggests that the total entrainment by the cylinder increases with decreasing aspect ratio (increasing blocking ratio) − as might have been expected from the lateral distribution of the entrainment rates in Figure 8.11. To allow for a better interpretation of this effect the data has been plotted as a function of current depth to cylinder diameter ratio in Figure 8.18 where the curves again represent a kind of entrainment law but now in terms of the aspect ratio.

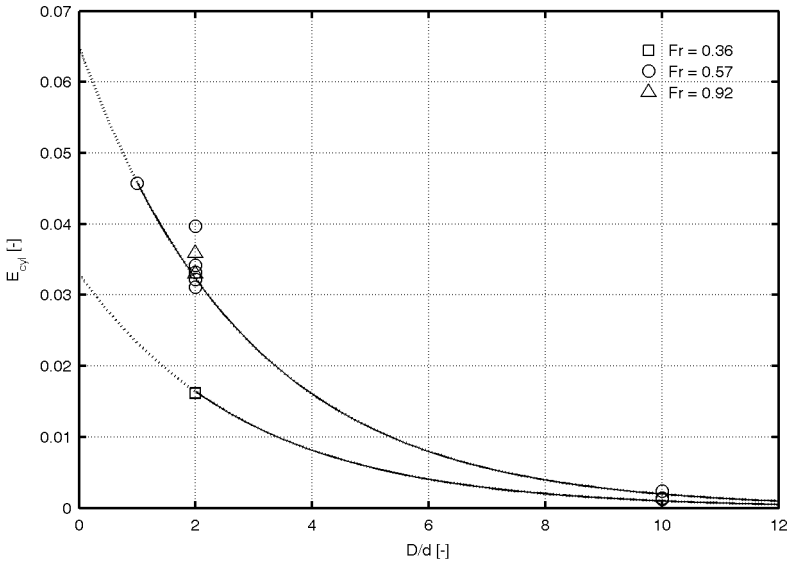

Figure 8.18: Total entrainment induced by a circular cylinder as function of the current depth to cylinder diameter ratio.

The data suggests the general form of this law being exponential:

$$E_{cyl} = m_2 e^{(n_2 D/d)}, \tag{8.7}$$

and the parameters found by a fit through the results for Fr = 0.57 (again ignoring case 1112) are n_2 = -0.35 and m_2 = 0.065. As the increase of entrainment with Froude number is limited the parameters for Fr = 0.92 are assumed to be the same, maybe with a slightly higher value for m_2. Due to the lack of data indeed the slope n_2 was assumed to be valid for all Froude numbers and the curve for Fr = 0.36 was found also adjusting m_2 only, which turned out to be m_2 = 0.033. Although the curves seem to represent the present data very well and nicely show the decrease of entrainment with increasing aspect ratio, the parameters (at least for Fr = 0.36) should be verified by additional data. It should also be noted that the entrainment law (8.7) looses validity for $D/d \rightarrow 0$ as at the limit entrainment will naturally vanish

and will not reach a finite value as indicated by the dotted lines. Thus, it might be interesting further to investigate the effect of the cylinder for very low aspect ratios in order to assess the ratio with maximum effect, but also this is left for future work.

Assuming that a larger Froude number for small aspect ratios will not significantly increase the entrainment rates the present data allows to asses the absolute maximum total entrainment rate induced by a circular cylinder which can be estimated not to be higher than about $E_{cyl} \approx 0.06$. However, the actual impact of the cylinder on the dilution of the current might be still a bit ambiguous. To shed some more light on the absolute values given above it is useful to relate them to the natural entrainment rates without the presence of a cylinder. This can be done regarding the total amounts of ambient fluid entrained into the current, the ratio of which will provide a measure for the actual consequence of the presence of a cylinder compared to the undisturbed case.

The total amount of entrained ambient fluid into an undisturbed density current can be given by

$$Q_E = U_s \cdot E \cdot A\,, \tag{8.8}$$

where U_s is the current speed, E is the natural entrainment rate of the current and A is the surface area over which the ambient fluid is entrained. The corresponding absolute amount of entrainment due to the cylinder is

$$Q_{E,cyl} = U_s \cdot E_{cyl} \cdot d^2\,, \tag{8.9}$$

where the factor d^2 reflects the fact that the total entrainment rate E_{cyl} given above was found by integration over an area normalized by the cylinder diameter. Combining (8.8) and (8.9) the impact of the cylinder on the dilution of the current can then be defined in terms of the ratio of entrainment induced by the cylinder to the natural entrainment:

$$\frac{Q_{E,cyl}}{Q_E} = \frac{E_{cyl}}{E} \cdot \frac{d^2}{A}\,. \tag{8.10}$$

The first term on the right hand side represents the actual impact of the cylinder as it defines the entrainment per unit area related to the natural entrainment without the presence of a cylinder. The corresponding values for the parameters investigated here are given in Table 8.3, where the values in brackets have been extrapolated.

	***Fr* = 0.36**	***Fr* = 0.57**	***Fr* = 0.92**
***D*/*d* = 1**	(1130)	920	(330)
***D*/*d* = 2**	800	650	230
***D*/*d* = 10**	(40)	30	(10)

Table 8.3: Total impact of a circular cylinder on a density current in terms of relative entrainment rates per unit area (E_{cyl} / E).

The values in the second column approve the above findings and reflect an increasing impact of the cylinder with decreasing aspect ratio. However, from the second row it is seen that the impact of the cylinder decreases with increasing Froude number which is the complete opposite from what was found for the entrainment rates in Figure 8.17 above. This is just due to the fact that the natural entrainment rates increase faster with Froude number than those induced by the cylinder (compare parameter n_1 with entrainment law (7.62)) which for larger Froude numbers are even stagnant. The absolute entrainment rates above are therefore relatively meaningless in terms of the actual impact of the cylinder on the current which can only be determined in comparison to the undisturbed situation.

The values given in Table 8.3 allow for an estimation of the global impact of an offshore wind energy farm on density currents in the Baltic Sea, which shall be shortly illustrated by a simple example based on the reference case 1121 above with Fr = 0.57 and D/d = 2. Assume the average distance of the wind energy devices to be 25.5 diameters (which presumably is even much more in a real wind farm) the normalized area in (8.10) is $A/d^2 = (25.5d)^2/d^2 \approx 650$ and the ratio of cylinder induced and natural entrainment is 1, which means that the natural entrainment rates within the wind farm are doubled. Assuming further that the natural entrainment of the current is constant over its whole way from the Sills to the deep basins, the ratio of the area of the wind farm and the surface of the current gives the impact of the

wind farm. In other words to increase the total amount of naturally entrained ambient fluid by only 1 % requires the total area of the wind farm (or many smaller ones) to make up 1 % of the total surface of the current which seems to be rather large.

Even if this simple example might seem to be quite academic it reflects a realistic situation to some degree and clearly demonstrates that the overall impact of offshore wind farms on the dilution of density currents in the Baltic Sea can be assumed to be rather small. However, this conclusion can actually only be drawn for purely two-dimensional currents but oceanic currents are usually subject to the effect of Coriolis forces. Hence, it is left to investigate the influence of Coriolis forces on the cylinder induced entrainment which will be done now in the next section.

8.3.6 Effect of Coriolis forces

The discussion in chapter 7 was focused on density currents under the influence of Coriolis forces and the numerical model could be shown to work very well for their simulation. However, for the present analysis Coriolis forces have been neglected by now as they induce lateral currents which complicate the flow around the cylinder and make the analysis of the fundamental processes very difficult. To demonstrate this complexity Figure 8.19 shows the flow field at different cross-sections in front of and behind the cylinder for the reference case 1121 but now with Coriolis forces.

The results can be compared to those without Coriolis forces presented in Figure 8.4 but it should be noted that the velocity vectors here are equally scaled in all cross-sections and the lower panels show other cross-sections than those in Figure 8.4. These differences have their seeds in the lateral current induced by the Coriolis forces which can be very well identified in the upper left panel at X = -5 where the influence of the cylinder is not intense yet. It clearly shows the typical pattern with a relatively slow component in positive Y-direction below the interface and a strong flow in negative Y-direction within the interface with velocities reaching up to 50 % of the current speed. The latter is the reason for the scaling of the velocity vectors and causes any disturbance within the interface to be transported laterally away from the cylinder.

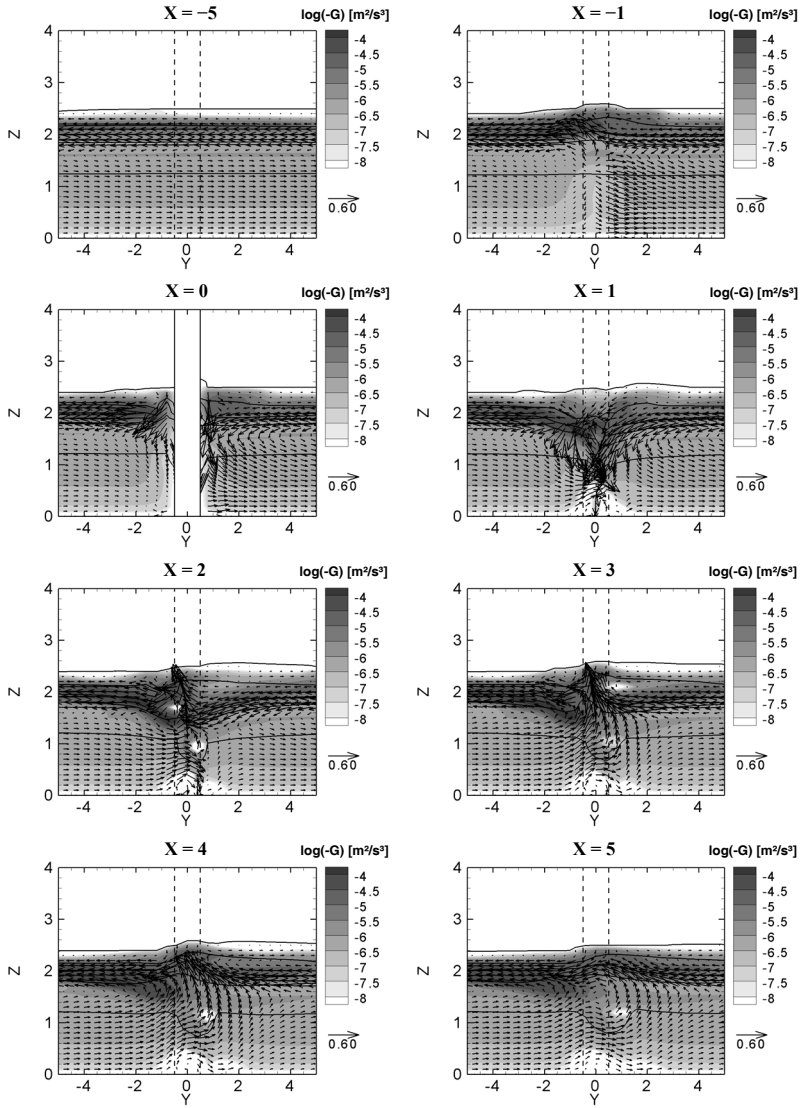

Figure 8.19: Flow field at different cross-sections in front of and behind the cylinder for the reference case 1121 with Coriolis forces. Note that in comparison to Figure 8.4 velocity vectors are equally scaled.

Note in this context that the view of all cross-sections presented here is against the flow direction (negative X-direction) which was not important up to now due to the symmetry of the flow patterns. Here, however, it implies that a current appearing to be directed to the left in the cross-sections presented in Figure 8.19 actually means a transport to the right in streamwise direction.

Due to the strong lateral current within the interface the cylinder wake is deflected to the right (in streamwise direction) and a presentation of cross-sections aligned at $Y = 0$ far away from the cylinder is actually not useful as indicated by the results at $X = 4$ and $X = 5$ showing the rapidly decaying influence of the cylinder. Even closer to the cylinder a sound analysis of the complex flow field based on the cross-sections presented here is also not possible and requires a different approach.

However, it is beyond the scope of the present work to go into the details but at least some basic features can be extracted from the results in Figure 8.19. The lifting of the interface in front of the cylinder at X = -1, the resulting strong downward currents around the cylinder at $X = 0$, $X = 1$ and $X = 2$ and the succeeding upward current at $X = 3$ and $X = 4$ can be clearly identified. The motion of the interface and the induced vortices caused by the vertical currents can also be detected. Due to the secondary current induced by the Coriolis force these vortices are transported laterally away from the cylinder. Alike the increased buoyancy production within the interface due to the cylinder shows the deflection to the right (in streamwise direction) caused by the lateral currents.

The complexity of the flow field suggests the patterns of entrainment rates being not less complicated. Thus the influence of Coriolis forces was only sparsely analyzed by comparing four cases at constant Froude number $Fr = 0.57$: case 1111, case 1121, case 1222 and case 1323 (cf. Table 8.1). Assuming the influence of the Reynolds number to be also an unimportant parameter for the present situation, a comparison of the first two cases with the same aspect ratio ($D/d = 2$) will provide an idea about the effect of Coriolis forces alone. For this purpose the spatial distribution of the additional entrainment rates for cases 1111 and 1121 is shown in Figure 8.20.

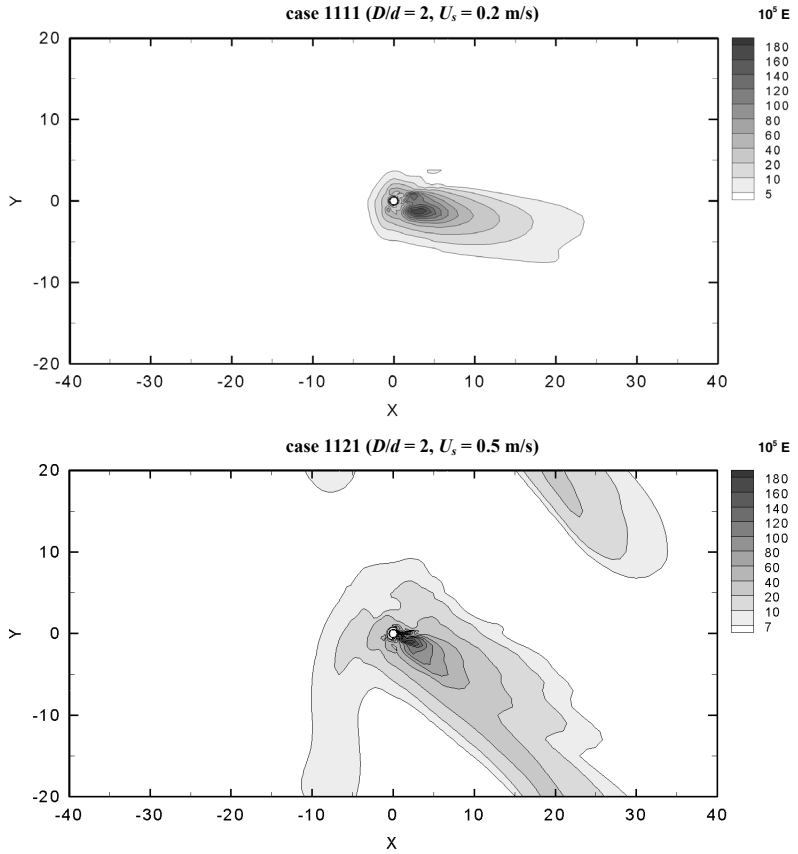

Figure 8.20: Influence of Coriolis forces on entrainment for two cases with the same aspect ratio (D/d = 2) but different current speeds (Ekman numbers). Note the different lowest contour levels.

Before the results are further discussed some comments on their representation must be given. For a better comparison with the results of the corresponding cases without Coriolis forces as shown in the preceding sections the scaling of the contours has been chosen to be the same except for the lowest contour levels. Although the natural entrainment rates of the undisturbed currents are $E \approx 2.5 \cdot 10^{-5}$ for case 1111 and $E \approx 3.5 \cdot 10^{-5}$ for case 1121 (recall the dependence of entrainment rates on the

Ekman number (chapter 7.1.5)) the lowest contour levels are 2 times higher. The reason for this choice is that in contrast to the cases without Coriolis forces above now the natural entrainment is well predicted by the numerical model and the changeover to the entrainment induced by the cylinder is much smoother. Therefore the threshold value for a distinct determination of the cylinder induced entrainment was defined to be twice the natural entrainment rate.

The entrainment rates nicely reflect the deflection of the cylinder wake to the right as expected from the discussion of the flow field above. As the lateral velocities due to Coriolis forces increase with the speed of the current the deflection for case 1121 with U_s = 0.5 m/s is much stronger than that for case 1111 with U_s = 0.2. Moreover it can be observed that the wake becomes longer with increasing speed of the current and even leaves the computational domain through the right boundary. However, due to the periodic boundary conditions it re-enters through the left boundary and by that the total area of influence of the cylinder is kept by the present domain size. The increase of the wake length suggests the existence of some kind of sustaining mechanism due to the lateral current which obviously also affects the entrainment rates caused by the bow wave in front of the cylinder. However, the physical background for this mechanism is not clear yet and poses an issue for further investigations.

Even if the area of influence of the cylinder is considerably different for the two cases the absolute entrainment rates are very similar and comparable to those found for the corresponding cases without Coriolis forces above. This significantly improves the credibility of the foregoing results which before might have seemed to be a bit shady due to the discrepancy of the numerical model for the simulation of purely two-dimensional undisturbed currents. It further shows that the maximum local entrainment rates induced by a circular cylinder obviously only depend on the Froude number and the current depth to cylinder diameter ratio. The former as a measure for the resistance of the current against disturbances and the latter as a measure for the intensity of these disturbances.

However, although the Froude number and the aspect ratio are identical for both cases regarded here the spatial distributions of entrainment are significantly different

which could be argued by the current speed so far. To more generally account for this effect it seems useful to introduce the Ekman number (7.50) as another governing parameter for the flow in analogy to the undisturbed currents discussed in chapter 7. The corresponding values for the two cases above are $K = 0.36$ for case 1111 and $K = 0.92$ for case 1121, suggesting that the area of influence of the cylinder and by that the total entrainment induced by the cylinder increase with the Ekman number. However, for reasons mentioned above it is beyond the scope of the present work to further investigate the influence of another parameter and this task is left for future research.

The resemblance of the absolute local entrainment rates with and without Coriolis forces found above indicates that the processes of mixing must also be comparable. Although the major interest here is on the actual result of mixing rather than the details of the processes involved it might be interesting to have a look at the spatial distribution of the bulk flux Richardson number at least to compare it with the results for purely two-dimensional currents presented above. Figure 8.21 shows the corresponding results for the two cases regarded here where again the scaling of the contours is identical to that used in the preceding sections.

Especially for the less deflected wake in case 1111 the similarity with the results presented in section 8.3.1 is striking with minimal efficiencies in the highly turbulent near wake and maximum values found farer away from the cylinder where entrainment rates have already decayed. Both cases have more or less identical maximum values of $Ri_{f,b} = 0.16$ which seems to be universal for this Froude number and aspect ratio.

Concerning the entrainment induced by the bow wave in front of the cylinder it can be seen that it is associated with about twice the efficiency of mixing of an undisturbed current. Also this is consistent with the findings above and supports the corresponding entrainment rates being caused by the cylinder even if the actual background of this phenomenon is not fully understood yet.

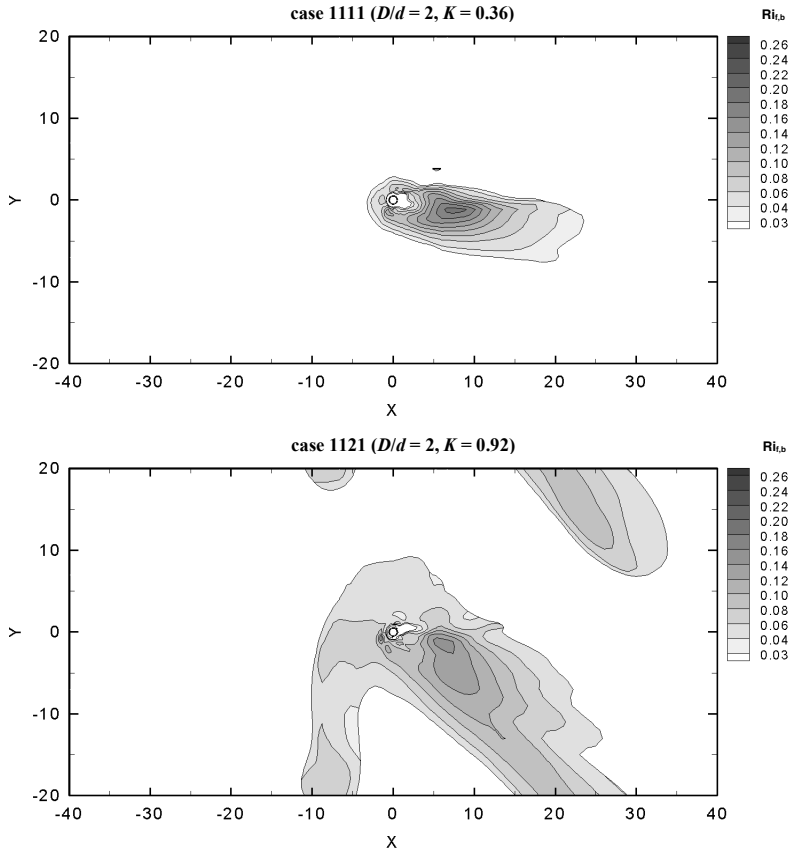

Figure 8.21: Influence of Coriolis forces on bulk flux Richardson number for two cases with the same aspect ratio (D/d = 2) but different Ekman numbers.

To sum up it can be concluded that the local processes of cylinder induced mixing are governed by the Froude number and the depth to diameter ratio alone while the spatial distribution and the total entrainment depend on the Ekman number. To at least partly approve these conclusions the spatial distribution for the remaining two cases 1222 and 1323 with constant Froude and Ekman number (Fr = 0.57, K = 0.92) but different aspect ratios are shown in Figure 8.22.

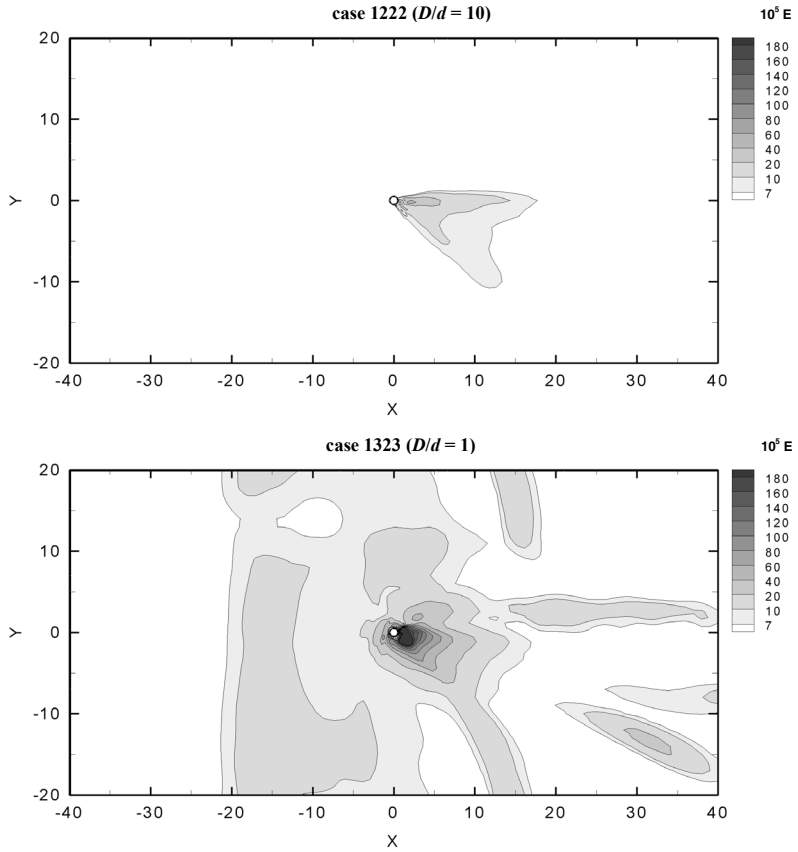

Figure 8.22: Influence of depth to diameter ratio on entrainment rate for cases with constant Froude and Ekman number (Fr = 0.57, K = 0.92).

At first sight the results appear to be consistent with the findings of section 8.3.3 with much lower entrainment rates for D/d = 10 and higher values for D/d = 1 compared to case 1121 shown above with D/d =2. Also the increasing intensities in front of the cylinder with decreasing aspect ratio are supported by the results above, even if the whole spatial distribution for case 1323 here looks a bit chaotic. The strange pattern for entrainment in this case might seem a bit ambiguous and should be checked for plausibility in the future, but at least it reflects the expected

sustaining effect of the Coriolis forces which can also be seen for case 1222. Here, however, the pattern looks much more reliable and compared to the corresponding case without Coriolis forces in Figure 8.11 the actual entrainment induced by the cylinder is much clearer defined even if the local values are of the same order.

By the spatial distribution of the cylinder induced entrainment discussed so far it could be shown that Coriolis forces obviously do not alter the absolute entrainment rates (governed by Fr and D/d only) but exert some kind of sustaining effect on mixing which increases with the Ekman number. Due to this effect the area of influence of the cylinder is much larger compared to that for currents without Coriolis forces suggesting that the total cylinder induced entrainment will also be larger. Even if it was identical the total impact of the cylinder, given by the ratio of cylinder induced entrainment to natural entrainment, would be larger in any case as the latter is generally smaller for currents with Coriolis forces. Table 8.4 summarizes the results for the four cases with Coriolis forces regarded here with the total entrainment and the total impact given in the first and second row, respectively.

	case 1111 (D/d = 2, K = 0.36)	**case 1323** (D/d = 1, K = 0.92)	**case 1121** (D/d = 2, K = 0.92)	**case 1222** (D/d = 10, K = 0.92)
E_{cyl}	0.046	0.168	0.119	0.009
E_{cyl} / E	1840	4800	3400	260

Table 8.4: Total entrainment and total impact of a circular cylinder for the four cases with Coriolis forces at constant Froude number, Fr = 0.57.

As expected from the larger area of influence the total entrainment induced by the cylinder is indeed much higher than that found in chapter 8.3.5 where the maximum possible value was claimed to be about $E_{cyl} \approx 0.06$. Despite the lower natural entrainment rates for the currents here also the total impact for the individual cases can be seen at first sight to be much larger than the values given in Table 8.3 above. Looking more closely and comparing the total impact in the last three columns in Table 8.4 with the corresponding values in the second column of Table 8.3 it can be noted that for small aspect ratios (case 1323 and case 1121) the total impact here is exactly 5.2 times larger than that without Coriolis forces. As the incoming current

was the same for all three cases also the ratio of the corresponding natural entrainment rates is constant (3.5/5 = 0.7) and it follows that the total entrainment induced by the cylinder is about 3.6 times larger. This constant relation implies that the slope n_2 = -0.35 found for the entrainment law given by (8.7) is interestingly also valid for the present cases with Coriolis forces. Using this slope a fit through the data suggests the other parameter to be m_2 = 0.24 which is exactly 3.6 times the value found in section 8.3.5, as might have been expected.

However, even if the general effect of Coriolis forces could be demonstrated by the present examples they do not allow for a precise predication about the influence of the Ekman number. If the parameter n_2 is really a universal constant or this was just a coincidence here must therefore be proved in future work. By now it can only be said that unlike for undisturbed density currents entrainment induced by a cylinder increases due to the effect of Coriolis forces. Concerning the impact of offshore wind energy farms on density currents in the Baltic Sea (cf. example in section 8.3.5) it can be concluded that even if the increase of the total impact due to Coriolis forces would be a factor of 10 (instead of 5.2 above) the overall effect might still be regarded to be of minor importance.

8.3.7 Concluding remarks

Before the complete thesis is summarized in the next chapter it is worth to draw some conclusions from the above discussions. Entrainment induced by a circular cylinder was found to be generally governed by four parameters, the cylinder Reynolds number, the Froude number, the depth to diameter ratio and, if Coriolis forces are present, the Ekman number. The Reynolds number in the present order of magnitude ($Re \approx 10^6$) was found to be unimportant while the other three parameters could be shown to have a certain effect on mixing and entrainment. The Froude number and aspect ratio govern the local intensities of mixing while the lateral extent of the area of influence of the cylinder basically depends on the Ekman number.

The numerical simulations above allowed for a detailed analysis of the flow field, entrainment rates and mixing efficiencies due to the cylinder and provided many

insights into the fundamental processes. The motivating question for the present work concerning the impact of offshore wind farms on the dilution of density currents in the Baltic Sea can be answered from the present data to be rather insignificant. However, there are still many open questions remaining which require further research not only from a scientific point of view:

- Are the proposed entrainment laws for the dependence on current depth to cylinder diameter ratio and (small) Froude numbers correct? If yes, what are the right parameters.
- When does the increase of entrainment begin to decay with larger Froude numbers and what is the effect of cylinders on supercritical currents (what is the entrainment law for higher Froude numbers)?
- How does entrainment behave for very low depth to diameter ratios and what is the absolute limit for cylinder induced entrainment?
- What is the exact influence of the Ekman number and are the proposed entrainment laws indeed independent of it (is n_2 a universal constant)?
- Will smaller Reynolds numbers become a governing parameter? If yes, can laboratory data used for predictions on larger scales or what is the scaling effect?
- What are the exact processes governing entrainment in the bow wave in front of the cylinder?
- What is the overall effect of a cylinder group and how do (closely spaced) cylinders influence each other?

Even if this list might be anything else but complete and it actually only refers to circular cylinders it clearly emphasizes that this interesting subject provides a lot of tasks for future work.

9 Summary and conclusions

The major goal of the present thesis was the investigation of the influence of circular cylinders on density currents motivated by the desire to determine the impact of planned offshore wind farms on the dilution of such currents in the Baltic Sea. The approach to the problem in the present case was based on detailed three-dimensional numerical simulations requiring a proper definition of the issues of matter and a thorough validation of the numerical model. By that the thesis can be basically divided into three parts, a basic introduction of the general physical background of the governing equations for the numerical model (chapters 2, 3 and 4), a discussion of the specific issues of the present problem and the modification and validation of the numerical model (chapters 5, 6 and 7) and finally the analysis of the simulations for the flow of density currents around a circular cylinder.

Mixing is generally associated with turbulence which therefore posed a crucial aspect for this thesis. After a short introduction to the general problem and the background of the basic equations in chapters 1 and 2 the nature of turbulence and its consideration in a numerical model were described very detailed in chapter 3. Special emphasis was placed on the Reynolds averaged Navier-Stokes (RANS) equations being the basis for all simulations in the present work. As it was not clear from the beginning which turbulence model is best suited for the present problem many different models were considered and thoroughly discussed.

The actual core of the present work begins in chapter 5 where the general features of the flow around a circular cylinder were discussed and the numerical model was validated by a comparison with data from the literature (Cantwell & Coles (1983)). It was demonstrated that the flow field around a cylinder depends on the cylinder Reynolds number and the peculiarities of the different flow regimes were illustrated. In view of the high Reynolds numbers to be expected for the actual problem here, the validation was carried out for Re = 140000 as no appropriate measurements for higher numbers exist. Several different turbulence models and grid resolutions were tested and the results were compared to the laboratory data and data of other numerical simulations from the literature. The focus was set on the turbulence in the

wake as it will be the major source for mixing of a density current. It could be shown that the grid resolution has no significant influence on the results as long as the boundary layer at the cylinder is fine enough resolved. Concerning the turbulence models it turned out that a Reynolds stress model (RSM) with the least modeling assumptions involved provides very reasonable results, as expected. However, in contrast to all other considered models, also the RNG k-ε model and the SST k-ω model could be shown to be equally well suited for the simulation of this kind of flow.

After the basic phenomena for the (unstratified) flow around a circular cylinder had been discussed and the numerical requirements for their simulation had been determined the general aspects of density stratification were presented in chapter 6. The processes associated with mixing were explained and the entrainment assumption parameterizing the effect of mixing which is a key issue for this work was introduced. Other important parameters to describe the effects and properties of stratified fluids, like the turbulent Prandtl number, gradient Richardson number, flux Richardson number, and stationary Richardson number were presented.

A major effect of stratification is the damping of turbulence which must also be regarded in the numerical model. This can be done by an additional term in the transport equations for the turbulent quantities accounting for the production of buoyancy. While its role in the turbulent kinetic energy equation is physically sound the corresponding effect on the dissipation rate is less clear but could be shown to be associated with the stationary Richardson number. By simulations of wind induced entrainment in a stably stratified fluid it was found that a reasonable value for the stationary Richardson number of $Ri_{st} = 0.25$ provides the best agreement with an empirical solution (Price (1979)) based on laboratory data (Kato & Phillips (1969)). Moreover this validation of the numerical model showed that mixing in a stratified shear layer is indeed mostly governed by the stationary Richardson number and the turbulent Prandtl number or the choice of turbulence model play an insignificant role.

Before the mixing of density currents induced by a cylinder was finally regarded it was necessary first to discuss the undisturbed nature of these currents and to validate the numerical model for their simulation. To get a better idea about the properties

and the behavior of undisturbed density currents a depth integrated theory (similar to that provided by Arneborg et al. (2007)) was derived in chapter 7 which also served as the major reference for the validation of the numerical model. As oceanic density currents are usually subject to Coriolis forces these were included in the theory as well as the numerical simulations. While the flow around a cylinder was found to be governed by the Reynolds number the governing parameters for density currents are the densimetric Froude number and (if Coriolis forces are present) the Ekman number and entrainment could be shown to be a function of both parameters.

The performance of the numerical model for the simulation of undisturbed density currents was inspected by means of one-dimensional simulations only resolving the vertical water column. A preliminary test approved that the choice of turbulence model has no significant influence on the results as long as the stationary Richardson number can be fixed which is not immediately possible for the RNG k-ε model due to an additional term in the dissipation rate equation. In spite of the good results for the unstratified cylinder flow in chapter 5 this model could therefore be regarded to be inappropriate for the intention of this work. Instead it could be concluded that the SST k-ω model is most well suited for the present purposes and therefore all following simulations were only performed with this model.

The comparison of numerical simulation results with the theory showed very nice agreement concerning all relevant properties of the current and the credibility of the model could be finally approved by a further validation against field measurements in the Arkona Basin (Arneborg et al. (2007)) even if the real situation could only be partly reflected within the one-dimensional domain. However, it was also shown that without the secondary lateral currents induced by the Coriolis forces the numerical simulations for the prediction of the long time evolution of undisturbed density currents in a one-dimensional model will inevitably fail. This is due to the zero gradient in the velocity profile below the interface which in case of the present two-equation turbulence models based on the turbulent viscosity assumption leads to a singularity in turbulence production and an ambiguous behavior of the current interface.

As the analysis of cylinder induced entrainment requires only the simulation of a small section of the current the erroneous prediction of turbulence production was claimed to be of minor importance which could be supported by reasonable results for simulations in a finite channel. Moreover it could be argued that the inherent discrepancy of the numerical model is insignificant for the planned simulations as the three-dimensional flow field in the wake of the cylinder prevents the singularity in turbulence production, anyway.

According to the motivation of this thesis the analysis of cylinder induced mixing in chapter 8 was based on simulations on a natural scale. However, to provide the outcome of this work with a more general matter all results were evaluated and presented by means of non-dimensional parameters governing the flow. For the present problem these were identified to be the densimetric Froude number, in terms of the general stability of the current, as well as the cylinder Reynolds number and the ratio of current depth to cylinder diameter, in terms of the flow properties around the cylinder. If Coriolis forces are further regarded the Ekman number could be shown to be a fourth governing parameter. However, the lateral currents induced by Coriolis forces significantly complicate the flow around the cylinder and inhibit an analysis of the basic effects. The major emphasis was therefore set on currents without Coriolis forces and the effect of the Ekman number was only shortly discussed at the end.

The influence of the other governing parameters on the flow field, entrainment rates and mixing efficiencies were thoroughly investigated by means of a parameter study. As could be expected from the discussion of unstratified cylinder flow in chapter 5 it turned out that the Reynolds number in the present order of magnitude ($Re \approx 10^6$) is rather unimportant. While the magnitude of the Reynolds number strongly depends on the scale of the flow the Froude number and aspect ratio are scale independent and could be shown to have a certain influence on the results.

A comparison of the spatial distributions of the entrainment rates showed that the local effect of the cylinder is quite significant with entrainment rates being up to 2 orders of magnitude larger than those of an undisturbed current. However, the area of influence of the cylinder is confined and was found to be only about 20 diameters

long and 6 diameters wide, more or less independent of Froude number and aspect ratio. On the other hand there is also some entrainment in front of the cylinder induced by the bow wave which showed up to change with both parameters even if it was not possible to find a clear dependence. As more than 90 % of the total entrainment is due to the wake the significance of the bow wave for the global effect of the cylinder is limited, anyway.

The global effect of the cylinder can be regarded as the total amount of additionally entrained ambient fluid found by integration of the local entrainment rates. Based on the admittedly sparse present data it was possible to provide some kind of entrainment laws for the dependence of the total entrainment on the Froude number and aspect ratio, respectively. The law for the latter showed an exponential decrease of entrainment with increasing depth to diameter ratio while that for the Froude number was assumed to be a potential law like for undisturbed density currents with entrainment increasing with Froude number. However, as was suggested by the local entrainment rates the potential law is only valid for smaller Froude numbers and the increase of the total entrainment gets less with higher Froude numbers. By that the maximum possible entrainment induced by a cylinder could be assessed to be limited and was found to be $E_{cyl} < 0.06$.

The actual impact of the cylinder on a density current cannot be defined by the total entrainment alone but must be seen in relation to the natural situation without the presence of a cylinder. The total impact, defined by the ratio of the total cylinder induced entrainment to the natural entrainment rate, could then be used for an estimation of the influence of offshore wind farms. By a simple though quite realistic example it was shown that the amount of additionally entrained Baltic Sea water into the current approximately scales with the area of potential wind farms. An increase of the natural entrainment by only 1 % requires the total area of wind farms to make up 1 % of the total surface of the current.

After the basic effects of cylinder induced mixing had been thoroughly analyzed, finally the effect of Coriolis forces was shortly discussed and the Ekman number was introduced as a further governing parameter. The complexity of the flow field around the cylinder was presented and it could be shown that entrainment in the

wake is deflected by the strong lateral currents within the interface due to the Coriolis forces.

In spite of the complex flow field and the deflection of the wake local entrainment rates and bulk flux Richardson numbers were found to be independent of the Ekman number but only depend on Froude number and aspect ratio as discussed before. Coriolis forces seemed to have generally a sustaining effect on entrainment such that the area of influence of the cylinder increases with increasing Ekman number and the total entrainment also gets larger. By an example typical for a situation in the Baltic Sea it could be shown that the total impact of a cylinder is about 5 times larger due to the presence of Coriolis forces. However, the effect of Coriolis forces and the influence of the Ekman number were only sparsely analyzed and definitely require further research.

It was the first time that the influence of cylindrical structures on mixing and entrainment in density currents has been investigated in such detail. Although this work provided many insights into the individual processes and allowed for a general estimate of the impact of circular cylinders on density currents, the present analysis can be regarded to be far from being complete. Some tasks for future work have been suggested in chapter 8.3.7, the most important being a complementation of the present dataset for the analysis of the Froude number and aspect ratio dependence of entrainment by the cylinder and a further analysis of the influence of the Ekman number to gain more confidence in the present results. Moreover, it might be desirable to reconsider the Reynolds number which is assumed to become an important parameter if it takes smaller values. As these are usually found on smaller scales it suggests the employment of laboratory experiments the results of which could also be used for a direct validation of the numerical model and a further approval of the validity of the present findings.

In any case, concerning the primal question of this work it might be concluded that the impact of offshore wind farms on the overall balance of density currents in the Baltic Sea is rather small.

10 References

AGARD, 1998. A Selection of Test Cases for the Validation of Large-Eddy Simulations of Turbulent Flows. AGARD−AR−345, AGARD Advisory Report 345.

Ahmed, F., and Rajaratnam, N., 1998. Flow around Bridge Piers. Journal of Hydraulic Engineering 124: 288−300.

Arneborg, L., 2002. Mixing efficiencies in patchy turbulence. Journal of Physical Oceanography 32, 1496−1506.

Arneborg, L., Fiekas, V, Umlauf, L., Burchard, H., 2007. Gravity Current Dynamics and Entrainment - a Process Study based on Observations in the Arkona Sea. Journal of Physical Oceanography 37, 2094−2113.

Aschenbach, E., 1968. Distribution of local pressure and skin friction around a circular cylinder in cross-flow up to Re = 5 x 10^6. Journal of Fluid Mechanics 34, 625 − 639.

Baringer, M. O., Price, J. F., 1997. Momentum and energy balance of the Mediterranean outflow. Journal of Physical Oceanography 27, 1678−1692.

Baumert, H., Peters, H., 2004. Turbulence Closure, Steady State, and Collapse into Waves. Journal of Physical Oceanography 34, 505−512.

Bosch, G., 1995. Experimentelle und theoretische Untersuchung der instationären Strömung um zylindrische Strukturen. Dissertation. Institut für Hydromechanik, Universität Karlsruhe, 206 pp.

Boussinesq, J., 1877. Théorie de l'Écoulement Tourbillant. Mémoires Présentés par Divers Savants Acad. Sci. Inst. Fr., 23: 46–50.

Boussinesq, J., 1903. Théorie Analytique de la Chaleur, 2iême partie. Gauthier Villars, Paris.

Breuer, M., 2000. A challenging test case for large eddy simulation: high Reynolds number circular cylinder flow. International Journal of Heat and Fluid Flow 21, 648−654.

Breuer, M., 2002. Direkte numerische Simulation und Large-Eddy Simulation turbulenter Strömungen auf Hochleistungsrechnern. Habilitation. Berichte aus der Strömungstechnik, Shaker Verlag, Aachen, 431 pp.

Briggs, W. L., van Emden, H., McCormick, S. F., 2000. A Multigrid Tutorial, Second Edition. Society for Industrial and Applied Mathematics (SIAM). 193 pp.

Burchard, H., 1995. Turbulenzmodellierung mit Anwendung auf thermische Deckschichten im Meer und Strömungen in Wattengebieten. Dissertation. GKSS-Forschungszentrum Geesthacht, GKSS 95/E/30, 299 pp.

Burchard, H., Baumert, H., 1995. On the performace of a mixed-layer model based on the k-ε turbulence closure. Journal of Geophysical Research 100, 8523−8540.

Burchard, H., Bolding, K., 2001. Comparative Analysis of Four Second-Moment Turbulence Closure Models for the Oceanic Mixed Layer. Journal of Physical Oceanography 31, 1943−1968.

Burchard, H., Lass, H. U., Mohrholz, V., Umlauf, L., Sellschopp, J., Fiekas, V., Bolding, K., Arneborg, L., 2005. Dynamics of medium-intensity dense water plumes in the Arkona Basin, Western Baltic Sea. Ocean Dynamics 55, 391−402.

Cantwell, B., Coles, D., 1983. An experimental study of entrainment and transport in the turbulent near wake of a circular cylinder. Journal of Fluid Mechanics 136, 321−374.

Canuto, V. M., Howard, A., Cheng, Y., Dubovikov, M. S., 2001. Ocean Turbulence. Part I: One-point Closure Model − Momentum and Heat Vertical Diffusivities. Journal of Physical Oceanography 31, 1413−1426.

Caulfield, C. P., Peltier, W. R., 1994. Three-dimensionalization of the stratified mixing layer. Physics of Fluids 6. 3803−3805.

Caulfield, C. P., Peltier, W. R., 2000. The anatomy of the mixing transition in homogeneous and stratified free shear layers. Journal of Fluid Mechanics 413, 1−47.

Cenedese, C., Whitehead, J. A., Ascarelli, T. A., Ohiwa, M., 2004. A dense current flowing down a sloping bottom in a rotating fluid. Journal of Physical Oceanography 34, 188−203.

Cheng, Y., Canuto, V. M., Howard, A. M., 2002. An improved model for the turbulent PBL. Journal of Atmospheric Sciences 59, 1550−1565.

Corcos, G. M., Sherman, F. S., 1984. The mixing layer: deterministic models of a turbulent flow. Part 1. Introduction and the two-dimensional flow. Journal of Fluid Mechanics 139, 29−65.

Cortesi, A. B., Yadigaroglu, G., Banerjee, S., 1998. Numerical investigation of the formation of three-dimensional structures in stably stratified mixing layers. Physics of Fluids 10, 1449−1473.

Cortesi, A. B., Smith, B. L., Yadigaroglu, G., Banerjee, S., 1999. Numerical investigation of the entrainment and mixing process in neutral and stably-stratified mixing layers. Physics of Fluids 11, 162−185.

Courant, R., Friedrichs, K., Lewy, H., 1928. Über die partiellen Differenzengleichungen der mathematischen Physik. Mathematische Annalen 100, 32–74.

Daly, B. J., Harlow, F. H., 1970. Transport Equations of Turbulence. Physics of Fluids 13, 2634−2649.

Deleersnijder, E., Luyten, P., 1994. On the practical advantages of the Mellor Yamada level 2.5 turbulence closure applied to marine modelling. Applied Mathematical Modelling 18, 55−62.

Djeridi, H., Braza, M., Perrin, R., Harran, G., Cid, E., and Cazin, S., 2003. Near-Wake Turbulence Properties around a Circular Cylinder at High Reynolds Number. Flow, Turbulence and Combustion 71: 19−34.

Ellison, T. H., Turner, J. S., 1959. Turbulent entrainment in stratified flows. Journal of Fluid Mechanics 6, 423−448.

Feistel, R., Nausch, G., Matthäus, W., Hagen, E., 2003. Temporal and spatial evolution of the Baltic deep water renewal in spring 2003. Oceanologica 45 623−642.

Fernando, H. J. S., 1991. Turbulent mixing in stratified fluids. Annual Review of Fluid Mechanics 23, 455−493.

Ferziger, J. H., Peric, M., 2002. Computational Methods for Fluid Dynamics, 3rd, rev. edition. Springer Verlag, Berlin. 423 pp.

Fischer, H. B., List, E. J., Koh, R. C., Y., Imberger, J., Brooks, N. H., 1979. Mixing in Inland and Coastal waters. Academic Press, 483 pp.

Fluent, 2005. Fluent 6.2 User's Guide. Fluent Inc. Lebanon, NH, USA.

Franke, R., 1991. Numerische Berechnung der instationären Wirbelablösung hinter zylindrischen Körpern. Dissertation. SFB 210 − Strömungsmechanische Bemessungsgrundlagen für Bauwerke, Universität Karlsruhe, SFB 210 – T 90, 181 pp.

Galperin, B., Kantha, L. H., Hassid, S., Rosati, A., 1988. A quasi equilibrium turbulent energy model for geophysical flows. Journal of the Atmospheric Sciences 45, 55−62.

Germano, M., Piomelli, U., Moin, P., Cabot, W. H.. 1991. A Dynamic Subgrid-Scale Eddy Viscosity Model. Physics of Fluids A 3, 1760−1765.

Germano, M., 1992. Turbulence: The filtering approach. Journal of Fluid Mechanics 238, 325−336.

Gibson, M. M., Launder, B. E., 1978. Ground Effects on Pressure Fluctuations in the Atmospheric Boundary Layer. Journal of Fluid Mechanics 86, 491−511.

GIGAWIND, 2004. Bau- und umwelttechnische Aspekte von Offshore Windenergieanlagen. Abschlussbericht 2000 − 2003. Universität Hannover. 60 pp. available at: www.gigawind.de

Halpern, D., 1974. Observations of the deepening of the wind-mixed layer in the north-east Pacific Ocean. Journal of Physical Oceanography 4, 454−466.

Holmboe, J., 1962. On the behavior of symmetric waves in stratified shear layers. Geofysiske Publikasjoner 24, 67−113.

Holt, S. E., Koseff, J. R., Ferziger, J. H., 1992. A numerical study of the evolution and structure of homogeneous stably stratified sheared turbulence. Journal of Fluid Mechanics 237, 499−540.

Howard, L. N., 1961. Note on a paper of John W. Miles. Journal of Fluid Mechanics 10, 509−512.

Issa, R. I., 1986. Solution of Implicitly Discretized Fluid Flow Equations by Operator Splitting. Journal of Computational Physics 62, 40−65.

Ivey, G. N., Imberger, J., 1991. On the Nature of Turbulence in a Stratified Fluid. Part I: The Energetics of Mixing. Journal of Physical Oceanography 21, 650−658.

Jakobitz, F. G., Sarkar, S., van Atta, C. W., 1997. Direct numerical simulations of the turbulence evolution in a uniformly sheared and stably stratified flow. Journal of Fluid Mechanics 342, 231−261.

Jongen, T., 1992. Simulation and Modeling of Turbulent Incompressible Flows. PhD thesis, EPF Lausanne, Lausanne, Switzerland.

Jürgensen, C., 1989. Entrainment introduced by piers, dams, and ships in a stratified channel flow. Dissertation. Series Paper 48, Institute of Hydrodynamics and Hydraulic Engineering, Technical University of Denmark, Lyngby, Denmark, 197pp.

Kader, B., 1981. Temperature and Concentration Profiles in Fully Turbulent Boundary Layers. International Journal of Heat and Mass Transfer 24, 1541−1544.

Kantha, L. H., Clayson, C. A., 1994. An Improved Mixed Layer Model for Geophysical Applications. Journal of Geophysical Research 99, 25235−25266.

Kato, H., Phillips, O. M., 1969. On the penetration of a turbulent layer into stratified fluid. Journal of Fluid Mechanics 37, 643−655.

Kato, M., Launder, B. E., 1993. The Modelling of Turbulent Flow around Stationary and Vibrating Square Cylinders. Proceedings of the 9th Symposium on Turbulent Shear Flows, Kyoto, 10-4-1.

Kolmogorov, A. N., 1941. The local structure of turbulence in incompressible viscous fluid for very large Reynolds numbers, Doklady Akademii Nauk SSSR [Proceedings of the Academy of Sciences of the USSR], Vol. 30: 299-303. Reprinted in English: Proceedings of the Royal Society of London, Series A: Mathematical and Physical Sciences, Vol. 434, No. 1890: 9−13.

Kolmogorov, A. N., 1941. Dissipation of energy in locally isotropic turbulence, Doklady Akademii Nauk SSSR, Vol. 32, pages 16-18. Reprinted in English: Proceedings of the Royal Society of London, Series A: Mathematical and Physical Sciences, Vol. 434, No. 1890, 15−17.

Kolmogorov, A. N., 1942. Equations of turbulent motion of an incompressible fluid. Izvestia Akademii Nauk SSSR, Seria Fizichezka 6, 56−58. Reprinted in English: Selected works, vol. I: Mathematics and mechanics, Kluwer, Amsterdam, 1991, 328–330.

Launder, B. E., Spalding, D. B., 1972. Lectures in Mathematical Models of Turbulence. Academic Press, London, England.

Launder, B. E., Reece, G. J., Rodi, W., 1975. Progress in the Development of a Reynolds Stress Turbulence Closure. Journal of Fluid Mechanics, 68, 537−566.

Launder, B. E., 1990. Phenomenological Modelling: Present… and Future? In: Lumley, J.L. (ed.), Whither Turbulence? Turbulence at the Crossroads. Springer Verlag, Berlin, pp. 439−485.

Leonard, B. P., 1979. A Stable and Accurate Convection Modelling Procedure based on Quadratic Upstream Interpolation. Computational Methods in Applied Mechanics and Engineering 19, 59−98.

Lien, F. S., Leschziner, M. A., 1994. Assessment of Turbulence Transport Models Including Non-Linear RNG Eddy-Viscosity Formulation and Second Moment Closure. Computers and Fluids 23, 983−1004.

Lilly, D. K., 1967. The representation of small-scale turbulence in numerical simulation experiments. Proceedings of the IBM Scientific Computing Symposium on Environmental Sciences, IBM Forum No. 320, 195−210.

Lilly, D. K., 1992. A Proposed Modification of the Germano Subgrid-Scale Closure Method. Physics of Fluids A 4, 633−635.

Lübcke, H., Schmidt, S., Rung, T., Thiele, F., 2001. Comparison of LES and RANS in bluff-body flows. Journal of Wind Engineering and Industrial Aerodynamics 89, 1471−1485.

Luyten, P. J., Deleersnijder, E., Ozer, J., Ruddik, K. G., 1996. Presentation of a Family of Turbulence Closure Models for Stratified Shallow Water Flows and Preliminary Application to the Rhine Outflow Region. Continental Shelf Research 16, 101−130.

Malcherek, A, 2001. Hydromechanik der Fließgewässer. Habilitation, Institut für Strömungsmechanik und Elektronisches Rechnen im Bauwesen, Universität Hannover.

Matthäus, W., Franck, H., 1992. Characteristics of major Baltic inflows − a statistical analysis. Continental Shelf Research 12, 1375−1400.

Mellor, G. L., Yamada, T., 1982. Development of a Turbulence Closure Model for Geophysical Fluid Problems. Review of Geophysics 20, 851−875.

Menter, F. R., 1994. Two-Equation Eddy-Viscosity Turbulence Models for Engineering Applications. AIAA Journal, 32 (8), 1598−1605.

Miles, J. W., 1961. On the stability of heterogeneous shear flows. Journal of Fluid Mechanics 10, 496–508.

Moum, J. N., Caldwell, D. R., Paulson, C. A., 1989. Mixing in the equatorial surface layer. Journal of Geophysical Research 94, 2005−2021.

Moum, J. N., Perlin, A, Klymak, J. M., Levine, M. D., Boyd, T., Kosro, P. M., 2004. convectively-driven mixing in the bottom boundary layer. Journal of Physical Oceanography 34, 2189−2202.

Munk, W. H., Anderson, E. R., 1948. Notes on the Theory of the Thermocline. Journal of Marine Research 3, 276−295.

Nausch, G., Matthäus, W., Feistel, R., 2003. Hydrographic and hydrochemical conditions in the Gotland Deep area between 1992 and 2003. Oceanologica 45, 557−569.

Nikuradse, J., 1932. Srömungsgesetzte in glatten Röhren. Verein deutscher Ingenieure (VDI), Forschungsheft Nr. 356, Berlin.

Nikuradse, J., 1933. Srömungsgesetzte in rauhen Röhren. Verein deutscher Ingenieure (VDI), Forschungsheft Nr. 361, Berlin.

Orszag, S. A., Staroselsky, I., Flannery, W. S. and Zhang, Y., 1996. Introduction to renormalization group modeling of turbulence. In Gatski, T. B., Hussaini, M. Y., and Lumley, J. L. (eds.), Simulation and Modeling of Turbulent Flows, Oxford University Press, New York, 155−183.

Osborn, T. R., 1980. Estimates of the Local Rate of Vertical Diffusion from Dissipation Measurements. Journal of Physical Oceanography 10, 83−89.

Patankar, S.V., Spalding, D.B., 1972. A Calculation Procedure for Heat, Mass and Momentum Transfer in Three-Dimensional Parabolic Flows. International Journal for Heat and Mass Transfer 15, 1787−1806.

Patel, V. C., Rodi, W., Scheurer, G., 1985. Turbulence Models for Near-Wall and Low Reynolds Number flows: A Review. AIAA Journal 23, 1308−1319.

Pedersen, Bo F., 1980. A monograph on turbulent entrainment and friction in two-layer stratified flow. Dissertation. Series Paper 25, Institute of Hydrodynamics and Hydraulic Engineering, Technical University Denmark, Lyngby, Denmark, 397 pp.

Pedersen, Bo F., 1986. Environmental Hydraulics: Stratified Flows. Lecture Notes on Coastal and Estuarine Studies 18, Springer Verlag, 278 pp.

Pope, S. B., 2000. Turbulent Flows. Cambridge University Press, Cambridge, UK, 771 pp.

Prandke, H., 2005. Microstructure sensors. In Baumert, H. Z., Simpson, J., and Sündermann, J. (eds.), Marine Turbulence: Theories, Observation, and Models. Results of the CARTUM Project, Cambridge University Press, 101−109.

Prandtl, L., 1925. Bericht über Untersuchungen zur ausgebildeten Turbulenz. ZAMM, 5 (2): 136–139.

Prandtl, L., 1945. Über ein neues Formelsystem für die ausgebildete Turbulenz. Nachrichten der Akademie der Wissenschaften Göttingen, Math.-Phys. Klasse, 6.

Prasad, A., and Williamson, C. H. K., 1997. The instability of the shear layer separating from a bluff body. Journal of Fluid Mechanics 333: 375−402.

Price, J. F., 1979. On the scaling of stress-driven entrainment experiments. Journal of Fluid Mechanics 90, 509−529.

Reynolds, O, 1895. On the Dynamical Theory of Incompressible Viscous Fluids and the Determination of the Criterion. Philosophical Transactions of the Royal Society, A 186, 123−164.

Reynolds, W. C., Hussain, A. K. M. F., 1972. The Mechanics of an Organized Wave in Turbulent Shear Flow. Part 3: Theoretical Models and Comparisons with Experiments. Journal of Fluid Mechanics 54, 263−288.

Rodi, W., 1976. A New Algebraic Relation for Calculating the Reynolds Stresses. Zeitschrift für Angewandte Mathematik und Mechanik 56, T219−T221.

Rodi, W., 1980. Turbulence Models and their Application in Hydraulics − A state of the Art Review. Technical Report, Institute of the Association for Hydraulic Research, Delft, The Netherlands.

Rodi, W., 1987. Examples of calculation methods for flow and mixing in stratified flows. Journal of Geophysical Research 92, 5305−5328.

Rohr, J. J., 1985. An experimental study of evolving turbulence in uniform mean shear flows with and without stable stratification. Dissertation. University of California, San Diego. 271 pp.

Roshko, A., 1961. Experiments on the Flow Past a Circular Cylinder at Very High Reynolds Numbers. Journal of Fluid Mechanics 10, 345−356.

Saddoughi, S. G., Veeravalli, S. V., 1994. Local Isotropy in Turbulent Boundary Layers at High Reynolds Number, Journal of Fluid Mechanics 268, 333−372.

Schumann, U., Gerz, T., 1995. Turbulent Mixing in Stably Stratified Shear Flows. Journal of Applied Meteorology 34, 33−48.

Shih, T.-H., Liou, W. W., Shabbir, A., Yang, Z. and Zhu, J., 1995. A New k-ε Eddy-Viscosity Model for High Reynolds Number Turbulent Flows - Model Development and Validation. Computers Fluids, 24(3), 227-238.

Shih, L. H., Koseff, J. R., Ferziger, J. H., Rehmann, C. R., 2000. Scaling and parameterization of stratified homogenous turbulent shear flow. Journal of Fluid Mechanics 412, 1−20.

Shih, L. H., Koseff, J. R., Ivey, G. N., Ferziger, J. H., 2005. Parameterization of turbulent fluxes and scales using homogeneous sheared stably stratified turbulence simulations. Journal of Fluid Mechanics 525, 193−214.

Simpson, J. E., 1987. Gravity currents: in the environment and the laboratory. Ellis Horwood series in environmental science, Ellis Horwood Limited, England, 244 pp.

Smagorinsky, J., 1963. General Circulation Experiments with the Primitive Equations. I. The Basic Experiment. Monthly Weather Review 91, 99−164.

Son, J. S., Hanratty, T. J., 1969. Velocity gradients at the wall for flow around a cylinder at Reynolds numbers from 5 x 10^3 to 10^5. Journal of Fluid Mechanics 35, 353 − 368.

Stigebrandt, A., 1985. A model for the seasonal pycnocline in rotating systems with application to the Baltic proper. Journal of Physical Oceanography 15, 1392−1404.

Stigebrandt, A., 1987. A model for the vertical circulation in the Baltic deep water. Journal of Physical Oceanography 17, 1772−1785.

Stewart, R. W., 1959. The problem of diffusion in a stratified fluid. Advances in Geophysics 6, 303−311.

Strang, E. J., Fernando, H. J. S., 2001. Entrainment and mixing in stratified shear flows. Journal of Fluid Mechanics 428, 349−386.

Thorpe, S. A., 1987. Transitional phenomena and the development of turbulence in stratified fluids: a review. Journal of Geophysical Research 92C, 5231−5248.

Turner, J. S., 1986. Turbulent entrainment: The development of the entrainment assumption, and its application to geophysical flows. Journal of Fluid Mechanics 173, 431−471.

Turner, J. S., 1973. Buoyancy Effects in Fluids. Cambridge University Press, 367 pp.

Umlauf, L., Burchard, H., Hutter, K., 2003. Extending the k-ω turbulence model towards oceanic applications, Ocean Modeling 5, 195−218.

Umlauf, L., Burchard, H., 2003. A Generic Length-Scale Equation for Geophysical Turbulence Models. Journal of Marine Research 61, 235−265.

Umlauf, L., Burchard, H., 2005. Second-order turbulence closure models for geophysical boundary layers. A review of recent work. Continental Shelf Research 25, 795−827.

Umlauf, L., Burchard, H., Bolding, K., 2005. GOTM − Scientific Documentation Version 3.2, Marine Science Reports No. 63, IOW − Institut für Ostseeforschung Warnemünde. See also: http://www.gotm.net.

UNESCO, 1981a. The Practical Salinity Scale 1978 and the International Equation of State of Seawater 1980. Tenth report of the Joint Panel on Oceanographic Tables and Standards, Sidney, B.C., September 1980. UNESCO Technical Papers in Marine Science, No. 36, 25 pp.

UNESCO 1981b. Background papers and supporting data on the Practical Salinity Scale 1978. UNESCO Technical Papers in Marine Science, No. 37. 144 pp.

Versteek, H. K., Malalasekera, W., 1996. An Introduction to Computational Fluid Mechanics: The Finite Volume Method. Prentice Hall. 272 pp.

van Doormal, J. P., Raithby, G. D., 1984. Enhancements of the SIMPLE Method for Predicting Incompressible Fluid Flows. Numerical Heat Transfer 7, 147−163.

von Kármán, T., 1930. Mechanische Ähnlichkeit und Turbulenz. Proceedings of the Third International Congress on Applied Mechanics, Stockholm, 85−105.

Wilcox, D. C., 1988. Reassessment of the scale-determining equation for advanced turbulence models. AIAA Journal 26 (11), 1299−1310.

Wilcox, D. C., 1998. Turbulence modeling for CFD. DCW Industries, Inc., La Canada, California.

Yakhot, V. and Orszag, S. A., 1986. Renormalization group analysis of turbulence. I. Basic theory. Journal of Scientific Computing 1, 3−51.

Zdrakovich, M. M., 1997. Flow around Circular Cylinders, Vol. 1: Fundamentals. Oxford University Press, New York.

Liste der bereits erschienenen Institutsberichte

01/1970 **Holz, K.-P.** Ergänzung des Verfahrens finiter Elemente durch Ecksingularitäten zur verbesserten Berechnung schiefwinkliger Platten. Dissertation, Techn. Univ. Hannover, 1970

02/1971 **Ehlers, K.-D.** Berechnung instationärer Grund- und Sickerwasserströmungen mit freier Oberfläche nach der Methode finiter Elemente. Dissertation, Techn. Univ. Hannover, 1971

03/1971 **Meissner, U.** Berechnung von Schalen unter großen Verschiebungen und Verdrehungen bei kleinen Verzerrungen mit Hilfe finiter Dreieckselemente. Dissertation, Techn. Univ. Hannover, 1971

04/1972 **Grotkop, G.** Die Berechnung von Flachwasserwellen nach der Methode der finiten Elemente. Dissertation, Techn. Univ. Hannover, Sonderdruck aus dem Jahresbericht 1971 d. SFB 79, H. 2, 1972

05/1973 **Schulze, K.-W.** Eine problemorientierte Sprache für die Dynamik offener Gerinne. Dissertation, Techn. Univ. Hannover, Mitteil. d. SFB 79, Heft 1, 1973

06/1977 **Beyer, A.** Die Berechnung großräumiger Grundwasserströmungen mit Vertikalstruktur mit Hilfe der Finite-Element-Methode. Dissertation, Fortschrittberichte der VDI-Zeitschriften, Reihe 4, Nr. 34, 1977

07/1977 **Ebeling, H.** Berechnung der Vertikalstruktur wind- und gezeitenerzeugter Strömungen nach der Methode der finiten Elemente. Dissertation, Fortschrittberichte der VDI-Zeitschriften, Reihe 4, Nr. 32, 1977

08/1977 **Gärtner, S.** Zur Berechnung von Flachwasserwellen und instationären Transportprozessen mit der Methode der finiten Elemente. Dissertation, Fortschrittberichte der VDI-Zeitschriften, Reihe 4, Nr. 30, 1977

09/1977 **Herrling, B.** Eine hybride Formulierung in Wasserständen zur Berechnung von Flachwasserwellen mit der Methode finiter Elemente. Dissertation, Fortschrittberichte der VDI-Zeitschriften, Reihe 4, Nr. 37, 1977

10/1979 **Hennlich, H.-H.** Aeroelastische Stabilitätsuntersuchung von Linientragwerken. Dissertation, Fortschrittberichte der VDI-Zeitschriften, Reihe 4, Nr. 49, 1979

11/1979 **Kalocay, E.** Zur numerischen Behandlung der Konvektions-Diffusions-Gleichung im Hinblick auf das inverse Problem. Dissertation, Univ. Hannover, 1979

12/1980 **Januszewski, U**. Automatische Eichung für ein- und zweidimensionale, hydrodynamisch-numerische Flachwassermodelle. Dissertation, Univ. Hannover, Fortschrittberichte der VDI-Zeitschriften, Reihe 4, Nr. 58, 1980

13/1982 **Carbonel Huaman, C.A.A.** Numerisches Modell der Zirkulation in Auftriebsgebieten mit Anwendung auf die nordperuanische Küste. Dissertation, Univ. Hannover, 1982

14/1985 **Tuchs, M.** Messungen und Modellierung am Deep Shaft. Dissertation, Univ. Hannover, 1984

15/1985 **Theunert, F.** Zum lokalen Windstau in ästuarien bei Sturmfluten - Numerische Untersuchungen am Beispiel der Unterelbe. Dissertation, Univ. Hannover, 1984

16/1985 **Perko, H.-D.** Gasausscheidung in instationärer Rohrströmung. Dissertation, Univ. Hannover, 1984

17/1985 **Crotogino, A.** Ein Beitrag zur numerischen Modellierung des Sedimenttransports in Verbindung mit vertikal integrierten Strömungsmodellen. Dissertation, Univ. Hannover, 1984

18/1985 **Rottmann-Söde, W.** Ein halbanalytisches FE-Modell für harmonische Wellen zur Berechnung von Wellenunruhen in Häfen und im Küstenvorfeld. Dissertation, Univ. Hannover, 1985

19/1985 **Nitsche, G.** Explizite Finite-Element-Modelle und ihre Naturanwendungen auf Strömungsprobleme in Tidegebieten. Dissertation, Univ. Hannover, 1985

20/1985 **Vera Muthre, C.** Untersuchungen zur Salzausbreitung in Ästuarien mit Taylor'schen Dispersionsmodellen. Dissertation, Univ. Hannover, 1985

21/1985 **Schaper, H.** Ein Beitrag zur numerischen Berechnung von nichtlinearen kurzen Flachwasserwellen mit verbesserten Differenzenverfahren. Dissertation, Univ. Hannover, 1985

22/1986 **Urban, C.** Ein Finite-Element-Verfahren mit linearen Ansätzen für stationäre zweidimensionale Strömungen. Dissertation, Univ. Hannover, 1986

23/1987 **Heyer, H.** Die Beeinflussung der Tidedynamik in ästuarien durch Steuerung - Ein Beitrag zur Anwendung von Optimierungsverfahren in der Wasserwirtschaft. Dissertation, Univ. Hannover, 1987

24/1987 **Gärtner, S.** Zur diskreten Approximation kontinuumsmechanischer Bilanzgleichungen. Institutsbericht, davon 4 Abschnitte als Habilitationsschrift angenommen, Univ. Hannover, 1987

25/1988 **Rogalla, B.U.** Zur statischen und dynamischen Berechnung geometrisch nichtlinearer Linientragwerke unter Strömungs- und Wellenlasten. Dissertation, Univ. Hannover, 1988

26/1990 **Lang, G.** Zur Schwebstoffdynamik von Trübungszonen in Ästuarien. Dissertation, Univ. Hannover, 1990

27/1990 **Stittgen, M.** Zur Fluid-Struktur-Wechselwirkung in flexiblen Offshore-Schlauchleitungen. Dissertation, Univ. Hannover, 1990

28/1990 **Wollrath, J.** Ein Strömungs- und Transportmodell für klüftiges Gestein und Untersuchungen zu homogenen Ersatzsystemen. Dissertation, Univ. Hannover, 1990

29/1991 **Kröhn, K.-P.** Simulation von Transportvorgängen im klüftigen Gestein mit der Methode der Finiten Elemente. Dissertation, Univ. Hannover, 1991

30/1991 **Lehfeldt, R.** Ein algebraisches Turbulenzmodell für Ästuare. Dissertation, Univ. Hannover, 1991

31/1991 **Prüser, H.-H.** Zur mathematischen Modellierung der Interaktion von Seegang und Strömung im flachen Wasser. Dissertation, Univ. Hannover, 1991

dito **Schröter, A.** Das numerische Seegangsmodell BOWAM2 1990 – Grundlagen und Verifikationen. Univ. Hannover, 1991

32/1992 **Leister, K.** Anwendung numerischer Flachwassermodelle zur Bestimmung von Wasserlinien. Dissertation, Univ. Hannover, 1992

33/1993 **Ramthun, B.** Zur Druckstoßsicherung von Fernwärmenetzen und zur Dynamik von Abnehmeranlagen. Dissertation, Univ. Hannover, 1993

34/1993 **Helmig, R.** Theorie und Numerik der Mehrphasenströmungen in geklüftet-porösen Medien. Dissertation, Univ. Hannover, 1993

35/1994 **Plüß, A.** Netzbearbeitung und Verfahrensverbesserungen für Tidemodelle nach der Finiten Element Methode. Dissertation, Univ. Hannover, 1994

36/1994 **Nöthel, H.** Statistisch-numerische Beschreibung des Wellen- und Strömungsgeschehens in einem Buhnenfeld. Dissertation, Univ. Hannover, 1994

37/1994 **Shao, H.** Simulation von Strömungs- und Transportvorgängen in geklüfteten porösen Medien mit gekoppelten Finite-Element- und Rand-Element-Methoden. Dissertation, Univ. Hannover, 1994

38/1994 **Stengel, T.** Änderungen der Tidedynamik in der Deutschen Bucht und Auswirkungen eines Meeresspiegelanstiegs. Dissertation, Univ. Hannover, 1994

39/1994 **Schubert, R.** Ein Softwaresystem zur parallelen interaktiven Strömungssimulation und -visualisierung. Dissertation, Univ. Hannover, 1994

40/1994 **Alm, W.** Zur Gestaltung eines Informationssystems im Küsteningenieurwesen. Dissertation, Univ. Hannover, 1994

41/1994 **Benali, H.** Zur Kopplung von FEM- und CAD-Programmen im Bauwesen über neutrale Datenschnittstellen. Dissertation, Univ. Hannover, 1994

42/1995 **Schröter, A.** Nichtlineare zeitdiskrete Seegangssimulation im flachen und tieferen Wasser. Dissertation, Univ. Hannover, 1995

43/1995 **Blase, Th.** Ein systemtechnischer Ansatz zur Modellierung von Hydraulik, Stofftransport und reaktionskinetischen Prozessen in Kläranlagen. Dissertation, Univ. Hannover, 1995

44/1995 **Malcherek, A.** Mathematische Modellierung von Strömungen und Stofftransportprozessen in Ästuaren. Dissertation, Univ. Hannover, 1995

45/1995 **Lege, T.** Modellierung des Kluftgesteins als geologische Barriere für Deponien. Dissertation, Univ. Hannover, 1995

46/1996 **Arnold, H.** Simulation dammbruchinduzierter Flutwellen. Dissertation, Univ. Hannover, 1996

47/1996 **Kolditz, O.** Stoff- und Wärmetransport im Kluftgestein. Habilitation, Univ. Hannover, 1996

48/1996 **Hunze, M.** Numerische Modellierung reaktiver Strömungen in oberflächenbelüfteten Belebungsbecken. Dissertation, Univ. Hannover, 1996

49/1996 **Wollschläger, A.** Ein Random-Walk-Modell für Schwermetallpartikel in natürlichen Gewässern. Dissertation, Univ. Hannover, 1996

50/1997 **Feist, M.** Entwurf eines Modellierungssystems zur Simulation von Oberflächengewässern. Dissertation, Univ. Hannover, 1997

51/1997 **Hinkelmann, R.** Parallelisierung eines Lagrange-Euler-Verfahrens für Strömungs- und Stofftransportprozesse in Oberflächengewässern. Dissertation, Univ. Hannover, 1997

52/1997 **Barlag, C.** Adaptive Methoden zur Modellierung von Strofftransport im Kluftgestein. Dissertation, Univ. Hannover, 1997

53/1997 **Saberi-Haghighi, K.** Zur Ermittlung der verformungsabhängigen Windbelastung bei Hängedächern. Dissertation, Univ. Hannover, 1997

54/1998 **Krüger, A.** Physikalische Prozesse im Nachklärbecken - Modellbildung und Simulation. Dissertation, Univ. Hannover, 1998

55/1998 **Wolters, A. H.** Zur Modellierung des instationären thermohydraulischen Betriebsverhaltens von Fernwärmeanlagen. Dissertation, Univ. Hannover, 1998

56/1999 **Jankowski, J. A.** A non-hydrostatic model for free surface flows. Dissertation, Univ. Hannover, 1999

57/1999 **Kopmann, R.** Mehrdimensionale Effekte in dimensionsreduzierten Gewässergütemodellen. Dissertation, Univ. Hannover, 1999

58/1999 **Kahlfeld, A.** Numerische Seegangsmodellierung als Bestandteil einer funktionellen Hafenplanung. Dissertation, Univ. Hannover, 1999

59/1999 Festschrift zum 60. Geburtstag von Prof. Dr.-Ing. Werner Zielke. Univ. Hannover, 1999

60/2000 **Kolditz, O., Zielke, W., Wriggers, P., Dürbaum, H.-J., Wallner, M.** 3. Workshop Kluft-Aquifere - Gekoppelte Prozesse in Geosystemen. Univ. Hannover, 2000

61/2001 **Malcherek, A.** Hydromechanik der Fließgewässer. Habilitation, Univ. Hannover, 2001

62/2001 **Thorenz, C.** Model Adaptive Simulation of Multiphase and Density Driven Flow in Fractured and Porous Media. Dissertation, Univ. Hannover, 2001

63/2001 **Kaiser, R.** Gitteradaption für die Finite-Elemente-Modellierung gekoppelter Prozesse in geklüftet-porösen Medien. Dissertation, Univ. Hannover, 2001

64/2001 **Rother, T.** Geometric Modelling of Geo-Systems. Dissertation, Univ. Hannover, 2001

65/2001 **Habbar, A.** Direkte und inverse Modellierung reaktiver Transportprozesse in klüftig-porösen Medien. Dissertation, Univ. Hannover, 2001

66/2001 **Weilbeer, H**.: Strömung und Kolkung an Wasserbauwerken. Dissertation, Univ. Hannover, 2001.

67/2002 **Hoyme**, H.: Mesoskalige morphodynamische Modellierungen am Beispiel der Meldorfer Bucht. Dissertation, Univ. Hannover, 2002

68/2004 **Moenickes, S**.: Grid Generation for Simulation of Flow and Transport Processes in Fractures-Porous Media. Dissertation, Univ. Hannover, 2004

69/2004 **Strybny, J.:** Ein phasenauflösendes Seegangsmodell zur Ermittlung von Bemessungsparametern für Küstenstrukturen. Dissertation, Univ. Hannover 2004

70/2004 **Weilbeer, J.:** Modellierung des Partikeltransports in Nachklärbecken als Mehr-phasenströmung. Dissertation, Univ. Hannover 2004

71/2006 **Mittendorf, K.:** Hydromechanical Design Paramters and Design Loads for Offshore Wind Energy Converters, Dissertation, Leibniz Univ. Hannover 2006

72/2006 **Kohlmeier, M.:**, Coupling of thermal, hydraulic and mechanical processes for geotechnical simulations of partially saturated porous media, Dissertation, Leibniz Univ. Hannover 2006

73/2006 **Schumacher, S.:**, Leistungsbestimmende Prozesse in Nachklärbecken – Einflussgrößen, Modellbildung und Optimierung , Dissertation, Leibniz Univ. Hannover 2006

74/2008 **Ziefle, G.:** Modeling Aspects of Coupled Hydraulic-Mechanical Processes in Clay Material, Dissertation, Leibniz Univ. Hannover 2008

75/2008 **Schimmels, S.:** Numerical Simulation of the Influence of Circular Cylinders on Mixing and Entrainment in Natural Density Currents, Dissertation, Leibniz Univ. Hannover 2007